DISSERTATION

TOWARD AN IMPROVED UNDERSTANDING OF THE SYNOPTIC AND MESOSCALE DYNAMICS GOVERNING NOCTURNAL HEAVY-RAIN-PRODUCING MESOCALE CONVECTIVE SYSTEMS

Submitted by

John M. Peters

Department of Atmospheric Science

In partial fulfillment of the requirements

For the Degree of Doctor of Philosophy

Colorado State University

Fort Collins, Colorado

Summer 2015

Doctoral Committee:

Advisor: Russ S. Schumacher

Sue van den Heever
Richard Johnson
Jeffrey D. Niemann
Morris Weisman

ABSTRACT

TOWARD AN IMPROVED UNDERSTANDING OF THE SYNOPTIC SCALE CONDITIONS ASSOCIATED WITH, AND THE DYNAMICS GOVERNING NOCTURNAL HEAVY-RAIN-PRODUCING MESOCALE CONVECTIVE SYSTEMS

In the first stage of this research, rotated principal component analysis was applied to the atmospheric fields associated with a large sample of heavy-rain-producing mesoscale convective systems (MCSs) that exhibited the training-line adjoining stratiform (TL/AS) morphology. Cluster analysis in the subspace defined by the leading two resulting principal components revealed two sub-types with distinct synoptic and mesoscale characteristics, which are referred to as warm-season type and synoptic type events respectively.

Synoptic type events, which tended to exhibit greater horizontal extent than warm-season type events, typically occurred downstream of a progressive upper-level trough, along a low-level potential temperature gradient with the warmest air to the south and southeast. Warm-season type events on the other hand occurred within the right entrance region of a minimally-to-anticyclonically curved upper level jet streak, along a low-level potential temperature gradient with the warmest low-level air to the southwest. Synoptic-scale forcing for ascent was stronger in synoptic type events, while low-level moisture was greater in warm-season type events. Warm-season type events were frequently preceded by the passage of a trailing stratiform (TS) type MCS, while synoptic type events often occurred prior to the passage of a TS type system.

An idealized modeling framework was developed to simulate a quasi-stationary heavy-rain-producing MCSs. A composite progression of atmospheric fields from warm season TL/AS MCSs was used as initial and lateral boundary conditions for a numerical simulation of this MCS archetype.

A realistic TL/AS MCS initiated and evolved within a simulated mesoscale environment that featured a low-level jet terminus, maximized low-level warm air advection, and elevated maximum in convective available potential energy. The first stage of MCS evolution featured an eastward moving trailing-stratiform type MCS that generated a surface cold pool. The initial system was followed by rearward off-boundary development (ROD), where a new line of convective cells simultaneously re-developed north of the surface cold pool boundary. Backbuilding persisted on the western end of the new line, with individual convective cells training over a fixed geographic region. The final stage was characterized by a deepening and southward surge of the cold pool, resulting in the weakening and slow southward movement of the training line.

The dynamics of warm season TL/AS MCSs are elucidated through the analysis of the idealized simulation, along with a simulation of an observed case. The environmental conditions external to the MCS contributed to the development of a new convective line west of the initial MCS, and displaced northward of the southwestern flank of the surface OFB. Southwesterly low-level flow was thermodynamically stabilized as it lifted over the southwestern OFB from a pattern of adiabatic cooling below latent heating. This flow traveled 80-100 km northeastward beyond the surface OFB to the point where large-scale lifting sufficiently destabilized the flow for deep convection. These factors explain the geographic offset of the second convective line from the surface OFB left by the forward-propagating MCS. Eventually the surface cold pool became sufficiently deep so that gradual ascent of parcels with moisture and instability over the feature began triggering new convection close to the OFB (rather than 80-100 km away from it), which eventually drove the system southward.

These results suggest that large-scale environmental factors were predominantly responsible for the quasi-stationary behavior of the simulated MCS, though upscale convective feedbacks played an important role in the complexity of the convective evolution.

ACKNOWLEDGEMENTS

This research was supported by National Science Foundation grant AGS-1157425. Stage IV precipitation data were obtained from the UCAR Earth Observing Laboratory. NARR data were obtained from the NCDC nomads server. Special thanks are given to the committee members – Sue van den Heever, Richard Johnson, Jeffrey Niemann, and Morris Weisman for their guidance and support through the process of this research.

We also give thanks to Stan Trier, Matt Parker, Pam Heinselman, Roebber, George Bryan, Elizabeth Thompson, Kelly Mahoney, Gary Lackmann and anonymous peer reviewers for helpful comments and discussion.

TABLE OF CONTENTS

CHAPTER 1

Introduction and Motivation

It has been well established in previous literature that the primary mechanism for heavy-rainfall generation in mesoscale convective systems (MCS) involves the continuous motion of individual convective elements within the larger convective system over a fixed geographic region (Chappell 1986; Corfidi et al. 1996; Doswell et al. 1996; Schumacher and Johnson 2005, 2006 – hereafter SJ2005, SJ2006; Schumacher and Johnson 2008; Schumacher 2009; Peters and Schumacher 2014, hereafter PS2014). Two processes – training and backbuilding of convection – are often at work during such MCS behavior. Training involves a convective line comprised of smaller convective scale updrafts that move in a line-parallel direction, resulting in their repeated motion over a fixed geographic region (often associated with the Training-Line Adjoining Stratiform, TL/AS SJ2005 MCS archetype). Backbuilding involves the repeated upstream (downstream) re-development (decay) of convective updrafts, resulting in a near-zero net motion of the larger convective system that they compose (often associated with the Backbuilding, BB SJ2005 MCS archetype).

The meso-γ (of order 100-1000 km) to synoptic scale (of order 1000-2000 km) characteristics of TL/AS systems were first explicitly cataloged by SJ2005 and SJ2006, though they are similar to the general environments of heavy rain producing MCSs identified by previous authors (e.g. Maddox et al. 1979; Moore et al. 2003). These authors showed that persistent lifting of air with high convective available potential energy (CAPE), and that is nearly saturated over a nearly stationary frontal boundary likely contributed to the geographically persistent behavior of TL/AS systems. The dynamics working on meso-β (of order 10-100 km) to meso-γ scales were addressed in more detail by Schumacher et al. (2010), Trier et al. (2010,

and Keene and Schumacher (2013), who showed local regions of maximized frontagenesis, isentropic up-glide enhanced by parcel displacement over cold pools, and convergence and deformation (sometimes) superimposed on meso-γ to synoptic scale frontal zone contributed to continuous regeneration of new convective cells on the upstream end of an MCS, and thus facilitated training of convection in TL/AS – like systems. It is unclear, however, to what degree the processes are generally at work for TL/AS systems, and few studies of addressed how the affects of convection on its surrounding environment (hereafter referred to as upscale convective feedbacks) influence their training and backbuilding behaviors.

This research intends to fill several gaps in our scientific understanding of TL/AS MCSs. The author first hypothesized that two distinct general synoptic flow patterns promote TL/AS MCSs, and that the convective morphology is of systems differ between the two types of synoptic setups – this hypothesis is addressed in Chapter 2. The author then performed a detailed case study of numerical simulations of an observed flash-flood producing TL/AS system to better understand the dynamics that particular case – this work is addressed in chapter 3. The case study also provided valuable "ground truth" for comparatively general dynamics elucidated by idealized simulations in later chapters. Chapter 4 describes the development of an idealized modeling framework to simulate a TL/AS system, and outlines initial results from that simulation. Chapter 5 analyzes the dynamics that were at work in the idealized simulation, and proposes general mechanisms for the quasi-stationary behavior of TL/AS systems (the general findings from the idealized simulation corroborated findings from the case study simulation in Chapter 3). Finally, Chapter 6 outlines ongoing and future work related to the material here.

The research was originally presented as four separate manuscripts – three of which (Peters and Schumacher 2014, 2015a, 2015b) have already been published in peer-reviewed

journals; one (Peters and Schumacher 2015c) has been submitted to a peer reviewed journal. The four manuscripts have been included as separate self-contained chapters. Each chapter has an introduction, experiment description, analysis of results, and conclusion/discussion.

CHAPTER 2

OBJECTIVE CATEGORIZATION OF HEAVY-RAIN-PRODUCING MCSS

2.1. Introduction

Previous studies of extreme rainfall events in the central and eastern United States (e.g. events that produced reported flash floods, Maddox et al. 1979; events that produced 24-hour precipitation greater than the 50-year recurrence interval for a given location, Schumacher and Johnson 2005; 2006) have shown that a large percentage of them result from mesoscale convective systems (MCSs, on the order of 60-75%). Specifically, MCSs tend to produce extreme rainfall when convective rainfall regions are nearly stationary (Back-building archetype, BB; Fig 1b), or where motion of a linear convective feature is predominantly line-parallel (Training-Line/Adjoining-Stratiform archetype, TL/AS; Fig. 1a), resulting in persistence of convective cells over a particular geographic region (Schumacher and Johnson 2005, 2006).

Composite analysis of such events show that they tend to thrive within an elevated conditionally unstable layer along the northern periphery of a southerly low-level jet, within a region of persistent isentropic upglide and associated large-scale layer lifting (Maddox et al. 1979; Moore et al. 2003; Schumacher and Johnson 2005; Schumacher and Johnson 2008). Since the aforementioned synoptic-scale environment is also conducive to progressive MCSs (which less commonly produce excessive rainfall amounts; e.g., Parker and Johnson 2000; Laing and Fritsch 2000), and sometimes progressive and quasi-stationary MCSs adjacent to one another (e.g. Corfidi 2003; the bow and arrow phenomenon described by Keene and Schumacher 2013), it is of particular meteorological importance to understand the specific meso-alpha to synoptic scale factors that are conducive to slow-moving MCSs (as well as the variability therein).

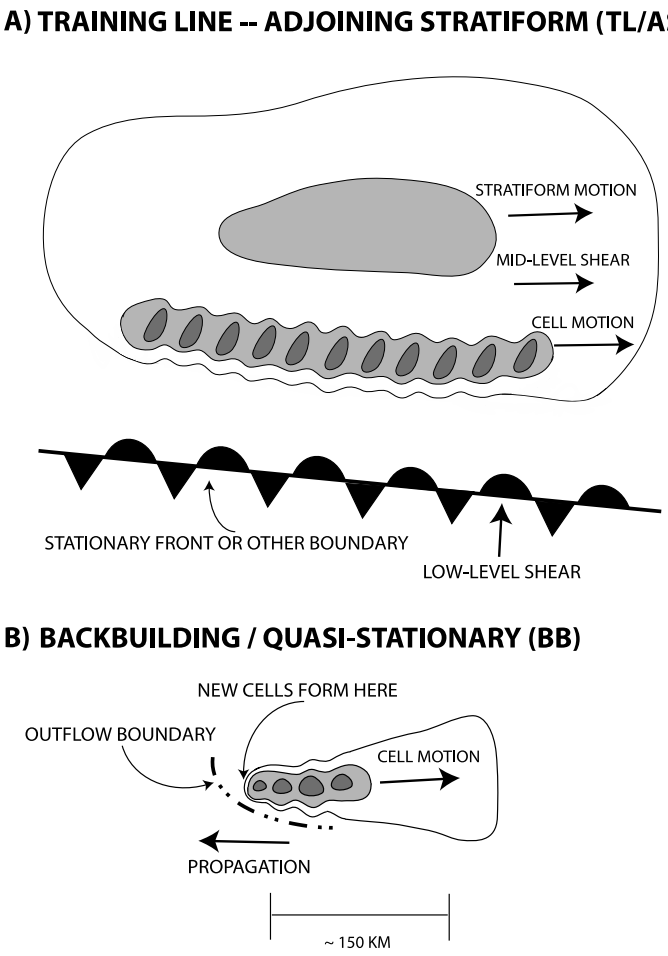

Fig. 2.1. Schematic of the salient radar reflectivity features associated with the two predominant heavy-rain-producing MCS archetypes: (a) TL/AS and (b) BB. From Schumacher and Johnson (2005).

Most composite analyses in previous studies of MCS archetypes have utilized groupings of cases selected based on their subjectively identified radar reflectivity characteristics. While a grouping of MCSs may exhibit similar radar morphologies, there is no guarantee that they occur within similar synoptic scale environments. For instance, previous authors have differentiated "synoptic-type" heavy rainfall, which often involves the passage of multiple distinct MCSs and where convection persists over a fixed geographic region for over 24 hours (Maddox et al. 1979; Schumacher and Johnson 2005) from those events where an individual MCS was responsible for the repeated passage of convection over a fixed location (the later would constitute the BB and

TL/AS categories). The aforementioned distinctions between the two event types were based on a fixed precipitation duration threshold or the subjective determination of whether rainfall areas in radar imagery were composed of one or multiple MCSs. This introduces a non-negligible degree of ambiguity into the event classification process, and there is no guarantee these subjectively determined distinctions define two dynamically different atmospheric phenomena.

Several previous authors have utilized Rotated Principal Component Analysis (RPCA, Schaefer and Doswell 1984; Jones et al. 2004; Mercer et al. 2012) as an objective method for sorting a sample of cases into sub-types based on their synoptic-scale atmospheric conditions (rather than their visual appearance in radar imagery). Composite analyses computed from such synoptic sub-types yield more specific information on the synoptic scale features that drive the phenomena of interest, since events exhibiting similar synoptic states are *objectively* grouped together. In addition, they highlight key patterns of variability within the larger sample of events.

In this study, we apply RPCA to atmospheric fields associated with a large sampling of heavy-rain-producing MCSs to analyze the variability in synoptic-scale atmospheric fields associated with this MCS archetype, and to highlight the role of synoptic-scale processes in the quasi-stationary MCS behavior. This research sets the stage for several subsequent high-resolution numerical modeling studies that will comprehensively analyze the convective scale dynamics of these MCSs. The organization of this paper is as follows. Section 2.2 outlines the results from RPCA on the atmospheric fields associated with the cases we selected. Composites of atmospheric fields for the resulting objectively identified synoptic sub-types are analyzed and compared in Section 2.3, and radar reflectivity characteristics of these sub-types are cataloged and compared in section 2.4. Section 2.5 describes mechanisms for which the synoptic scale

environment contributed to the observed MCS behaviors in radar reflectivity, and our results are summarized and discussed in the context of existing literature and ongoing/future work in section 2.6.

2.2. Statistical Analysis of Events

2.2.a) Case Selection

A database of heavy-rain-producing events was obtained by automatically searching daily gridded precipitation data from the NOAA Climate Prediction Center Daily US Unified Precipitation (NOAA/OAR/ESRL PSD, Boulder, Colorado, USA, from their Web site at http://www.esrl.noaa.gov/psd/) for 24-hour grid point precipitation accumulation totals exceeding 12.5 cm in a 24-hour period between the years of 2002 and 2011 (this search yielded 401 events). The analysis was constructed from rain gauge observations in the continental US, interpolated onto a 0.25 x 0.25 degree grid. The coarse resolution of this precipitation dataset (e.g. relative to stage IV precipitation, which is available on a 4km x 4km grid) served as an additional restricting criterion, whereby highly localized heavy precipitation events (such as those produced by individual convective cells or slow moving supercells) that may have produced over 12.5 cm at a few points on a fine grid did not produce sufficient rainfall on the coarse grid and were thereby intrinsically screened out.

We then subjectively examined WSR-88D composite radar reflectivity from the UCAR MMM Image archive at http://www.mmm.ucar.edu/imagearchive/ in order to identify cases where the heavy rainfall was produced by training of convection associated with an MCS. Rather than attempting to exclude “synoptic-type” and “backbuilding” type events from our database of events, we included all events where >50 dBz echoes persisted over the region of >

12.5 cm of rainfall accumulation for 6 hours or more, and where a well-defined mesoscale convective vortex (MCV) was not present prior to the initiation of the convective system that produced heavy rain (defined as a localized mid-level cyclonic vorticity maxima that developed in association with a preceding MCS and lasted over 24 hours). The idea was to keep the criteria for case selection very general, and to allow the statistical analysis to objectively classify sub-groups. Note that another major difference in the methodology for case selection when compared to Schumacher and Johnson (2005) and other flash flood studies is the usage of a flat rainfall accumulation criterion rather than a recurrence interval criterion (thus removing any dependence on geography from the case selection process). This method identified 50 cases during this 10-yr period, which was a desirable number of cases for the subsequent statistical analysis (i.e. 50 cases was not prohibitively many for computational purposes, and not prohibitively few as to preclude statistically robust results).

2.2.b) RPCA

As discussed in section 2.1, a major caveat to the methodology of subjectively classifying convective morphology based on radar appearance is that a grouping of convective systems may have similar reflectivity characteristics, but exhibit notably contrasting governing dynamics and associated synoptic scale environments. For instance, a composite analysis constructed from a grouping of events exhibiting considerable variability in the placement of a feature such as a low level front would (in the composite analysis) likely reflect a much weaker temperature gradient than that of individual events due to the averaging involved in such a computation. Thus the thermodynamic characteristics of the composite may exhibit little similarity to that of individual events. It is therefore advantageous to group subsets within the larger radar-reflectivity based

classification that exhibit similarities in their associated atmospheric fields, and generate a separate composite for each subset.

A simple objective approach to such event "grouping" is described by Mercer et al. (2012) in the context of tornado outbreaks, where principal component analysis (PCA) was applied to the atmospheric fields associated with a sampling of events, and a cluster analysis was subsequently performed in the subspace defined by the Principal Component (PC) responsible for the largest percentage of the variance in atmospheric fields among cases. The following sub-section describes how we applied this statistical approach to our dataset in order to obtain composites of atmospheric fields for two synoptically distinct heavy-rain-producing MCS sub-types.

For each of the 50 events, three-hourly North American Regional Reanalysis (NARR; Mesinger et al. 2006) data were obtained at three hour intervals for 15 hours prior to 15 hours after the time of the maximum 1-h point rainfall accumulation from the National Centers for Environmental Prediction (NCEP) stage IV precipitation accumulation analyses (Lin and Mitchell 2005). The NARR data were subsetted to a 51 by 51-grid point (1600-km by 1600-km) area centered at the location of the maximum 1-h accumulation. Following the approach of Mercer et al. (2012), the average of three-dimensional temperature, U and V wind components, mixing ratio, and geopotential height fields over all times and cases (i.e. the average was computed over n x m time frames on a given vertical level, where n is the number of cases and m is the number of time frames per case) were subtracted from these data, and variables were subsequently normalized at each vertical level by the standard deviation in space and time at that particular level. This standardization process transformed the five three-dimensional variables of interest into non-dimensional data with a standard deviation of 1, which exhibited consistent

variability horizontally and vertically (The climatological values of the non-standardized data often exhibit considerable vertical variability, which is unfavorable for PCA). The data were then reshaped into a rectangular matrix **Z**, with dimensions of 5NMK x 11*n*, where N and M are the number of grid points in the X and Y directions respectively, K is the number of vertical levels (the factor of 5 on NMK results from there being 5 separate variables considered), and *n* is the number of separate cases (the factor of 11 on *n* results from there being an 11 time frame progression for each case, since data are obtained for 15 hours prior and 15 hours after the time maximum rainfall accumulation at 3 hour intervals in each case). The correlation matrix **R** of **Z** was computed using the formula

$$\mathbf{R} = \frac{1}{5NMK - 1}\mathbf{Z}^T\mathbf{Z}. \quad (2.1)$$

The values in **R** correspond to spatial correlations between atmospheric time "snapshots" rather than temporal correlations between grid points (note that correlation values in **R** reflect correlations between atmospheric fields at different times from the same case, as well as correlations between cases). This choice (to compute spatial rather than temporal correlations) was optimal given that the goal here was to obtain objective comparisons between cases (see Richman 1986 and Mercer et al. 2012 for more in depth discussions on the issue). The decomposition of **Z** in terms of principal components is

$$\mathbf{Z} = \mathbf{F}\mathbf{P}^T, \quad (2.2)$$

where **F** is a 5NMK x 11n matrix of PCs, and **P** is a 11n x 11n matrix of PC loadings, or "scores" (Wilks 2006). **P** was obtained from the eigenvector decomposition of **R**, where

$$\mathbf{R} = \mathbf{E}\mathbf{D}\mathbf{E}^T, \quad (2.3)$$

and

$$\mathbf{P} = \mathbf{E}\mathbf{D}^{1/2}, \quad (2.4)$$

where E is a matrix of the eigenvectors of R, and D is a diagonal matrix of the singular values belonging to each eigenvector in E. Note that PCs themselves need not be computed. We rather focus on the distribution of loadings in the vector subspace defined by the leading two principal components in our subsequent analysis.

2.2.c) Identification of TL/AS Synoptic Sub-types

PC patterns are analogous to Empirical Orthogonal Functions (EOFs) – they correspond to spatial patterns of variability within the atmosphere; for instance, two separate EOFs of a northern hemispheric sea level pressure time series correspond to the Northern Annular Mode and the North Atlantic Oscillation respectively, with a positive (negative) loading on each respective EOF indicating a positive (negative) phase of these patterns (Thompson and Wallace 1998). In the case of our analysis, principal components highlighted the most prominent spatial differences between our cases – i.e. two cases with similar loadings on a particular principal component pattern exhibited more synoptic similarity to each other than two cases with substantially different loadings on that particular pattern. Principal components, by design, are ordered in the matrix **F** based on the magnitude of their contribution to the variance of data set. In practice, a small number of leading principal components often explain a large percentage of the variance of a time series, and the degrees of freedom within a data set are substantially reduced by only considering the variability within the loadings of a few leading patterns.

The orientation of a particular eigenvector associated with a PC may not necessarily point in the local direction of maximum variability within a data set, however, owing to the constraint of orthogonality (all cross correlations between PC loadings are necessarily zero). The orthogonality constraint is optimal when a particular analysis aims to isolate distinct dynamical

processes between individual PCs (e.g. the identification of signatures of dynamically distinct teleconnection patterns); however, it has been shown that the practice of rotating loadings on a number of the leading PCs (Rotated Principal Component Analysis) by means of a linear transformation often results in spatial PC patterns that exhibit more realistic atmospheric structures (i.e. more physically interpretable) than PCs corresponding to un-rotated loadings (a more detailed discussion of this issue is provided by Richman 1986 and Mercer et al. 2012). We therefore performed a VARIMAX rotation (Wilks 2006) on the leading 10 PC loadings of our data and obtained 10 new rotated PC loadings. Note that the ratios of the variance of the leading four PC loadings to the sum of the variance of the leading 10 PC loadings were 0.71, 0.11, 0.07, and 0.04 respectively, indicating that the leading rotated PC explained an overwhelming percentage of the total variance. Patterns within the subspaces defined by trailing PCS (i.e. PCs 3, 4, 5, etc) were also examined – they were ultimately excluded from the case selection analysis due to the lack of coherent multi-modalities within their subspaces.

We then analyzed scatter plots of loadings of our cases in the rotated PC1/PC2 (RPC1/RPC2) subspace (Fig 2, top panel). It was immediately evident that the RPC1/RPC2 loadings did not change considerably for most cases over the 30-hour time progressions considered, since blue lines are short relative to the expanse of the phase space, and do not stray far from the average value over that time period. We therefore considered only the 30-hour time average RPC loadings for each case, which greatly reduced computation times by reducing the number of data points from 550 to 50.

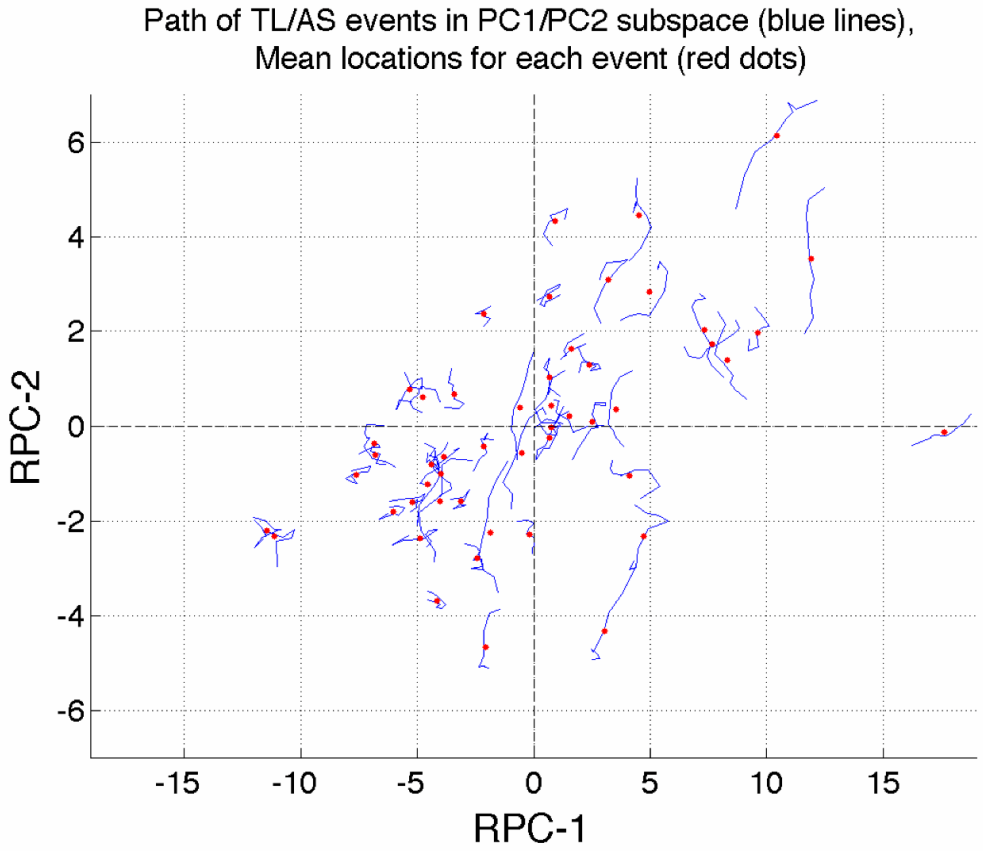
Path of TL/AS events in PC1/PC2 subspace (blue lines),
Mean locations for each event (red dots)
RPC-2
RPC-1
6
4
2
0
-2
-4
-6
-15
-10
-5
0
5
10
15

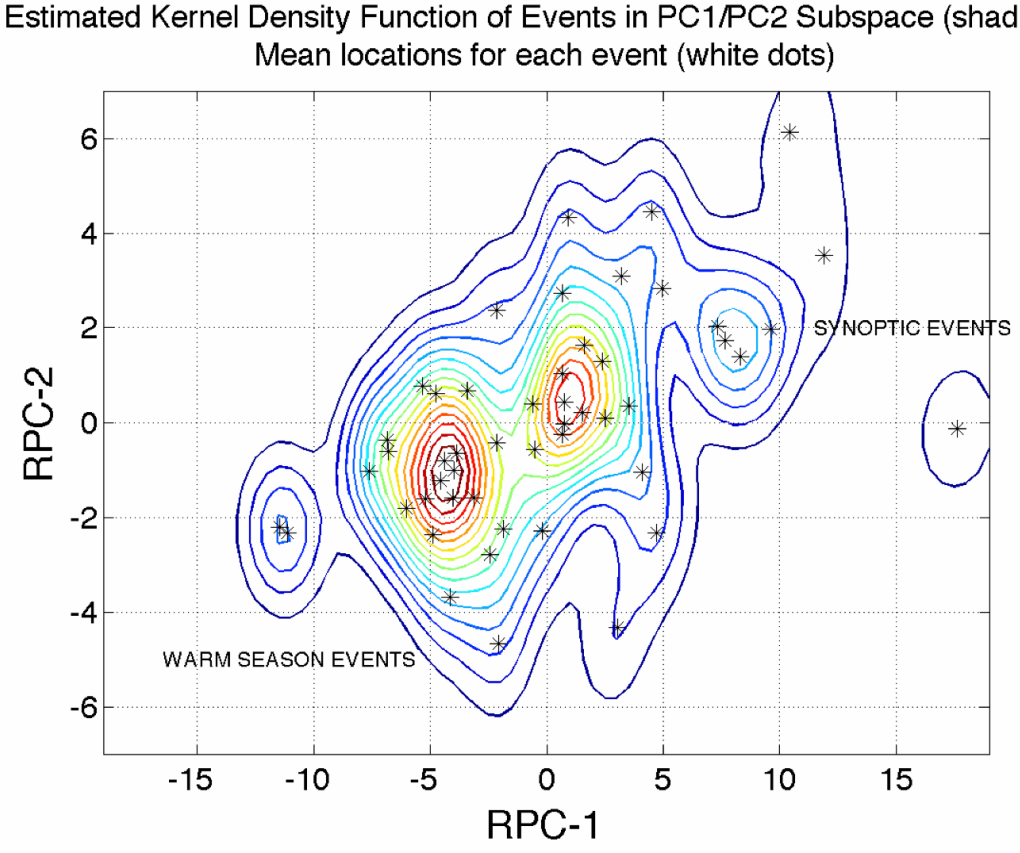
Estimated Kernel Density Function of Events in PC1/PC2 Subspace (shading),
Mean locations for each event (white dots)
SYNOPTIC EVENTS
WARM SEASON EVENTS
RPC-2
RPC-1
6
4
2
0
-2
-4
-6
-15
-10
-5
0
5
10
15

Fig. 2.2. Top panel: Scatter plot of the temporal mean RPC1 and RPC2 loadings over the 36 hours of NARR data analyzed for each event (red stars), and the 18 hour path of each event through the RPC1 and RPC2 subspace (blue lines). Bottom panel: Estimated kernel density function of atmospheric states in the RPC1 and RPC2 subspace over all events and all times (color contours), and the temporal mean RPC1 and RPC2 loadings over the 36 hours of NARR data analyzed for each event (black stars). Synoptic type events were defined in cluster analysis as those exhibiting a positive temporal mean RPC1 loading, while warm-season-type events exhibited a negative RPC1 loading (i.e. the RPC-1 = 0 line divided case between each cluster). Note that synoptic-type events tended to also exhibit a positive RPC2 loading, and warm-season-type events tended to also exhibit a negative RPC2 loading.

The estimated probability density function of these states (Fig. 2.2, bottom panel) revealed two pronounced event population maxima within the subspace, with local maxima in the upper right and lower left quadrants (relative to the origin), along with several less pronounced local maxima (note that since most of the less pronounced maxima consisted of 1-2 events, their sample size was insufficient for them to be considered separately from the more populated local maxima). A less coherent bimodal distribution was also evident in the un-rotated PC1/PC2 subspace (not shown). Later in this section, we describe how the results from RPCA are used to generate synoptic composites for two TL/AS sub-types. Composites computed from RPCs exhibited substantially greater differences between the two synoptic subtypes than those computed from un-rotated PCs, which served as an a posteriori justification for the usage of RPCs in our analysis hereafter (i.e. RPCs provided a more coherent separation into distinct sub-types).

There are various methods for objectively identifying groupings, or "clusters" within a distribution of points in 2-dimensional space (i.e. the RPC1/RPC2 loadings). We followed the methodology of Mercer et al. (2012) and performed k-means cluster analysis (Wilks 2006) in the RPC1/RPC2 subspace. This method utilizes an iterative algorithm to fit the data into a pre-specified number of clusters (assuming each datum only belongs to one cluster). Though additional objective algorithms are typically utilized in order to determine the optimal number of clusters (Mercer et al. 2012) prior to k-means cluster analysis, we circumvented this step and subjectively specified that the algorithm fit to 2 clusters (k=2, k being the number of clusters),

given the bimodality evident in Fig 2. Cases were flagged with a 1 (24 events) or 2 (26 events) based on which cluster they belonged to, and composites of NARR atmospheric fields were subsequently computed for each cluster. We also performed k-means cluster analysis with the data fit to more than 2 clusters (k>2), and compared the results (not shown) to the analysis presented in this paper. Clusters 2 and 3 from the k=3 solution yielded nearly identical atmospheric composites to one another, and solutions for k > 3 yielded additional clusters comprised of only 1-2 events (i.e. their presence was highly sensitive to sampling).

Note that while we refer to RPCA as an "objective" method, contrasted with "subjective" case sorting, we must note that (as with most statistical methods), there remain subjective "choices" to be made through the execution of the method (e.g. number of PCs to consider for cluster analysis, number of clusters to fit the data to). The RPCA method does, however, dramatically reduce the role of such subjective choices in case selection over fully subjective methods, and thereby dramatically decreases the degrees of freedom involved.

2.3. Composites of Synoptic Sub-Types

As will be illustrated later in this section the most notable differences in composite atmospheric fields between cluster 1 and cluster 2 type events were evident between their upper-level jet and low-level thermodynamic structures. Cluster 1 events occurred downstream of a progressive upper-level trough and featured a classic low-level cyclone structure with a well-defined low-level trough, trailing cold front, and preceding warm front. They were subsequently termed "synoptic sub-type events" due to their association with the aforementioned features. Cluster 2 events occurred within the right-entrance region of a low-amplitude anticyclonically curved upper-level jet streak, and only exhibited a discernable warm front at low levels.

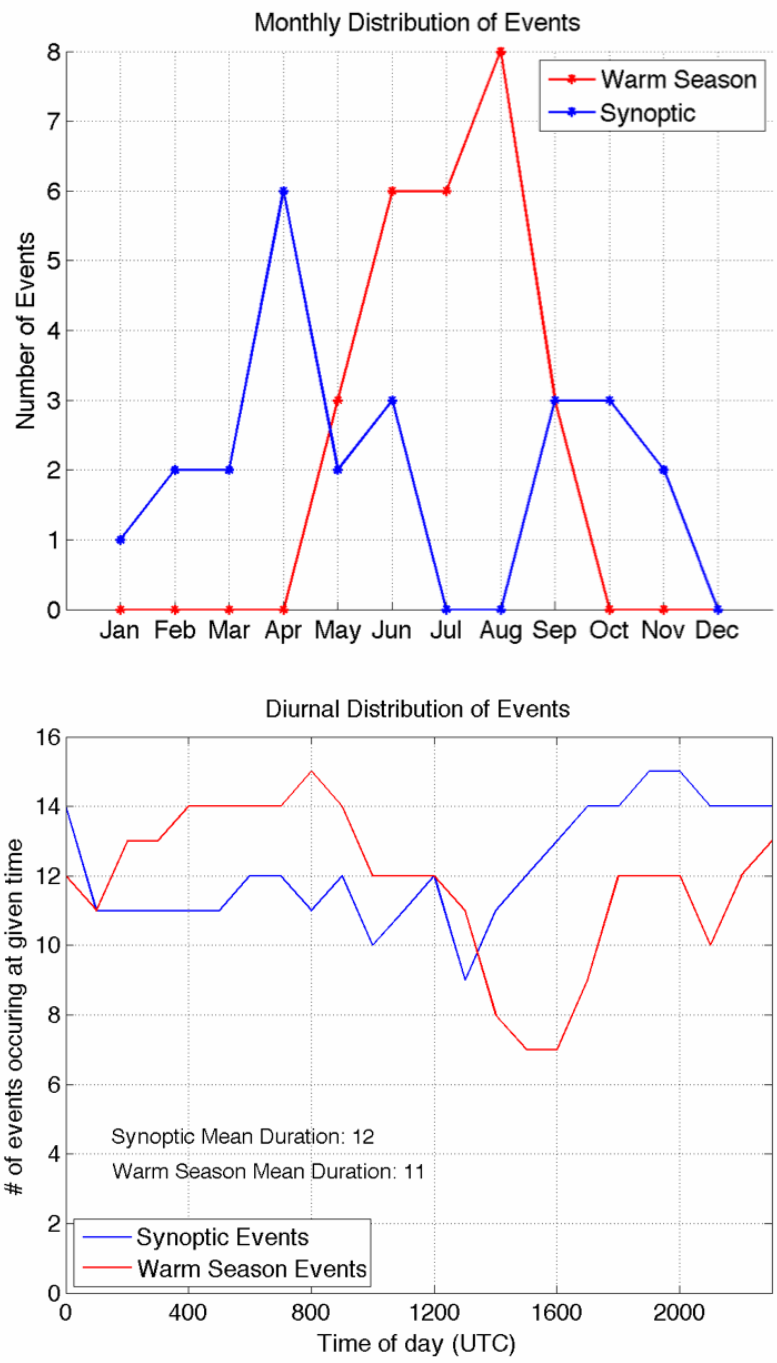

Fig. 2.3. Top panel: the seasonal frequency of synoptic-type (blue) and warm season type (red) events. Bottom panel: the diurnal frequency of synoptic-type (blue) and warm season type (red) events. The start time for each event was subjectively determined to be the time when the convection associated with the TL/AS system developed within, or moved into the region of heavy rainfall accumulation, and the end time was subjectively determined to be when convection dissipated or left the region of heavy rainfall accumulation. An "event" was added t each 1-hour bin if a TL/AS MCS was ongoing during that 1-hour timeframe.

They were termed “warm season sub-type events” since the aforementioned synoptic scale environment is more characteristic of the North American summertime (see Fig. 2.2 for the location of these sub-types within the RPC1/RPC2 subspace). The seasonal frequencies of these events (shown in Fig. 2.3) were sharply contrasted between the two subtypes, with synoptic type events frequently occurring in the spring and fall months (when high-amplitude troughs are more frequent), and warm-season events being predominantly confined to the summer months.

The warm season cases exhibited a diurnal peak in frequency during the overnight and early morning hours (~300-900 UTC), while synoptic-type events exhibited a diurnal peak in frequency during the afternoon and evening hours (~ 1700-100 UTC; Fig. 2.3). Note that the association of warm season heavy rainfall events with the nocturnal jet maximum is well established in previous literature on MCSs, MCCs, and heavy convective rainfall (e.g. Pitchford and London 1962; Maddox et al. 1979, Maddox 1980, 1983; Augustine and Caracena 1994; Moore et al. 2003; Schumacher and Johnson 2005; Tuttle and Davis 2006; Monaghan et al. 2010). A comparison of the spatial distribution of events between the two sub types (Fig. 2.4) shows a slight northward preference for warm season events relative to synoptic type events, which is intuitively consistent with the time of the year when the ingredients for convection more frequently reach the north central US. Note also that both event types were restricted to regions east of the Rocky Mountains and west and south of the Appalachian Mountains (no geographical constraint was imposed during the case selection process). Table 1 indicates which synoptic sub-type each of the cases considered in this study belongs to.

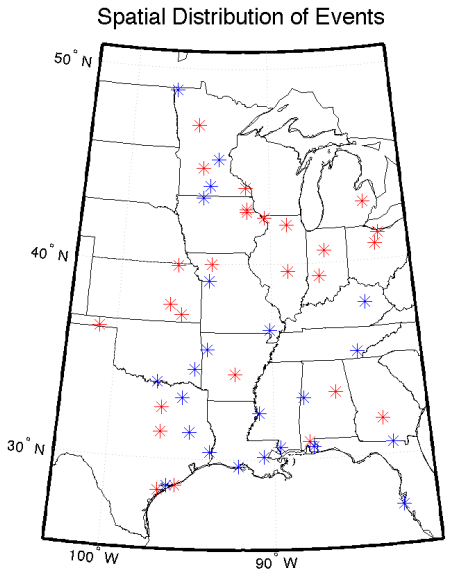

Fig. 2.4. Locations of event centroids for synoptic events (blue stars) and warm season events (red stars). Star locations correspond to the location where the maximum 1-hour point precipitation accumulation value was observed for a given event.

Table 2.1. List of the cases used to generate composite analyses, their latitudes and longitudes, and synoptic subtype. Locations correspond to the grid point in stage IV precipitation analysis that experienced the maximum 1-hour precipitation accumulation from the TL/AS MCS. Warm season events are italicized.

Date	Subtype	Longitude	Latitude	Date	Subtype	Longitude	Latitude
3-Mar-02	Synoptic	-82.88	30.63	15-Sep-04	Synoptic	-94.63	43.38
19-Mar-02	Synoptic	-94.88	34.63	19-Oct-04	Synoptic	-87.81	35.05
8-Apr-02	Synoptic	-94.13	35.63	2-Nov-04	Synoptic	-96.38	28.63
11-Jun-02	Synoptic	-96.88	48.88	1-Apr-05	Synoptic	-87.63	30.63
23-Jun-02	*Warm Season*	*-95.13*	*47.13*	4-Jun-05	Synoptic	-94.13	39.13
22-Aug-02	*Warm Season*	*-90.38*	*42.38*	*10-Aug-05*	*Warm Season*	*-96.88*	*31.38*
19-Oct-02	Synoptic	-95.63	33.13	*25-Aug-05*	*Warm Season*	*-96.63*	*37.88*
21-Feb-03	Synoptic	-93.88	30.38	25-Sep-05	Synoptic	-89.63	44.00
7-Apr-03	Synoptic	-90.88	32.38	2-Jan-06	Synoptic	-82.63	27.38
8-Apr-03	Synoptic	-92.13	29.63	*22-Jun-06*	*Warm Season*	*-82.63*	*41.38*
6-May-03	Synoptic	-84.63	35.38	*8-Sep-06*	*Warm Season*	*-83.38*	*31.88*
8-May-03	*Warm Season*	*-86.13*	*33.38*	23-Sep-06	Synoptic	-90.13	36.63
18-May-03	*Warm Season*	*-87.88*	*30.88*	26-Oct-06	Synoptic	-95.13	31.38
12-Jun-03	*Warm Season*	*-92.38*	*34.38*	*19-Aug-07*	*Warm Season*	*-91.69*	*43.91*
25-Jun-03	Synoptic	-93.63	45.38	*21-Aug-07*	*Warm Season*	*-82.86*	*40.83*
5-Jul-03	*Warm Season*	*-86.38*	*40.63*	*7-Sep-07*	*Warm Season*	*-96.19*	*39.91*
21-Jul-03	*Warm Season*	*-96.88*	*28.38*	*7-Jun-08*	*Warm Season*	*-86.78*	*39.33*
29-Aug-03	*Warm Season*	*-95.88*	*37.38*	*25-Jun-08*	*Warm Season*	*-93.94*	*40.00*
1-Sep-03	*Warm Season*	*-88.88*	*39.63*	30-Apr-09	Synoptic	-97.19	33.91
28-Nov-03	Synoptic	-90.63	30.13	*8-Aug-09*	*Warm Season*	*-94.69*	*44.91*
6-Feb-04	Synoptic	-88.13	33.13	*9-Aug-09*	*Warm Season*	*-83.44*	*43.00*
26-Apr-04	Synoptic	-89.63	30.63	*13-Jun-10*	*Warm Season*	*-101.11*	*36.58*
14-May-04	*Warm Season*	*-95.88*	*28.63*	*23-Jul-10*	*Warm Season*	*-91.61*	*42.66*
31-May-04	Synoptic	-83.88	37.88	*24-Jul-10*	*Warm Season*	*-88.86*	*42.00*
29-Jul-04	*Warm Season*	*-96.88*	*32.63*	*28-Jul-11*	*Warm Season*	*-91.61*	*42.83*

Upper-level features associated with synoptic type events were more zonally progressive than those corresponding to warm-season type events, with the upper level trough axis in synoptic type events having moved from ~ 112 deg. W to 105 deg. W longitude in 18 hours (Fig. 2.5), whereas little discernable zonal translation of upper level features occurred in warm-season events (Fig. 2.6).

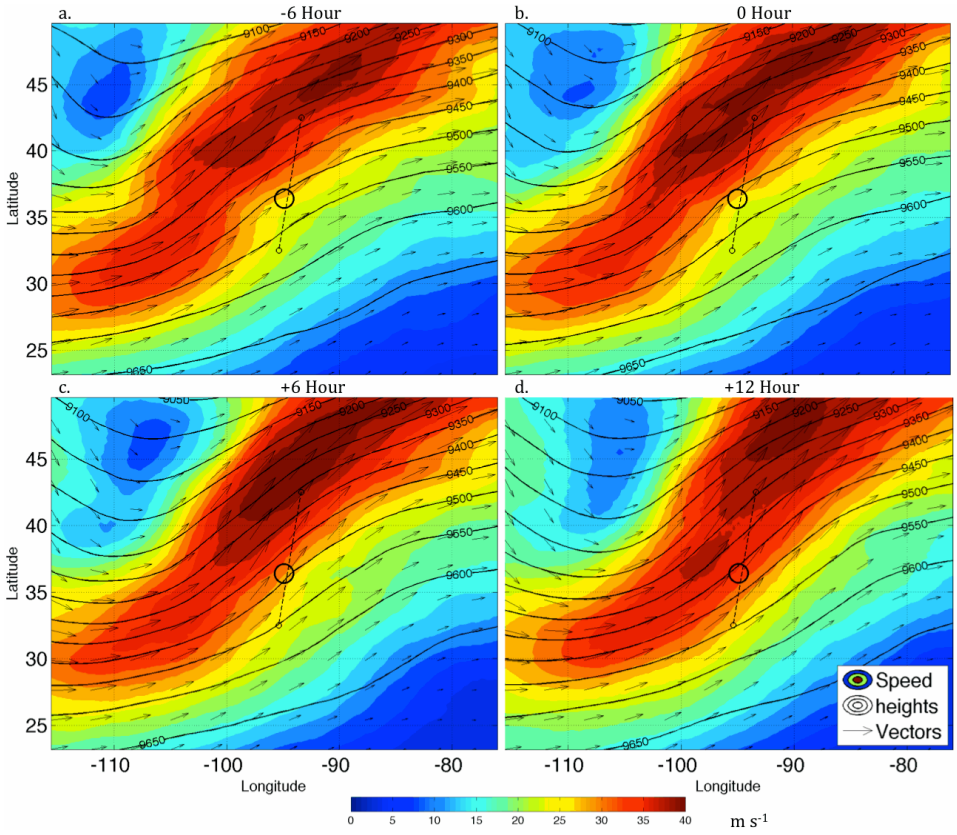

Fig. 2.5. 18-hour event-centered composite progression from 24 synoptic type events of 300 hPa wind speed (m/s, shading), wind vectors (arrows), and geopotential height (black lines at intervals of 50 m) from 6 hours prior (a), the time of (b), 6 hours after (c) and 12 hours after (d) peak 1-hour rainfall accumulating was observed at the event location. A solid black circle at the center of each frame indicates the point location of maximum 1-hour rainfall accumulation. The specific latitudes and longitudes shown are arbitrarily selected to illustrate the spatial scale. The dashed black line near the center of each panel shows the cross-section path in Fig. 2.13.

Although both event types remained within the right entrance region of an upper level jet streak throughout the 18-hour evolution, 300-hPa peak wind speeds associated with the composites of synoptic type events were considerably stronger (~40-45 m/s) than those associated with warm-

season type events (~25-30 m/s). This is consistent with a climatologically stronger jet in the spring and fall months compared with the warm season over the U.S.

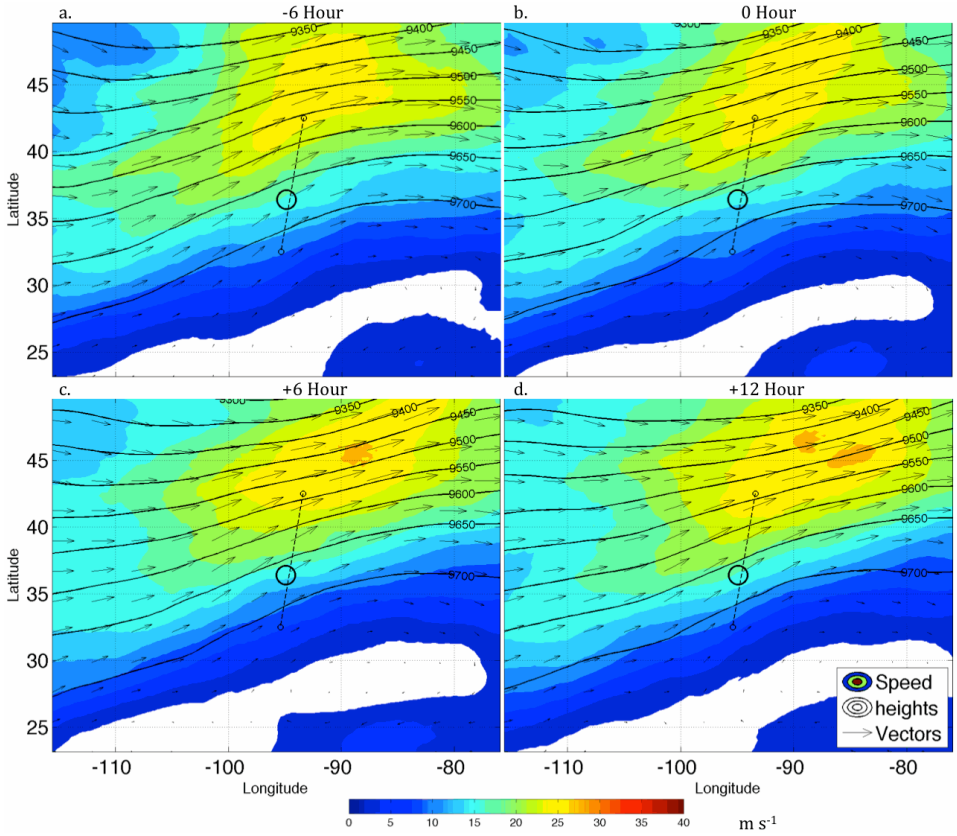

Fig. 2.6. Same as Fig. 2.5, but for warm-season type events. The cross section path along the dotted line now corresponds to Fig. 2.14.

Both event types occurred within a generally east-west oriented temperature gradient at the northern nose of a southerly low-level jet, with warm air to the south (Figs. 7 and 8). The axis of warm air in synoptic type events initially resided to the south and southwest of the MCS location, and translated to the southeast of the event location through time. A cooler air mass that was initially to the west slowly progressed eastward during the 18-hour period, eventually reaching the event location (Fig. 2.7).

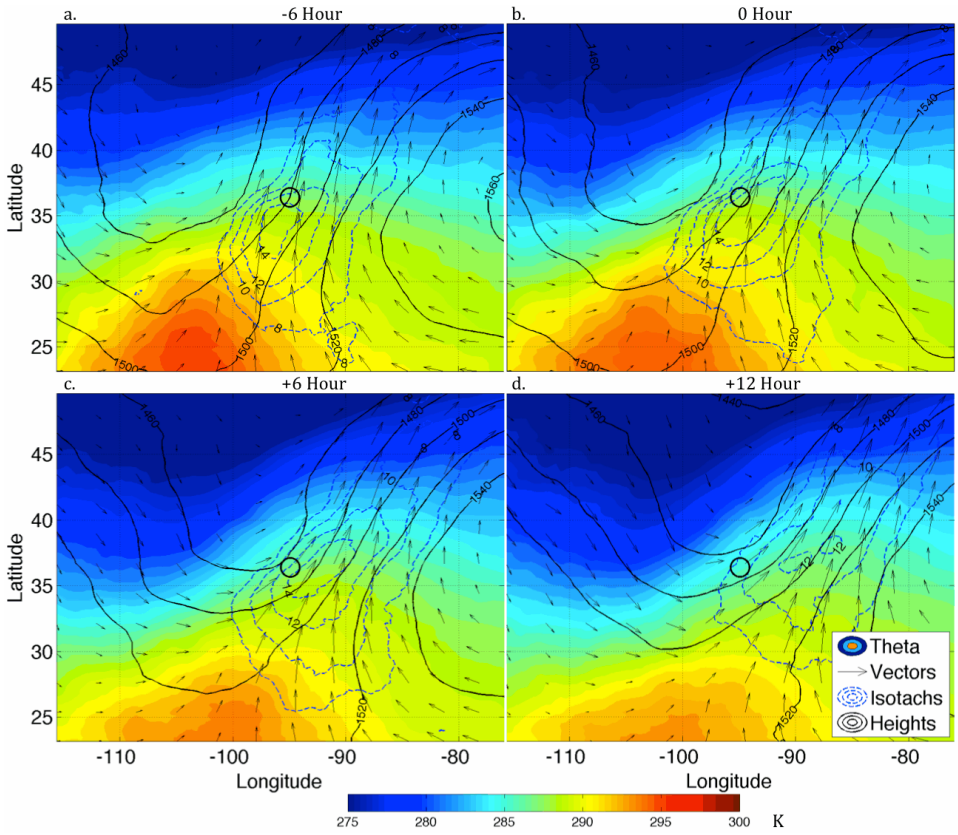

Fig. 2.7. 18-hour event-centered composite progression from synoptic type events of 850 hPa potential temperature (K, shading), wind speed (blue dashed contours at intervals of 2 m/s, starting at 8 m/s), wind vectors (black arrows), and geopotential height (black lines at intervals of 20 m). Panel times are the same as those in Fig. 2.4. A solid black circle at the center of each frame indicates the point location of maximum 1-hour rainfall accumulation. The specific latitudes and longitudes shown are arbitrarily selected to illustrate the spatial scale.

Warm-season type events, on the other hand, featured a broader warm axis to the south, southwest, and west of the event location, with cooler air having remained far separated to the north of the event location (Fig. 2.8). Note that the low-level jet in warm-season cases reached maximum intensity at the time of peak rainfall, and weakened considerably 12 hours after peak rainfall, suggesting that the jet intensity was influenced by the diurnal boundary layer heating/cooling cycle. This may explain why warm season events exhibit a peak diurnal frequency during the overnight hours, which coincides with the diurnal maximum in jet strength. In contrast, the low-level jet in synoptic type events remained at roughly the same intensity

through the 18-hour progression of rainfall, suggesting that the jet strength here was predominantly regulated by the low-level horizontal pressure gradient.

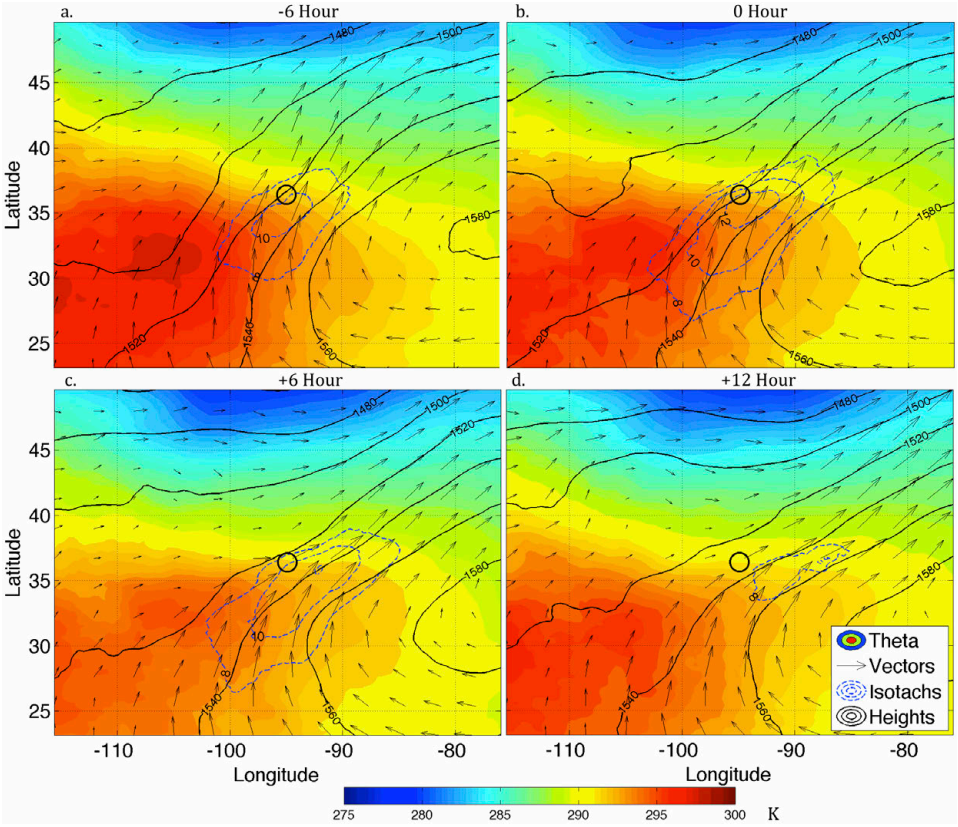

Fig. 2.8. Same as Fig. 2.7, but for warm-season type events.

Both event types featured a persistent supply of low-level moisture to the event location by southerly inflow (Figs. 2.9 and 2.10). Warm-season type events featured considerably more low-level moisture than synoptic-type events, though low-level temperatures in warm-season type events were also warmer (and thus the spatial expanse of near-saturated relative humidity values was smaller for warm season events).

The stronger winds aloft and more persistently strong low-level jet in synoptic type events compared with warm-season type events suggested that synoptic-type events also featured stronger large-scale forcing for ascent. Both event types occurred within a persistent, locally maximized region of low-level warm air advection, though this region was much broader and

exhibited greater peak values in the case of synoptic type events (Figs. 11 and 12) – this may partially explain why synoptic type MCSs tend to exhibit greater spatial extent than warm season MCSs (an attribute which is discussed in greater detail in the next section).

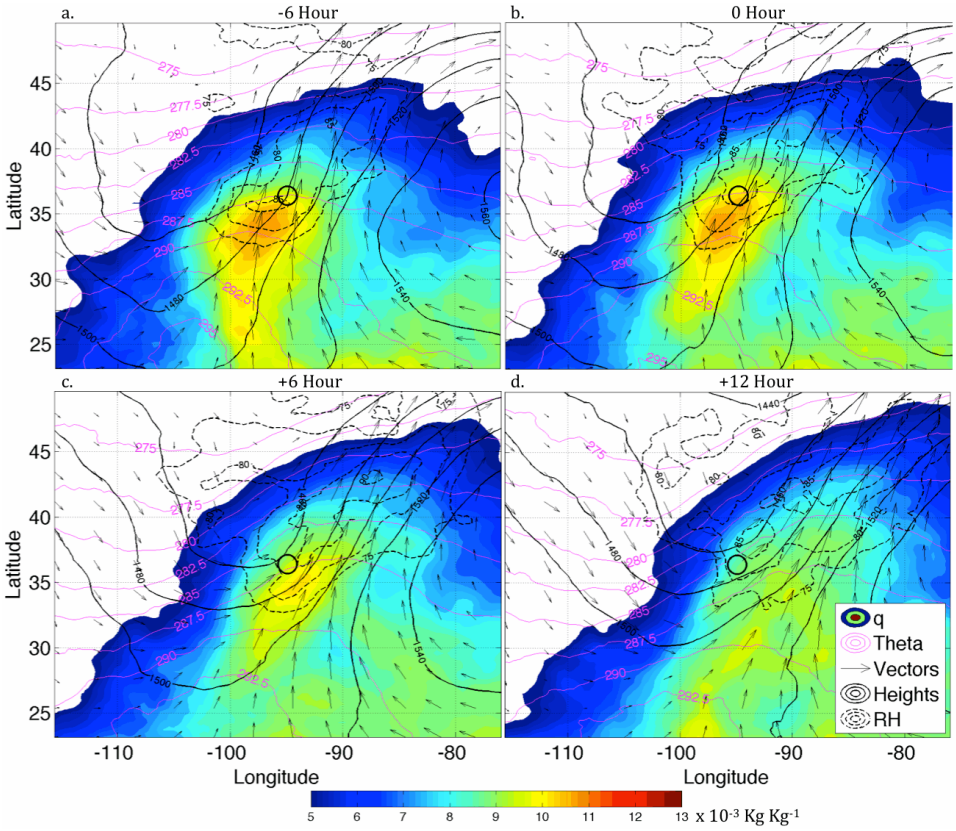

Fig. 2.9. 18-hour event-centered composite progression from synoptic type events of 850 hPa mixing ratio (shading, x 10^{-3} Kg Kg^{-1}), relative humidity (%, black dashed contours at intervals of 5 % starting at 75%), wind vectors (black arrows), geopotential height (black lines at intervals of 20 m), and potential temperature (K, magenta contours). Panel times are the same as those in Fig. 2.4. A solid black circle at the center of each frame indicates the point location of maximum 1-hour rainfall accumulation. The specific latitudes and longitudes shown are arbitrarily selected to illustrate the spatial scale.

South-north vertical cross sections show an upward slope in isentropes at low levels in both case types (Figs. 13 and 14), which in conjunction with the generally southerly low-level flow, is illustrative of warm air advection (note that up sloping isentropes were present throughout the depth of the troposphere in synoptic cases).

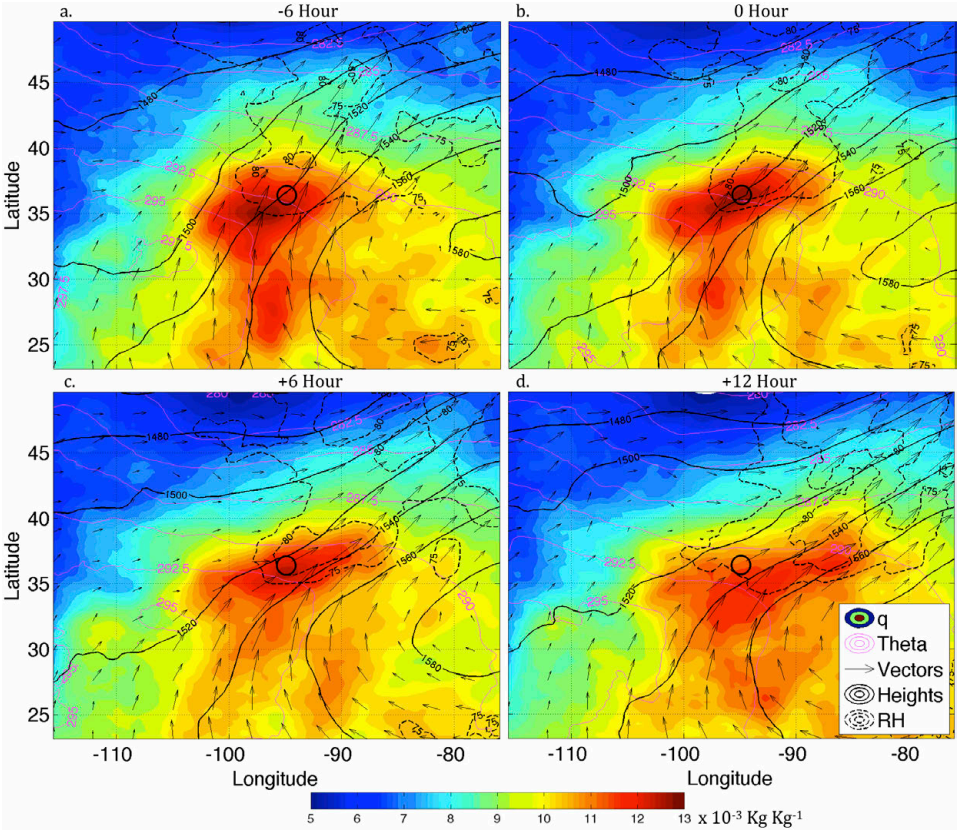

Fig. 2.10. Same as Fig. 2.9, but for warm-season type events.

Both case types also exhibited locally maximized low-level convergence and frontogenesis (which has been associated with nocturnal MCSs, Augustine and Caracena 1994; Junker et al. 1999; Moore et al. 2003; Galarneau et al. 2010) along the nose of the low-level jet, locally maximized upper level divergence within the right entrance region to the upper level jet streak, and maximized ascent between the convergent and divergent regions (Figs. 13 and 14). Convergence, divergence, and ascent magnitudes, as well as the north-south expanse of these quantities were considerably greater in synoptic type events than in warm-season type events. Although warm-season events exhibited considerably greater low-level moisture than synoptic-type events (Figs. 9 and 10), the expanse of near-saturated air parcels was greater for synoptic

events due to low-level temperatures also having been greater in the case of the former (and saturation mixing ratios subsequently higher).

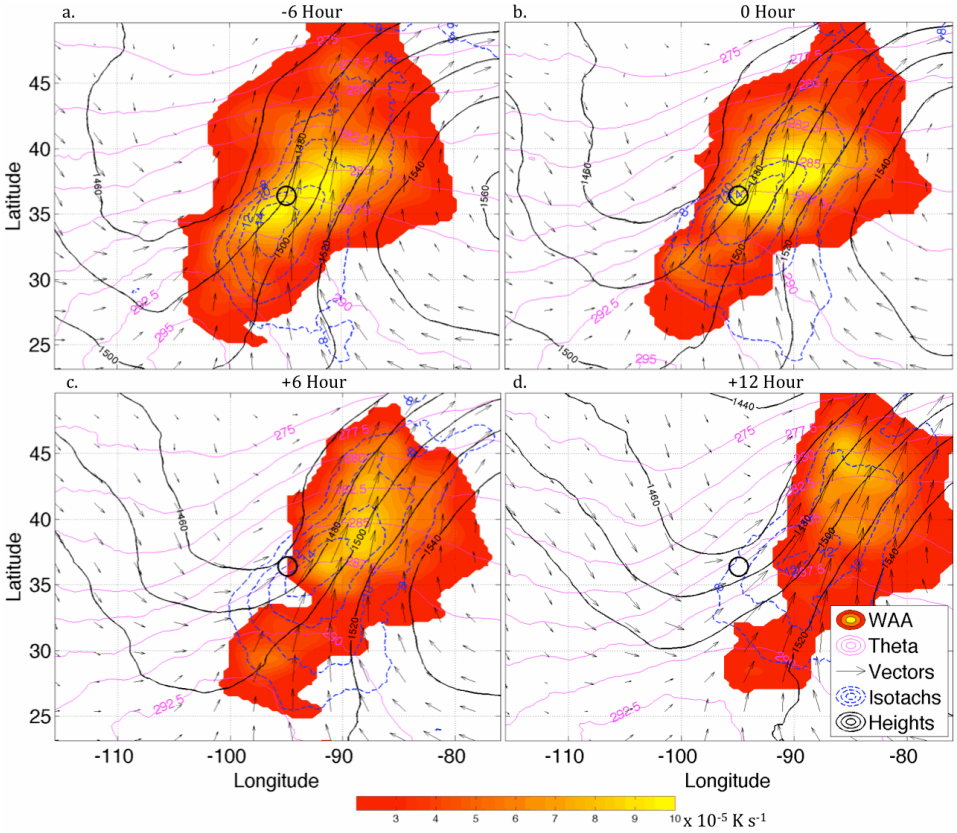

Fig. 2.11. 18-hour progression from synoptic type events of 850 hPa potential temperature advection (x 10^{-5} K s^{-1}, shading; values below 2 x 10^{-5} K s^{-1} have been removed; derivatives were computed from composite atmospheric fields), wind speed (blue dashed contours at intervals of 2 m/s, starting at 8 m/s), wind vectors (black arrows), geopotential height (black lines at intervals of 20 m), and potential temperature (K, magenta contours). Panel times are the same as those in Fig. 2.4. A solid black circle at the center of each frame indicates the point location of maximum 1-hour rainfall accumulation. The specific latitudes and longitudes shown are arbitrarily selected to illustrate the spatial scale.

In order to obtain a sense for the variability of individual cases about the composite images examined earlier in this section, we computed the standard deviation of representative atmospheric fields at each grid point within our domain over synoptic and warm season cases:

$$\sigma_f(x,y,p,t) = \sqrt{\frac{1}{n-1}\sum_{i=1}^{n} f(x,ym,z,t,c_i)}, \quad (2.5)$$

where f is any arbitrary atmospheric field, n is the number of either warm season or synoptic cases (depending on which event type we were computing the standard deviation quantity for), t is the time removed from peak stage IV 1-hour rainfall, and c_i is a case number.

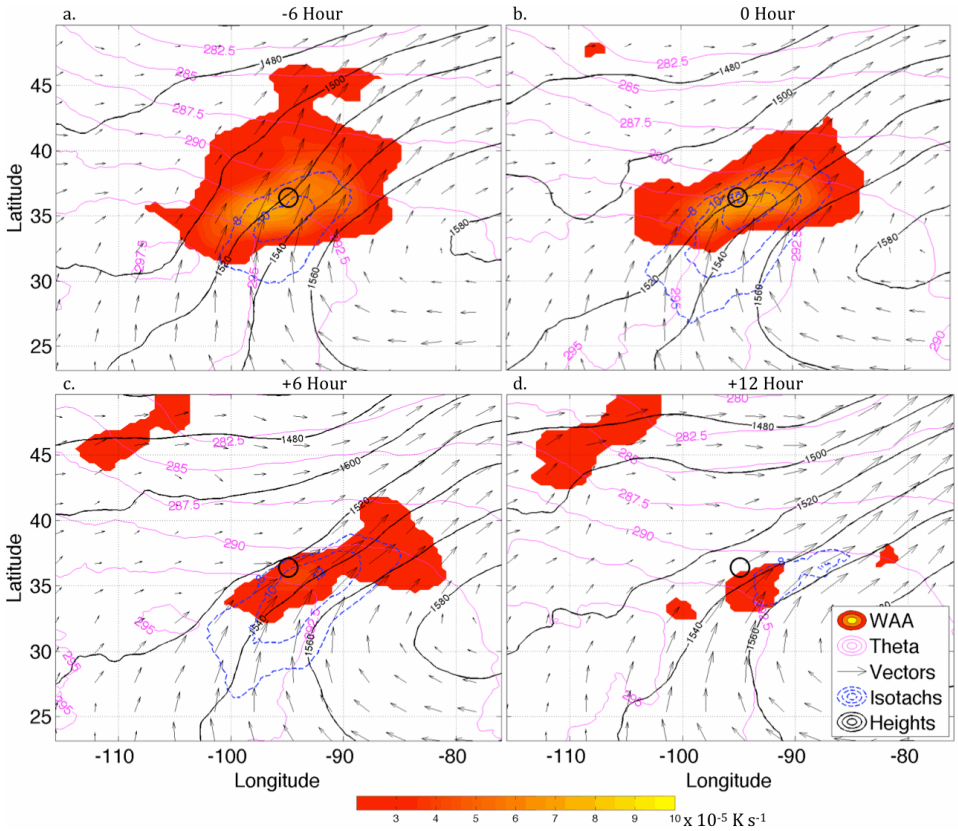

Fig. 2.12. Same as Fig. 2.11, but for warm-season type events.

Example maps of the 850 hPa wind speed and direction standard deviations are shown in Fig. 2.15. Note that synoptic events exhibit considerably greater standard deviation in wind speed through the low-level jet region (~6-7 m/s) than warm season events (~ 3.5-4.5 m/s) (this is consistent with the greater degree of variability apparent associated with synoptic type event cluster in the RPC1/RPC2 subspace). Additional fields analogous to those depicted in Fig. 2.15 were examined (not shown), and exhibited similar spatial patterns of variance to those evident in the wind speed variability figures (as well as greater variance within synoptic fields over warm season fields). Interestingly, the variability of wind direction within the low-level jet region is

comparable between the two event types – in fact the southwesterly direction of the low-level jet seems to be a fixture of all events (with a standard deviation of only 10-25 degrees in wind direction within the low-level jet between the two case types).

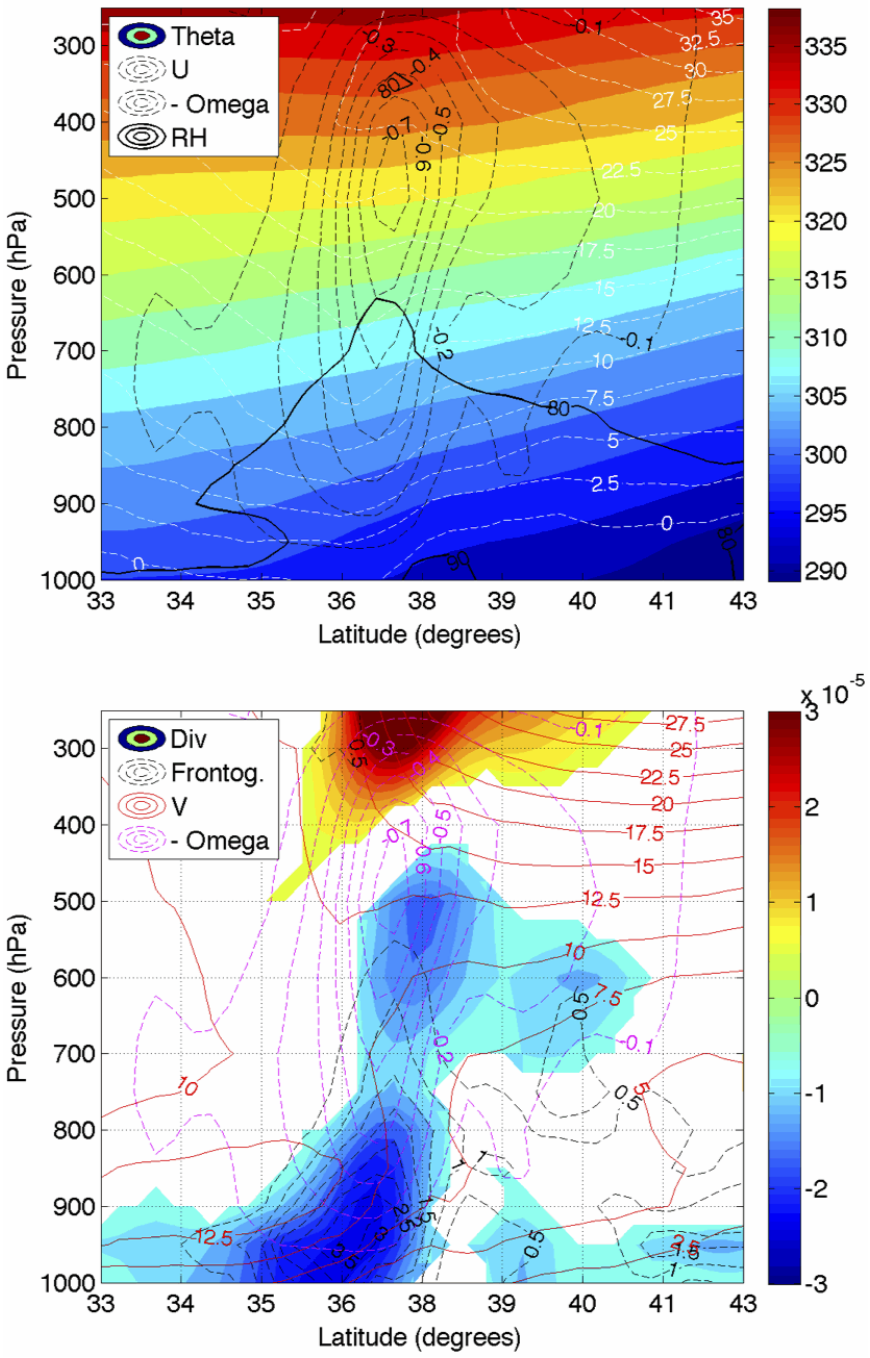

Fig. 2.13. Cross-sections through the dotted line in Fig. 2.4 for synoptic type events, at the time of maximum 1-hour rainfall accumulation. Top panel: potential temperature (K, shading), zonal wind

velocity (m/s, white dotted contours), negative pressure vertical velocity (Pa/s, dotted black contours), and relative humidity (%, solid black contours). Bottom panel: horizontal divergence (x 10^{-5} s^{-1}, shading), negative pressure vertical velocity (Pa/s, dotted magenta contours), meridional wind speed (m/s, solid red contours), and horizontal frontogenesis (K/s, dotted black contours, multiplied by 10^{10}).

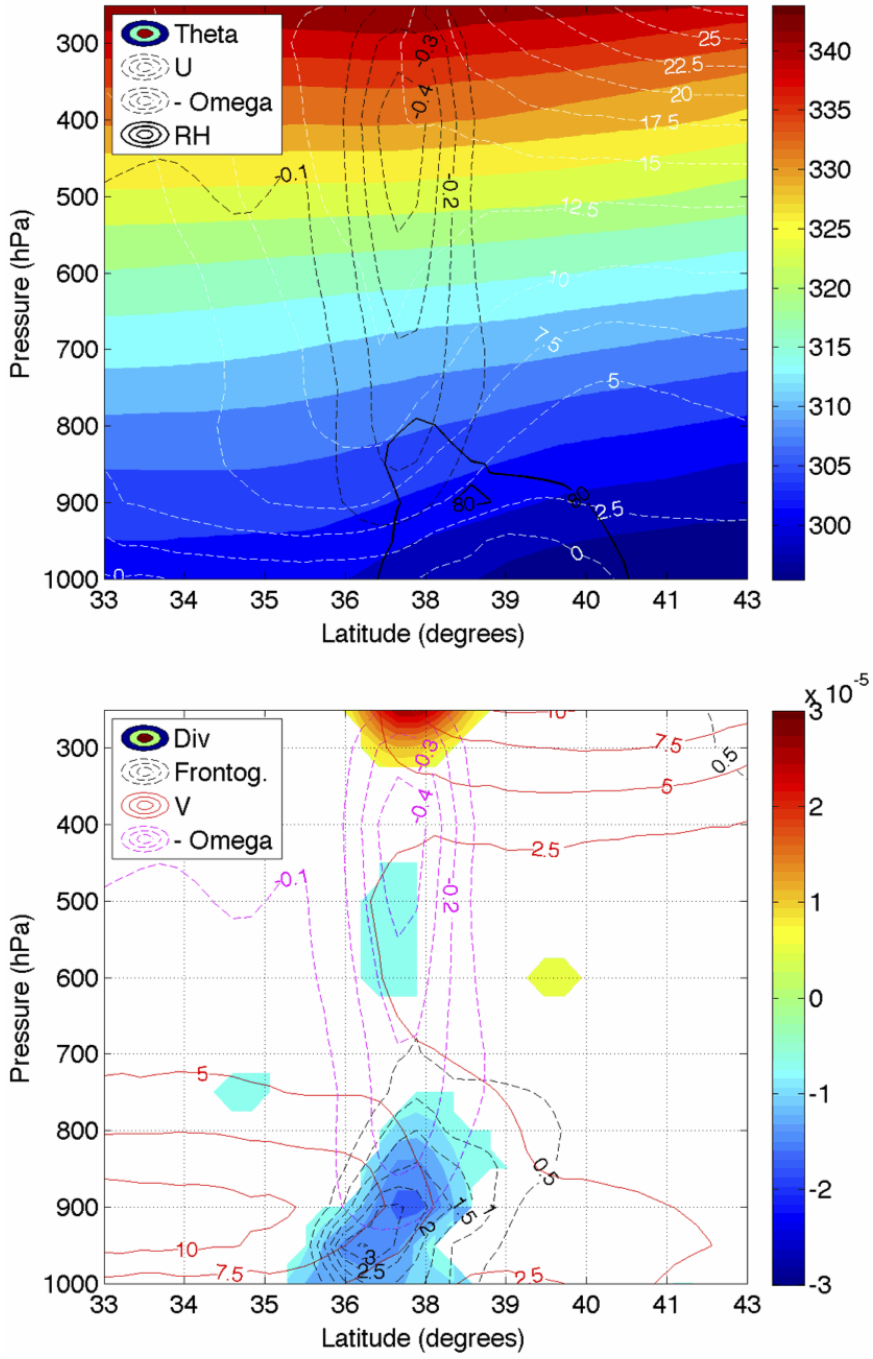

Fig. 2.14. Same as Fig. 2.13, but for warm-season type events.

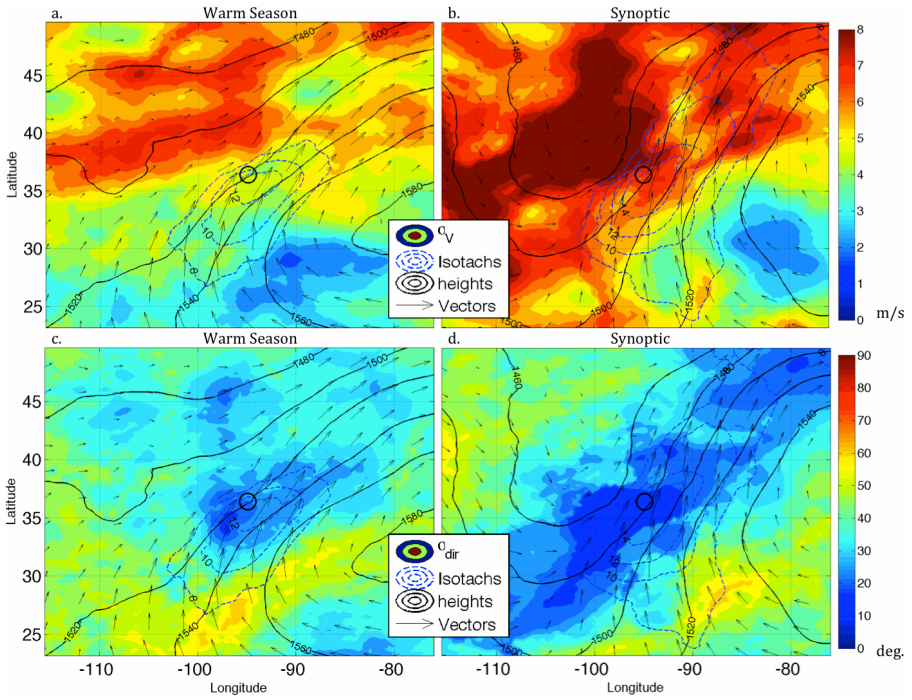

Fig. 2.15. Plots of the standard deviation (σ see equation 5 in the text) of 850 hPa wind speed for warm season (panel *a*, shading, m/s) and synoptic (panel *b*, shading, m/s) events, the standard deviation of wind direction for warm season (panel *c*, shading, degrees) and synoptic (panel *d*, shading, degrees). Geopoential height (solid black contours, m, at intervals of 40 m), wind vectors (black arrows), and wind speed (blue dotted contours, m/s starting at 8 m/s and at intervals of 2 m/s) are shown in all panels. All panels are valid at the time of maximum 1-hour rainfall accumulation from stage IV precipitation analysis. A solid black circle at the center of each frame indicates the point location of maximum 1-hour rainfall accumulation. The specific latitudes and longitudes shown are arbitrarily selected to illustrate the spatial scale.

2.4. Radar Reflectivity and Precipitation Accumulation Area Characteristics

We subjectively analyzed composite radar reflectivity imagery (warm season events, Fig. 2.16; synoptic events, Fig. 2.17) to determine whether the two synoptic sub-types presented in this work exhibited notable differences in their salient radar features in addition to the differences in synoptic-scale atmospheric fields discussed in section 2.3.

Representative composite radar reflectivity images for three synoptic type events show that training convection often developed as a broken line of individual convective cells (Fig. 2.16) along a nearly stationary warm front (less commonly a slow-moving cold front).

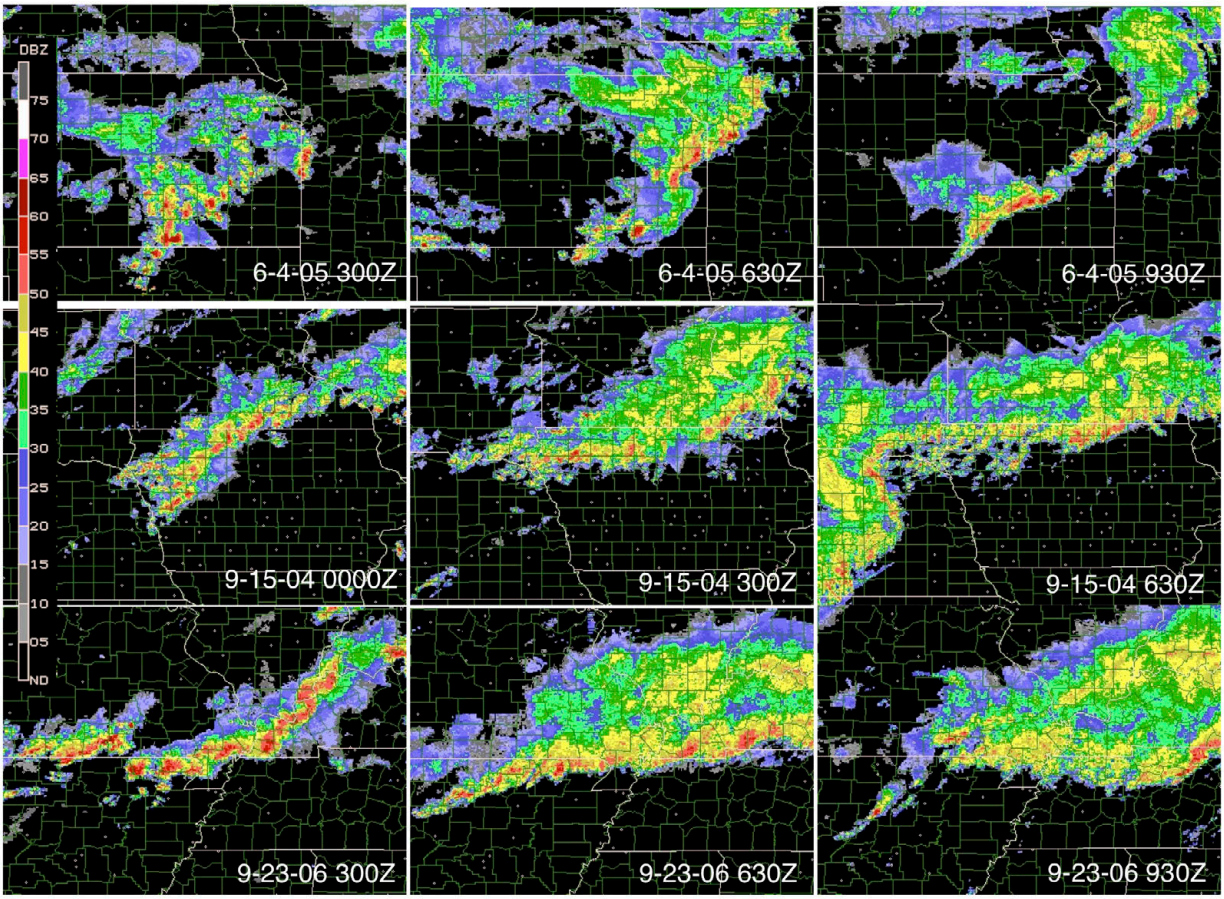

Fig. 2.16. Composite radar reflectivity images from three different synoptic-type events. Dates and times for each image are listed in the lower-right corner.

Initial convection then evolved upscale into a linear MCS within 1-5 hours, with the motion of individual convective cells paralleling the linear convective region. The areal extent of synoptic-type MCSs was often highly elongated in the direction of the convective line, with a very high aspect ratio of convective line "length" to stratiform precipitation "width" (this is evident in radar images of all three events in Fig. 2.16). Thus, in many cases the length of the training line was sufficient so that predominantly line-parallel motion would bring an extended period of convective rainfall to a particular region without the line re-generating (i.e. backbuilding) upstream. Cessation of training convection was often accompanied by the passage of a progressive cold front and a progressive Trailing Stratiform (TS, e.g. Houze et al. 1989, 1990; Parker and Johnson 2000) type squall line – this is evident in the right panel of Fig. 2.16 for the

case occurring on 15 September 2004 (though a trailing TS squall line occurred in all three of the cases shown in this figure).

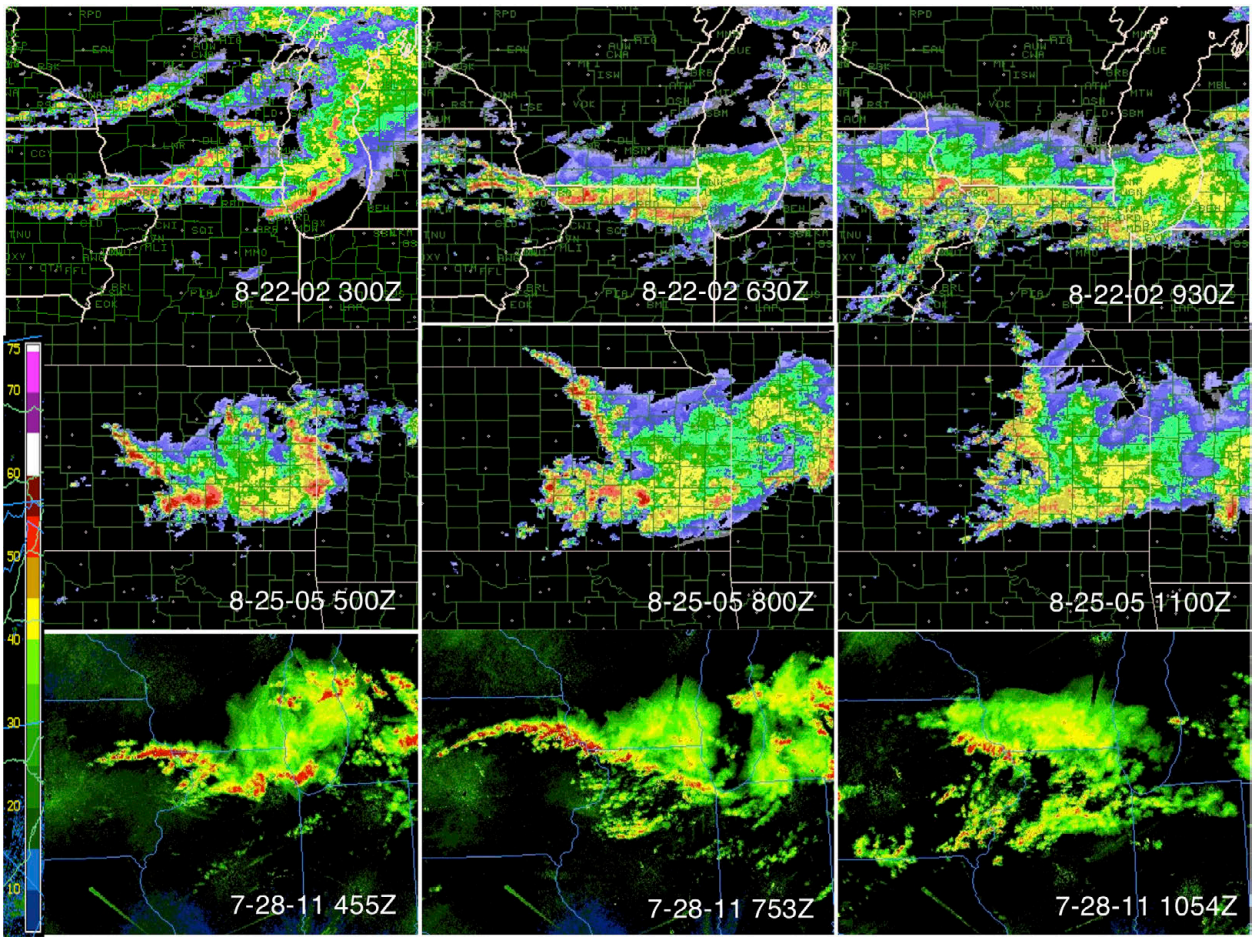

Fig. 2.17. Same as Fig. 2.15, but for warm-season-type events. The color scale top two events corresponds to the color bar in Fig. 2.16; the color scale of the bottom event corresponds to the color bar on the lower left.

The radar reflectivity presentations of synoptic type events suggest that the aspect ratios (and overall sizes) of these events were often larger than that for warm season events (this is somewhat evident when comparing radar imagery in Fig. 2.16 to Fig. 2.17). This is further supported by Fig. 2.18, which shows precipitation accumulation composites for both event types. Synoptic events exhibited greater area of 20 mm of rainfall accumulation than warm season type events, though maximum precipitation accumulation values within the warm season composite were greater than the analogous quantity for synoptic type events. The average precipitation

accumulation value through the composite domain for synoptic type events was 24.6 mm, while the analogous quantity for warm season type events was 16.6 mm. These statistics show that warm season events tend to produce less expansive, but more concentrated precipitation areas than synoptic type events, while the total precipitation production in synoptic type events tends to be greater.

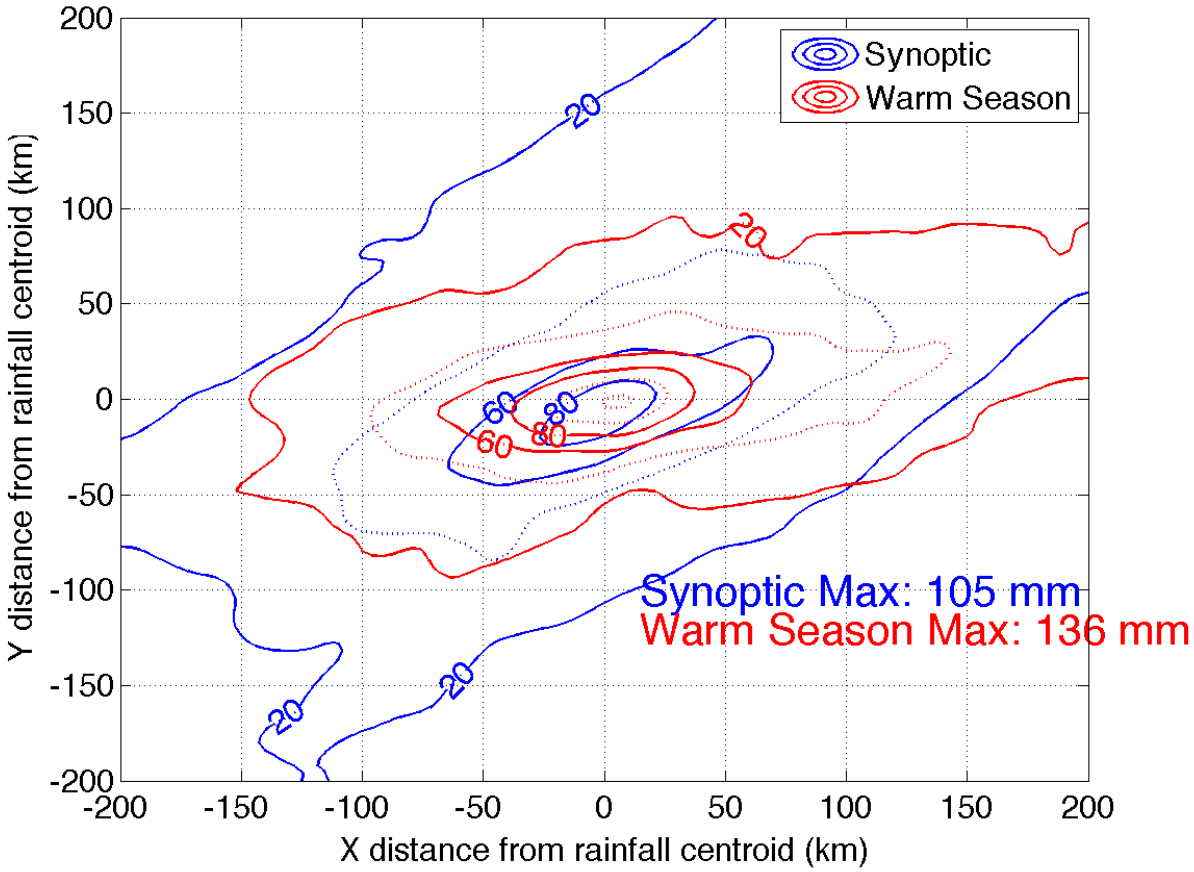

Fig. 2.18. Composites of 12-hour accumulated precipitation (mm) from stage IV precipitation for synoptic type (dotted blue contours) and warm season type (dotted red contours) events (contour intervals are 20 mm). The 12-hour precipitation accumulation time frame was temporally centered at the hour of maximum 1-hour precipitation accumulation, and spatially centered at the maximum point value within the 1-hour period of maximum precipitation accumulation. The 20, 60, and 80 mm contours have been bolded and labeled for the purpose of comparison between the two event types. Maximum precipitation accumulation values are the maximum point value for each event type.

Initial development of convective cells associated with warm-season events often occurred to the rear of a progressive TS type MCS, north of a slow moving warm frontal boundary. Interestingly, this rear development in the wake of a TS type MCS passage often occurred well north of the implied gust front at the southern periphery of the cold pool produced by the initial MCS (see radar imagery of the 22 August 2002 and 25 August 2005 cases in Fig. 2.17) – we will hereby refer to this phenomena as rearward off-boundary development (ROD). In some cases ROD occurred to the rear of a well-defined bowing line segment, akin to the "bow-and-arrow" phenomena described by Keene and Schumacher (2013), while in other cases the initial progressive MCS was less organized, and did not exhibit bowing line segments. Our initial analysis of several real-data and idealized numerical simulations (which is not discussed here, but will be comprehensively analyzed in future studies) suggest that similar dynamical processes to those described by Keene and Schumacher (2013) are responsible for the ROD events observed in our cases. Prolonged regeneration of convection on the upstream side of the MCS occurred in almost every warm-season case (in contrast to the synoptic type events), which resulted in the upstream flank of the MCS remaining quasi-stationary (see Corfidi 2003; Schumacher and Johnson 2005,2006; Schumacher 2009).

In order to quantify the degree to which each TL/AS MCS subtype exhibited the characteristics that have been discussed in this section, the radar reflectivity features present in each case were subjectively cataloged. We specifically noted whether the MCS occurred along a warm, cold, or stationary surface front, whether an initial or trailing progressive MCS was present, and whether ROD occurred. If a particular event occurred along a frontal boundary, the boundary was typically very slow moving – thus arose difficulties in distinguishing warm/cold fronts from truly stationary fronts. Surface boundaries were therefore considered stationary if

there was little-to-no cross-boundary component of surface flow (i.e. near-zero surface temperature advection). Roughly half of cases occurred along warm fronts, and only around of fifth occurred along cold fronts or fully stationary fronts. Fig. 2.19 summarizes the prevalence of these properties between both MCS subtypes. Initial progressive MCSs prior to the onset of training convection were far more frequent in warm-season type cases than synoptic type cases, while trailing progressive MCSs following the training of convection were far more frequent in synoptic type cases than warm-season type cases.

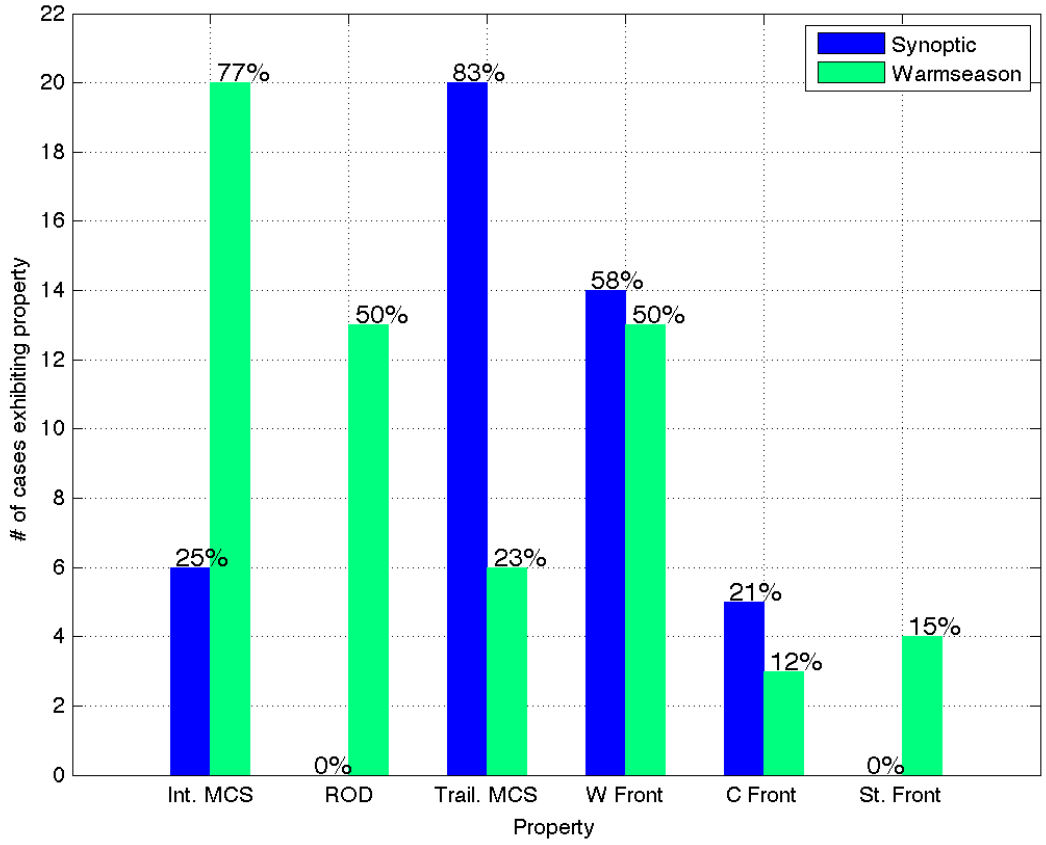

Fig. 2.19. Summary of frequency of subjectively defined composite radar-reflectivity attributes for each sub-type: Initial MCS passage prior to TL/AS system (int. MCS), rearward off-boundary development (ROD), trailing separate MCS passage at the end of the heavy rain producing MCS lifetime (Trail. MCS), heavy rain producing MCS occurring on a warm front (W Front), cold front (C Front), or stationary front (St. Front). Bars indicate the number of events exhibiting each attribute, and percentage values indicate the percentage of cases within each sub-type exhibiting a particular attribute. Note that 23% of warm

season events and 21% of synoptic events did not occur in conjunction with a discernable frontal boundary.

The ROD phenomena occurred in 50% of warm-season type cases, and in none of the synoptic type cases. The prevalence of these phenomena in warm-season cases is not surprising, considering the 850 hPa composites for warm-season type cases shown in Fig. 2.8 are very similar to the composites computed exclusively from bow-and-arrow cases shown in Keene and Schumacher (2013).

2.5. Synoptic scale factors contributing to observed radar reflectivity evolutions

An important fixture to the composite progressions for both sub-types is that the synoptic scale features *continuously* supplied the ingredients for organized convection to the location where heavy rainfall events occurred through most of the 18-hour time progression. These ingredients included moisture and conditional instability within southerly system-relative inflow, persistent synoptic-scale lifting which included convergence and isentropic up-glide along the nose of a low-level jet, frontogenetic lift along a quasi-stationary frontal boundary, and divergence within the right entrance region to an upper level jet streak.

Additional aspects of the vertical wind profile in the MCS region may have also promoted quasi-stationary MCS behavior. Corfidi et al. (1996) and Corfidi (2003) presented a simple and effective method for predicting upwind propagating MCS motion based on a vertical wind profile from a proximity sounding. These authors separate the MCS motion vector into a contribution by the mean wind through the cloud bearing layer (advection), and the propensity for individual convective cells to continuously redevelop in the direction of the low-level inflow (propagation), where

(2.6) $$\mathbf{V}_{MCS} = \mathbf{V}_{CBL} - \mathbf{V}_{LLJ} \ ,$$

(2.7) $$\mathbf{V}_{CBL} = \frac{1}{4}\left(\mathbf{V}_{850} + \mathbf{V}_{700} + \mathbf{V}_{500} + \mathbf{V}_{300}\right),$$

and

(2.8) $$\mathbf{V}_{LLJ} = \mathbf{V}_{850}.$$

Here the subscript MCS refers to the system motion vector (hereby Corfidi motion vectors, CMVs), CBL refers to the mean wind through the cloud bearing layer, LLJ refers to the wind velocity of the low level jet (estimated as the 850 hPa wind velocity in this case), and numeric subscripts indicate wind velocities on isobaric levels.

In section 2.6 we discussed the propensity for warm-season type events to exhibit geographically fixed back-building, while many of the synoptic type events simply translated in a line parallel fashion without back-building. This behavior is partially explained by the horizontal distribution of CMVs near the event location. In the case of synoptic type events, CMVs ranged from ~ 7 – 10 m/s near the event location, and tended to be oriented perpendicular (parallel) to the low level temperature gradient (front) (Fig. 2.20). In the case of warm season type events, however, CMV magnitudes near the event location were smaller and did not parallel the low-level front between 0 and +6 hours. Time series of CMV magnitudes at the event locations for both event types, along with the angle between the CMV and a vector perpendicular to the temperature gradient vector (i.e. parallel to the low-level frontal boundary) are shown in Fig. 2.21. Note that warm-season CMV magnitudes were roughly half that of synoptic, and warm season vector orientations strayed considerably (> 20 degrees) from the low-level frontal orientation, while synoptic CMVs remained nearly perfectly parallel to the low-level front.

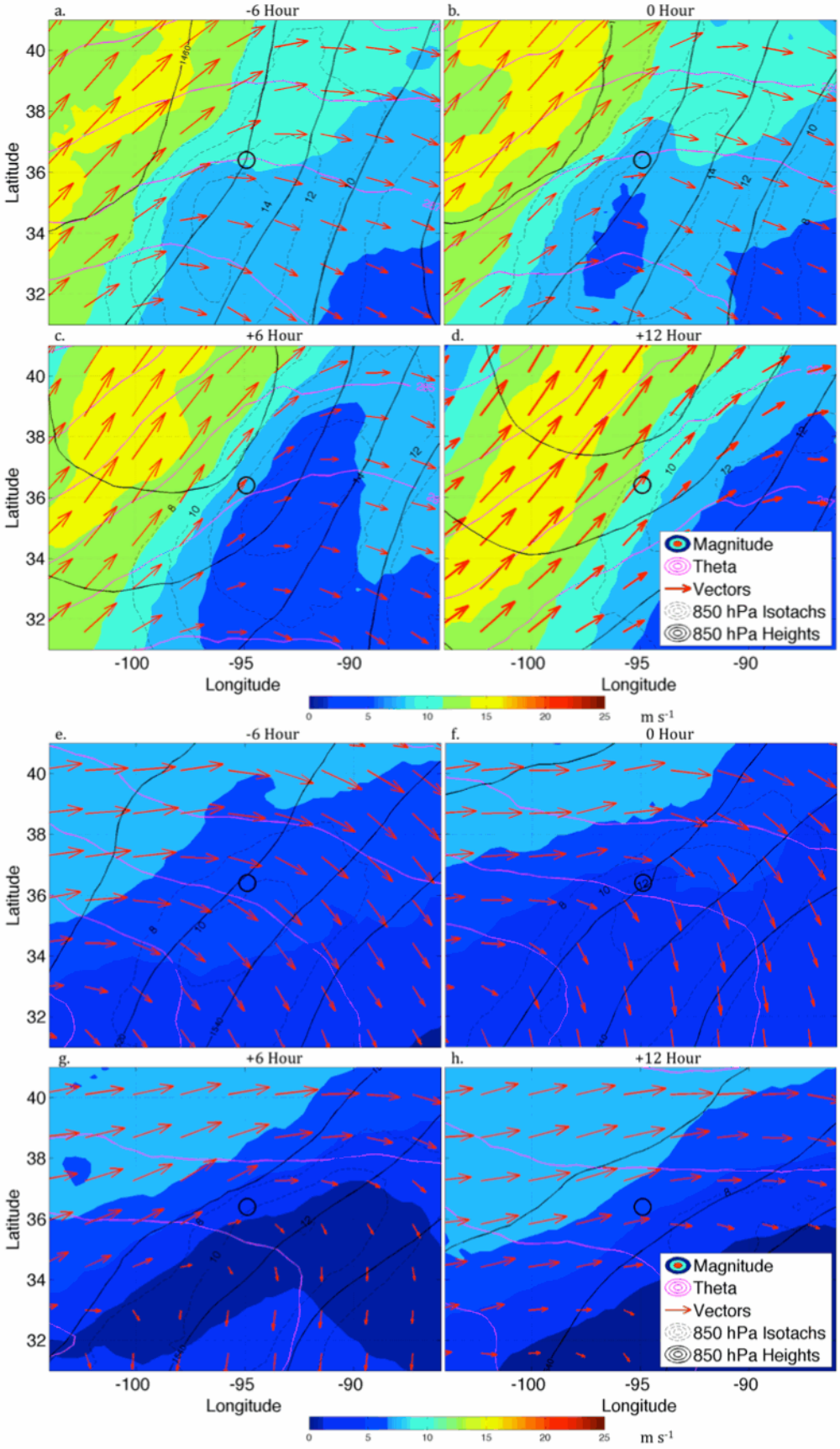
a.
-6 Hour
b.
0 Hour
c.
+6 Hour
d.
+12 Hour
e.
-6 Hour
f.
0 Hour
g.
+6 Hour
h.
+12 Hour
Latitude
Longitude
40
38
36
34
32
-100
-95
-90
Magnitude
Theta
Vectors
850 hPa Isotachs
850 hPa Heights
0
5
10
15
20
25
m s-1

Fig. 2.20. CMV magnitudes (m/s, shading) and vectors (arrows), potential temperature (K, magenta contours), 850 hPa isotachs (m/s, dotted contours), and 850 hPa heights (solid black contours at intervals of 20 m; contour locations and values are identical to Figs 7 and 8) for synoptic type events (top 4 panels) and warm-season type events (bottom 4 panels).

This analysis provides further evidence that in the case of warm season type events, quasi-stationary behavior predominantly resulted from upstream propagation that nearly canceled advection by the mean flow, while in the case of synoptic type events training predominantly resulted from system motion that paralleled a frontal boundary (and subsequently the linear convective region, which also tended to parallel the frontal boundary).

Our application of the Corfidi vector approach here to estimate MCS motion – though effective at demonstrating key differences in the vertical wind profile characteristics between the two sub-types – may be ultimately insufficient at explaining backbuilding and training due to the mentioned influences of synoptic scale forcing for ascent on the convective systems that we have considered in this paper, along with their elevated nature (these caveats to the approach are discussed by Corfidi 2003). Specifically, while the approach outlined by these authors is shown to be statistically successful at predicting MCS motion, little insight is given into the dynamics that specifically contribute to upwind propagation. For instance, the nose region of the low-level jet provides robust low-level mesoscale lift and is a potential contributor to continuous convective re-development (e.g., Stensrud and Fritsch 1993) – especially as it enhances nocturnally (which may explain why many of the systems analyzed here exhibited nocturnal peaks in intensity).

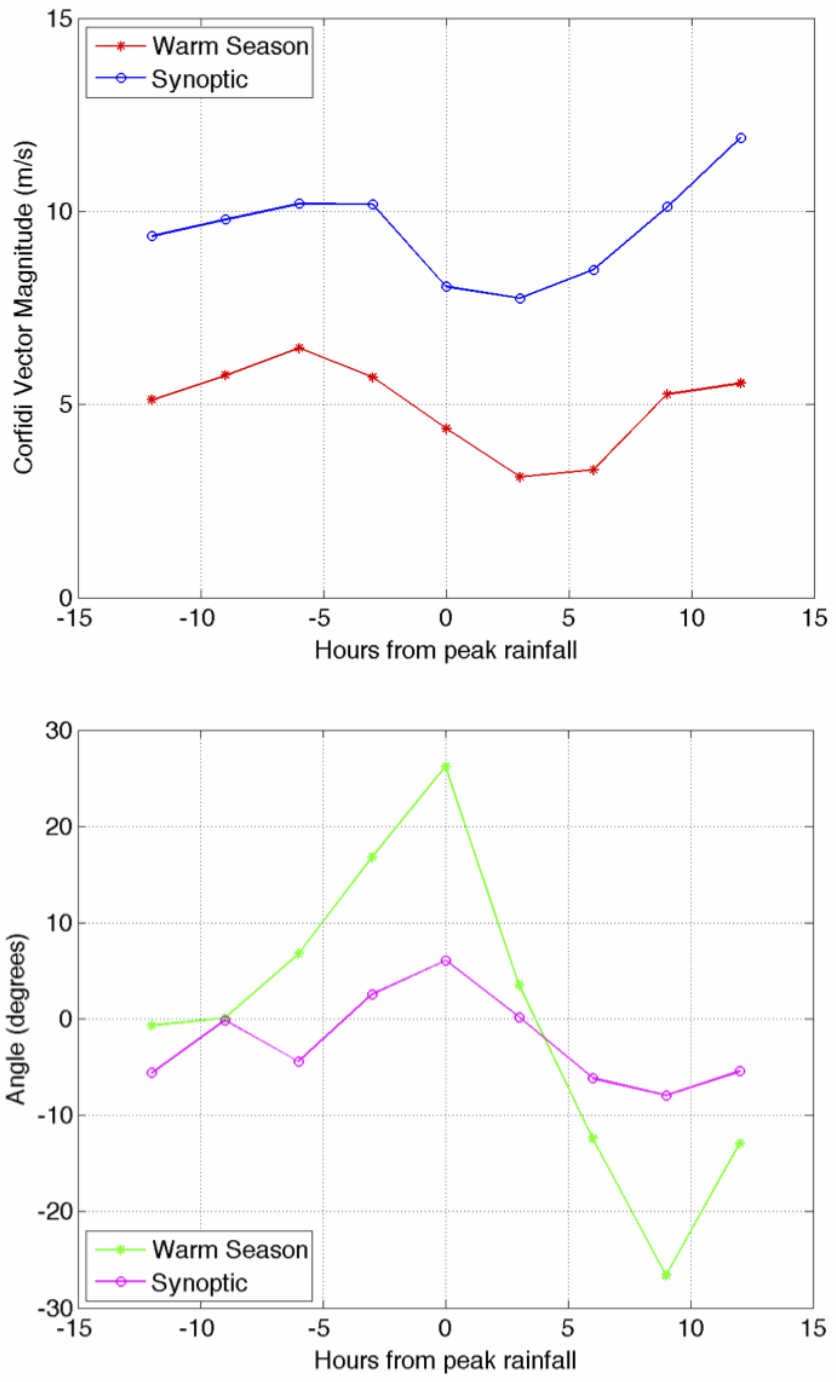

Fig. 2.21. Top panel: time series of CMV magnitudes at the location of peak 1-hour rainfall within both the synoptic and warm-season composites. Bottom panel: time series of the angle between a unit vector parallel to the CMV, and a unit vector perpendicular to the temperature gradient vector. Times indicate hours from the time where peak 1-hour rainfall accumulation occurred at the event location (i.e. -10 hours indicates 10 hours before peak 1-hour rainfall, and +10 hours indicates 10 hours after peak 1-hour rainfall).

Furthermore, the convective-scale nonhydrostatic pressure perturbation field immediately adjacent to the convective system may exhibit a low-level nonhydrostatic high-pressure maxima (Rotunno and Klemp 1982), given the vertical wind shear profile commonly associated with these systems (Schumacher and Johnson 2005), which would promote continuous convective redevelopment along the southwestern periphery of the system. Additionally, the composite CMV magnitudes discussed in section 2.5 for warm-season type events, though smaller than synoptic CMV magnitudes, are non-zero; however, many of the observed warm-season systems remain absolutely stationary for several hours. This further suggests that there are dynamics contributing to upwind propagation in the MCS cases considered in this paper that are not comprehensively explained by the statistical relationship established in the Corfidi studies. A suite of real data and quasi-idealized numerical simulations of the convective systems considered in this paper have been conducted, and are currently being analyzed – through these simulations, and among other goals, we seek to address the mesoscale dynamics that contribute to upwind propagation of the convective systems analyzed here.

2.6. Summary and Discussion

In this study, rotated principal component analysis was applied to the atmospheric fields associated with a large sample of heavy-rain producing TL/AS MCSs. Cluster analysis in the subspace defined by the leading two resulting RPCs revealed two-distinct synoptic sub-types within the broader TL/AS category, which were referred to as warm-season-type and synoptic-type events respectively. Separate composites of both types of events revealed synoptic features that have been typically associated with elevated MCSs, such as a southerly low-level jet and meridionally oriented low-level potential temperature gradient to the south, as well as locally maximized isentropic up-glide within the region where the MCS initiated and evolved.

Other aspects of the synoptic environments evident in the composite atmospheric fields exhibited considerable differences between the two event types. Warm-season type events typically occured within the right entrance region of a minimally-to-anticyclonically curved upper level jet streak, with the warmest low-level air to the southwest. These upper level thermodynamic and flow regimes are characteristic of the North American summer (hence the name "warm season" given to this event type). On the other hand, synoptic-type events, which tended to exhibit greater horizontal extent than warm-season-type events, typically occurred downstream of a progressive upper-level trough, along a low-level potential temperature gradient with the warmest air to the southeast. These upper level thermodynamic and flow regimes are more characteristic of the spring and fall transition months, where strong synoptic systems are more prevalent (hence the name "synoptic" given to these events). Synoptic scale forcing for ascent was typically stronger for synoptic type events, while low-level moisture was typically greater for warm season type events.

Subjectively identified radar reflectivity characteristics and the synoptic frontal boundary type (if any) that the MCS developed along were cataloged for each event type. Synoptic-type events were often followed by the passage of a progressive TS-type MCS, while warm-season type events were often preceded by the passage of such systems. Roughly 50% of all cases occurred along a nearly stationary warm front, while a few cases occurred near a cold front or did not coincide with a well-defined synoptic boundary. 50% of warm-season-type events exhibited a behavior known as rearward off-boundary development (ROD), whereby linear convection re-generated to the rear of a progressive TS-type MCS, north of the southern periphery of the cold pool generated by the initial system.

Our results from the RPCA applied to atmospheric fields associated with MCS events highlight the utility of such methods as an objective supplement to the current subjective MCS archetype classification methods. Several aspects of the RPCA outcome (and the composites generated therein) are noteworthy in the context of past studies of the types of convective systems considered here – specifically the Maddox et al. (1979) and Schumacher and Johnson (2005) studies where different types of events are subjectively differentiated from one another. For instance, some events that clearly constituted a TL/AS radar morphology (e.g. the 23 Sept. 2004 Ohio River Valley and 15 Sept. 2004 Iowa/Minnesota events shown in Fig. 2.15, which were classified here as synoptic sub-type events) occurred within similar synoptic environments to events that would likely be subjectively classified as Maddox et al. (1979) "synoptic-type events" (e.g. the 2 Nov 2004 Gulf Coast event). Likewise, other events that also clearly constituted a TL/AS radar morphology (e.g. the 25-May 2005 Kansas and 28-Jul 2011 Iowa events shown in Fig. 2.15, which were classified here as warm season sub-type events) occurred in synoptic environments that were notably different from our synoptic sub-type category – in fact, the composites for the warm-season-type cases subjectively exhibit closer similarities to those from Keene and Schumacher (2013) for bow-and-arrow type events, and Schumacher and Johnson (2005) for Backbulding/Quasi-Stationary type events. The former comparison (to bow-and-arrow events) is supported by the visual similarity of the ROD behavior that is frequently observed here in warm season cases to the bow-and-arrow phenomena, the latter comparison is supported by the fact that backbuilding behavior was observed in a number of our warm-season type cases. The overarching observation here is that the dividing lines between case types laid out by quasi-objective RPCA method do not necessarily coincide with the subjective case classifications based on radar imagery.

From a predictive standpoint, it is noteworthy that two different types of synoptic environments are conducive to heavy-rain-producing convective systems. For instance, a forecaster may notice a short-to-medium range synoptic-scale environment within a numerical weather prediction model solution that resembles the archetype for synoptic events presented in this study, and make note of the potential for a heavy rain episode in their forecast discussion. During the summer months, however, a forecaster should shift the focus of their analysis of model solutions to recognize synoptic-scale environments that are conducive to warm season events (which again, exhibit quite different synoptic scale characteristics).

On a final note, while the analysis presented here has reinforced the salient characteristics commonly associated with quasi-stationary MCSs by previous authors, as well as identified key ways in which these characteristics vary among cases, a valuable supplemental study would involve the comparison between the characteristics of quasi-stationary MCSs and their progressive counterparts (which have not been addressed in any detail here). For instance, while a southwesterly wind direction within the low-level jet (which, by means of propagation, largely cancels the predominantly southwesterly advective component of storm motion as evident in the Corifidi vector analysis) is clearly a salient characteristic of both event types, it is unclear whether this characteristic specifically differentiates slow-moving MCS events from faster moving progressive MCS events.

CHAPTER 3

GOVERNING DYNAMICS OF AN OBSERVED WARM SEASON TL/AS EVENT

3.1. Background

A large percentage of flash floods in the United States result from heavy convective rainfall associated with specific breeds of mesoscale convective systems (MCSs, on the order of 60-75%, e.g. Maddox et al. 1979; Moore et al. 2003; Schumacher and Johnson 2006), where the character of the system's motion results in extended production of heavy rain over a fixed geographic location. "Training" of convection and upstream backbuilding constitute the two predominant mechanisms for heavy rainfall production by MCSs (e.g., Chappell 1986; Corfidi et al. 1996; Doswell et al. 1996; Schumacher and Johnson 2005; Schumacher 2009). Training involves a convective line in which individual cells predominantly move in the line-parallel direction, resulting in repeated motion of cells over a particular geographic region, while back-building involves the repeated geographically-fixed upstream (downstream) regeneration (decay) of convective cells, resulting in the convective region of an MCS being quasi-stationary. Schumacher and Johnson (2005) termed the two MCS archetypes that most frequently exhibit these behaviors the training line – adjoining stratiform (TL/AS) and backbuilding (BB) archetypes.

The first-order requirement for these phenomena is a continuous supply of the ingredients for moist convection (e.g., Johns and Doswell 1992) to the MCS location by the synoptic scale environment. This typically constitutes a supply of warm, moist air by the low-level jet with the vertical maxima in convective available potential energy (CAPE) and minima in convective inhibition residing above the surface (hereinafter referred to as elevated, e.g., Moore et al. 2003; Schumacher and Johnson 2006; Wilson and Roberts 2006; Corfidi et al. 2008). Persistent low-

level lifting is also often present associated with isentropic upglide and convergence along the nose of a low-level jet (Maddox et al. 1979; Augustine and Caracena 1994; Laing and Fritsch 2000; Moore et al. 2003; Schumacher and Johnson 2005; 2006; 2008; Peters and Schumacher 2014). The factors contributing to the convective-scale organization and evolution of such convective systems, however, remain poorly understood due to their propensity to occur within nocturnal elevated environments, where the well studied mechanisms for propagation of surface-based convection do not necessarily apply. Furthermore, they are often preceded and/or followed by the passage of a progressive trailing stratiform (TS, Parker and Johnson 2000) MCS (Corfidi 2003; Peters and Schumacher 2014), which undoubtedly influences the local kinematic and thermodynamic environments. In many instances where a training MCS is preceded by a separate progressive MCS, the linear convective region of the training system may be offset from the periphery of the low-level cold pool generated by preceding convection ("bow and arrow effect," Keene and Schumacher 2013; "Rearward Off-boundary Development" [ROD], Peters and Schumacher 2014 – this phenomenon is described in greater detail in later sections). Additionally, in the case of quasi-stationary systems, the region of upstream back-building often remains stationary for several hours without obvious orographic influencing factors or a stationary atmospheric boundary (e.g. dryline, outflow boundary) that would intuitively promote such behavior. While previous authors (e.g. Bosart and Sanders 1981; Fritsch et al. 1994; Trier and Davis 2002; Schumacher and Johnson 2008; 2009; Schumacher 2009) show that such instances of quasi-stationary behavior are sometimes explained by the presence of a mesoscale convective vortex (MCV), not all cases involve an obvious MCV. Other potential mechanisms for upstream propagation include standing gravity waves and bores residing along the interface between the stable boundary layer and overlying conditionally unstable air (Crook and Moncrieff

1988; Schmidt and Cotton 1990; Stensrud and Fritsch 1993; Parker 2008; French and Parker 2010; Schumacher and Johnson 2008; Schumacher 2009; Trier et al. 2010; 2011).

This research constitutes the initial phase of a series of numerical modeling experiments that aim to comprehensively address the dynamics of elevated quasi-stationary MCSs – specifically TL/AS systems that occur in the absence of an obvious MCV (since simulations of systems occurring in conjunction with an MCV have been intensively studied by previous works; e.g. Schumacher and Johnson 2008 and 2009, and Schumacher 2009). The work presented here involves a detailed case study a numerical simulation of an observed flash-flood producing TL/AS event that occurred over Dubuque, Iowa on 28 July 2011. The evolution of this system was complex, and featured may of the aforementioned phenomena that frequently occur in the case of quasi-stationary MCSs including preceding/succeeding MCS passages, ROD, and upstream back-building. The organization of this paper is as follows. Section 3.2 provides an overview of the synoptic scale setup that led to this event, and describes aspects of the observed radar evolution. Section 3.3 describes the numerical modeling configuration used to simulate the event, section 3.4 outlines characteristics of the simulated MCS, which is dynamically analyzed in section 3.5. Section 3.6 summarizes the findings presented here and outlines ongoing and future work.

3.2. Event Overview

A flash-flood-producing TL/AS MCS produced over 150 mm of rainfall accumulation across a large E-W oriented swath near Dubuque, Iowa, with local rainfall totals as high as 380 mm during the evening of 27 July and early morning hours of 28 July 2011 (National Weather Service Quad Cities Office 2011).

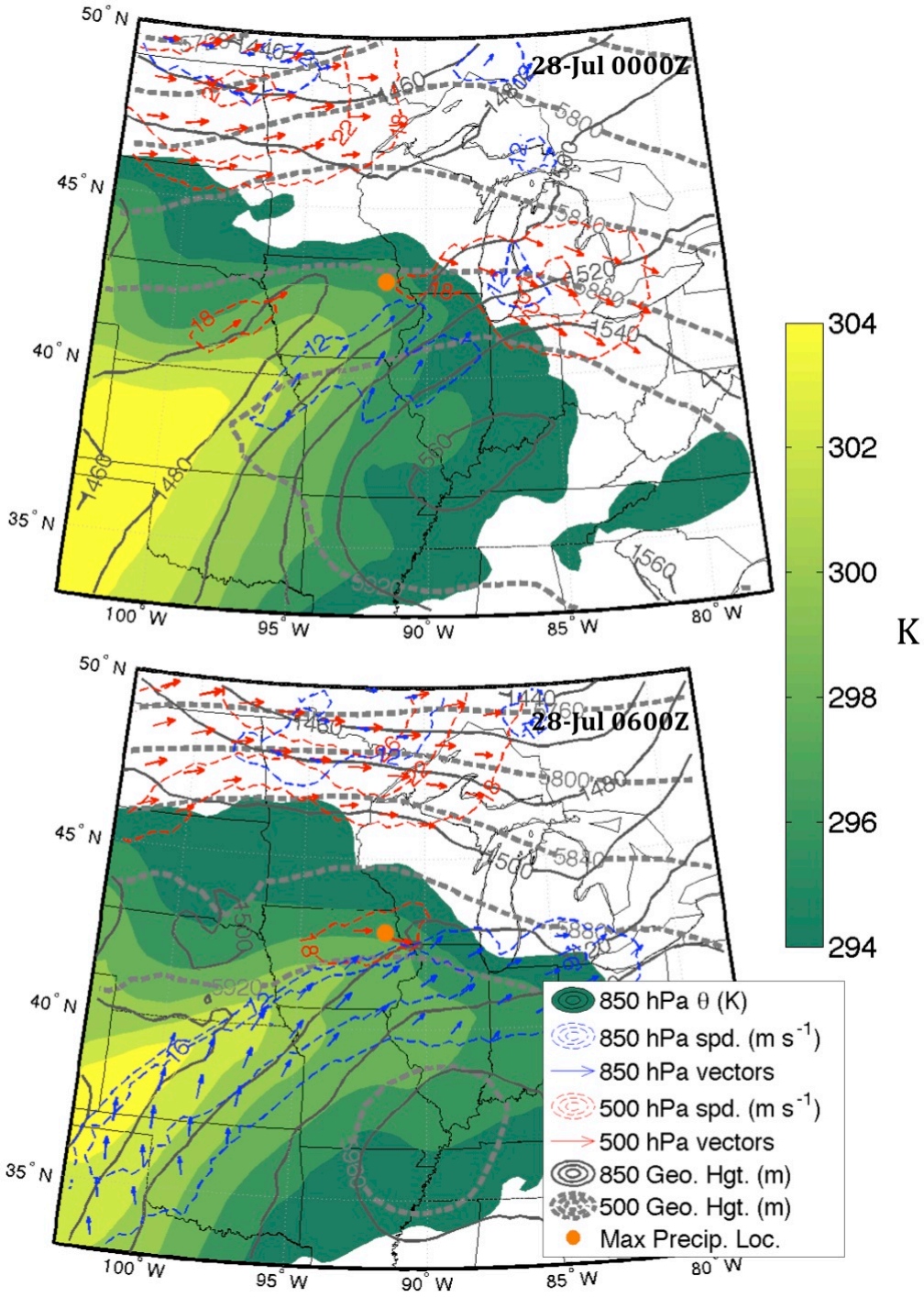

Fig. 3.1. Regional summary of the atmospheric setup leading to the 28 July 2011 TL/AS MCS. Maps were constructed from the NARR. Quantities shown are 850 hPa potential temperature (shading), 850 hPa geopotential height (solid dark gray contours, at intervals of 20 m), 850 hPa wind speed > 12 m/s (dashed blue contours at intervals of 4 m/s), 850 hPa wind vectors (blue arrows), 500 hPa geopotential height (dashed light gray contours, at intervals of 40 m), 500 hPa wind speed > 18 m/s (dashed red contours, at intervals of 4 m/s), 500 hPa wind vectors (red arrows), and the location of maximum observed rainfall (orange dot).

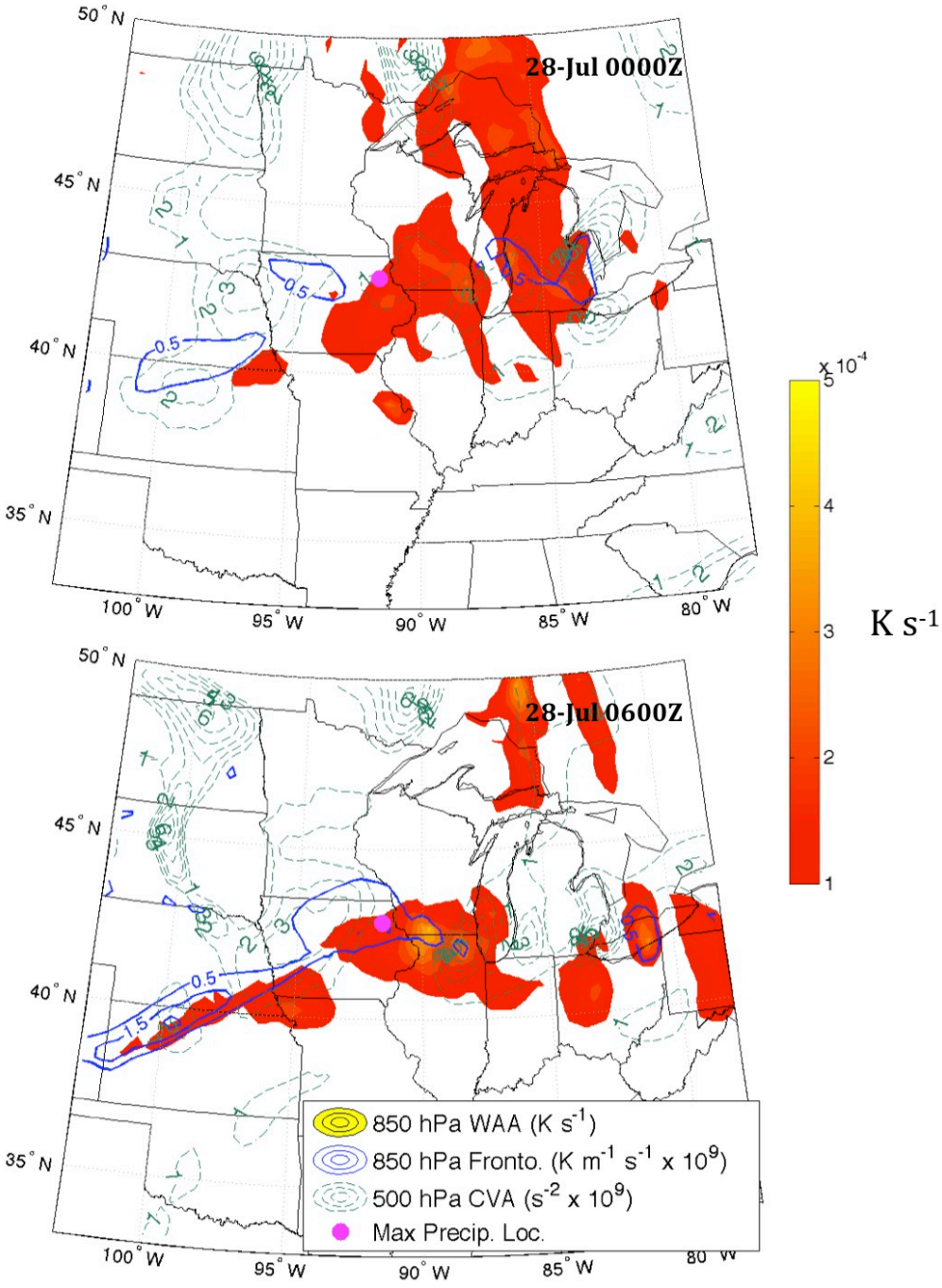

Fig. 3.2. Summary of the regional large-scale forcing associated with the 28 July 2011 TL/AS MCS. Warm air advection (WAA) is shaded, with values below 1 x 10^{-4} K s^{-1} removed. Blue contours are horizontal frontogenesis, with a contour interval of 1 x 10^{-9} K $m^{-1}s^{-1}$ multiplied by 10^{9}. Green dashed contours are cyclonic vorticity advection (CVA), with a contour interval of 1 x 10^{-9} s^{-2} multiplied by 10^{9}. The magenta dot denotes the location where the maximum 1-hour precipitation accumulation total was observed.

Figs. 3.1 and 3.2, which show analyzed atmospheric fields from the North American Regional Reanalysis (NARR, Mesinger et al. 2006), summarize the regional atmospheric setup that led to this event. The initial convection associated with the TL/AS MCS developed at roughly 0000 UTC 28 July 2011 along the northwestern periphery of a low-level anticyclone, northern periphery of a southwesterly low-level jet, and beneath a mid-level ridge with weak mid-to-upper level winds (Fig. 3.1). The region local to the event was characterized by sustained low-level warm air advection fed by a southwesterly low-level jet, along with low-level deformation and corresponding frontogenesis (Figs. 3.1 and 3.2). A weak midtropospheric shortwave trough approached the region of interest from the west and contributed to modest cyclonic vorticity advection (CVA; Figs. 3.1b and 3.2). This overall synoptic environment was characteristic of the composite TL/AS environment shown by Schumacher and Johnson (2005), and more specifically the warm-season type events described by Peters and Schumacher (2014) (contrasted with synoptic-type events, which typically occur in conjunction with stronger flow aloft, a stronger low-level cyclone, trailing cold front, and preceding warm front). A fixture of the synoptic-scale setups for such events (including the one studied here) is that the environment provided a *sustained supply* of moisture, instability, and lift (the basic ingredients for deep, moist convection) to the region where heavy rainfall occurred.

A series of composite radar reflectivity images spanning the evolution of this MCS are shown in Fig. 3.3. Convection initially developed as a multi-cell cluster of storms near Dubuque at approximately 0000 UTC on 28 July (Fig. 3.3a). These storms organized upscale into a small progressive TS type MCS that moved eastward and dissipated over northern IL (Fig. 3.3b,c).

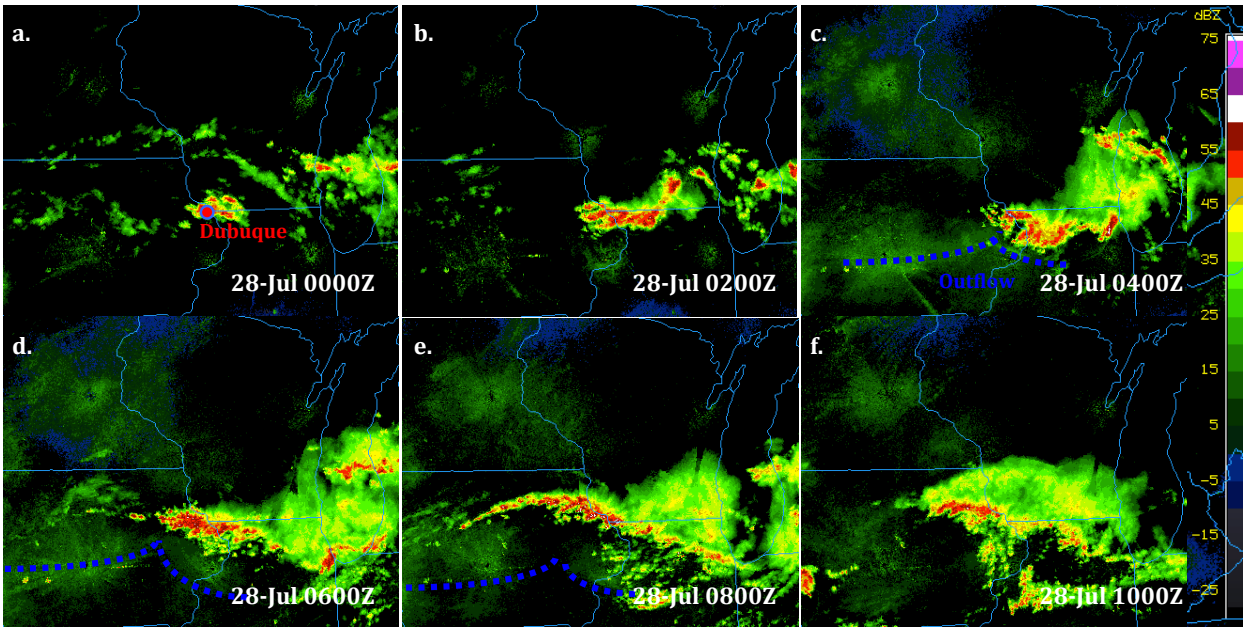

Fig. 3.3. Observed composite radar reflectivity images (dBZ, shading) from 0000 UTC through 1000 UTC on 28 July 2011 depicting the evolution of the MCS detailed in this study.

An observed sounding taken from Davenport, Iowa at 0000 UTC revealed a highly unstable boundary layer with surface based CAPE (SBCAPE) near 5000 J/Kg (Fig. 3.4), and maps of NARR-analyzed MUCAPE showed localized regions of SBCAPE near 6000 J/kg – these observations suggest the aforementioned first round of thunderstorms was rooted in the planetary boundary layer (PBL). The cold pool produced by this system, along with nocturnal radiational cooling, then stabilized the PBL and set the stage for subsequent rounds of elevated convective activity (see Fig. 3.5, where the lifted parcel level near the maximum precipitation location is above the surface by 0600 UTC). In the wake of this initial MCS, an east-to-west oriented convective line developed (ROD) and became quasi-stationary, with convection backbuilding to the west of Dubuque and individual convective cells moving predominantly in the convective-line-parallel direction (Fig. 3.3d-f). ROD is distinguished from other mechanisms for upstream MCS propagation in that a discrete convective line simultaneously re-develops upstream of the initial MCS elevated above the cold pool left by the initial system, and well removed from (usually north of) the surface outflow boundary.

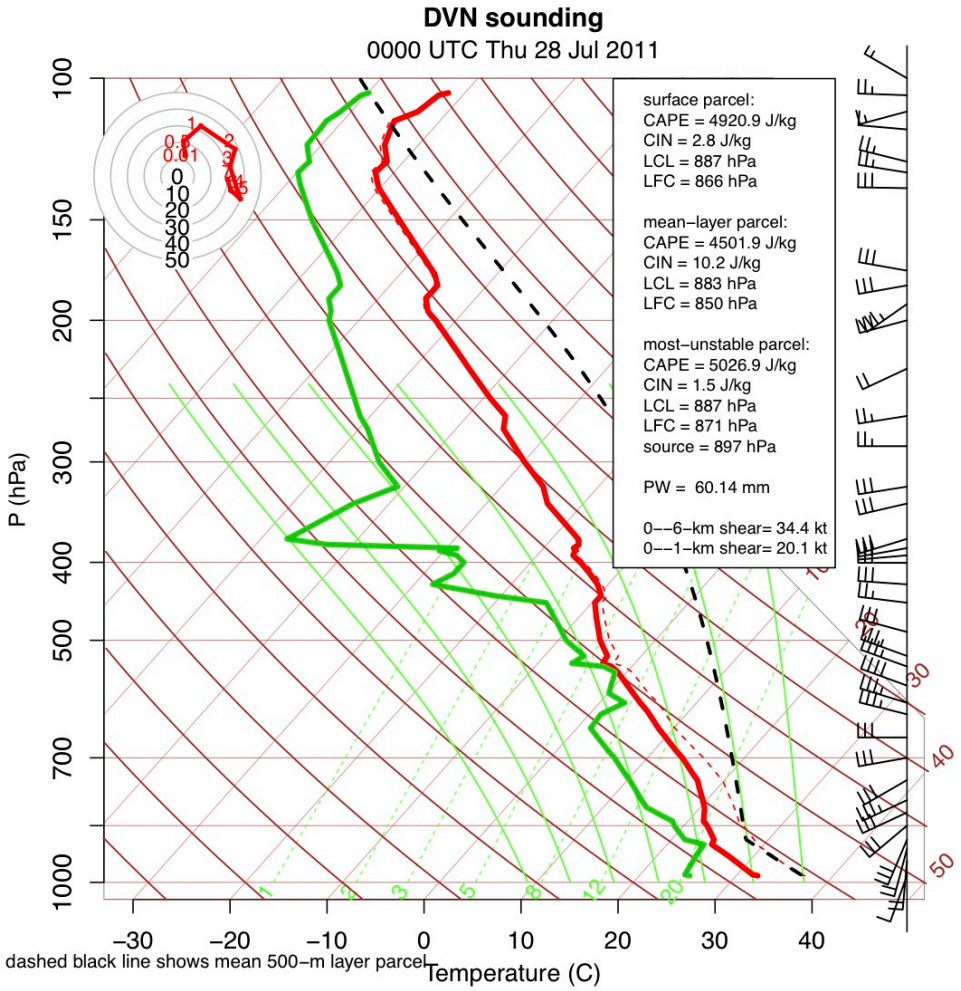

Fig. 3.4. Observed upper-air sounding taken at 0000 UTC 28 July 2011 from the Davenport, IA NWS weather forecast office.

Then, following the occurrence of ROD, fixed upstream backbuilding of convection continued along the western end of the line until approximately 1300 UTC on the 28 July after which the TL/AS MCS weakened and another separate progressive MCS moved through the region (not shown in Fig. 3.3). The time evolution of precipitation produced by the MCS is summarized in Fig. 3.6. The most intense observed point-precipitation rates occurred with the first round of convective activity. The ROD episode is also evident as an abrupt westward propagation of the precipitation axis at 0800 UTC (as notated in the figure). This analysis will serve as a means of

comparison between the observed MCS evolution and the simulated evolutions that are discussed in the next section.

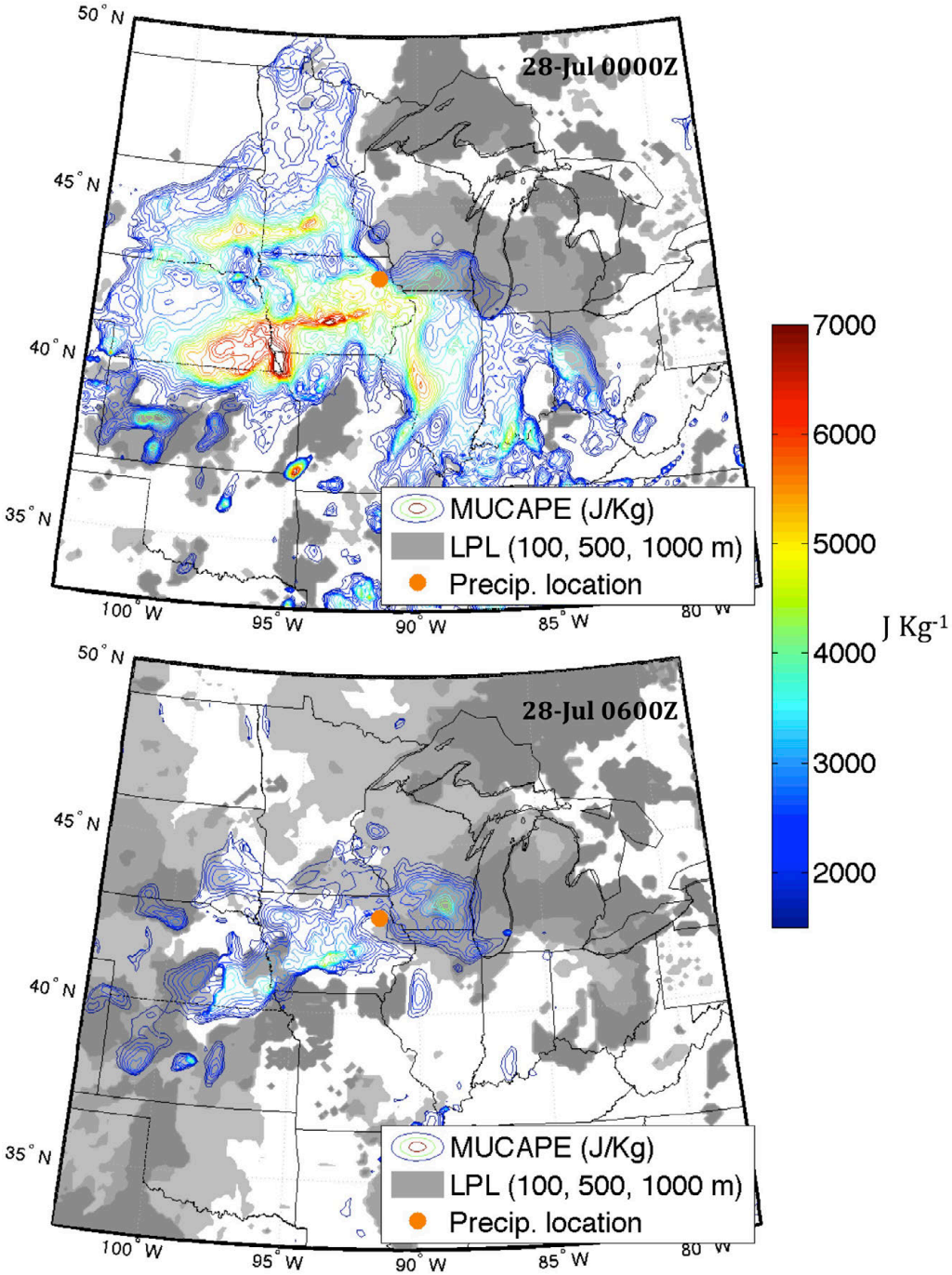

Fig. 3.5. Analysis of most unstable CAPE (MUCAPE) computed from the Rapid Update Cycle (Benjamin et al. 2003) analysis (color contours, J/Kg at intervals of 100 J/Kg), the height of the maximum CAPE value (m, gray shading at 100, 500, and 1000 m increasing increments denoted by increasing darkness of gray shading), and the location of maximum observed rainfall (orange dot) at (a) 0000 UTC and (b) 0600 UTC 28 July 2011.

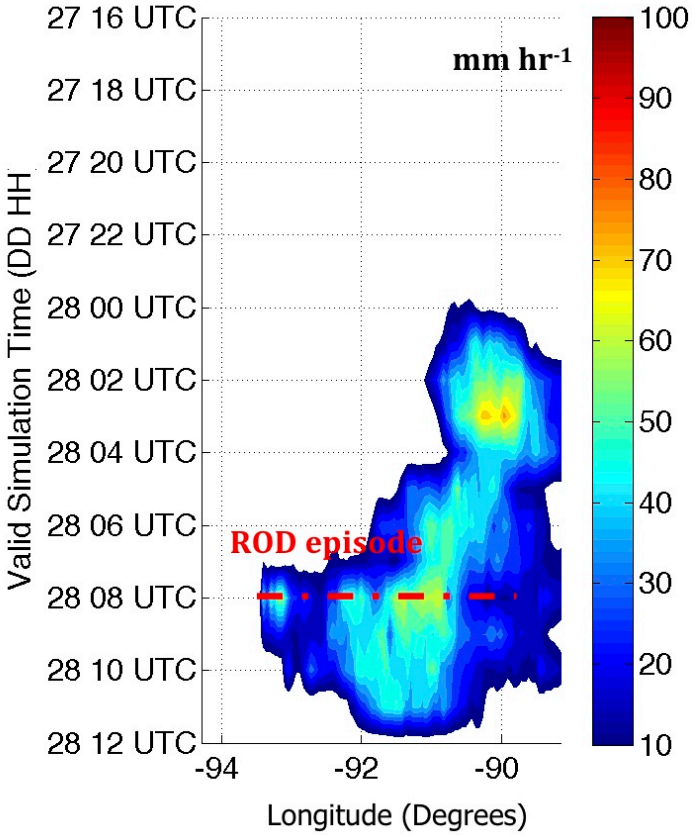

Fig. 3.6. Hovmöller diagram of the maximum 1-hour point precipitation total (mm) in the ST4 analysis within 10 grid points (at a 4 km grid spacing) north or south of each ST4 grid point along a zonally oriented line through the point indicated by the orange dot in Fig. 1 (at approximately 42.5 degrees latitude).

3.3. Model configuration

Version 3.4.1 of the Advanced Research Weather Research and Forecasting Model (WRF-ARW; Klemp et al. 2007; Skamarock et al. 2008) was run with a two-domain nested structure to simulate the 28 July 2011 MCS, with the interface between the two domains configured in one-way mode (i.e. the outer domain provided lateral boundaries to the inner domain only, and no feedback from the inner domain to the outer domain was allowed). The horizontal grid spacing was 15 km for the outer domain, which utilized a convective parameterization scheme, and 3 km for a convection-allowing inner domain. Horizontal domain dimensions were 3000 km and 1200 km for the outer and inner domains respectively, and both

domains featured 36 vertical sigma levels (see Fig. 3.7 for the locations of both domains). All simulations were run from 1200 UTC 27 July 2011 to 1200 UTC 29 July 2011 with both domains active through this entire time.

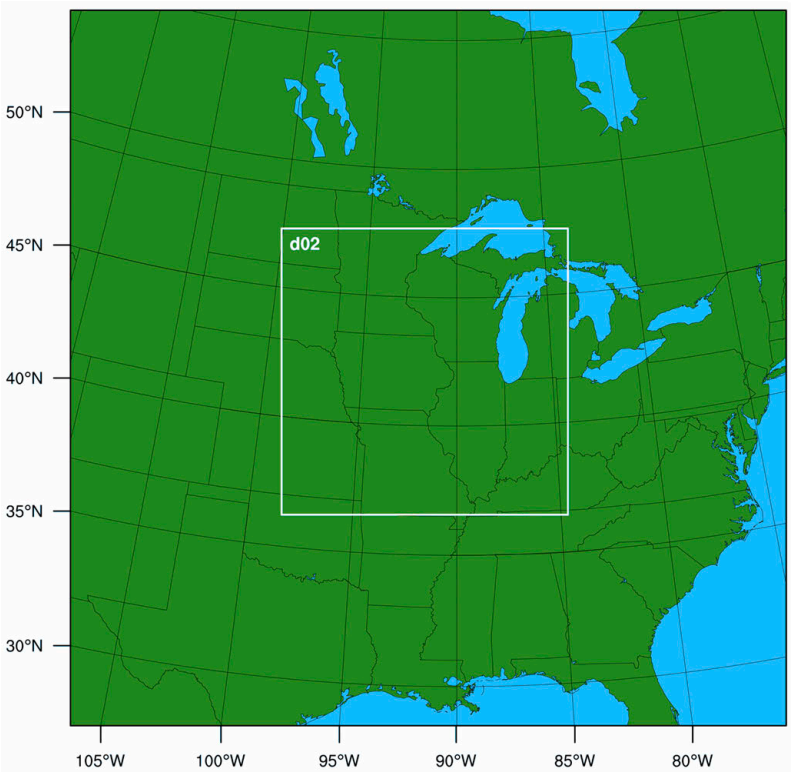

Fig. 3.7. Locations of both model domains. The periphery of the map denotes the edge of the outer domain, and the white square denotes the edge of the inner domain.

Four simulations were conducted with differing microphysical parameterization schemes and initial and lateral boundary conditions (ICs and LBCs respectively) as a first order test of the sensitivity of the simulated MCS evolution to these parameters. A summary of the model parameters used for each simulation is given in Table 3.1. The NARR was used as ICs and LBCs for three simulations, which featured Thompson microphysics (THOM run), Morrison microphysics (MORR run), and Kessler microphysics (KESS run).

Table 3.1. List of WRF-ARW grid resolutions, grid dimensions, physical parameterizations and nudging configurations used in this study. Quotations indicate that the parameter is the same as the model configuration in the column to the left. The outer domains for each of the four simulations featured the Grell-3 cumulus parameterization scheme, and all other parameters the same as their respective inner domains

Domain	**THOM Outer**	**THOM Inner**	**MORR Inner**	**KESS Inner**	**ERAI Inner**
Grid Spacing	15 km	3 km	""	""	""
Domain Dimensions	3000 x 3000 km	1200 x 1200 km	""	""	""
Vertical Sigma Levels	36	36	""	""	""
Model Top Pressure	100 hPa	""	""	""	""
ICs and LBCs	NARR	""	""	""	Era-Interim[9]
Microphysics	Thompson[1]	Thompson[1]	Morrison[2]	Kessler[3]	Thompson[1]
Longwave Radiation	RRTM[4]	""	""	""	""
Shortwave Radiation	Dudhia[5]	""	""	""	""
Surface Layer	Eta Similarity	""	""	""	""
Land Surface Model	NOAA Land Surface Model[6]	""	""	""	""
Boundary Layer Physics	MYJ[7]	""	""	""	""
Cumulus Parameterization	Grell-3[8]	*none*	""	""	""

[1] Thompson et al. (2008)
[2] Morrison et al. (2008)
[3] Kessler (1969)
[4] Miawer et al. (1997)
[5] Dudhia (1989)
[6] Mitchell et al. (2005)
[7] Janjic (1994)
[8] Grell and Devenyi (2002)
[9] Dee et al. (2011)

Note that the Kessler microphysics scheme excludes ice physics, and a comparison between the results of this simulation and those employing the more sophisticated schemes provides a first order assessment of the sensitivity of the convective evolution to ice processes. In the final

simulation, Era-Interim (Dee et al. 2011) was used for ICs and LBCs in place of the NARR with the Thompson microphysics scheme (ERAI run).

The 24-hour simulated precipitation accumulation totals from the simulations are compared to observed precipitation in Fig. 3.8.

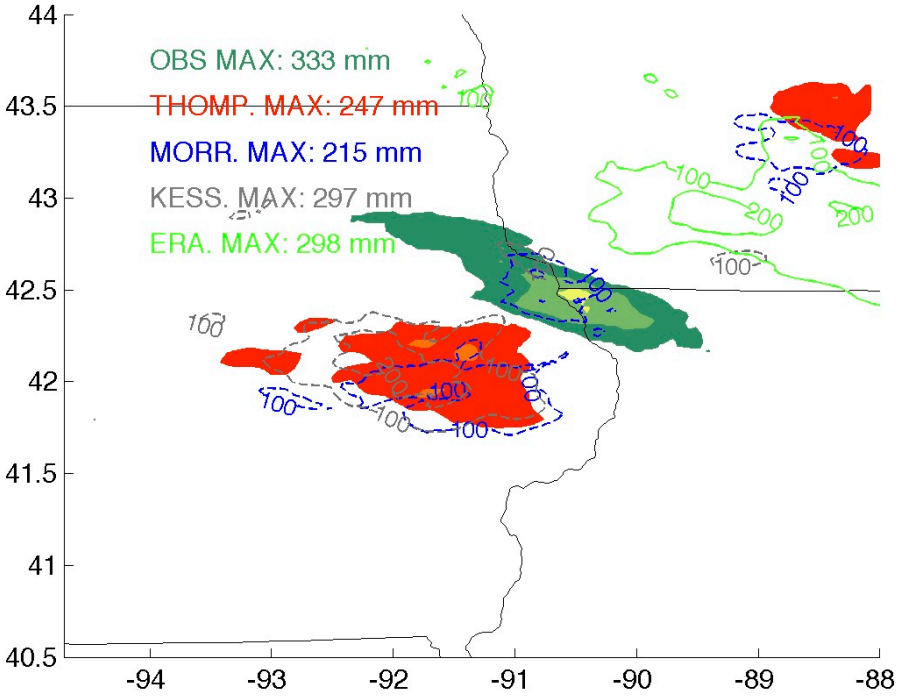

Fig. 3.8. Comparison of the ST4 24-hour accumulated precipitation analysis ending at 1200 UTC 28 July 2011 (green shading at intervals of 100 mm, lighter colors indicate greater totals) to modeled accumulated precipitation totals over the same timeframe from the THOM (red shading at intervals of 100 mm, lighter colors indicate greater totals), MORR (dashed blue contours at intervals of 100 mm), KESS (dashed gray contours at intervals of 100 mm), and ERAI (solid green contours at intervals of 100 mm) simulations.

While the maximum point totals varied between 200 and 300 mm among simulations, which is a slight under prediction, all three NARR-driven simulations produced a large swath of maximized accumulated rainfall displaced approximately 100 km to the southwest of the observed maxima. Interestingly, the Era-Interim driven simulation produced a precipitation maxima with a displacement of nearly equal magnitude but opposite direction (to the northeast). While an investigation of the precise mechanisms that contributed to such biases is beyond the scope of

this study, these results suggest that the evolution of the 28 July 2011 MCS exhibited greater sensitivity to synoptic scale conditions (i.e. ICs and LBCs) than internal convective processes. This result is supported by the work of Peters and Roebber (2014), who showed that a large percentage of the variance in modeled placement of heavy precipitation produced by TL/AS systems was explained by uncertainty in synoptic scale atmospheric conditions.

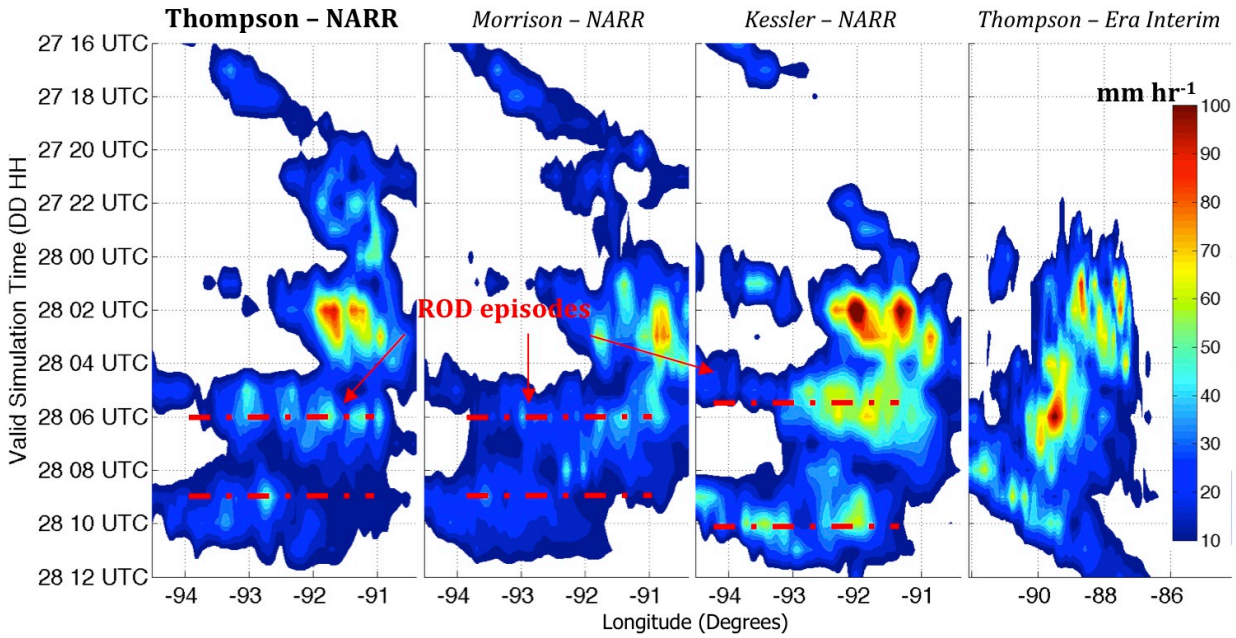

Fig. 3.9. Hovmöller diagrams of the maximum 1-hour point precipitation total (mm) for four different model simulations within 15 grid points (at a 3 km grid spacing) north or south of each model grid point along a zonally oriented line at approximately 42 degrees latitude for the NARR driven simulations, and 43 degrees north for the Era-Interim driven simulation.

Fig. 3.9, which summarizes the time evolution of precipitation in the simulations, facilitates further comparison between the simulations and observations. The NARR-driven simulated MCSs underwent two distinct ROD episodes (only one occurred in observations) – one at approximately 0400 UTC and a second at 0700 UTC, which is a potential explanation for the slightly lower modeled accumulated precipitation values relative to observations (i.e. the cold pool surges resulted in convection briefly exiting the region of heaviest rainfall accumulation).

These events are evident in Fig. 3.10, which shows representative simulated radar reflectivity images from the THOM run.

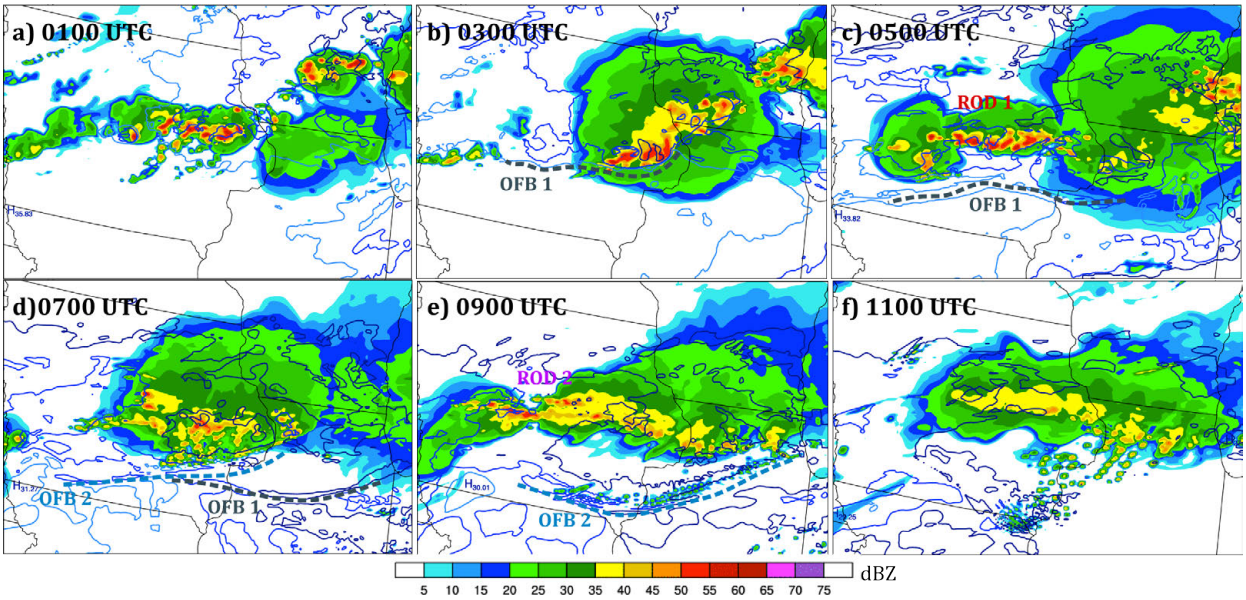

Fig. 3.10. Simulated radar reflectivity images (shading, dBZ) of the modeled MCS from 0100 UTC through 1100 UTC 28 July 2011. Surface temperature contours of 25, 27 and 29 deg. C are dark blue, blue, and light blue contours respectively.

The Era-Interim driven simulated MCS, however, did not exhibit a coherent ROD episode (though backbuilding convection did gradually propagate upstream, and the system remained elevated over a cold pool). Our subjective analysis of simulated reflectivity indicated that each of the NARR-driven simulations reproduced the salient radar-observed features of the observed MCS remarkably well, with the timing of convective initiation associated with the TL/AS and dissipation of the system approximately an hour delayed in the model. The characteristics of the simulated radar reflectivity form the Era-interim driven simulation (not shown), on the other hand, were noticeably different from observations and the NARR driven simulations.

The THOM run overall best mimicked the observed evolution of the MCS in simulated reflectivity and featured a more complete microphysics package than the KESS run (which produced a closer maximum precipitation total to OBS, but may have done so for the "wrong

reasons," owing to the absence of ice phase in the microphysics scheme). We therefore chose to concentrate our dynamical analysis of the evolution of this event on output from the THOM run as a proxy for high-resolution four-dimensional observations of the environment (which are unavailable for this event). As a supplementary check of the similarity between our simulation and observed MCS, we compared maps of analyzed atmospheric fields from the SPC national sector mesoanalysis archive (not shown) to the analogous fields produced by our model simulation, and found the overall evolution of these fields to be similar.

Finally, in order to test the sensitivity of the convective evolution to horizontal and vertical grid spacing, an additional simulation was conducted with a 3rd 1km inner nest centered at the MCS location, 50 vertical levels (increased from 36 in the other four simulations), and all other attributes the same as the THOM run. The subjective evolution of the MCS on both the 3km and 1km domains in this run remained very similar to that of the THOM run. While a substantially finer horizontal resolution than that afforded by 3km (and even 1km) grid spacings is required to resolve the dynamics of individual convective updrafts (Bryan et al. 2003), the horizontal grid spacing used here has been shown in previous studies (e.g. Weisman et al. 1997, Schwartz et al. 2009) to emulate MCS-scale processes. Since the focus of this study will be to assess the dynamics of MCS-scale processes and their influence on the convective system of interest (which occur on the order of 10-100 km), the lower effective resolution threshold of our grid spacing (~ 7 dx, or ~ 20 km) is sufficient here, deeming the computational expense of analyzing the 1-km simulation unnecessary.

3.4. Characteristics of the Simulated MCS

3.4.a. Kinematic and thermodynamic structures

Fig. 11 shows snapshots from the time evolution of surface winds and potential temperature perturbations θ', computed by subtracting the full θ field from a Barnes filtered θ field with a radius of influence of 150 km (see Barnes 1964). The results of the Barnes filtering processes were found to be insensitivity to small changes in the magnitude of this parameter, and a value of 150 km was subjectively determined to isolate synoptic scale wavelengths from the features produced by the convective system.

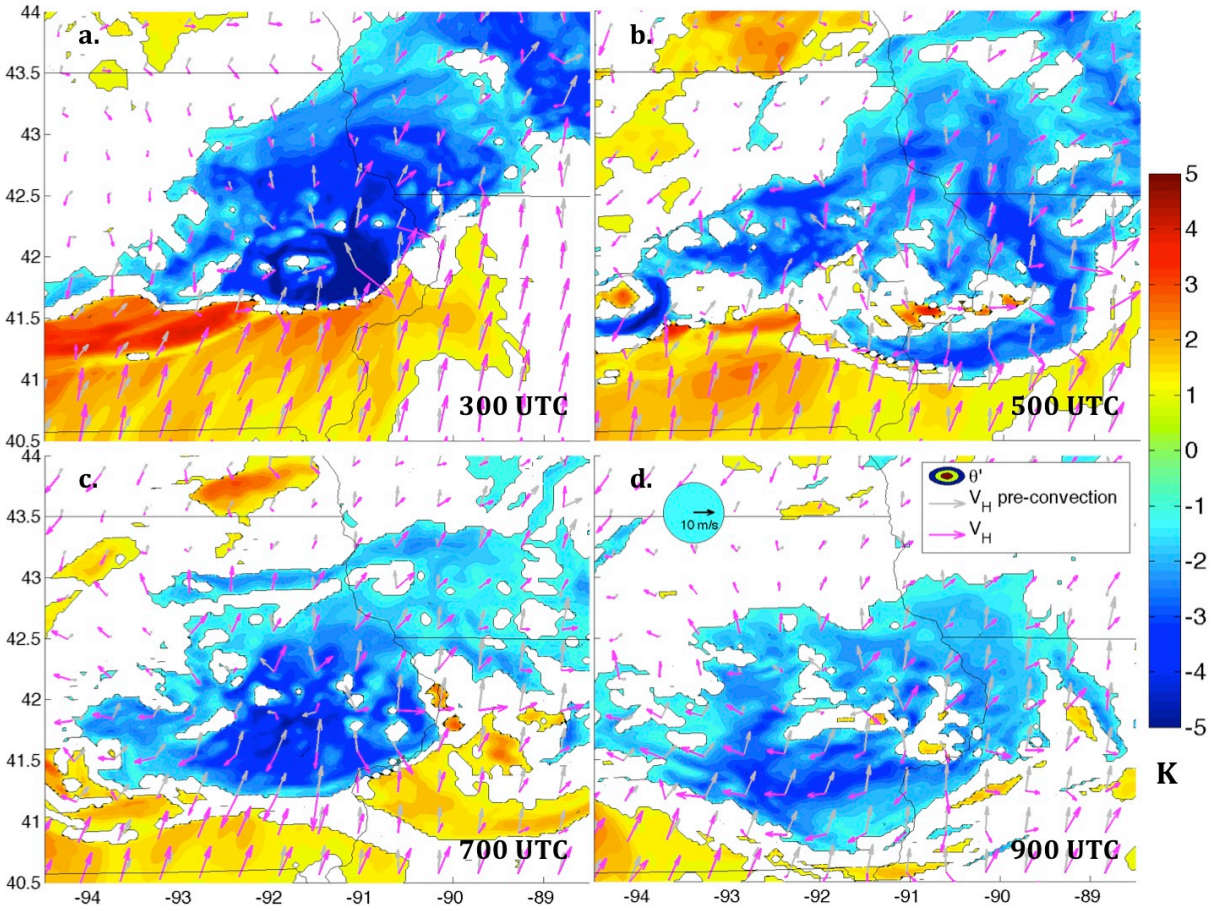

Fig. 3.11. Perturbation potential temperature (θ') on the first model sigma level (shading, K), wind vectors on the first model sigma level at the valid time indicated in each panel (magenta arrows, m/s), wind vectors on the first model sigma level at 2300 UTC 27 July 2011 (gray arrows, m/s; included to illustrate the change in wind between 2300 UTC and the valid time in each frame).

A surface cold pool was evident throughout the evolution of the MCS, with the cold pool expanse and intensity having been maximized at 0300 UTC (Fig. 3.11a) and 0700 UTC (Fig. 3.11c). Local neutral-to-warm anomalies were also present within the cold pool (especially evident in Fig. 3.11b,d) – features that have been observed in previous studies of elevated convective systems with cold pools (e.g. Schumacher 2009).

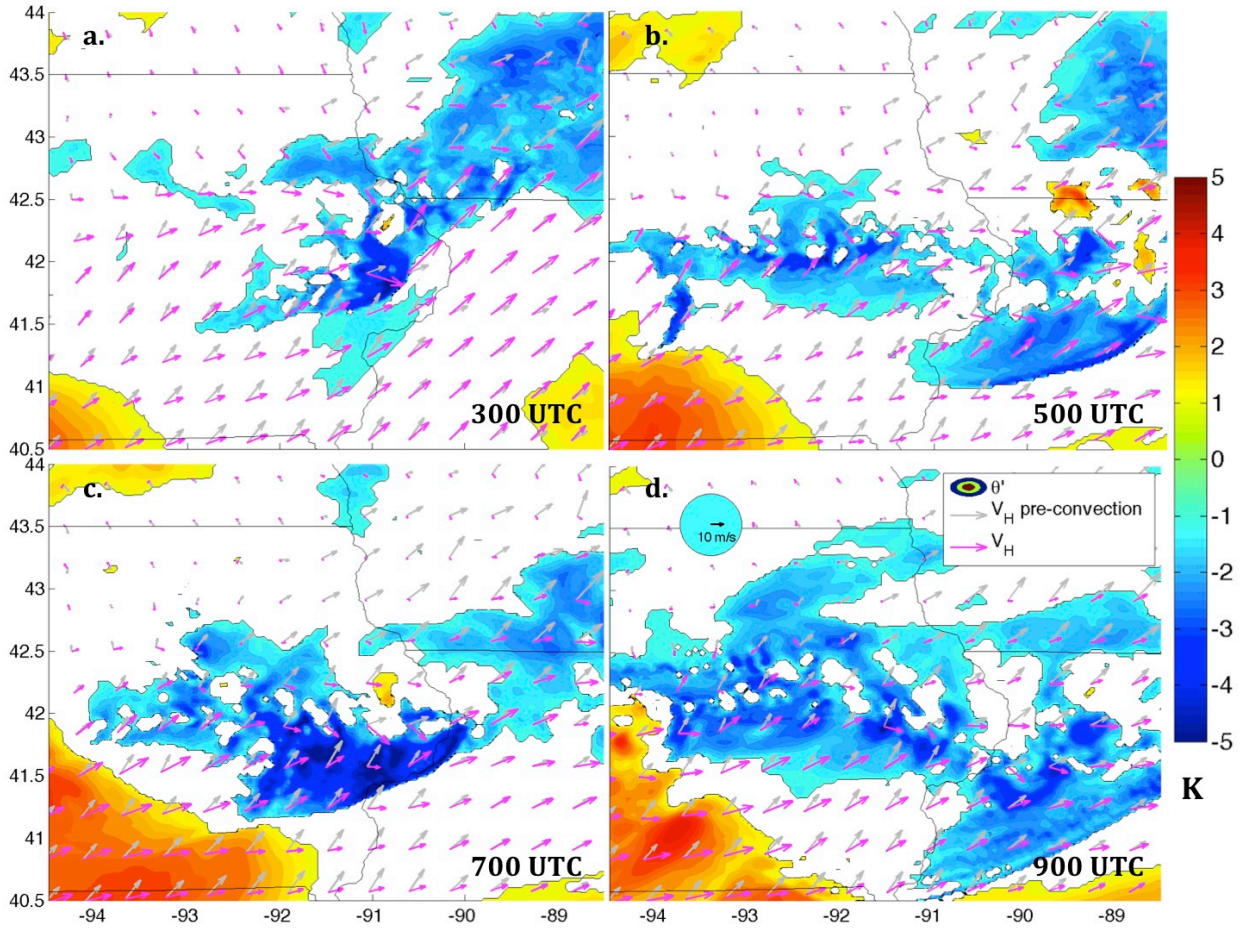

Fig. 3.12. Same as Fig. 3.11, but for the 8th model sigma level. The average pressure on this level was roughly 820 hPa.

The component of flow within the cold pool orthogonal to the outflow boundary along the southwestern periphery of the system was strongest at 0300 UTC and 0700 UTC, which illustrates the southward movement of this boundary during these times (0300 UTC and 0700 UTC were during the first and second cold pool surges respectively). Conversely, the

southwestern outflow boundary was ill defined at 0500 UTC, and the outflow boundary normal wind component within the cold pool along the southwest flank was weak at 0900 UTC.

The analogous quantities to those shown in Fig. 3.11 are shown in Fig. 3.12 for the 8th model sigma level, corresponding to approximately the 820-hPa surface. While a cold anomaly was still evident along the southeast periphery of this system at this level (Fig. 3.12a,b), unmodified sigma 8 flow rose over the surface cold pool along the southwest periphery of the system and directly entered the region where ROD occurred between 0400 UTC and 0500 UTC (Fig. 3.12b – shown in greater detail in the next sub-section). The effect of the west-to-east passage of convection on the sigma 8 flow field was to induce a considerable westerly flow component at ~ 41.75 degrees north (Fig. 3.12c), as well as to generate a zonally oriented horizontally confluent flow pattern to the west of the system. This zonally oriented confluence served as a potential linear organizational mechanism for subsequent rounds of upstream (relative to the progressive MCS segment) convective activity.

Fig. 3.13 shows a four-hour time evolution (0100 UTC through 0400 UTC) of CAPE and convergence on the 8th model level that temporally encompassed the first ROD episode. As the initial grouping of convective cells progressed from west to east between 0100 UTC (Fig. 3.13a) and 0200 UTC (Fig. 3.13b), CAPE values to the rear of the system north of the surface cold pool boundary were near zero (having been presumably stabilized by convective overturning). Between 0300 UTC (Fig. 3.13c) and 0400 UTC (Fig. 3.13d), however, southwesterly flow overran the surface cold pool boundary to the rear of the system and CAPE here increased substantially, eventually leading to new convective development in this region (ROD) by 0400 UTC (Fig. 3.13d, we will hereafter refer to these CAPE resurgence periods as “return flow” episodes). Prior to ROD and within the wake of the 0100-0200 UTC (Fig. 3.13a,b) progressive

MCS, a well-defined east-to-west oriented convergence band developed at 0300 UTC at roughly 42.2 degrees north (Fig. 3.13c), within which new convective cells eventually developed. Fig. 14 provides evidence that the source of "CAPE revitalization" in the MCS upstream wake region just prior to ROD was a result of high θ_e air ("high θ_e" refers to a local maximum in the vertical distribution of this quantity) being transported up and over the surface cold pool by southwesterly flow (Fig. 3.13).

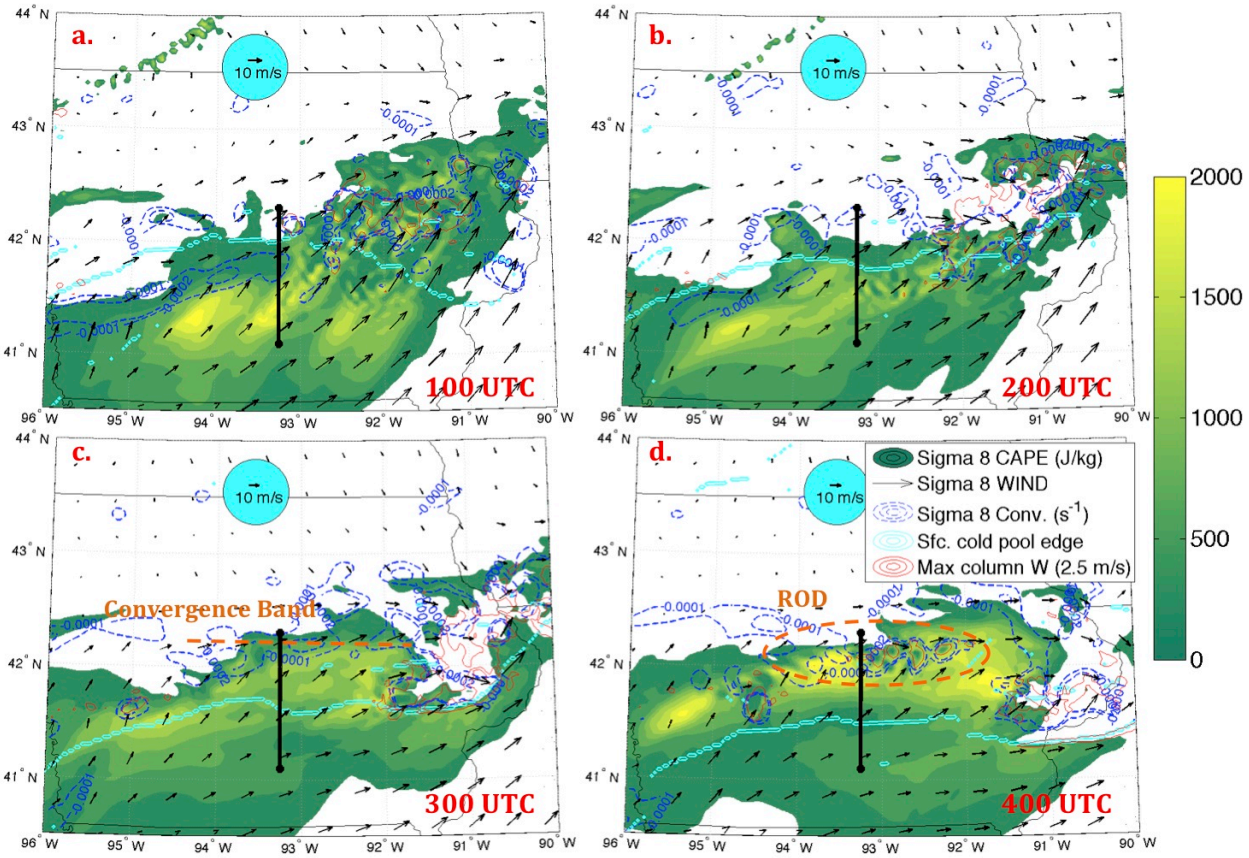

Fig. 3.13. CAPE for parcels lifted from the 8th model sigma level (shading), flow vectors on the 8th model sigma level (black arrows), convergence on the 8th model sigma level (blue dotted contours, starting at -1 x 10^{-4} s^{-1} and decreasing at intervals of -1 x 10^{-4} s^{-1}), surface cold pool boundaries defined as a local maxima in the surface temperature gradient in conjunction with a decrease in potential temperature of 2 K or more within 8 grid points to the north (cyan lines), and maximum column vertical velocity (red contour corresponding to 2.5 m/s). Valid times on 28 July 2011 are listed in the lower-right corner. The solid black line indicates the path of cross sections shown in Fig. 3.14 and 3.15.

Two outflow boundaries (OFBs) are evident at 200 and 230 UTC (notated in Fig. 3.14a,b), with OFB 1 presumably having been generated by convection prior to the 000 UTC round of

convective activity that marked the onset of the studied MCS, and OFB 2 having been left between 000 and 200 UTC by the first progressive convective surge associated with the studied MCS. The maximum θ_e at 0200 UTC (Fig 14a) and minimum in convective inhibition (CIN) within the cross section resided near OFB 1 (~41.3 to 41.7 deg. N). A region of lifting along, and localized to OFB 1 is also evident at approximately 41.3 degrees north (Fig. 3.14a,b). Between 0230 UTC and 0330 UTC (Fig. 3.14b-d), the maximum θ_e shifted northward above the cold pool boundary into the 41.8-42.2 deg. N range.

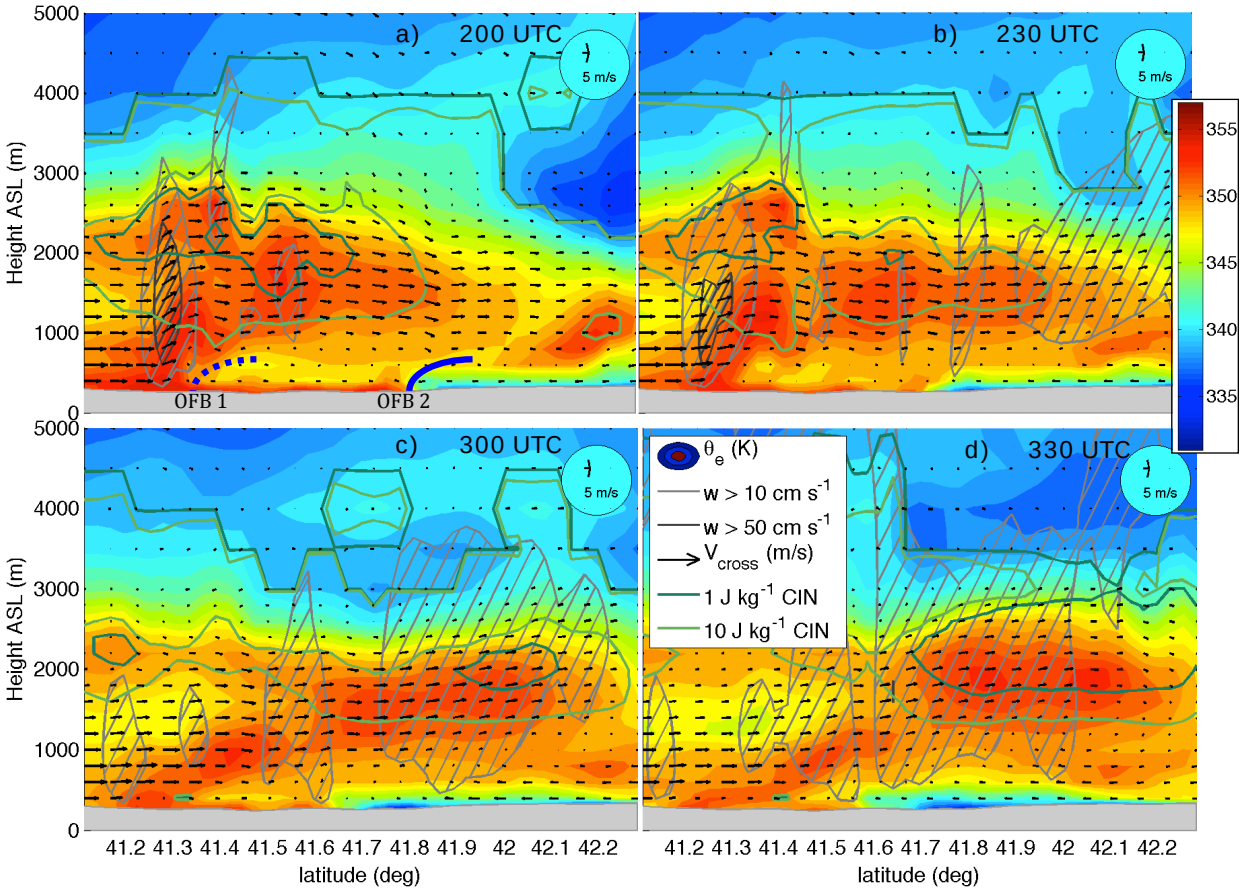

Fig. 3.14. Cross sections along the black line in Fig. 3.13 of equivalent potential temperature (θ_e, shading), the 1 and 10 J/Kg convective inhibition contours (CIN, dark and light green solid lines respectively), cross-section parallel wind vectors (black arrows, m s^{-1}), and regions of vertical velocity greater than 10 cm/s (hatched light gray regions) and 50 cm/s (hatched dark gray regions).

CIN gradually eroded near the maximum θ_e values during this timeframe, and had approached zero throughout the entire vertical column near 42.1 deg. N (this is where a new convective

updraft initiated approximately 10 minutes later). The horizontal extent of lifting in the north-south direction also expanded during this timeframe, and there was arguably enhanced lifting over the enhanced low θ_e region north of OFB 2, suggesting that gradual lifting over the cold pool played a role in eroding CIN.

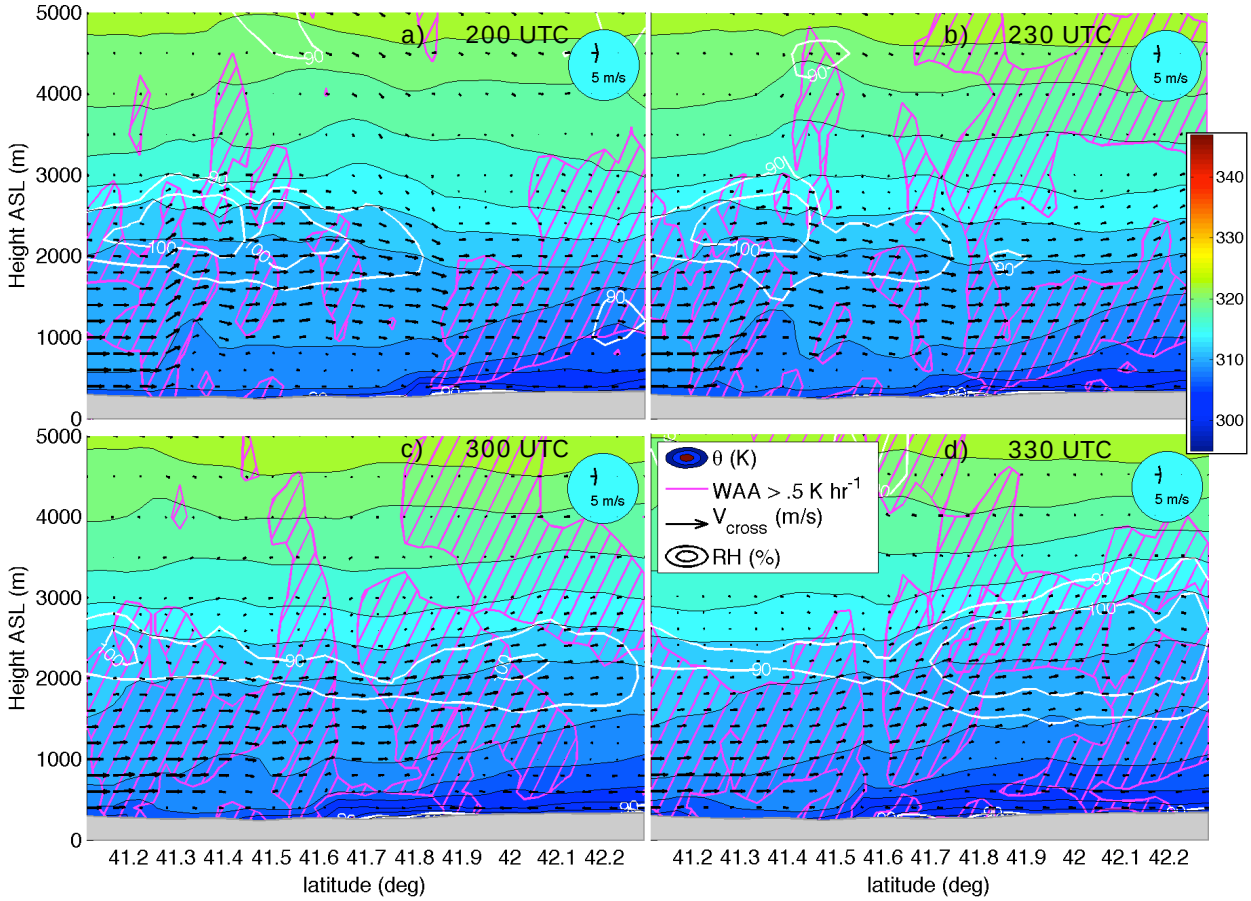

Fig. 3.15. Cross sections along the black line in Fig. 3.13 of potential temperature (θ, shading), the 90 and 100 % relative humidity contours (white solid lines), cross-section parallel wind vectors (black arrows, m s^{-1}; arrows lengths have been scaled so that the ratio of the units of the horizontal and vertical velocity components is unity), and regions of warm air advection greater than .5 K hr^{-1} (gray hatched regions).

An upward arch in isentropes near OFB 1 was evident during the 0200-0230 UTC timeframe (Fig. 3.15a,b), which reflects dynamically forced adiabatic ascent and descent as flow passes the outflow boundary. This lift was apparently insufficient to trigger deep convection, perhaps due to the 3000-4000 m layer remaining convectively inhibited (Fig. 3.14a,b).

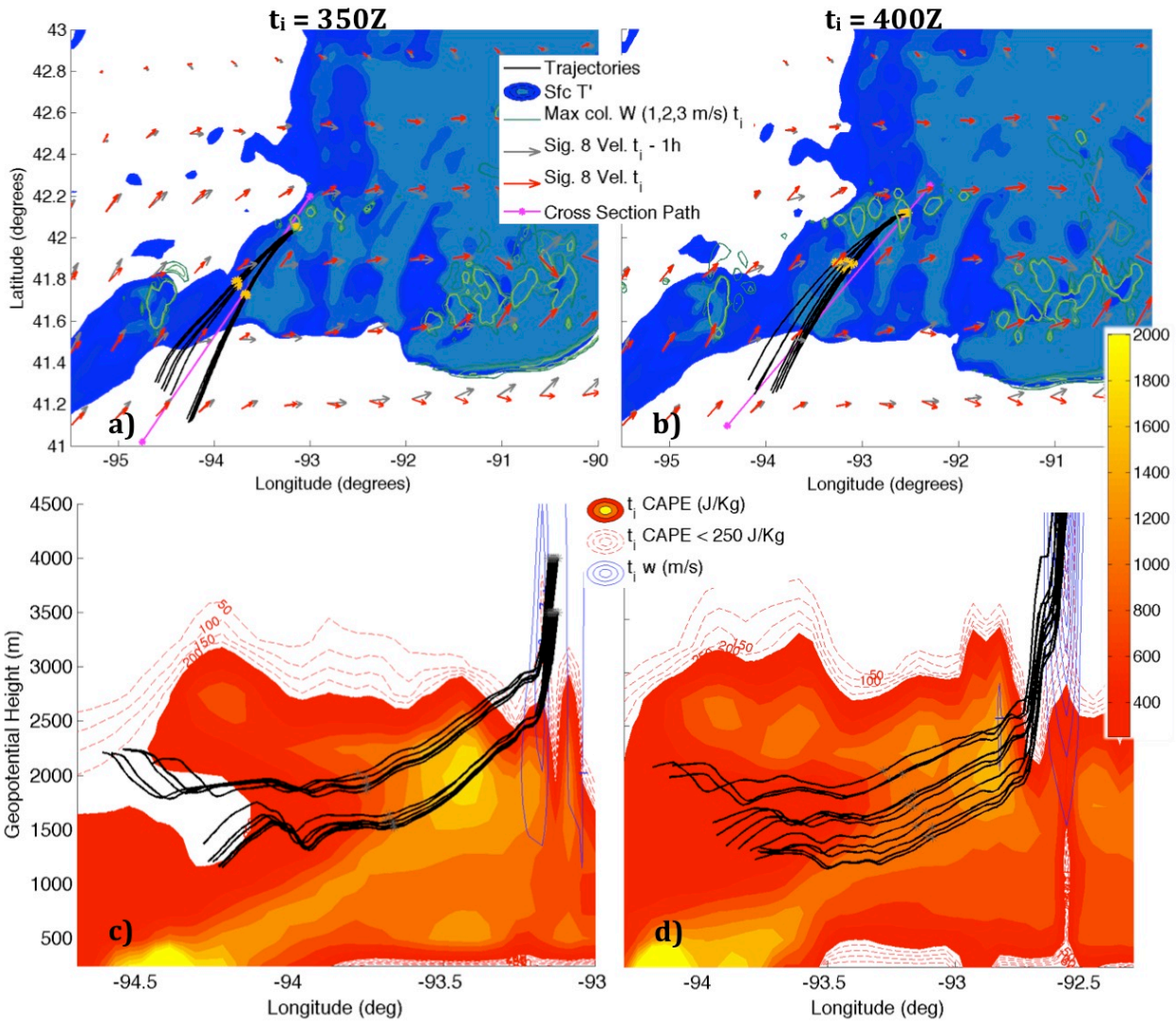

Fig. 3.16. Top panels: The horizontal path of back trajectories initialized within updrafts (black lines – yellow stars denote the location at initialization, and 1 hour prior to initialization), surface -1 K potential temperature anomalies at the time of trajectory initialization (shading, -2, -1.5, -1, -.5 K contours), maximum column vertical velocities at the time of trajectory initialization (solid green contours, 1, 2, and 3 m/s), and wind vectors at the time of trajectory initialization (red arrows) and 1 hour prior to trajectory initialization (green arrows) on the 8th model sigma level. Bottom panels: cross sections of CAPE (shading, J/Kg) and vertical velocities (blue solid contours, m/s) along the magenta dashed lines with starred ends in the top panels valid at the trajectory initialization times. Red dotted contours show CAPE values below the shading threshold of 250 J/Kg. Trajectory paths are projected onto the cross sections (black lines). Trajectory initialization times (t_i) for each column of figure panels are listed at the figure top, and initialization heights were 3500 and 4000 m for the 0350 UTC initializations (as evident in the figure), and 5800 and 6800 m for the 0400 UTC initializations.

The north-south prevalence of low-level warm-air advection increased between 230 UTC and 300 UTC (Fig. 3.15b,c) as the southeasterly low-level jet re-entered the region that was affected by the progressive MCS (this is evident in Fig. 3.13, and discussed in greater detail in section

3.5.b). WAA spanned the entire north-south extent of the cross section including regions south of the surface outflow boundary, suggesting that there was a large-scale contribution to this process in addition to enhanced lifting over the cold pool. A region of saturation at ~ 2000 m expanded between 0300 UTC and 0330 UTC (Fig. 3.14c,d), which is the region where ROD convection eventually developed. Figs. 3.14 and 3.15 suggest that the northward separation of ROD convection from the OFB(s) was regulated by the time (and horizontal distance) required for air to reach saturation and erode convective inhibition through the entire lower troposphere.

Sets of back trajectories were initialized within two separate updrafts within ROD convection to the rear of the first progressive MCS segment – one updraft at 0350 UTC and another at 0400 UTC – with both trajectory sets having been initialized 10 minutes after the first appearance of vertical velocity exceeding 1 m/s associated with the updraft. The horizontal and vertical paths of these trajectories are shown in Fig. 3.16. Air parcels originated within southwesterly low-level return flow, and remained elevated in the 3 hours prior to their initialization. Their paths shortly prior to their entry into convective updrafts coincided with vertical maxima in CAPE (Fig. 3.16c,d). There is evidence of initial vertical oscillations of air parcels, which presumably occurred as they interacted with the southern periphery of the surface cold pool. All air parcels then experienced gradual lifting for roughly an hour before entering convective updrafts, during which they ascended 500-1000 m from their lowest positions. Fig. 3.17, which depicts diagnostic quantities along the trajectory paths, shows that the gradual ascent that occurred prior to convective onset coincided with initial cooling of the air parcel relative to its surroundings (evident in negative T' values), along with gradually increasing relative humidity. The coincidence of increasing relative humidity, negative T' (presumably due to adiabatic cooling), and prolonged gradual ascending motion corroborates our earlier assertion

that layer lifting was locally enhanced near the convection (perhaps resulting from lifting over the cold pool). This gradual lifting echoes the results of Trier et al. (2010, their Fig. 18b) in a similar back-building MCS, as well as the trajectory results of Keene and Schumacher (2013) and Trier et al. (2014)'s calculations of parcel buoyancy for elevated MCSs.

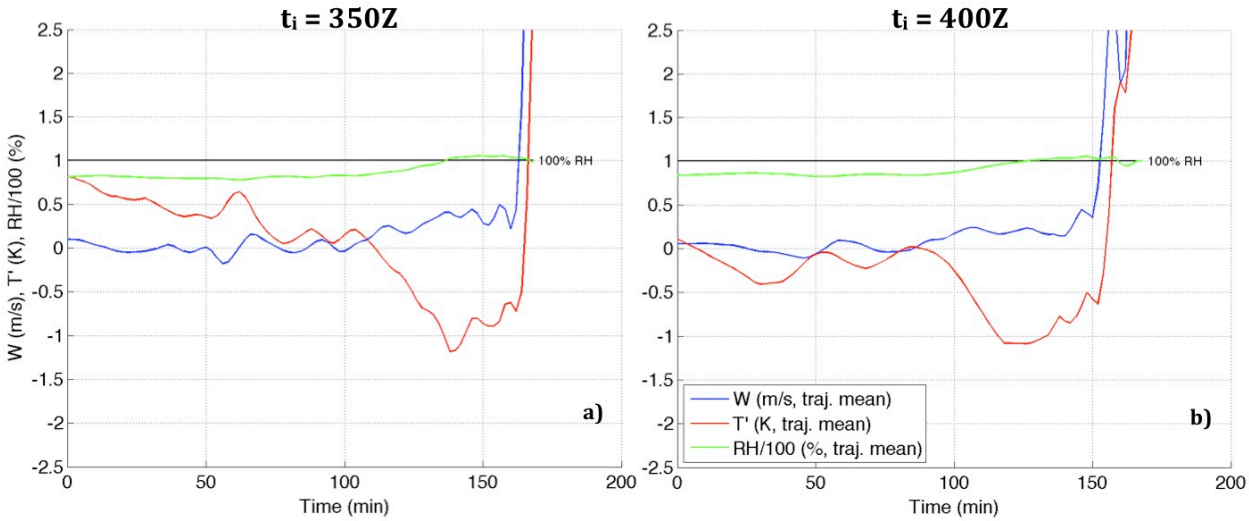

Fig. 3.17. Time series' of mean vertical velocities (blue lines, m/s), potential temperature anomalies (red lines, K), and relative humidity (green lines, %/100) over all trajectory paths for back trajectories initialized at 0350 UTC (panel a) 0400 UTC (panel b).

3.4.b. Vertical wind shear along the outflow boundary

Previous authors have demonstrated that horizontal variations in the outflow-boundary-relative environmental wind shear orientation along the flanks of a cold pool explain asymmetries in the system's structure (e.g. Rotunno et al. 1988; Corfidi 2003; Weisman and Rotunno 2003; Parker 2007; French and Parker 2010). Rotunno et al. 1988 showed that in many cases of linear MCSs, the ratio $\frac{C}{\Delta U}$ explains the optimality for vertically upright updrafts along the outflow boundary, where C is the cold pool velocity and ΔU is the magnitude of the vertical wind shear in the warm buoyant air adjacent to the cold pool, over the depth of the cold pool. Specifically, $\frac{C}{\Delta U} \approx 1$ corresponds to a robust kinematically forced vertical jet along the cold pool edge, which may easily lift parcels with nonzero CAPE to their levels of free convection (LFCs).

Ratios much smaller (larger) than 1 result in weaker upshear (downshear) tilted lofting of air parcels, and lifting associated with negative ratios is small and shallow, when compared to positive ratios.

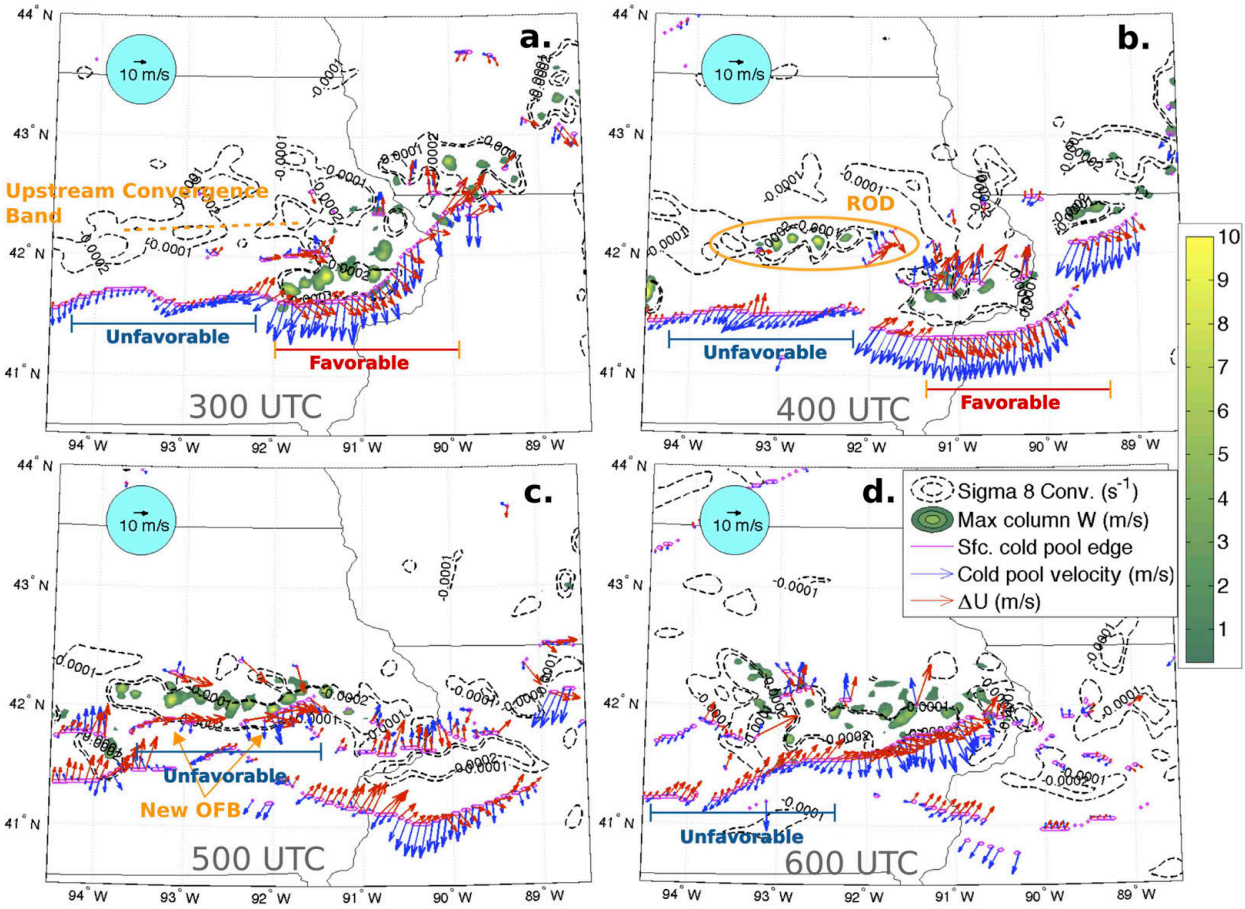

Fig. 3.18. Maximum column vertical velocity (shading, starting at 1 m s^{-1}), convergence on the 8th model sigma level (black dotted contours, starting at -1 x 10^{-4} s^{-1} and decreasing at intervals of -1 x 10^{-4} s^{-1}), surface cold pool boundaries (magenta lines, as defined in the Fig. 3.13 caption), estimated cold pool velocity vectors along the cold pool boundary (blue arrows), and estimated vertical wind shear vectors over the depth of the cold pool at the cold pool boundary (red arrows). Cold pool velocity vectors were estimated by the wind velocity 4 grid points north of a given point on the magenta line (within the cold pool), and vertical wind shear vectors (ΔU) were estimated as the vector difference between the wind 4 grid points south of a given point on the magenta line at the height of the cold pool depth (defined as the height of the first instance in the vertical of θ' > -.5 K) and the surface wind velocity at that point. Valid times on 28 July 2011 are listed at the bottom of each panel.

In cases where convective systems produce radial outflow in a vertically sheared environment, the sense of the $\frac{C}{\Delta U}$ ratio will favor convective development along the downshear outflow

boundary (where the vertical wind shear vector points from cold to warm air) as opposed to the upshear outflow boundary (where the vertical wind shear vector points from warm to cold air). The aforementioned principles suggest that the vertically varying shear direction evident in Fig. 4 (as is common for TL/AS type systems) was likely a contributing factor to the propensity for convection to persist near the southeastern cold pool periphery, while remaining well removed from the southwestern cold pool periphery.

Fig. 3.18 shows vertical wind shear vectors over the depth of the cold pool **(ΔU**) in the warm air to the south of the cold pool from 300 UTC (Fig. 3.18a) to 600 UTC (Fig. 3.18d). Estimated cold pool velocity vectors (see figure caption for the computation of this quantity) are also included to facilitate understanding of the motion (or lack thereof) of the outflow boundary over this timeframe. While we do not quantitatively address the $\frac{C}{\Delta U}$ ratio (as in Rotunno et al. 1988), we may consider situations in Fig. 18 along the cold pool edge in which **ΔU** vectors point toward warm air (cold air) as being the favorable (unfavorable) flanks of the cold pool for sustained triggering of convection.

Favorable wind shear conditions existed for initiating convection along the surging southeastern periphery of the cold pool at 0300 UTC (Fig. 3.18a), where robust convection resided near the outflow boundary. Along the southwestern cold pool periphery (to the south of the upstream wake region of the progressive MCS segment) however, vertical wind shear over the cold pool depth was minimal during the 0300 UTC to 0400 UTC timeframe (Fig. 3.18a,b). This resulted in sub-optimal lifting along the boundary, which was apparently insufficient to overcome the substantial CIN in the lower troposphere evident in Fig. 3.14. Surface wind vectors within the cold pool near the outflow boundary were oriented nearly parallel to the outflow boundary between 0300 (Fig. 3.18a) and 0400 UTC (Fig. 3.18b), which contributed to

the nearly stationary character of the boundary over this timeframe. In contrast, flow direction within the cold pool along the southeastern periphery was strongly oriented perpendicular to the boundary, which contributed to the substantial southeastward movement of the boundary over the same timeframe.

By 0500 UTC (Fig. 3.18c), **ΔU** vectors along the far southwestern cold pool periphery were oriented toward the cold pool. Convection along the western MCS flank had generated an enhanced local surface cold anomaly at this time (Fig. 3.11b), resulting in a new outflow boundary being analyzed just to the south of the convective line (this feature is notated in the 0500 UTC panel in Fig. 9). By 0600 UTC (Fig. 3.18d), however, the outflow boundary that had been newly analyzed at 0500 UTC (Fig. 3.18c) had moved southward, while the convective line remained stationary (this event constituted the onset of the second ROD episode). The southward movement of the new outflow boundary between 0500 (Fig. 3.18c) and 0600 UTC (Fig. 3.18d) likely resulted from a substantial northerly wind component within the cold pool and orthogonal to the outflow boundary over this timeframe. **ΔU** vectors along this outflow boundary remained unfavorably oriented toward the cold pool between 0500 (Fig. 18c) and 0600 UTC (Fig. 18d), potentially explaining why convection did not "follow" the outflow boundary southward.

3.5) Dynamical mechanisms for MCS organization

The low-level flow changes occurred as the eastward moving convective segments influenced the behavior of the MCSs in several ways. Low-level flow to the rear of convective segments temporarily turned from southwestward to westward, which disrupted the transport of potentially unstable air to the region where ROD would eventually occur. The low-level flow direction in the aforementioned region then returned to southwesterly, allowing for potentially

unstable flow to travel northward past the surface outflow boundary and eventually trigger ROD convection. In this section we analyze the low-level horizontal momentum budget in order to better understand the mechanisms for this behavior.

3.5.a. Analysis framework

Starting with the anelastic horizontal momentum equation in height coordinates (bolded letters denote vectors):

$$\frac{\partial \mathbf{V_h}}{\partial t} = -(\mathbf{V}\cdot\nabla)\mathbf{V_h} - \frac{1}{\rho_0}\nabla_h p - f\hat{\mathbf{k}}\times\mathbf{V}, \quad (3.1)$$

where $\mathbf{V}_h$ is the horizontal wind velocity vector and all other terms retain their traditional meanings, we separated the contributions to the local time tendency into those due to the separate terms on the right hand side (RHS) of equation (3.1):

$$\left(\frac{\partial \mathbf{V_h}}{\partial t}\right)_{HM} = -(\mathbf{V_h}\cdot\nabla)\mathbf{V_h}, \quad (3.2)$$

$$\left(\frac{\partial \mathbf{V_h}}{\partial t}\right)_{VM} = -w\frac{\partial \mathbf{V_h}}{\partial z}, \quad (3.3)$$

$$\left(\frac{\partial \mathbf{V_h}}{\partial t}\right)_{PG} = -\frac{1}{\rho_0}\nabla_h p - f\hat{\mathbf{k}}\times\mathbf{V}, \quad (3.4)$$

Here, we have assumed large-scale atmosphere dominated by geostrophic balance, and convectively induced flow deviations from geostrophy therefore dominate the RHS of equation (3.4).

In order to estimate the contributions to the change in wind through a layer in the atmosphere during a specified period of time, we temporally integrated RHS of equations (3.2-3.4). For instance, when these operations are applied to equation (3.4), we obtain the following:

$$(3.5)\quad \Delta\mathbf{V}_{PG}(t_1,t_2,x,y,z) = -\int_{t_1}^{t_2}\left[\ \frac{1}{\rho_0(z)}\nabla_h p(t,x,y,z) + fk\times\mathbf{V}(t,x,y,z)\ \right]dt,$$

where the Δ symbol denotes the local velocity difference between t_2 and t_1. All integrations were estimated by Riemann summations over model output at 10-minute intervals. These time-integrated quantities are hereby referred to in the text as $\mathbf{\Delta V_{HM}}$, $\mathbf{\Delta V_{VM}}$, and $\mathbf{\Delta V_{PG}}$ respectively.

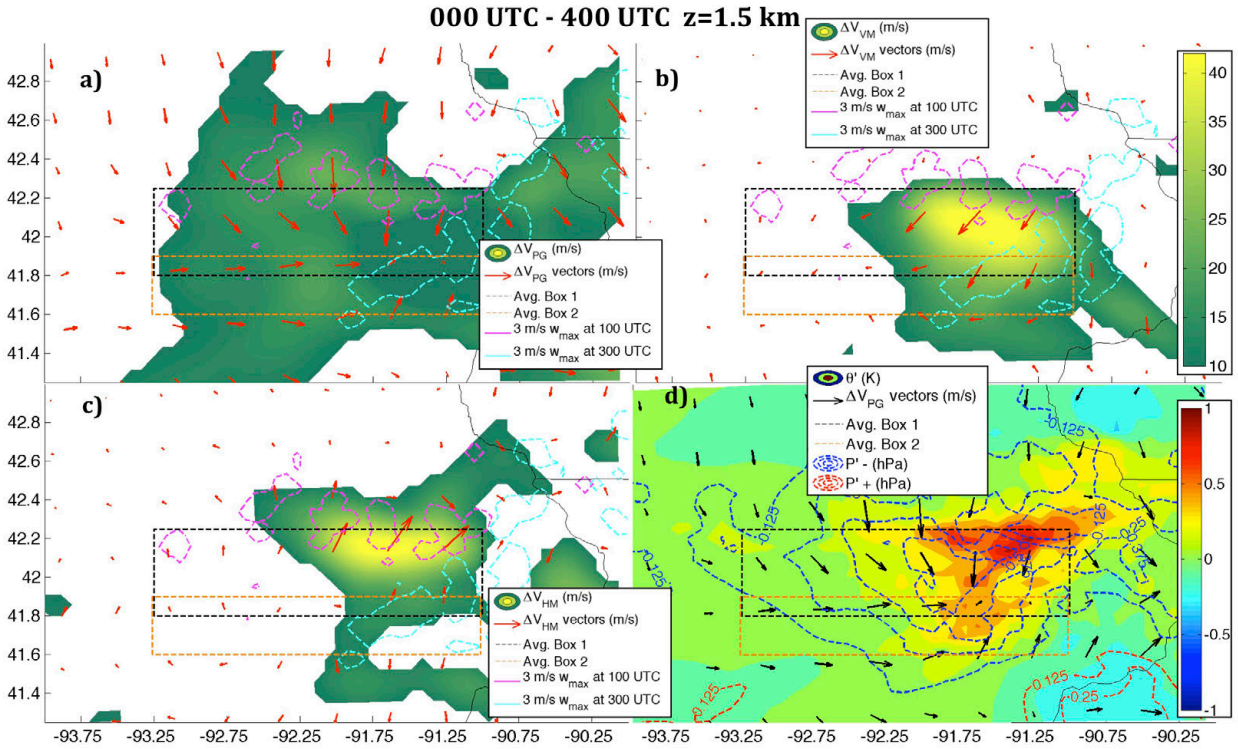

Fig. 3.19. Panel (a): the magnitude of Δv_{PG} (shading, m/s) and Δv_{PG} vectors (red arrows); panel (b): the magnitude of Δv_{VM} (shading, m/s) and Δv_{VM} vectors (red arrows); panel (c): the magnitude of Δv_{HM} (shading, m/s) and Δv_{VM} vectors (red arrows). Panel (d): temporally averaged 2-10 km potential temperature anomalies (shading, K), temporally averaged pressure anomalies (hPa: negative, blue dashed contours, and positive, red dashed contours), and Δv_{PG} vectors (black arrows). Panels (a-c): the 3 m/s maximum column vertical velocity contours at 0100 UTC (magenta contour) and 0300 UTC (cyan contour) on 28 July 2011. All panels: spatial average boxes for time series' computations in Fig. 3.24. All quantities aside from maximum column vertical velocities and temporally averaged potential temperature anomalies were assessed on the 1.5 km geopotential height surface. Temporal integrations and averages were computed from 0000 UTC – 0400 UTC.

3.5.b. Spatial patterns of dynamical quantities

We analyzed the quantities $\mathbf{\Delta V_{HM}}$, $\mathbf{\Delta V_{VM}}$, and $\mathbf{\Delta V_{PG}}$ at the 1.5-km level over two separate time periods: 0100-0400 UTC 28 July (Fig. 3.19), and 0400-1000 UTC 28 July (Fig. 3.20). The former timeframe was chosen in order to investigate mechanisms for changes to the low-level horizontal wind that occurred to the rear of the first progressive convective segment, and to determine how such wind changes may have contributed to the behavior of the MCS. The timeframe of the passage of the progressive convective segment through box 1 in Fig. 3.19 was 0100 UTC to 0300 UTC (see simulated radar reflectivity in Fig. 10), and ROD occurred in this region began between 350 UTC and 400 UTC.

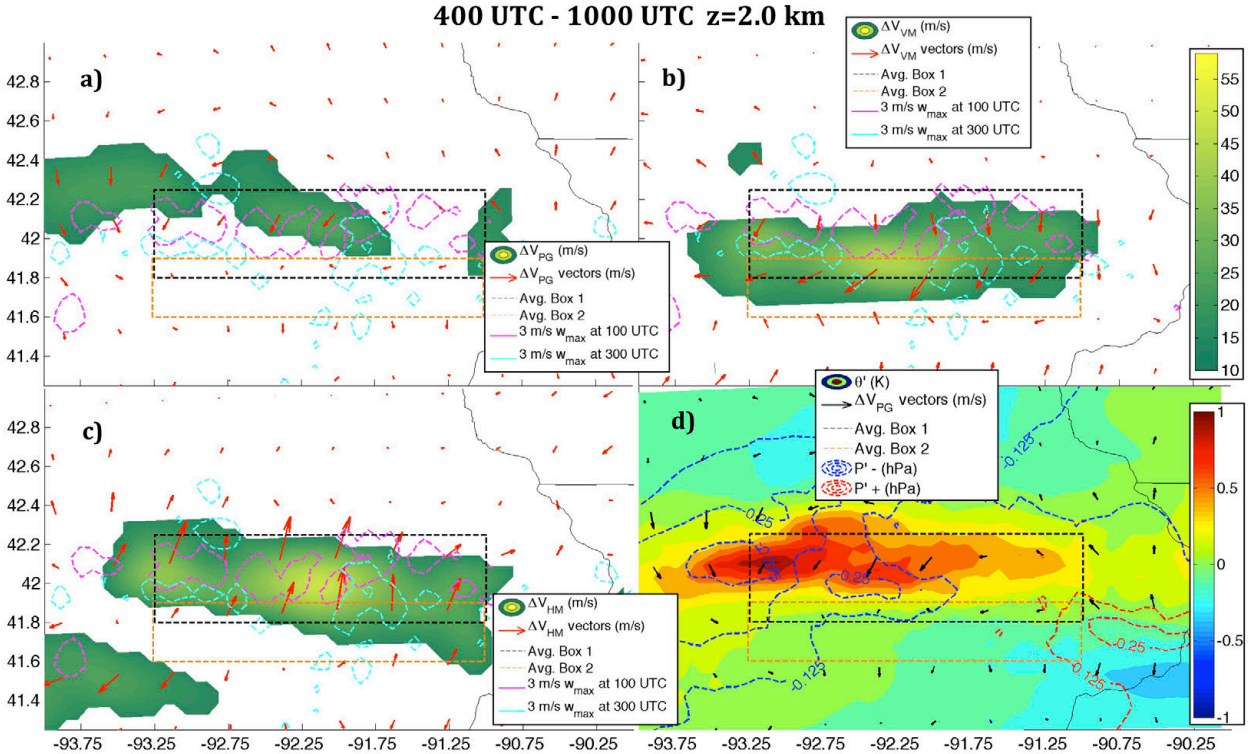

Fig. 3.20. Same as Fig. 3.19, but for 0400 UTC – 1000 UTC and on the 2.0 km geopotential height surface. 3 m/s maximum column vertical velocity contours now correspond to 0500 UTC (magenta) and 0700 UTC (cyan).

$\mathbf{\Delta V_{PG}}$ vectors were northerly through the northern portion of Box 1 and turned westerly through the central and southern portions of Box 1 and box 2, suggesting that low-level pressure

perturbations associated with the passage of the initial progressive MCS were responsible for the changes of the low-level from southwesterly to westerly in this region (this change is evident in Fig. 3.11a). Low-level temporally averaged low-pressure perturbations coincide well with regions of midtropospheric temporally averaged warming in convective updrafts (which is maximized in the region affected by the progressive MCS; Fig. 3.20d), implicating latent heating in the generation of such low-level pressure anomalies. These patterns are consistent with mechanisms for MCS rear-inflow-jet generation in squall lines (Smull and Houze 1987; Weisman 1992), where buoyancy-induced low-level low-pressure perturbations along the progressive convective line promote horizontal flow accelerations into the rear of the line.

$\mathbf{\Delta V_{VM}}$ vectors were northeasterly in the eastern portion of Box 1 (the primary region affected by the passage of the progressive MCS), whereas $\mathbf{\Delta V_{HM}}$ vectors were southwesterly through nearly the same region. We may conjecture here that (a): the former is primarily a result of upward transport resulting from deep convective overturning – that is, flow with southwesterly low-level wind shear encountering regions of upward motion, resulting in the replacement of fast southwesterly wind at this level with slower southwesterly wind from below, and (b): the latter is primarily a result of unmodified (where "modified" refers to convectively altered) southwesterly flow within the low-level jet replacing modified westerly and northwesterly flow to the rear of the initial progressive MCS (both of these arguments were deduced from the wind structures evident in Figs 3.11 and 3.12). Note that while the latter argument is rather intuitive based on an investigation of Fig 12a, the former will be investigated more comprehensively in the next section. The patterns of $\mathbf{\Delta V_{VM}}$ and $\mathbf{\Delta V_{HM}}$ were similar from 0400-1000 UTC (Fig. 3.20) to those evident in Fig. 3.19, and we may invoke similar arguments to (a) and (b) earlier in this section to explain their patterns.

The pattern of $\mathbf{\Delta V_{PG}}$ from 0400-1000 UTC (Fig. 3.20) is notably different than that from 0000-0400 UTC (Fig. 3.19), exhibiting northeasterly orientation in the western portion of Box 1, northwesterly orientation west of Box 1, and small magnitude elsewhere. This shows that pressure gradient forces along the line acted to maintain the confluent flow pattern that had initial been generated by the first eastward moving convective segment.

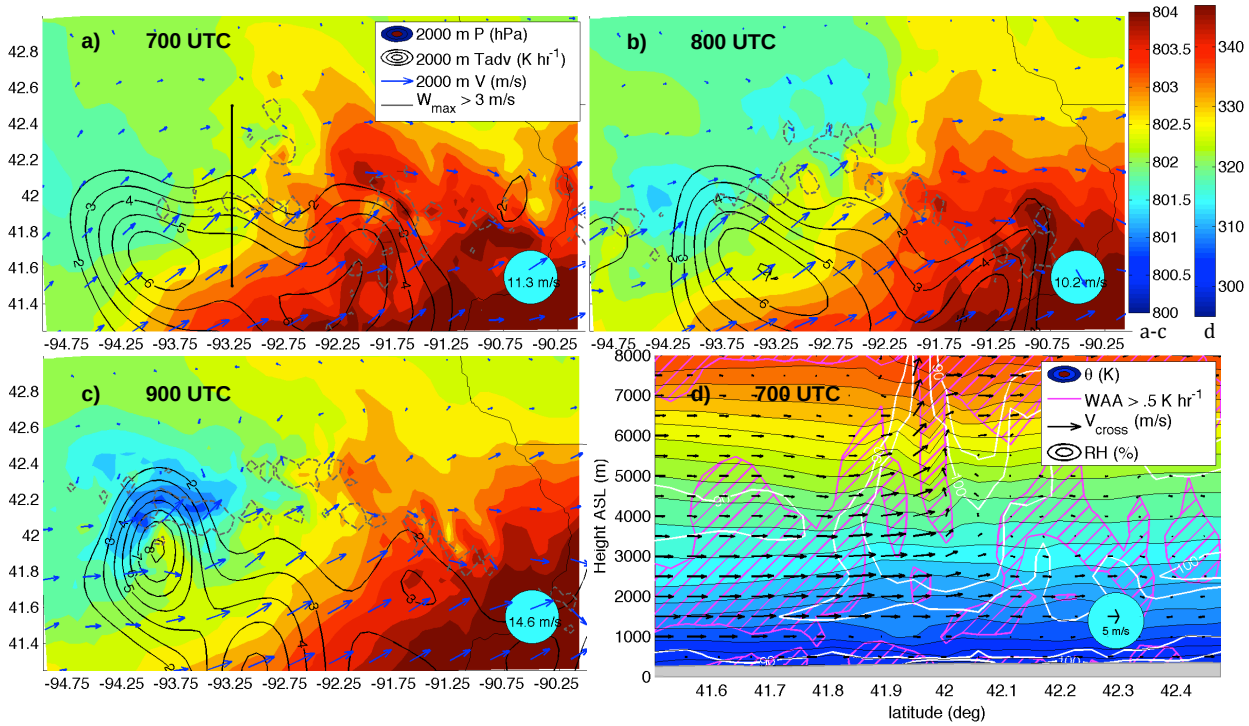

Fig. 3.21. Panels a-c: Pressure on the 2 km geopotential height surface (shading, hPa, see left colorbar), 2 km horizontal warm air advection (black contours, K hr^{-1}), 2 km horizontal wind vectors (blue arrows, m/s) , and the 3 m/s maximum column vertical velocity contour (gray dashed line). Panel d: Same as Fig. 15, but at 700 UTC along the black solid line in (a) (see right colorbar).

While the low-pressure anomaly evident from 0000-0400 UTC was not present during this timeframe, a regional low-pressure anomaly had developed along the upstream end of the convective line, with the minimum in low-level low pressure (near the west side of Box 1) having coincided with a maximum in upper tropospheric heating. Once again, the coincidence between upper-level heating and low-level low pressure suggests that the former was responsible for, or enhanced the latter.

Fig. 3.21 reveals that the low-pressure anomaly west of the MCS extended well beyond the immediate region of convection associated with the convective system, which suggests that large-scale processes were partially responsible for the presence of this feature. A marked deepening of the low close to convection on the western end of the system is evident between 700 UTC (Fig. 3.21a) and 900 UTC (Fig. 3.21c), further suggesting that convective latent heating enhanced this feature. North-south oriented cross sections (Fig. 3.21d) just east of the local maximum low-pressure reveal upward sloping isentropes with northward extent within southerly flow feeding updrafts (specifically between 41.7 and 41.9 degrees north in Fig. 3.21d), along with gradually increasing relative humidity within this flow prior to its entry into updrafts. This in combination with downward sloping isentropes at mid-levels above the region of low-level upslope is similar to the pattern typically observed in association with MCVs (Raymond and Jiang 1990, Schumacher and Johnson 2008; see their Fig. 3). The upstream low-pressure anomaly may have facilitated upstream backbuilding by locally enhancing low-level isentropic upglide (see Figs 3.21a-c) and layer lifting, priming air parcels for entry into deep convection.

Two additional sets of back trajectories were initialized at 0650 UTC and 0740 UTC within two separate updrafts along the upstream (western) flank of the MCS where sustained upstream backbuilding was occurring. The horizontal and vertical paths of these trajectories are shown in Fig. 3.22. Analogous diagnostic quantities to those shown in Fig. 3.17 are shown for the 650 and 740 UTC trajectory initializations in Fig. 3.23. Air parcels that eventually entered updrafts once again originated well above the surface – between the 2000 and 2500 m geopotential height levels (the surface height here was ~ 300 m). CAPE values to the rear of the system were far lower than those associated with ROD convection between 0400-0500 UTC (Fig. 3.23c,d), and in some cases their origins appear to be above the level of maximized CAPE (Fig. 3.23c,d, this is

especially evident in the analysis of the trajectories initialized at 0650 UTC). parcels into a convective updraft).

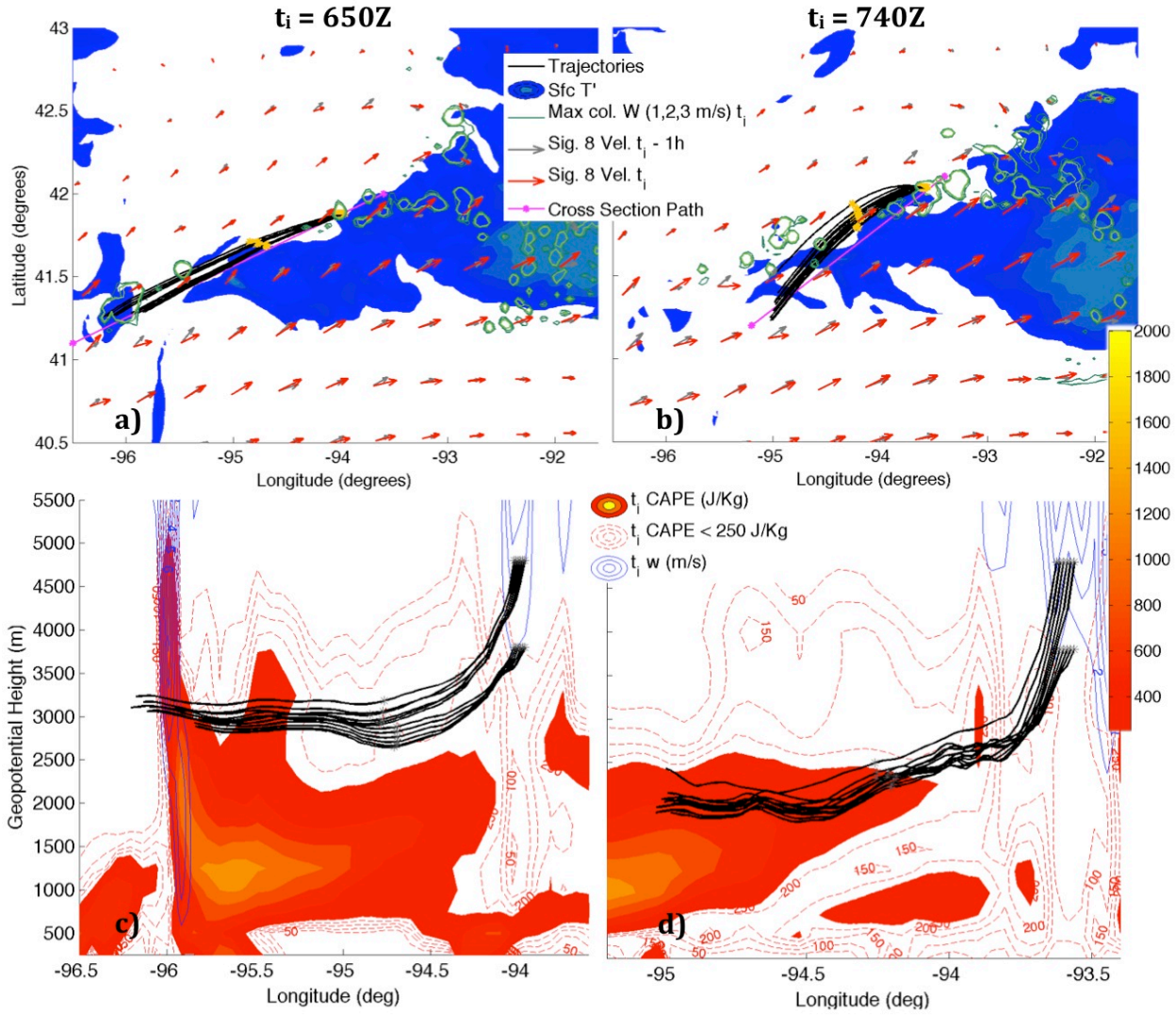

Fig. 3.22. Same as Fig. 3.16, but for back trajectories initialized at the listed times. Initialization heights were 3800 m and 4800 m for both initialization times (as evident in the figures).

3.5.c. Influence of dynamical quantities on the MCS evolution

There are also indications of 30-60 minutes of gradual layer lifting within the paths of the air parcels (Fig. 3.23), similar to those evident in the analysis of the previous two back-trajectory analyses (e.g. steady gradual vertical motion, decreasing T' values, and increasing RH prior to the entry of parcels into a convective updraft).

3.5.c. Influence of dynamical quantities on the MCS evolution

The magnitude of the southerly component of southwesterly inflow into the western end of the MCS briefly abated during both southward cold pool surge events, which disrupted of the supply of high CAPE air to the upstream end of the MCS, and resulted in a temporary cessation of the training of convection (as illustrated in section 3.4.a). In this sub-section, we analyze time series (Fig. 3.24) of the instantaneous local tendencies (e.g. equations 2-4), along with the time-integrated changes in the *v* wind component (e.g. equation 5) to better understand the mechanisms for these cold pool surges.

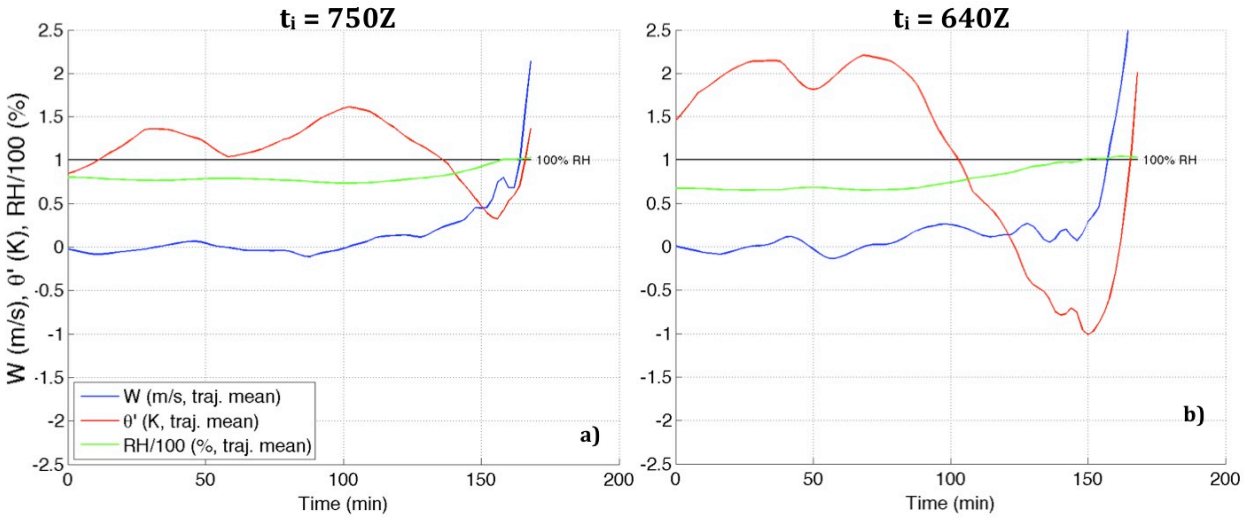

Fig. 23. Same as Fig. 3.17, but for the back trajectory initialization times listed.

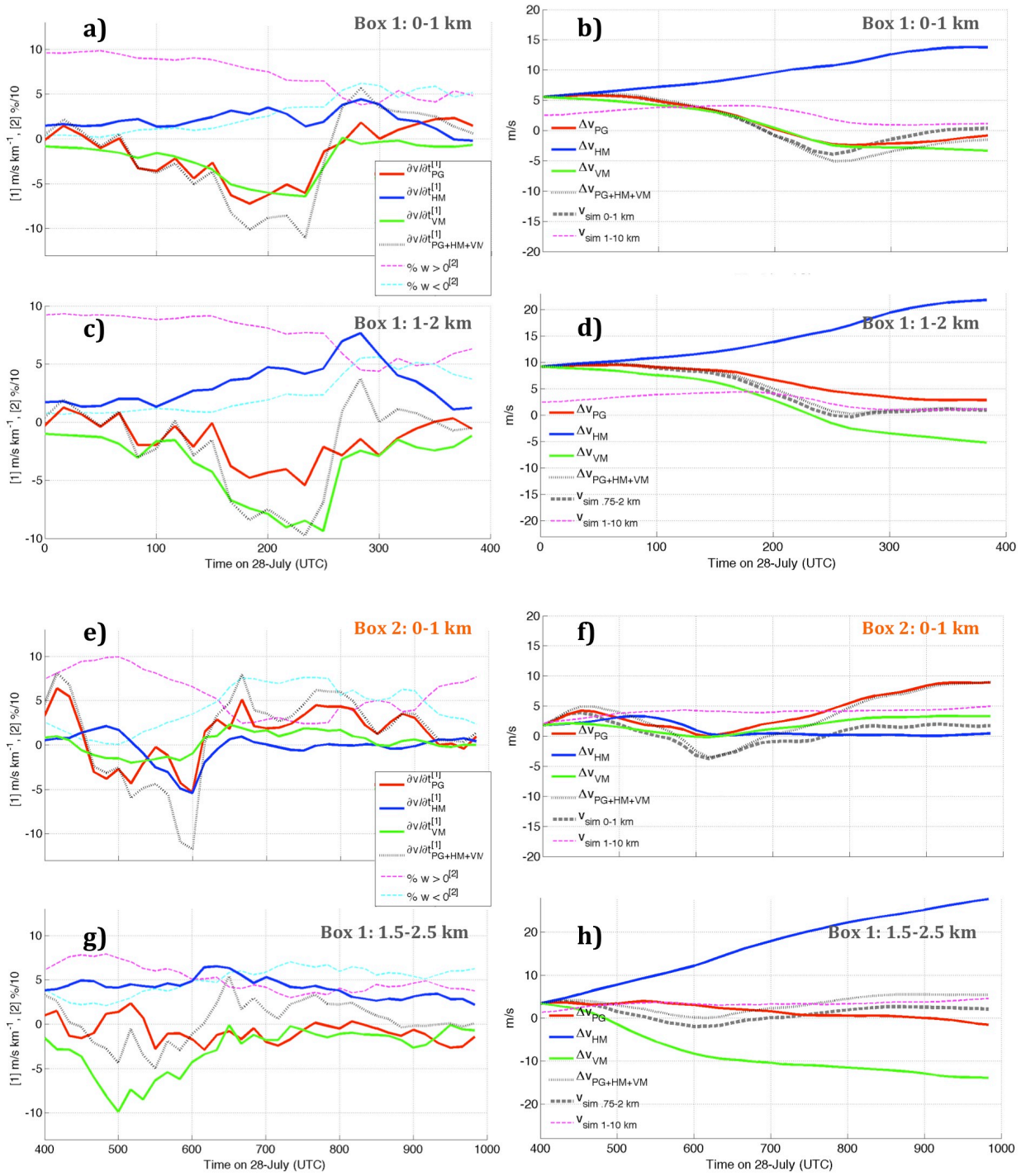

Fig. 3.24. Panels (a, c, e, g): Time series of the contributions to $\frac{\partial v}{\partial t}$ by pressure gradient accelerations (red lines, m/s hr^{-1}), horizontal momentum advection (blue lines, m/s hr^{-1}), vertical momentum advection (green lines, m/s hr^{-1}), and the sum of these contributions (gray dotted lines, m/s hr^{-1}), and the percentage of positive contribution to southward vertical momentum advection accelerations by upward momentum advection (magenta dashed lines, % x 10^{-1}), and downward momentum advection (cyan dashed lines, % x 10^{-1}). Panels (b, d, f, h): Time series of the contributions to $\Delta v + v_i$ by pressure gradient accelerations (red

lines, m/s), horizontal momentum advection (blue lines, m/s), vertical momentum advection (green lines, m/s), the sum of these contributions (gray dotted lines, m/s), the simulated v wind component (black dashed lines), and the pressure-weighted mean 1-10 km v wind component (magenta dashed lines) (v_i, the v component of the wind at the beginning of each time series, has been added to each quantity in these panels). Times in panels (a-d) are from 0000 UTC to 0400 UTC on 28 July, 2011), and times in panels (e-h) are from 0400 UTC to 1000 UTC on 28 July, 2011). Computations aside from 1-10 km mean winds were averaged horizontally over box 1 for panels (a-d, g, h), and box 2 for panels (e, f), and vertically over the 0-1 km layer for panels (a,b,e,f), the 1-2 km layer for panels (c,d), and the 1.5-2.5 km layer for panels (g,h).

Since the mean tropospheric flow (see the 1-10 km mean wind in Fig. 3.24b,d,f,h) was oriented northward throughout the lifetime of the MCS, southward movement of convection during cold pool surges was likely related to propagation along the cold pool edge rather than fluctuations in the orientation of steering flow.

We focused on the dynamics of the two southward cold pool surges that preceded ROD episodes considering accelerations in the 0-1 km geopotential height layer (hereby "lower layer;" the approximate depth of the cold pool), and on the accompanying changes to the low level flow structure (low-level refers to flow just above the cold pool in the maximum CAPE layer) by considering analogous accelerations in the 1-2 km (000-400 UTC) and 1.5-2.5 km (400 UTC-1000 UTC) layers (hereby "upper layer;" the approximate low-level inflow and maximum potential instability layer). The upper layer was raised .5 km for the second timeframe to avoid the influence of the cold pool (which had deepened by this timeframe).

$\frac{\partial v}{\partial t}_{PG}$ and $\frac{\partial v}{\partial t}_{VM}$ (hereafter denoted δPG and δVM respectively) exhibited southerly tendencies that peaked during the first cold pool surge (~0150-0300 UTC; Fig. 3.19a,c), while $\frac{\partial v}{\partial t}_{HM}$ (δHM) exhibited an opposing northerly tendency. Furthermore, because the vertical velocity (and thus the momentum transport) was primarily upward during this time period, this corroborates our earlier conjecture that upward transport of southerly momentum away from this layer (especially along the outflow boundary where low-level upward motion is common) was

the primary process related to δVM at work here. The mechanism for a surging cold pool in the lower layer likely resulted from pressure gradient accelerations driven by the cold pool mesohigh (see Fig. 3.20) and vertical motion along the cold pool edge (and thus upward momentum transport) having been sufficiently strong to overcome opposing ambient southerly flow. These factors resulted in a change from 5 m/s southerly flow at 0000 UTC to nearly 5 m/s northerly flow at 0250 UTC (Fig. 3.19b) in the lower layer. Similar tendency patterns were evident in the upper layer, as southward δPH and δVM reduced the initial 10 m/s southerly flow in this layer to near zero during the first cold pool surge by 0230 UTC (Fig. 3.19d). This was followed by a strong southerly wind tendency contributed by δHM at ~ 0230-0240 UTC (Fig. 3.19c; this is likely the low-level flow "resurgence" described in section 3.4.b, see Fig. 3.20) resulting in an increase in the southerly flow magnitude to 1-2 m/s.

During the second cold-pool surge (which occurred between 0500 and 0600 UTC), δPG and δVM once again exhibited southerly tendencies in the lower layer in box 2 (Fig 3.24e). Box 2 was chosen for the lower-layer analysis during this time frame in order to adequately capture southward accelerations associated with the cold pool – the signatures of such accelerations were less apparent in Box 1. Note that δHM was initially oriented northward at 0500 UTC, but shifted to a southward orientation by 600 UTC. This is likely a result of northerly flow within the cold pool inundating this region as the outflow boundary moved south of the southern boundary of the box, combined with a northward oriented gradient in the magnitude of *v*. The aforementioned southward accelerations contributed to brief southerly wind of 5 m/s between ~530 and 700 UTC (the outflow boundary passage) within this layer (Fig. 3.24f).

δPG and δVM contributed predominantly southward tendencies in the upper layer between 400 and 1000 UTC (Fig 24g), with the exception of brief northward δPG orientation

before and during the second cold pool surge at 0430 and 0530 UTC. The behavior of δPG is consistent with low-level northerly accelerations into updrafts. The magnitude of southward δVM was maximized during the development of ROD convection (~ 400 to 500 UTC) and the second cold pool surge (~ 0500 to 0630 UTC). Upward momentum transport was once again the predominant contributor to δVM during the cold pool surge, pointing to upward transport of southwesterly momentum away from this layer as the primary process here. After 0630 UTC, the contribution from downward momentum transport exceeded that of upward momentum transport, suggesting that downward transport of northerly momentum played a significant role beyond that time. δHM exhibited a consistent northward tendency throughout the 0400-1000 UTC timeframe, which likely reflects a persistent northward push of southerly momentum within the low-level jet. The magnitude of the net wind tendency gradually decreased toward the end of the timeframe as the aforementioned forces approximately balanced each other.

In summary, cold pool surges occurred when the cold pool became sufficiently strong to induce a southward oriented pressure gradient, lifting along the cold pool edge transported southerly flow south of the cold pool above it, and southward tendency due to these factors became sufficiently strong to overcome the northward push ("push" refers to the role of δHM) of unmodified near-surface flow.

As discussed earlier, convection propagated along the southeastern cold pool flank during each southward cold pool surge. As convection moved south, upward momentum transport of southerly flow in convective updrafts away from the layer of instability, downward transport of northerly momentum into this layer in convective downdrafts, and southward pressure gradient accelerations into the rear of convective updrafts (relative to their motion) combined to exhibit a southward wind tendency. This southward tendency canceled the southerly component of

southwesterly MCS-relative inflow, interrupting the supply of convective instability to the western end of the CMS and temporarily disrupting upstream backbuilding. Southwesterly inflow then re-entered the western flank of the MCS via horizontal momentum advection. These factors – the interruption and subsequent re-introduction of southwesterly MCS-relative inflow, and the fact that the re-introduced southwesterly flow was sufficiently convectively inhibited (and insufficiently lifted along the boundary) so as to require northward travel beyond the southwestern outflow boundary before gradual lifting could re-initiate convection (as discussed in section 3.4.a) potentially explain the northward separation of convection from the surface outflow boundary (which is characteristic of the ROD phenomena).

3.6. Summary and Conclusions

This study details the results and analysis of a numerical simulation of a quasi-stationary MCS produced a swath of 12-hour rainfall in excess of 300 mm across eastern Iowa on 28 July 2011, with the purpose of elucidating the organizational dynamics of this system. The synoptic-scale environment associated with this system was characteristic of existing synoptic archetypes for warm-season flash flooding events, and featured a southwesterly low-level jet (which supplied warm, moist air at low levels\), persistent low-level convergence and warm air advection, and a quasi-stationary low-level frontal boundary. Our simulation reproduced the salient radar-observed and accumulated rainfall characteristics of the observed MCS. The following summarizes the results from our dynamical analysis of the simulated MCS (A visual summary is depicted in the schematic shown in Fig. 3.25.):

- Despite the presence of a stable boundary layer and elevated maximum CAPE throughout the lifetime of the MCS, a surface cold pool was present throughout the lifetime of the MCS.
- Two southeastward surges of the cold pool and convection occurred in the simulation (one occurred in the observed system). Elevated high θ_e air was transported to the rear of each of these convective segments as they moved out of the region of where the heaviest rainfall occurred. This air was lifted to saturation; CIN was eroded, and the flow triggered new convection (referred to as Rearward Off-boundary Development, ROD), which reinvigorated heavy rainfall production over the fixed geographic region. Lifting was accomplished by persistent large-scale warm air advection, with potential enhancement from gradual ascent over the cold pool left by earlier convection and an upstream low-level mesolow. Large-scale processes were presumed to have been the impetus for this pressure feature, which was enhanced by latent heating associated with convective updrafts.
- The cold-pool-normal vertical wind shear profile over the depth of the cold pool along the southeastern cold pool flank was more favorable for kinematic lifting along the boundary than the analogous profile along the southwestern cold pool flank. This potentially explains why convection propagated along (did not propagate along) the southeast (southwest) outflow boundary during the lifetime of the MCS. The northward separation of convection from the outflow boundary on the western side of MCS resulted from parcels being convectively inhibited, and insufficiently lifted along the boundary, therefore requiring additional northward travel and lift to achieve sufficiently expansive saturation and erosion of convective inhibition.

- Cold pool surges that preceded the ROD phenomena occurred when the pressure gradient associated with the cold pool mesohigh and lifting along the outflow boundary (specifically the southeast flank) of southerly flow away from the boundary layer contributed to a net southward flow acceleration along the outflow boundary.
- As convection followed the southeastern cold pool flank during cold-pool surges, forces associated with convective overturning changed the wind direction in their wake from southwesterly (providing storm relative inflow of unstable air) to westerly and northwesterly, which temporarily disrupted the supply of instability to the western flank of the MCS. Southwesterly flow associated with the low-level jet then replaced convectively overturned air and re-introduced instability to the western MCS flank, allowing for ROD. These processes explain why upstream backbuilding was interrupted prior to ROD episodes.

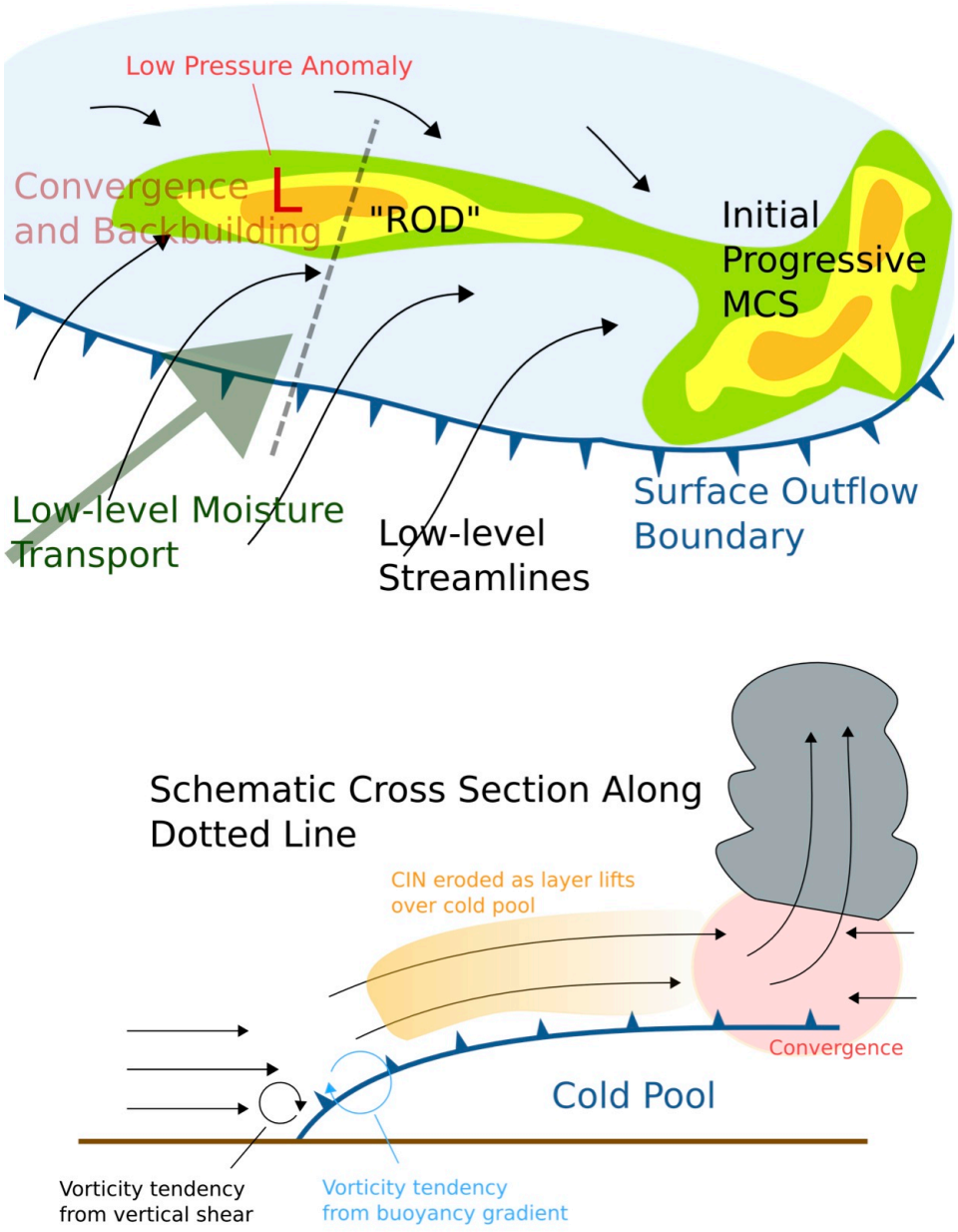

Fig. 3.25. Schematic diagram of the salient features and processes associated with the 28 July 2011 TL/AS MCS.

CHAPTER 4

THE SIMULATED STRUCTURE AND EVOLUTION OF A QUASI-IDEALIZED TL/AS MCS

4.1. Introduction

It has been well established in previous literature that the primary mechanism for heavy-rainfall generation in mesoscale convective systems (MCS) involves the continuous motion of individual convective elements within the larger convective system over a fixed geographic region (Chappell 1986; Corfidi et al. 1996; Doswell et al. 1996; Schumacher and Johnson 2005, 2006 – hereafter SJ2005, SJ2006; Schumacher and Johnson 2008; Schumacher 2009; Peters and Schumacher 2014, hereafter PS2014). Two processes – training and backbuilding of convection – are often at work during such MCS behavior. Training involves a convective line comprised of smaller convective scale updrafts that move in a line-parallel direction, resulting in their repeated motion over a fixed geographic region (often associated with the Training-Line Adjoining Stratiform, TL/AS SJ2005 MCS archetype). Backbuilding involves the repeated upstream (downstream) re-development (decay) of convective updrafts, resulting in a near-zero net motion of the larger convective system that they compose (often associated with the Backbuilding, BB SJ2005 MCS archetype). Note that while the TL/AS and BB MCSs represent the primary archetypes that exhibit these behaviors, they sometimes occur in other MCS types as well (such as the parallel stratiform and leading stratiform archetypes described by Parker and Johnson 2000).

While these mechanisms for heavy rainfall production occur on relatively small spatial scales (of order 10-100 km), the convective systems that exhibit these behaviors typically occur in conjunction with specific meso-alpha-to-synoptic (> 200 km) scale phenomena, such as

locally maximized low-level warm-air advection (WAA) and convergence along the nose of a low-level jet, a supply of low-level convective available potential energy (CAPE; air with CAPE is hereby referred to as "potentially buoyant"), low-level frontal circulations, and upper level jet streaks (Maddox et al. 1979; Crook and Moncrieff 1988; Augustine and Caracena 1994; Moore et al. 2003; SJ2005, SJ2006; PS2014). The common concurrence of training and backbuilding MCSs with such external forcing for ascent suggest that their existence depends on such processes.

The traditional idealized modeling approach for investigating the dynamics of mesoscale convective processes (such as system propagation) has often involved the simulation of isolated convective systems within an otherwise horizontally homogeneous thermodynamic and kinematic environment (e.g. Weisman and Klemp 1984; Rotunno et al. 1988; Fovell and Dailey 1995; Fovell and Tan 1998; Parker and Johnson 2004a,b). Although such simulations are ideal for isolating specific convective process, since their signatures easily stand out within an otherwise pristine and noise-free surrounding environment, the simulation framework prohibits the inclusion of large-scale thermodynamic and kinematic horizontal gradients and circulations that are important to particular types of MCSs (such as those that exhibit training and backbuilding behaviors). A more sophisticated idealized modeling approach is therefore required for the generation of a meaningful idealized simulation of training/backbuilding MCSs (while retaining the benefits of traditional idealized simulations).

Several novel methodologies for the inclusion of horizontally inhomogeneous features into idealized environments have been utilized in recent literature. Crook and Moncrieff (1988) and Schumacher (2009) applied forced low-level convergence into an otherwise horizontally homogeneous environment to simulate the effects of large scale forced ascent. Mahoney et al.

(2009) artificially constructed a zonal jet and associated baroclinic zone by varying the meridional tropospheric temperature (and thus the meridional pressure and wind fields by the assumption of thermal wind balance), whilst retaining zonal homogeneity. These authors successfully simulated a realistic trailing stratiform type MCS (TS, e.g. Houze et al. 1989, 1990; Parker and Johnson 2000) in order to ascertain the role of vertical momentum transport in rear inflow jet generation and cold pool behavior. In an earlier study, Coniglio and Stensrud (2001) simulated a progressive TS type MCS by constructing a large-scale environment from composite atmospheric fields that were generated from averaging over several observed cases. While both strategies were effective in simulating their intended MCS archetype in a realistic manner, the Coniglio and Stensrud (2001) composite strategy is an ideal starting point for the simulation of training/backbuilding MCSs, since the strategy used by these authors retained both zonal and meridional inhomogeneity, which is required for the presence of structures such as the low-level jet terminus and upper level jet streaks.

The primary goal of this study is to (1) outline the construction of a model framework that was used to simulate a warm-season type (see PS2014) TL/AS MCS from atmospheric fields composited over observed cases, with the primary hypothesis being that the basic dynamics of upwind propagation and heavy rainfall production are generalizable among individual events. While the analysis of the simulated system here will focus on the precipitation, thermodynamic, and kinematic anomalies produced by the system, future articles will analyze the dynamics of the simulated MCS discussed in this article. The organization of this paper is as follows: section 4.2 briefly reviews the compositing procedure of PS2014 and describes the numerical modeling configuration, section 4.3 documents the evolution of the simulated convective system, and

section 4.4 provides an article summary, concluding remarks, and outlines several hypotheses that will be tested in future studies.

4.2. Experiment Design

4.2.a. Case Selection and Composite Construction

PS2014 applied rotated principal component analysis (RPCA) to the atmospheric fields associated with a large group of TL/AS events (50 cases subjectively identified as such based on their radar methodology) and found two distinct modes of synoptic organization (see Mercer et al. 2012 for the application of RPCA in a similar context). These two modes, referred to as "synoptic type" events (24 cases), and "warm season" type events (26 cases), exhibited considerable differences in their moisture, kinematic, and thermodynamic fields despite similarities in their radar-indicated morphology and evolution. Warm season events (Fig. 4.1) were contrasted with synoptic type events for their typical occurrence during the summer months (with synoptic-type events predominantly occurring during the transition seasons), their association with weaker synoptic scale forcing for ascent and deep-layer wind shear than synoptic type events, and their propensity to exhibit both upstream backbuilding and training of convective radar echoes over fixed geographic regions. Additionally, the evolution of warm season events frequently featured quasi-discrete upstream propagation events characterized by the rearward off-boundary development phenomenon (ROD; PS2014, discussed in greater detail later in this section) and sometimes the more specific bow-and-arrow effect (Keene and Schumacher 2013) – both phenomena are characterized by the simultaneous development of a convective line to the rear of a progressive MCS, and north of the outflow-boundary (OFB) left by the initial system.

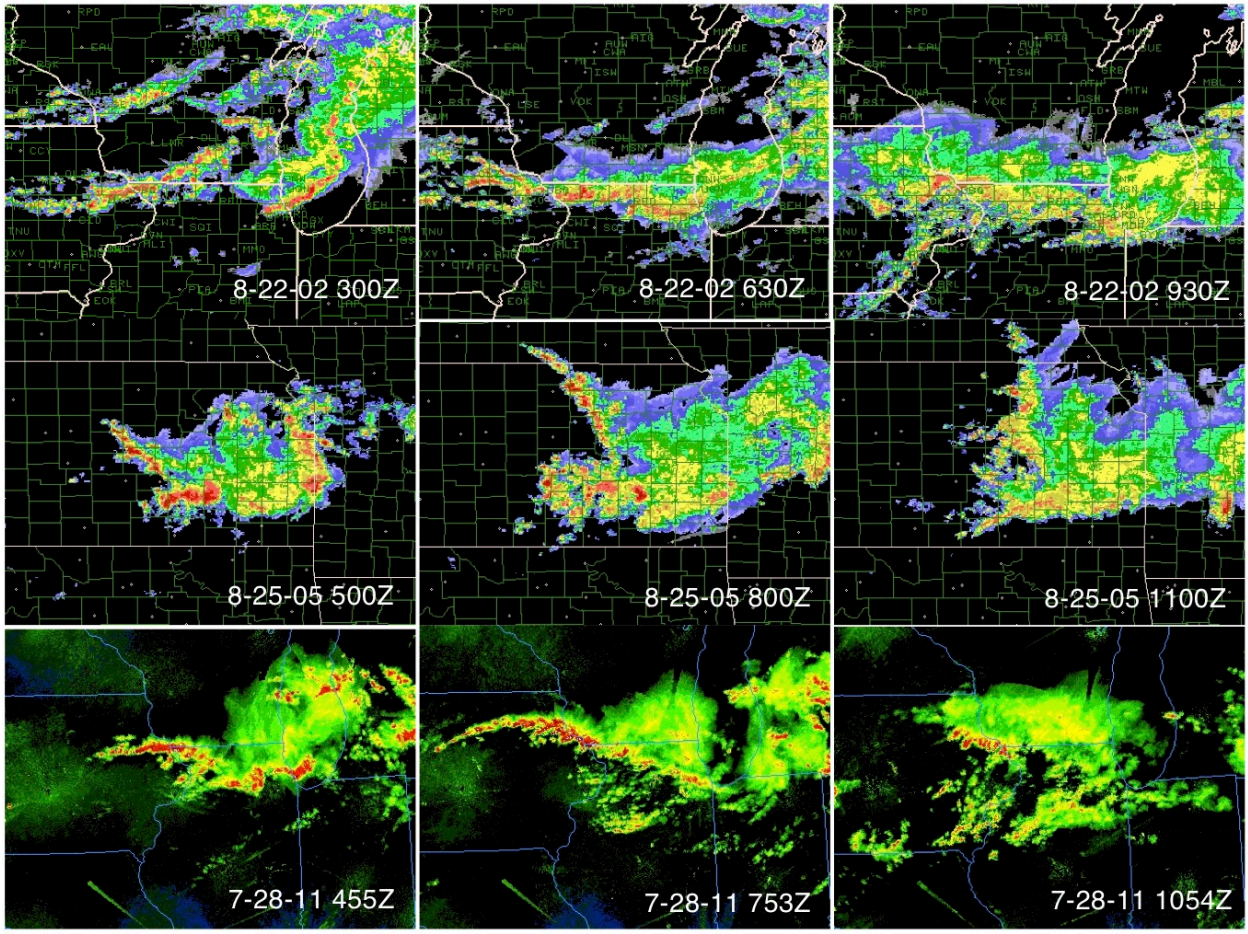

Fig. 4.1. Representative composite radar reflectivity images from three heavy-rain-producing warm-season TL/AS MCSs (each row constitutes a separate event). Valid dates and times are in the lower right corner of each panel. From PS2014.

Since we are interested in elucidating dynamical mechanisms for such upstream propagation behaviors, this analysis will focus on an idealized simulation of the warm-season type TL/AS events (simulations and dynamical analysis of synoptic type events will be described in future articles). A brief overview of the composite fields from warm season events is provided here, and additional details regarding the methods of their computation and structure can be found in PS2014. Using the North American Regional Reanalysis (NARR; Mesinger et al. 2006), composite atmospheric progressions were spatially centered at the location of the maximum 1-hour precipitation accumulation in the Stage IV precipitation analysis (Lin and

Mitchell 2005, hereby be referred to as ST4 analysis) and temporally centered at the time of the maximum 1-hour accumulation.

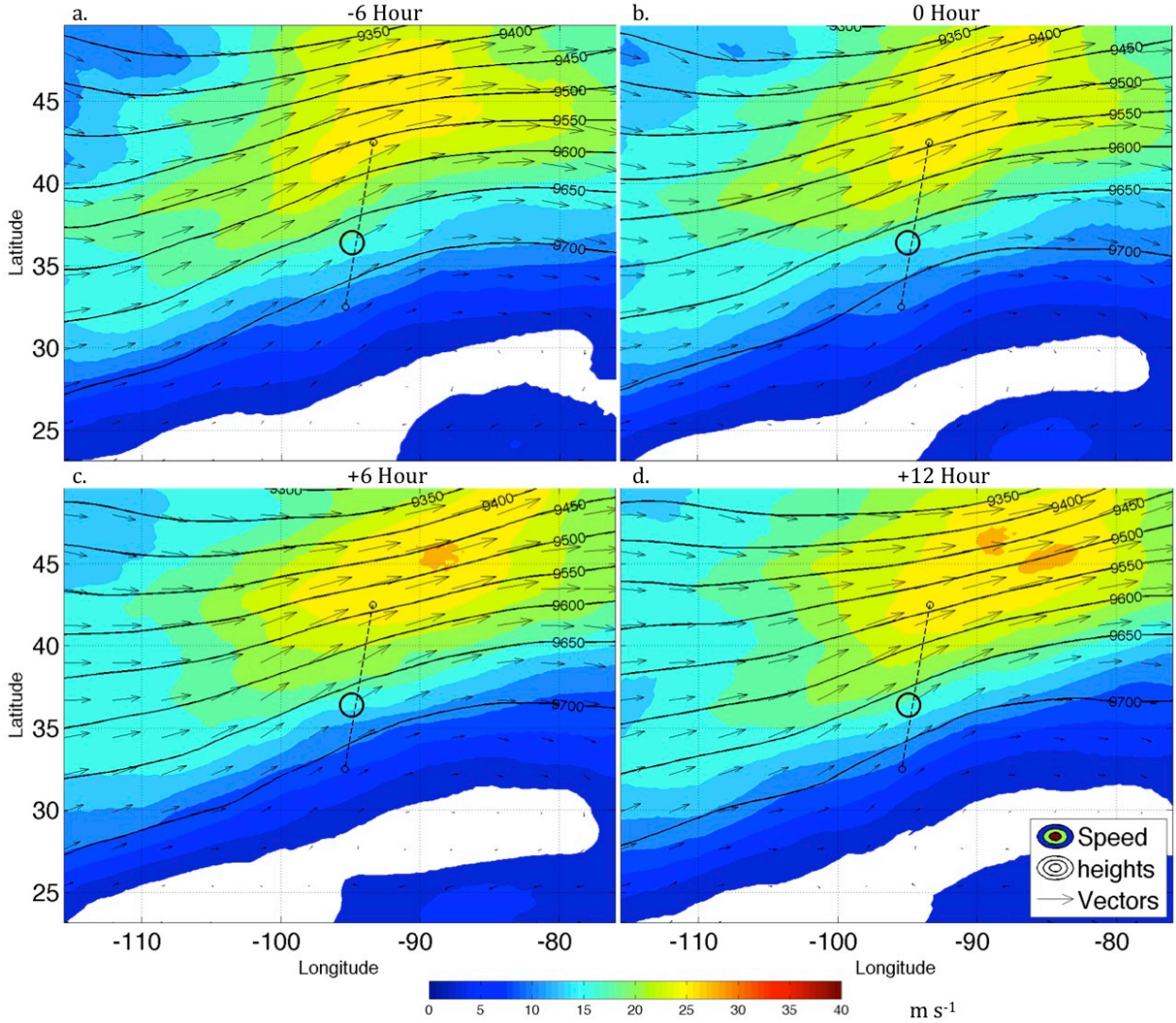

Fig. 4.2. 18-hour event-centered composite progression from 26 warm season events of 300 hPa wind speed (m/s, shading), wind vectors (arrows), and geopotential height (black lines at intervals of 50 m) from 6 hours prior (a), the time of (b), 6 hours after (c) and 12 hours after (d) peak 1-hour rainfall accumulating was observed at the event location. A solid black circle at the center of each frame indicates the point location of maximum 1-hour rainfall accumulation. The specific latitudes and longitudes shown are arbitrarily selected to illustrate the spatial scale. From PS2014.

Selected composite fields on the 300-hPa isobaric surface are shown for warm season events in Fig. 4.2. They typically occurred within the right entrance region to an anticyclonically curved upper level jet streak (this upper level jet configuration is common in the summer months over the eastern US). At 850 hPa (Fig. 4.3), a broad axis of warm air typically extended to the

south, southwest, and west of the event location, with the event having occurred within a meridionally oriented temperature gradient (typically a quasi-stationary or warm front). The heaviest rainfall was typically produced along the northern nose of a southwesterly low-level jet, within a region of locally maximized low-level convergence and WAA.

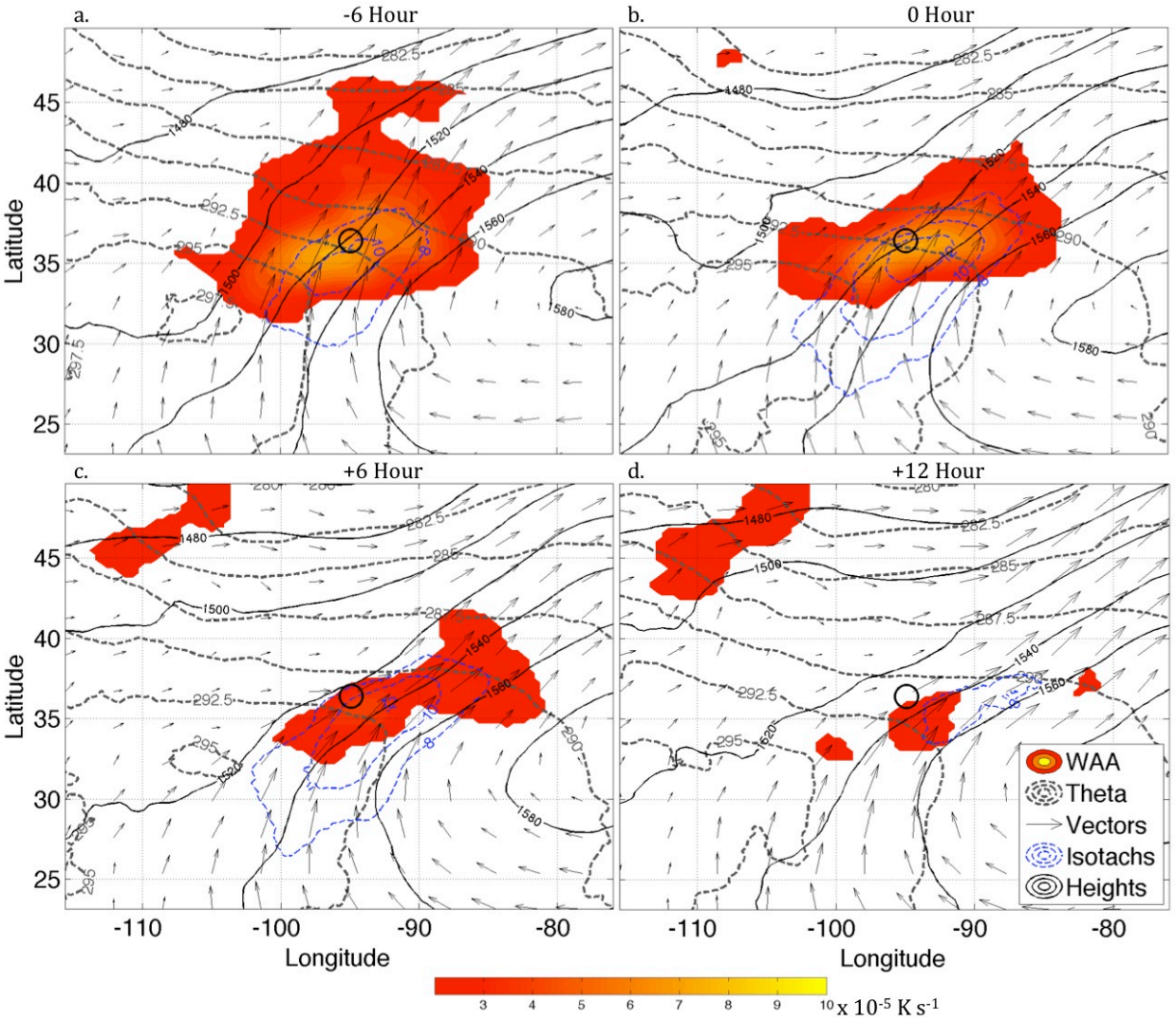

Fig. 4.3. 18-hour progression from warm season events of 850 hPa potential temperature advection (x 10^{-5} K s^{-1}, shading; values below 2 x 10^{-5} K s^{-1} have been removed; derivatives were computed from composite atmospheric fields), wind speed (blue dashed contours at intervals of 2 m/s, starting at 8 m/s), wind vectors (black arrows), geopotential height (black lines at intervals of 20 m), and potential temperature (K, dashed gray contours). Panel times are the same as those in Figs. 1 and 2. A solid black circle at the center of each frame indicates the point location of maximum 1-hour rainfall accumulation. The specific latitudes and longitudes shown are arbitrarily selected to illustrate the spatial scale. Adapted from PS2014.

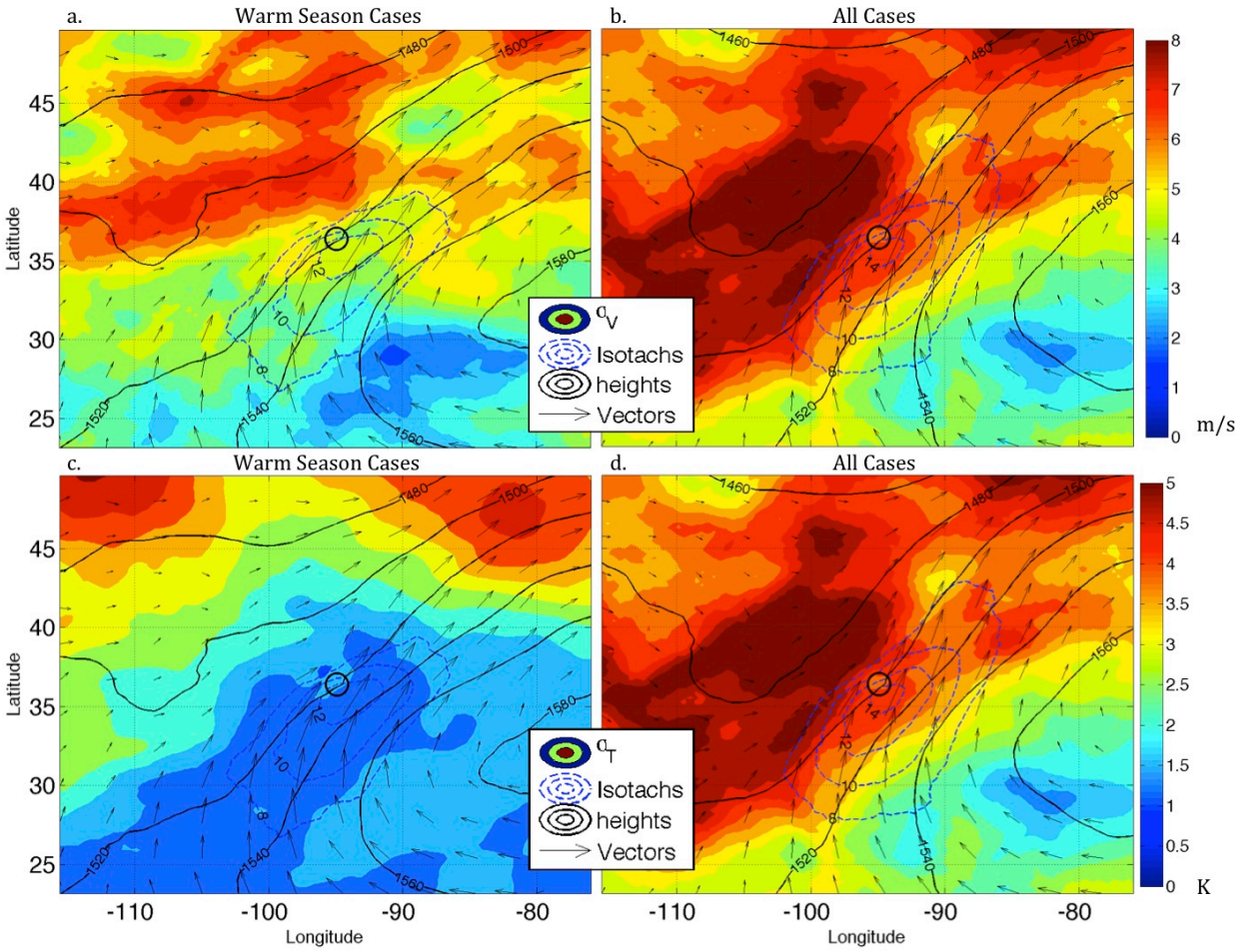

Fig. 4.4. Plots of the standard deviation (σ, see equation 1 in the text) of 850 hPa wind speed for 26 warm season events (panel *a*, shading, m/s) and 50 training convective events containing both warm season and synoptic even types (panel *b*, shading, m/s) events, the standard deviation of temperature for warm season (panel *c*, shading, K) and all events (panel *d*, shading, K). Geopotential height (solid black contours, m, at intervals of 40 m), wind vectors (black arrows), and wind speed (blue dotted contours, m/s starting at 8 m/s and at intervals of 2 m/s) are shown in all panels. All panels are valid at the time of maximum 1-hour rainfall accumulation from stage IV precipitation analysis (see PS2014). A solid black circle at the center of each frame indicates the point location of maximum 1-hour rainfall accumulation. The specific latitudes and longitudes shown are arbitrarily selected to illustrate the spatial scale. Adapted from PS2014.

The advantage of the consideration of composite atmospheric fields from the statistically sorted methodology of PS2014 to the analogous composite fields computed over all cases is illustrated when comparing the standard deviation of representative atmospheric fields at each grid point within our domain for the 26 warm season case to that for all 50 cases (Fig. 4.4), where

$$(4.1) \quad \sigma_f(x,y,p,t) = \sqrt{\frac{1}{n-1}\sum_{i=1}^{n} f(x,y,z,t,c_i)},$$

f is any arbitrary atmospheric field, n is the number of cases considered in the computation, t is the time removed from peak stage IV 1-hour rainfall, and c_i is a case number (see PS2014 where this quantity is introduced in greater detail). Note that standard deviation values – especially near the event location and along the low-level jet – are considerably lower when computed over the 26 warm-season cases only, than when computed over all 50 cases. This indicates less variability in the placement of atmospheric structures relative to the event location among warm season cases than among all cases.

4.2.b. Control (CNTL) simulation

The numerical simulations in this study were conducted with Version 3.4.1 of the Advanced Research Weather Research and Forecasting Model (WRF-ARW; Klemp et al. 2007; Skamarock et al. 2008). Composites of temperature, geopotential height, specific humidity, u, and v wind components were horizontally interpolated onto the model domain on the 1000, 950, 900, 850, 800, 750, 700, 600, 500, 400, 300, 250, 200, and 150 hPa isobaric surfaces. No terrain variation was included, with the surface geopotential height set to 0 m. Surface values for the aforementioned quantities were linearly interpolated to the surface based on their values and geopotential heights on adjacent pressure surfaces. These data were then input into the WRF-ARW real-data pre-processor (which vertically interpolates data onto the model vertical levels and hydrostatically balances the initial and lateral boundary conditions; Skamarock et al. 2008).

All simulations were configured in "real" mode (contrasted with "ideal" mode, see Skamarock et al. 2008). Several preliminary runs were conducted on a 4 km grid at differing start times relative to the 1-hour peak rainfall time in the composites (e.g. start times of 18 hrs,

15 hrs, and 12 hrs prior to peak rainfall to allow for more or less spin-up time), and with different approaches to dealing with model physics (e.g. the choice over whether to use a land-surface model) in order to (1) determine whether an MCS would develop at all, and (2) to determine the model configuration that best reproduced a realistic MCS (i.e., exhibiting characteristics that subjectively resembled observed TL/AS cases). Once this configuration was achieved, the simulation was re-run with the addition of a 1.33 km inner nest initialized two hours prior to the first observed convection in the 4 km domain, and centered at the location of the MCS (see the previous sub-section for the inner domain position). The final simulation was run at 4 km from 15 hours prior to 15 hours after peak rainfall time in the composites, and at 1.33 km from 5 hours prior to 15 hours after peak rainfall (see Table 4.1).

Table 4.1. Comparison of the timetable of the composite evolution (top row, in terms of time removed from peak 1-hour rainfall observed in ST4 precipitation), outer domain and inner domain simulations (middle and bottom rows respectively, in terms of elapsed time from the simulation start). The notions t_{comp} and t_{sim} for which the listed times correspond to are shown in the second column from right.

Composites	t_{comp}	*-15*	*-12*	*-9*	*-6*	*-3*	*0*	*3*	*6*	*9*	*12*	*15*
4 km Grid	t_{sim}	**0**	**3**	**6**	**9**	**12**	**15**	**18**	**21**	**24**	**27**	**30**
4/3 km Grid	t_{sim}	**-**	**-**	**-**	**-**	***12***	***15***	***18***	***21***	***24***	***27***	***30***

Note that while the inner domain was initialized after the outer domain, we will hereby refer to simulation times on the inner domain in terms of their time elapsed from the start of the 4 km domain. The configuration featured a one-way feedback nested structure with the outer domain having dimensions of 2712 x 2712 km, inner domain dimensions of 1000 x 800 km, and the lower-left corner of the inner domain positioned at grid point (300, 300) in the outer domain. The outer domain was assigned an arbitrary center latitude of 40 degrees north, and a center longitude of 88 degrees west.

Though the observed events used to construct composites typically occurred during the early morning hours (PS2014), there was considerable spread among the exact times of the 1-

hour peak rainfall. Despite this, the evolutions of the low-level stability profile and horizontal pressure gradient at the location of the low-level jet maximum (Fig. 4.5) show signatures of a diurnal low-level jet intensity cycle, with the temporal LLJ maxima coincident with the maximum low-level stability (and not perfectly correlated with the low-level horizontal pressure gradient).

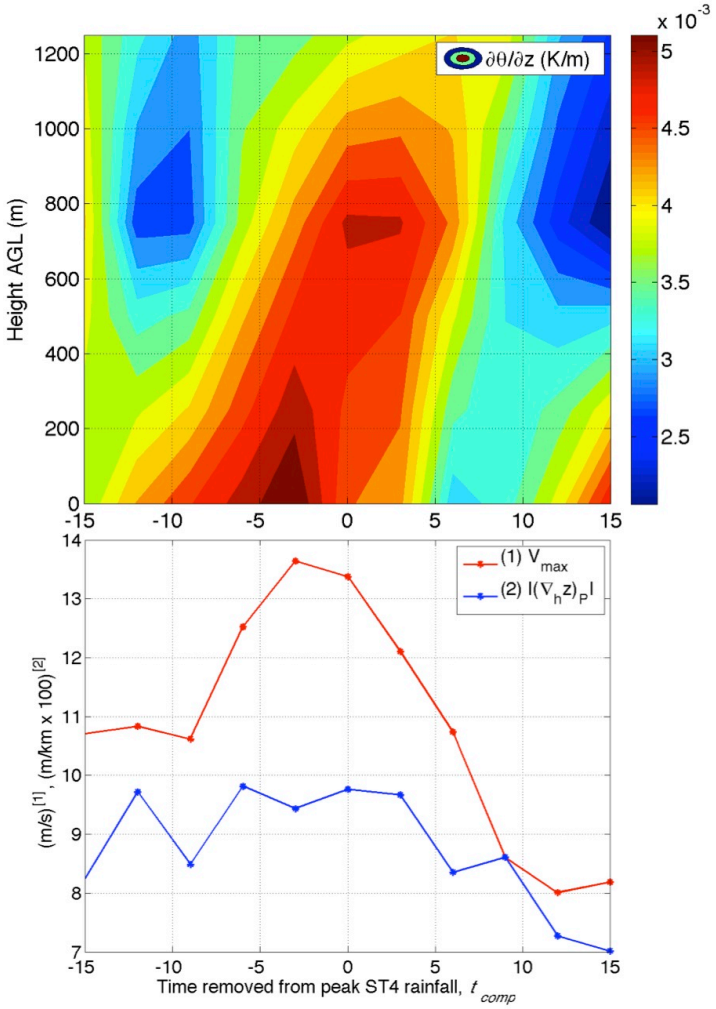

Fig. 4.5. Top panel: Time-height diagram of the vertical profile of static stability (shading, measured as $\frac{\partial \theta}{\partial z}$, K/m) below the maximum point wind speed value at 850 hPa in the composite progression. Bottom panel: time series of the maximum 850 hPa wind speed (red line) and the magnitude of the horizontal geopotential height gradient on the 850 hPa isobaric surface (blue line) in the composite progression.

Surface-to-atmosphere heat fluxes in preliminary simulations produced spurious near-surface temperature fluctuations, and it was unclear where to align our composite progression within the

diurnal radiative cycle. Land-atmosphere fluxes were therefore turned off in our final modeling configuration, resulting in a nearly perpetually stable boundary layer (characteristic of a nocturnal environment) through the course of our simulation (discussed in greater detail in the next subsection). Surface friction was minimized by treating the lower boundary in land use and surface characteristic categories as that of water (while keeping the land-surface flag set to that of land).

While certain attributes of the simulation configuration here may seem rather arbitrary (e.g. the positioning/size of the inner/outer domains and the choice to turn off land/surface fluxes), the environment associated with the simulated MCS exhibited considerable qualitative similarities to that commonly observed in TL/AS events (as will be discussed later), and we therefore justify the modeling configuration *a posteriori* given the success of our simulation at producing a realistic MCS within an environment consistent with those observed to support such systems. Certainly other domain sizes, resolutions, and positioning may have yielded equally successful results.

The grid spacing of both domains was sufficiently small to explicitly represent convective processes (although insufficiently small to properly resolve individual convective updrafts; Bryan et al. 2003), and no cumulus parameterization was used in either domain. Table 4.2 lists the other model parameters and physics options used in all of the modeling experiments described here. The nonlinear relationship between many of the aforementioned quantities over which linear averaging was conducted posed a significant obstacle to conducting simulations from the composite atmospheric fields.

Table 4.2: List of WRF-ARW grid resolutions, grid dimensions, physical parameterizations and nudging configurations used in this study.

Domain	**Outer Domain**	**Inner Domain**	*Notes*
Grid Spacing	4 km	4/3 km	Inner domain start: i=300,j=300 on outer domain
Domain Dimensions	2712 x 2712 km	1000 x 800 km	
Vertical Sigma Levels	32	""	
Model Top Pressure	150 hPa	""	
ICs and LBCs	NARR composites	""	
Microphysics	Thompson	""	Thompson et al. (2008)
Longwave Radiation	RRTM	""	Miawer et al. (1997)
Shortwave Radiation	Dudhia	""	Dudhia (1989)
Surface Layer	Eta Similarity	""	
Land Surface Model	*none*	*none*	
Boundary Layer Physics	MYJ	""	Janjic (1994)
Cumulus Parameterization	*none*	*none*	

For instance, the choice between compositing over specific humidity or relative humidity was not entirely obvious, and the two choices do not yield equivalent results owing to the nonlinear Clausius-Clapeyron relationship. Likewise, there was no guarantee that the composited atmospheric fields retained their dynamical balances (e.g. gradient wind balance, hydrostatic balance) that are typically characteristic of the synoptic scale atmosphere (though the WRF real data processor "re-balances" these fields, there was no guarantee that the resulting balanced atmospheric state would emulate states from observed cases sufficiently to produce a realistic simulation). Finally, it was clear that the model solution on the model domain would diverge from the composited atmospheric state as the simulation time increases – though such deviations may be partially constrained by the continuous passage of information into the model lateral boundaries. It was therefore important to comprehensively assess the degree to which such deviations caused the simulated environment to deviate from that that is characteristic of the events that we aimed to simulate.

All simulations that were conducted from raw composite fields resulted in substantially delayed convection initiation (CI, with timing approaching the end of the simulation). Model simulations often exhibit unrealistically suppressed convection when they are initialized from observed or composite soundings with any convective inhibition (e.g., Parker and Johnson

2004c; Naylor and Gilmore 2012), and a common solution is to slightly increase relative humidity at low-levels. Here, the initial relative humidity was increased in accordance with the following formula, which allowed for more realistic CI timing in the simulations:

$$(4.2)\quad RH_m(p) = \begin{cases} RH_i(p) + A\exp\left[-\dfrac{(p_{ref} - p)^2}{\sigma^2} \right] & \text{if } (p_{ref} - p)^2 \le p_{cutoff}^2 \\ RH_i(p) & \text{if } (p_{ref} - p)^2 > p_{cutoff}^2 \end{cases},$$

where RH_m is the modified relative humidity, RH_i is the relative humidity value from the composite data, A is the amplitude of the added perturbation (set to 10%), p is pressure (hPa), p_{ref} is the pressure level of the maximum added perturbation (900 hPa), the σ parameter (set to 50 hPa) controls the rate of amplitude decrease as the vertical distance from p_{ref} increases, and p_{cutoff} (400 hPa) is the maximum vertical distance in hPa from p_{ref} within which the relative humidity was modified. The relative humidity perturbation in equation (2) was added uniformly (i.e. no variation in x and y) across all points within the composite analyses prior to them having been interpolated onto the model domain and processed by the WRF real data processor (all simulations analyzed here featured this added perturbation).

4.2.c. No Microphysics (NOMP) simulation

We ran a second simulation by restarting WRF 1 hour before the first convective updrafts associated with the simulated MCS were observed in the CNTL simulation with the microphysics scheme turned off (all other configuration attributes were the same as the CNTL simulation for this second run). The purpose of this simulation was to assess the similarity between the simulated environment and that of the composites, and later to define convective perturbation fields. We hereby refer to this simulation as the *no microphysics* run (NOMP). Henceforth, the time removed from peak rainfall in the composites will be referred to as t_{comp} and

the time removed from the start of the simulations will be referred to as t_{sim}. We reiterate that at t_{sim} = 15 hr, composite atmospheric fields from t_{comp} = 0 hr are provided as lateral boundary conditions. Table 1 further facilitates the comparison between t_{comp} and t_{sim}.

It is worth noting that unrealistic phenomena may arise when simulating an atmosphere where large regions of supersaturation are achieved (such as the region where the MCS developed in the CNTL simulation) and the effects of latent heating are neglected. For instance, regions of combined supersaturation and lift may become unrealistically cool due to adiabatic cooling of ascending parcels without latent heating to compensate for such cooling. If sufficient unrealistic cooling occurred, a corresponding low-level high-pressure anomaly would be expected in the NOMP simulation, which would contaminate the perturbation pressure fields that are analyzed in subsequent sections. We thoroughly examined temperature and pressure fields in the NOMP simulation (not shown) and found no evidence of such unrealistic anomalies, which suggests that vertical velocities (and adiabatic cooling) in the NOMP simulation were insufficiently strong to produce such unrealistic effects. Furthermore, the patterns and magnitudes of perturbations in later sections are comparable to those commonly observed in simulations and observations of MCSs, and we therefore assume that they (perturbation fields) are dominated by the influence of deep convection associated with the MCS simulated here.

A representative comparison of the atmospheric fields in the NOMP solution to the analogous fields in the composites is shown in Fig. 4.6. The low-level jet maximum in the simulation was displaced considerably farther northward in relation to the composites, and exhibited a peak in wind speed 6-9 hours after the analogous wind speed maxima in the composites. The upper level flow was also slightly stronger, and the low-level flow slightly weaker in the simulation.

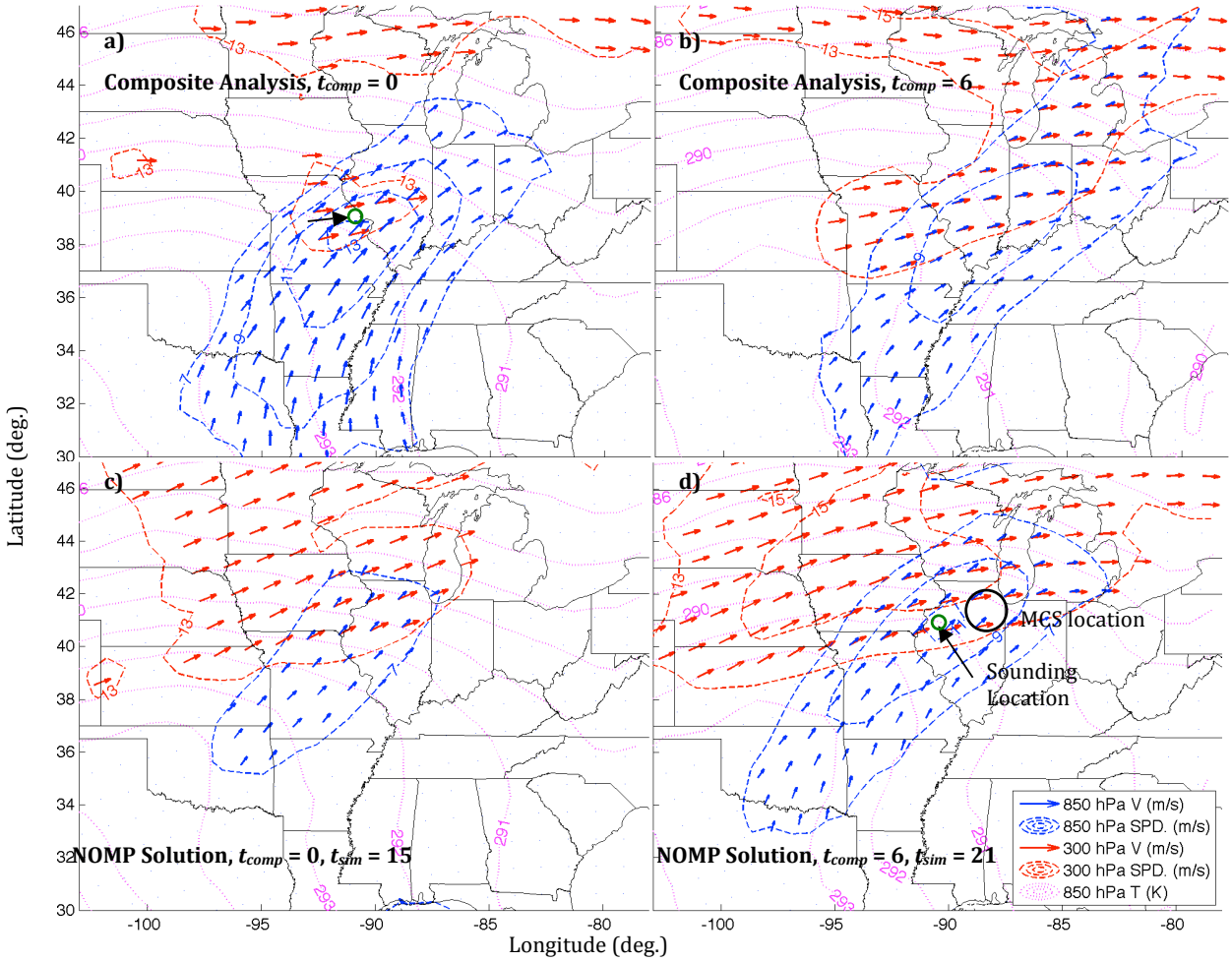

Fig. 4.6. Comparison of the synoptic scale environments in the warm-season composites (top panels) used as ICs and LBCs for WRF simulations to the synoptic scale solution on the 4 km NOMP domain (bottom panels), valid at (left panels) and 9 hours after (right panels) the time of heaviest 1-hour rainfall accumulation in the composites (note that the corresponding simulation times are also included). Red arrows are 300 hPa wind vectors, dotted red contours are 300 hPa wind speeds (m/s) at intervals of 2 m/s, starting at 13 m/s; blue arrows are 850 hPa wind vectors and blue dotted contours are 850 hPa wind speeds (m/s) at intervals of 2 m/s, starting at 7 m/s; magenta dotted contours are 850 hPa wind speed (K) at intervals of 1 K. Green dots and black arrows indicate the location of the vertical profiles shown in Fig. 9.

While the horizontal temperature distributions were qualitatively similar between the simulation and composites, the nose of the low-level jet was displaced northward in the simulation at its peak intensity (compare Fig. 4.6d to Fig. 4.6a), resulting in a northward displacement of the maximum simulated WAA.

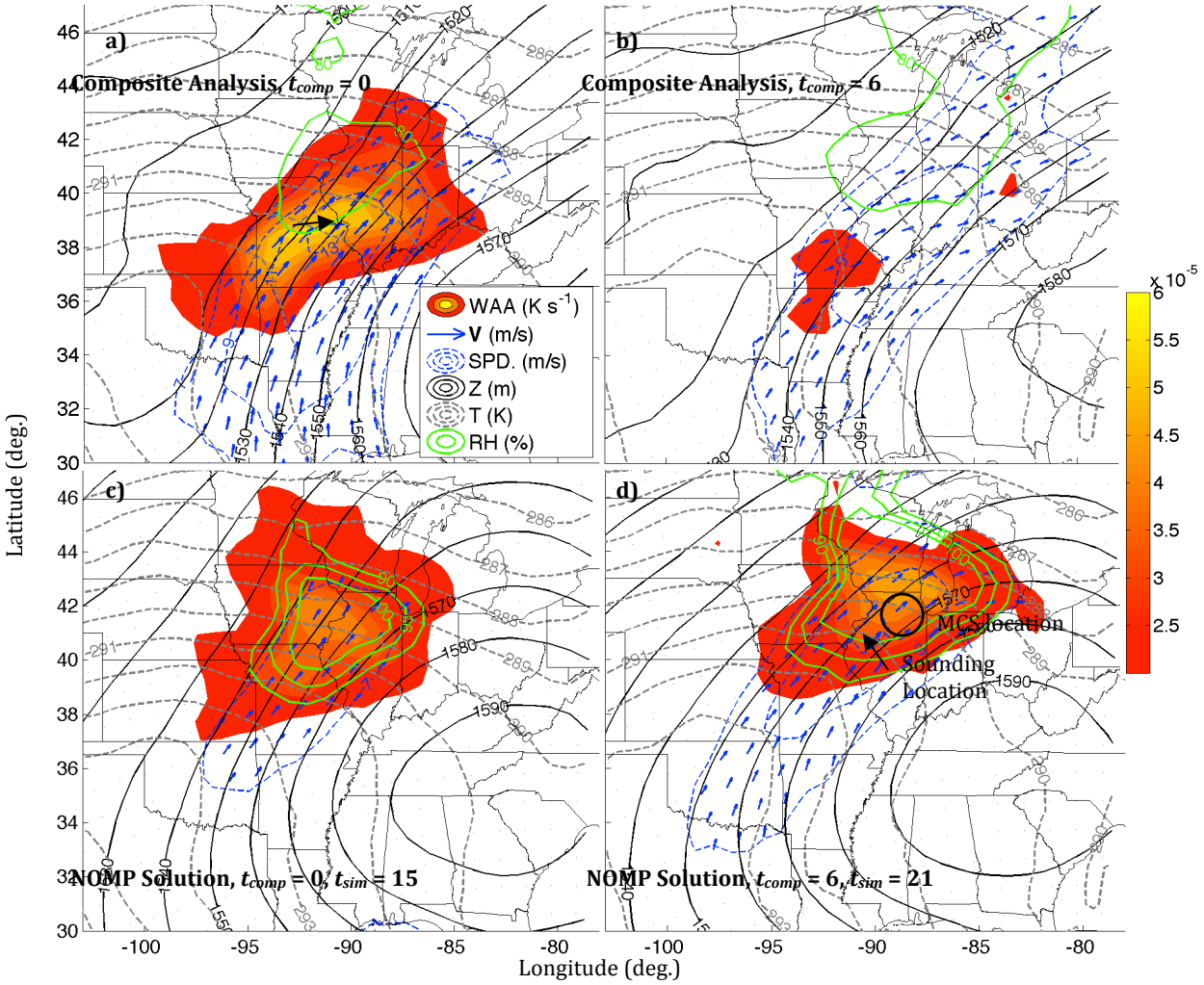

Fig. 4.7. Same as Fig. 6, but here 850 hPa WAA (shading, K s^{-1}), 850 hPa wind vectors (blue arrows, m/s), 850 hPa wind speed (dashed blue contours, m/s at intervals of 2 m/s, starting at 7 m/s), 850 hPa geopotential height (black solid contours, m), 850 hPa temperature (dashed magenta contours, K), and 850 hPa relative humidity (solid green contours, %), are shown to facilitate the comparison of synoptic scale forcing for ascent between the composites and simulation.

Although it is difficult to disentangle the various potential contributions to such differences between the model solution and composite progression, it is likely that the highly nonlinear nature of the advective component of the governing equations contributed significantly to such differences (i.e. the average of the instantaneous contributions to the time tendency of variables resulting from advection over many cases differed from the advection of the mean values of

quantities by the mean wind once the composite initial and lateral boundary conditions began evolving in the simulation).

As noted by various past studies (e.g. Maddox 1979; Doswell et al.1996; Moore et al. 2003; Schumacher and Johnson 2005; Peters and Schumacher 2014a), persistent low-level lifting associated with low-level WAA and convergence along the nose of a low-level jet is often characteristic of the environment of heavy-rain-producing MCSs. In the composite progression used to drive our simulations, the intensity of low-level WAA had begun to subside between t_{comp} = 3 and 6 hr (see Fig. 13 in PS2014). Fig. 4.7 reveals that, while WAA intensity in the composite progression had decreased considerably by t_{comp} = 6 hr relative to t_{comp} = 0 hr, WAA remained intense through this timeframe in the simulation (t_{sim} = 15-24 hr) at the location of the MCS, resulting in a persistent region of saturation at 850 hPa. As will be discussed in greater detail in later sections, the MCS in the CNTL simulation reached a subjectively determined maturity approximately 6 hours after peak rainfall in the composites (t_{sim} = 21 hr).

A comparison between Fig. 4.8 and Fig. 4.5 suggests that the diurnal low-level jet intensity cycle evident in the composites was not present in the simulation. In fact, two distinct low-level jet maxima are evident in Fig. 8 – one at simulation t_{sim} = 7 hr, and another at roughly simulation t_{sim} = 21 hr (the second maxima occurred during the lifetime of the MCS, and may be correlated with the magnitude of the horizontal pressure gradient during this timeframe). There is also little evidence in the low-level static stability field of a diurnal stability cycle, with the major temporal changes in the top panel having occurred near the beginning of the simulation (likely related to model "spin-up"). These differences in the low-level jet character between the simulation and composites were likely a result of the combination of a missing diurnal heating

cycle in the planetary boundary layer, along with the absence of terrain (both of these factors strongly regulate the plains low-level jet intensity, Du and Rotunno 2014).

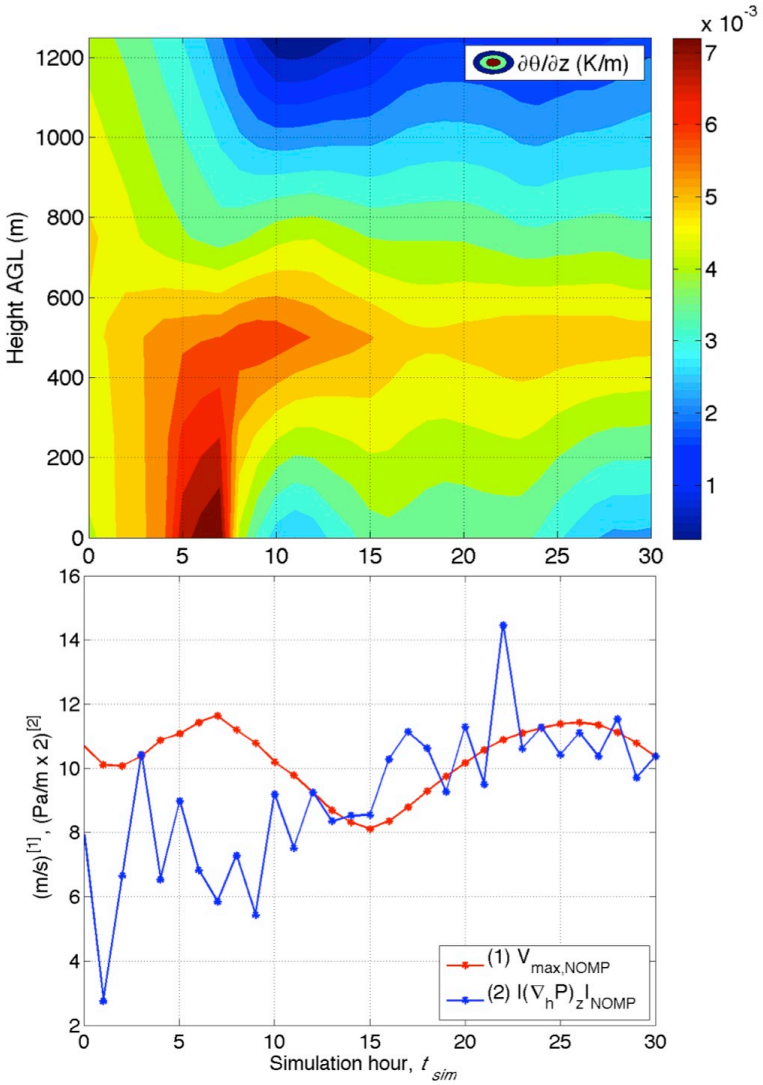

Fig. 4.8. Analogous quantities to those in Fig. 4.5, but for the NOMP simulation. Here, the maximum wind speed value at 1.25 km AGL has been assessed rather than the maxim wind speed at 850 hPa. The blue line in the bottom panel subsequently depicts a time series of the horizontal pressure gradient (Pa/m x 2) at the location of the maximum 1.25 km AGL wind speed rather than the horizontal geopotential height gradient on an isobaric surface. The location of the maximum wind speed at this level varied considerably with time; therefore, the stability profile in the top panel was assessed at the sounding location indicated in Fig. 4.7d.

The delayed low-level jet intensity maximum in the simulation relative to the composite progression, and persistent intense WAA in the MCS region in the simulation beyond the timeframe were therefore advantageous outcomes, since they resulted in the simulated MCS

environment remaining suitably analogous to the timeframe where the MCSs occurred in the composites. Further comparisons will therefore focus on the simulated environment at the northern periphery of the low-level jet in the CNTL simulation at t_{sim} = 21 hr (which was a representative example of the low-level inflow region to the simulated MCS), and along the northern periphery of the low-level in the composites at t_{comp} = 0 hr (the time of peak MCS intensity in the observed cases).

Vertical temperature and moisture profiles from the aforementioned locations and times are shown in Fig. 4.9. Interestingly, the composite sounding lacks a discernible stable layer near the surface, exhibits maximum CAPE values at the lowest analysis level (all the cases used to construct the composite were characterized by most unstable CAPE rooted in an elevated layer, PS2014), and convective inhibition through all potentially buoyant layers. While this is a curious attribute, given the nature of the cases used in composite construction, it is potentially an artifact of differing topographic heights between cases (and reanalysis data being interpolated onto sub-surface isobaric levels for some cases), and/or differing depths of the near-surface stable layer. The model sounding, however, does exhibit a stable layer near the surface (which may have been re-introduced during the dynamical balancing conducted by the WRF real-data processor, and maintained by the lack of fluxes from surface to atmosphere), as well as a maximum (minimum) in CAPE (convective inhibition) above the surface (between 900 and 800 hPa). The shapes of the vertical wind profiles (Fig. 9 hodograph) were qualitatively similar between the simulation and composite times and locations (Compare to Schumacher and Johnson 2005 where winds were slightly stronger, presumably due their composite pool containing both warm season and synoptic type events).

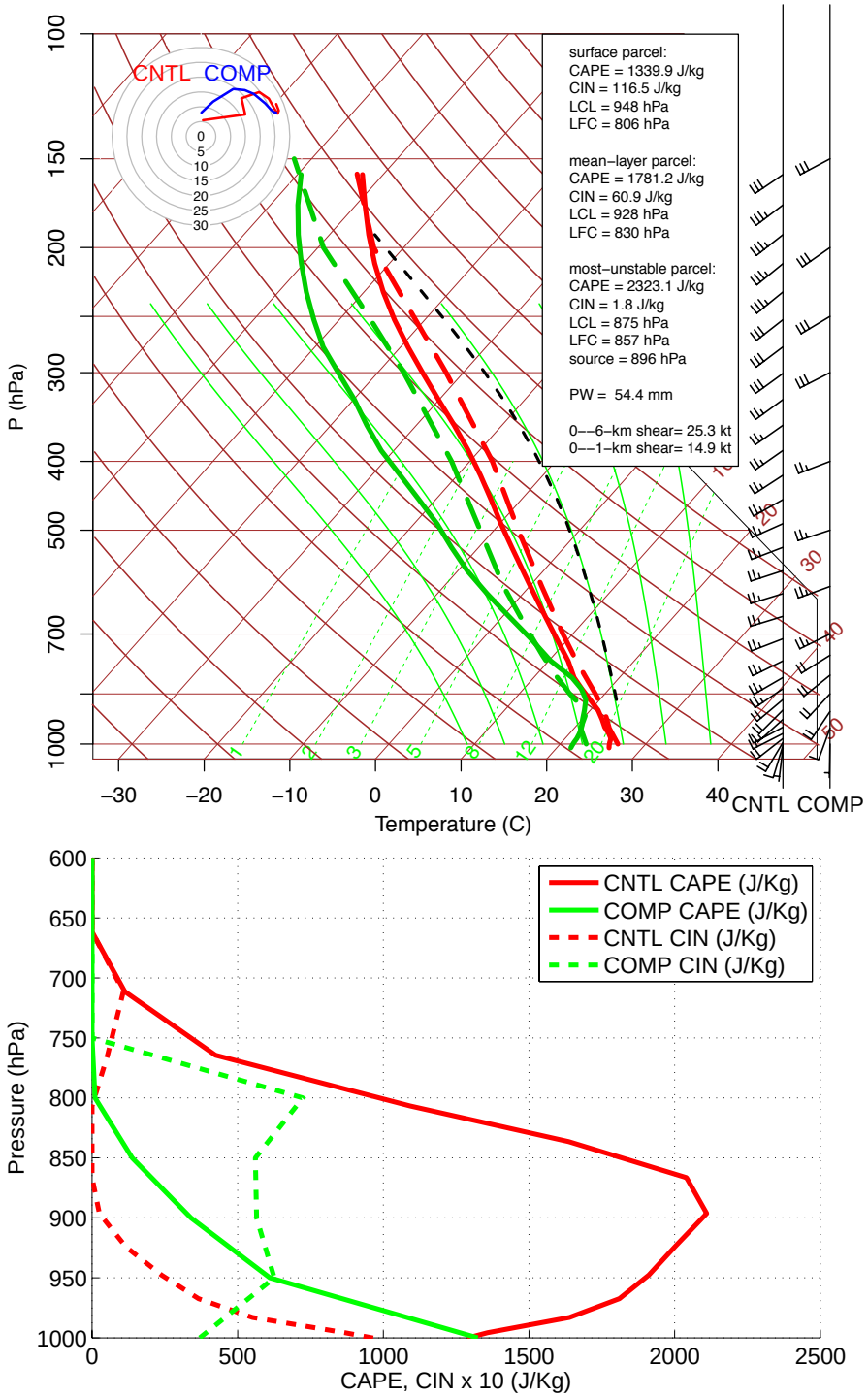

Fig. 4.9. Top panel: Skew T – Log P diagram depicting vertical profiles [composite (CNTL) at the time of peak 1-hour rainfall, CNTL outer domain 6 hours after peak rainfall] of temperature (solid red), dew point (solid green), wind barbs), and a hodograph (upper left inset, units on concentric circles are kts) (solid blue line, solid red line). Sounding locations are black arrows in Fig. 6. Bottom panel: Vertical profiles of CAPE (J Kg^{-1}, solid green line, solid red line) and CIN (J Kg^{-1}, dashed green line, dashed red line).

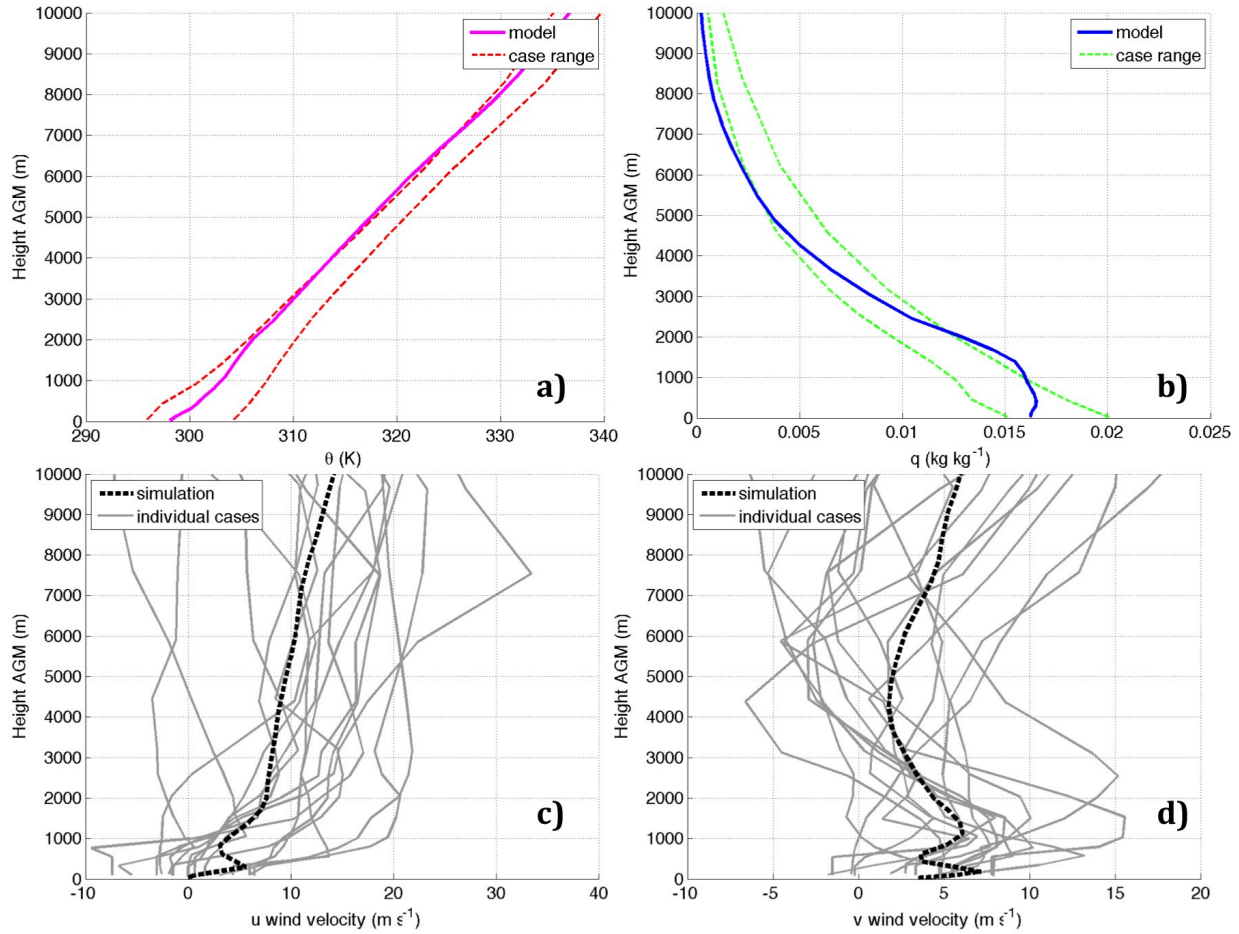

Fig. 4.10. Panel a: vertical profile of potential temperature from the CNTL simulation at the same time and location as Fig. 9 (solid magenta line, K), and the analogous profile from the composites at the same time and location as Fig. 9 +/- the standard deviation of potential temperature at each level, computed over all warm season cases. Panel b: analogous to panel a, but for water vapor mixing ratio (Kg Kg^{-1}). Bottom panels: vertical profile of the *u* (panel c) and *v* (panel d) wind components (dashed gray lines, m/s) from the CNTL simulation at the same time and location as the top panels, and the analogous profiles from the NARR for individual cases (gray lines, m/s) at the location of maximum 1-hour rainfall accumulation for each case.

The simulated temperature profile resides near the cold periphery of the range of values among composited cases above 2 km (Fig. 4.10a), whereas the simulated moisture profile resides near/beyond the upper end of the moisture range between 1 and 2 km, and gradually approaches the dry edge of this range by 5 km AGL (Fig. 4.10b, note that the simulated moisture profile contains the added moisture from equation 2). Differences in the former comparison are a result of the simulated profile we are examining being further north (and slightly cooler) than the composite profile, and differences in the later comparison predominantly arise from our addition

of low-level moisture in the simulation ICs and LBCs. The *u* and *v* velocity profiles (Fig. 4.10c,d) fall well within the range of composited cases. A spike in wind speed values below 500 m is evident in the simulated profiles of both wind components (Figs. 4.10c,d). Curiously, no analogous feature was present in the composited wind profiles (Figs. 4.10c,d).

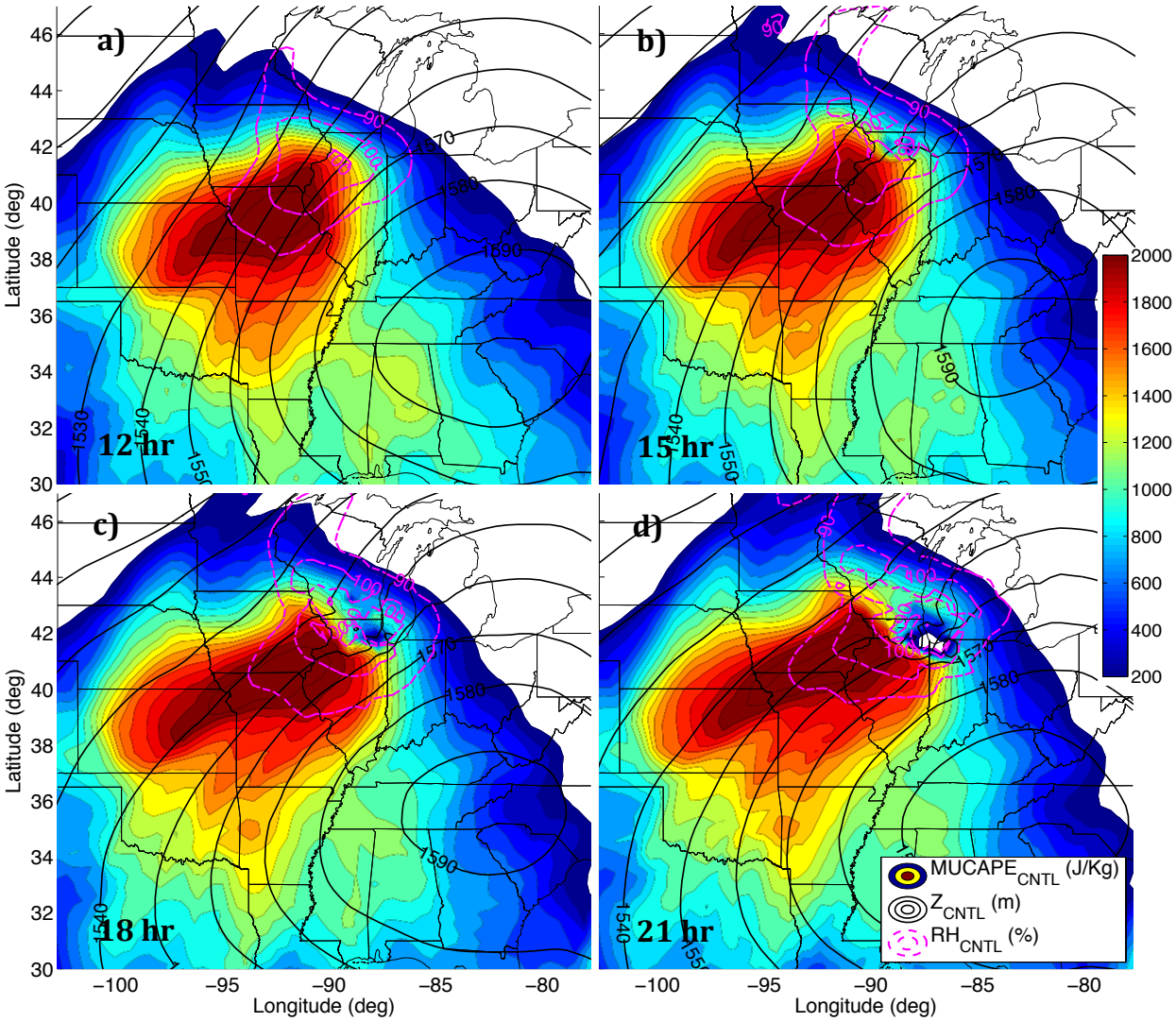

Fig. 4.11. CAPE from the CNTL outer domain for parcels lifted from the 850 hPa surface (shading, J/Kg), 850 hPa geopotential height (black counters, m at intervals of 10 m), and 850 hPa relative humidity (magenta dashed contours, %) for t_{sim}= 12 hr (panel a), t_{sim} = 15 hr (panel b), t_{sim} = 18 hr (panel c), and t_{sim} = 21 hr (panel d). CAPE is shown for the CNTL, rather than the NOMP simulation to emphasize the location of the MCS relative to the supply of instability. The analogous CAPE field from the NOMP simulation was nearly identical outside the region obviously affected by the MCS.

We examined observed soundings within the inflow region of warm-season cases, and found similar features in nearly half of the observed cases (not shown) – the absence of this feature in

the composited profiles is likely due to the low vertical resolution of the isobaric NARR data used in this study.

The modeled CAPE profile in Fig. 4.9 exhibits considerable qualitative similarities to the vertical equivalent potential temperature (θ_e, which is often spatially correlated with CAPE) composite profile shown in Fig. 13b from Moore et al. (2003) for elevated heavy-rain producing MCSs. The horizontal distribution of low-level CAPE (Fig. 4.11) was characterized by a plume of maximized CAPE extending along the low-level jet to the southwest flank of the MCS (the location of which is notated in Fig. 4.11) throughout the evolution of the simulated MCS. Persistent low-level transport of such potentially buoyant parcels into the southwest flank of the MCS, along with the implied low-level lifting associated with low-level WAA maintained the three required ingredients for convection throughout the MCS lifetime (i.e. moisture, instability, and lift).

4.3. Evolution of Precipitation and Thermodynamic Characteristics of the Simulated MCS

In this section we detail characteristics of the life cycle of the MCS that developed within the CNTL simulation. Three major stages of the life cycle of the system are then identified, and the perturbation temperature, pressure, and wind field are analyzed at the surface and on the 1.5 km above ground level (AGL) height surface for each stage of evolution. *Perturbation Fields* (denoted by primes) are hereby defined as the grid point difference between the value of a particular field in the CNTL solution and the value of that field in the NOMP solution at the identical valid time. These (perturbation) fields are defined in such a way so as to highlight the changes to the environment that are exclusively a result of convective processes.

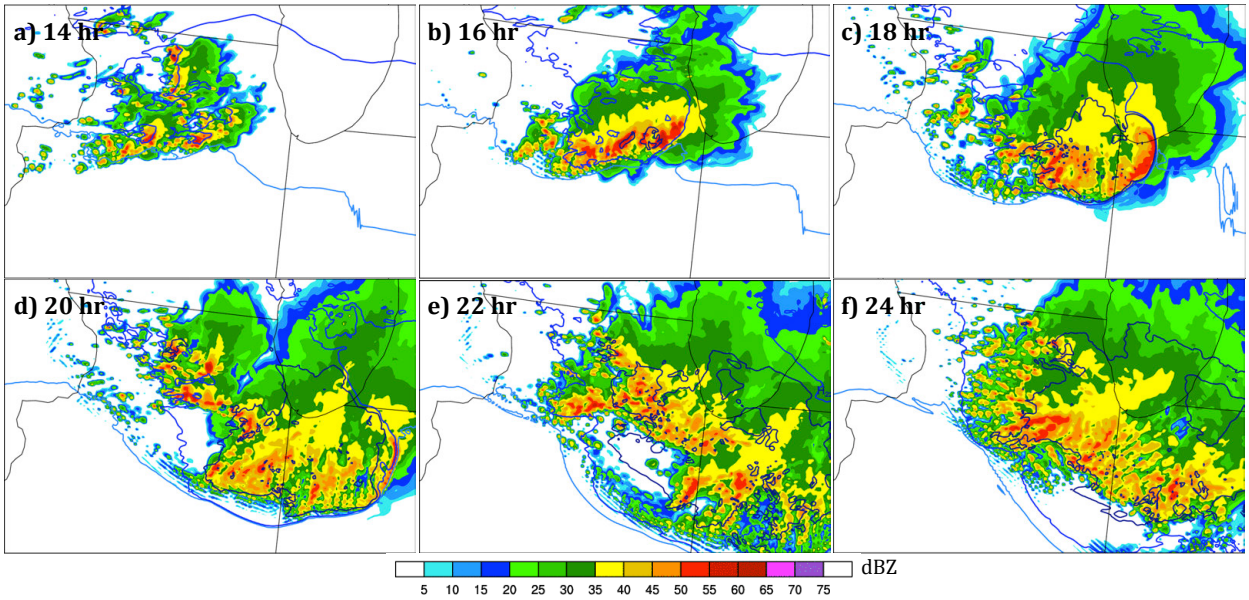

Fig. 4.12. Simulated composite radar reflectivity images from the CNTL run (shading, dBz), and surface temperature contours (dark blue: 21 C; blue: 22 C; light blue: 23 C). Simulation times are shown in the upper left of each panel.

The first deep convective features developed between t_{sim} = 11 and 12 hr on the 1.33 km domain, consisting of an approximately 150 x 150 km region of scattered convective cells along the terminus of the simulated low level jet (not shown). By t_{sim} =15 hr, these cells had intensified and organized upscale into an east-southeastward moving MCS (Fig. 4.12a). By t_{sim} = 19 hr (Fig. 4.12c), new convection had begun to organize upstream (west-northwest) of the initial progressive MCS and north of the OFB left by the initial system; this is an example of ROD. Geographically fixed upstream backbuilding ensued between t_{sim} = 19 hr and 25, with convective echoes training to the ESE of the region of upstream backbuilding toward the rear of the remnants of the initial progressive convective system (Fig. 4.12c,d,e,f).

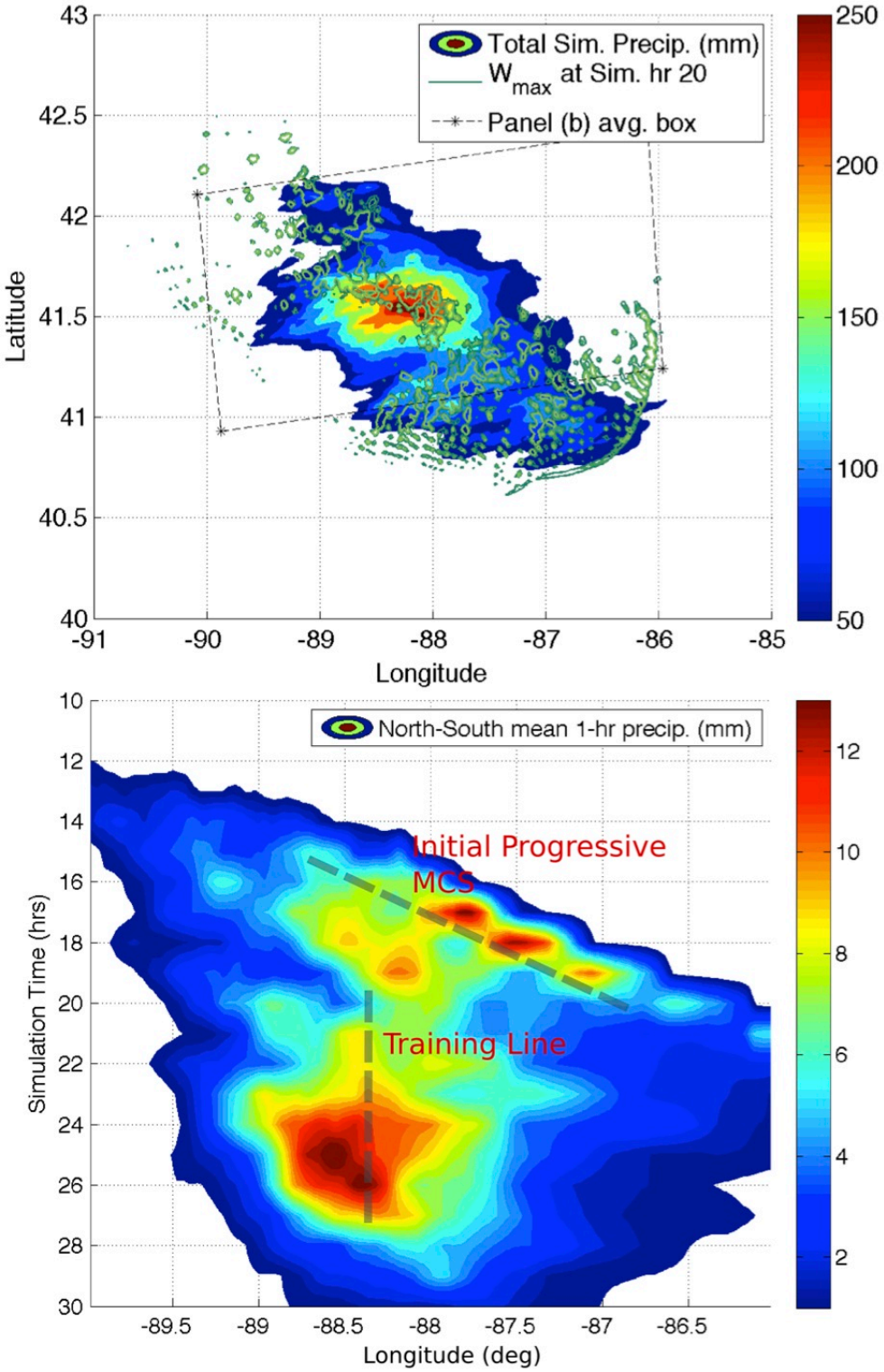

Fig. 4.13. Panel a: total simulation accumulated precipitation for the 1.33 km domain (shading, mm). Maximum column vertical velocities at simulation hour 20 (green contours at 2, 3, and 4 m/s) are included to illustrate the positioning of the training convective line during the lifecycle of the MCS. Panel b: Hovmöller diagram of 1-hour North-to-South grid-point-averaged precipitation accumulation (shading, mm) computed over the box denoted by a dotted black line in panel a.

Convection gradually weakened and moved southward beyond the times shown in Fig. 4.12. Note the visual similarity between the evolutions of the convective system depicted in Fig. 4.12 to the observed cases in Fig. 1, with all three of the observed cases having exhibited similar initial progressive MCS passages and subsequent ROD, training, and geographically fixed upstream backbuilding (though, as shown by PS2014, not all warm season cases exhibited ROD).

Maximum total-simulation-accumulated-precipitation values for the inner domain solution were greater than 250 mm (Fig. 4.13), which is comparable to many observed events that produced flash floods (308 mm from the 7 May 2000 eastern MO event, Schumacher and Johnson 2008; 333 mm from the 28 July 2011 eastern IA event, PS2014). The Hovmöller diagram in Fig. 4.13b summarizes the convective evolution of the simulated MCS, with the initial progressive MCS evident as a diagonal swath of enhanced precipitation between 14 hr and 20 hr (notated in Fig. 4.13b), and the training line evident as a vertically oriented swath of precipitation between 20 hr and 28 hr (also notated in Fig. 4.12b).

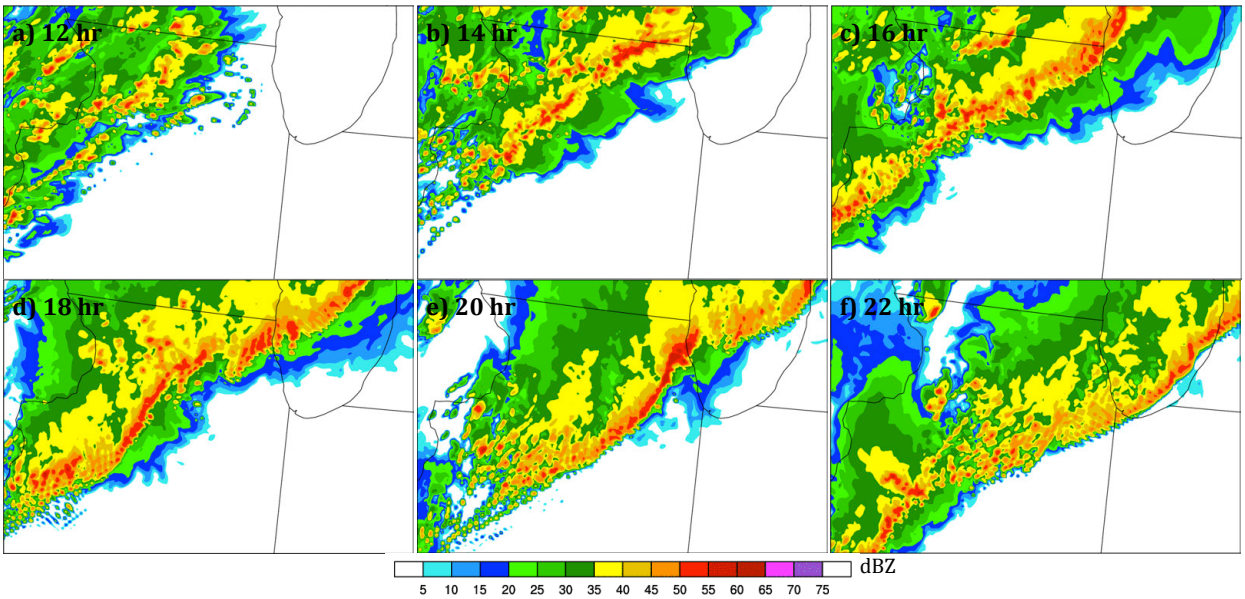

Fig. 4.14. Simulated composite radar reflectivity images from the simulation driven by synoptic-type composite initial and lateral boundary conditions (shading, dBZ, with an otherwise identical model

configuration to the CNTL run). Simulation times for the 4-km domain are shown in the lower right panel of each figure. The peak 1-hour rainfall in the composites occurred at simulation hour 12.

The convective evolution in an analogous simulation driven by synoptic type composites (Fig. 4.14) was markedly different from the warmseason type composite driven simulation (Fig. 4.12). In the synoptic sub-type simulation, an MCS with southeast-to-northwest oriented convective line, and a higher along-line to across-line axis ratio than the warmseason type MCSs, moved in predominantly convective-line parallel direction for over 6 hours, producing a broad swath of rainfall totals in excess of 150 mm. While the results of the synoptic type simulation are not discussed in detail here, it is noteworthy that the primary mechanism for heavy rainfall production in that simulation appears to have been convective-line parallel MCS motion combined with a very long convective line, whereas the warmseason type MCS encompassed a comparatively smaller geographic region, but featured continuous upstream backbuilding – results that are consistent with behavior observed in radar imagery, and deduced from analysis of Corfidi vectors (see Corfidi et al. 1996) in PS2014. We analyze temperature, pressure, and wind perturbation fields associated with the warmseason simulation in the following sub-sectons.

4.3.a. Initial Non-stationary Convection

The first 6 hours (t_{sim} = 12-18 hr) of active simulated convection were characterized by a TS type east-southeastward moving MCS that exhibited similar radar reflectivity characteristics to those identified in various previous studies of forward propagating squall lines (e.g. Parker and Johnson 2000; Coniglio and Stensrud 2001; Mahoney et al. 2009).

Despite the system having developed within an environment characterized by a stable boundary layer (see the vertical CAPE profile in Fig. 4.9), a well-defined surface cold pool (Fig. 4.15a,c) was evident beneath and to the rear of the forward moving MCS, with minimum surface

temperature perturbations of -5 K near the forward convective flank. The southeastern flank of the cold pool progressed eastward between t_{sim} = 16 and 18 hr, (Fig. 4.15a,b) while the southwestern flank remained roughly stationary (the implications of this behavior with respect to MCS motion are further discussed in Corfidi 2003). This is potentially explained by a significant OFB-perpendicular flow component within the cold pool, and along the southeastern flank (evident within the full wind field), contrasted with a comparatively smaller OFB-perpendicular flow component within the cold pool, and along the southwestern flank.

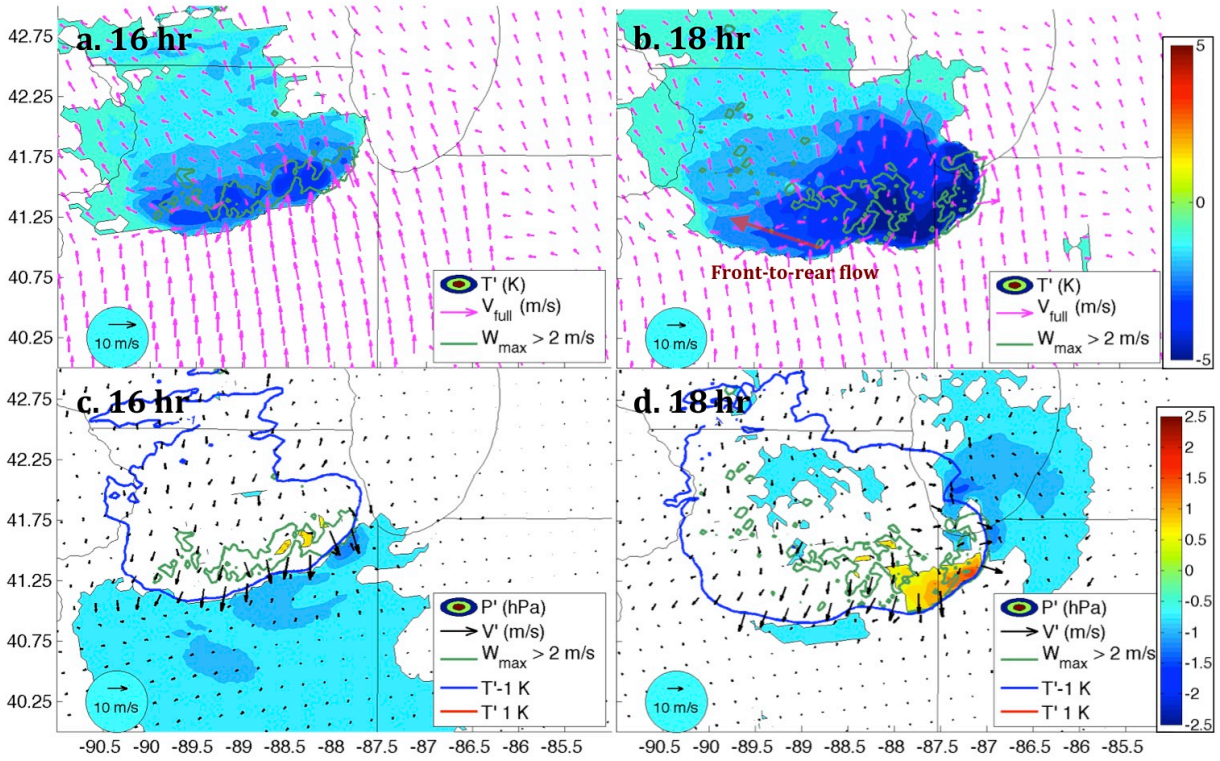

Fig. 4.15. Quantities on the lowest model level at simulation hours 16 and 18. Top panels (a, c): Surface temperature perturbations (T', shading, K [with areas of |T'| < 1 K masked in white]), defined as T_{CNTL}-T_{NOMP}, maximum surface to 300 hPa vertical velocities (green contours at 1, 2, and 3 m/s), and surface wind vectors from the CNTL run (magenta arrows). Bottom panels (b, d): surface pressure perturbations (shading, hPa [with areas of |P'| < .5 hPa masked in white]) defined as P_{CNTL}-P_{NOMP}, maximum surface to 300 hPa vertical velocities (green contours at 1, 2, and 3 m/s), and surface wind perturbation vectors (magenta arrows) defined as V_{CNTL}-V_{NOMP}.

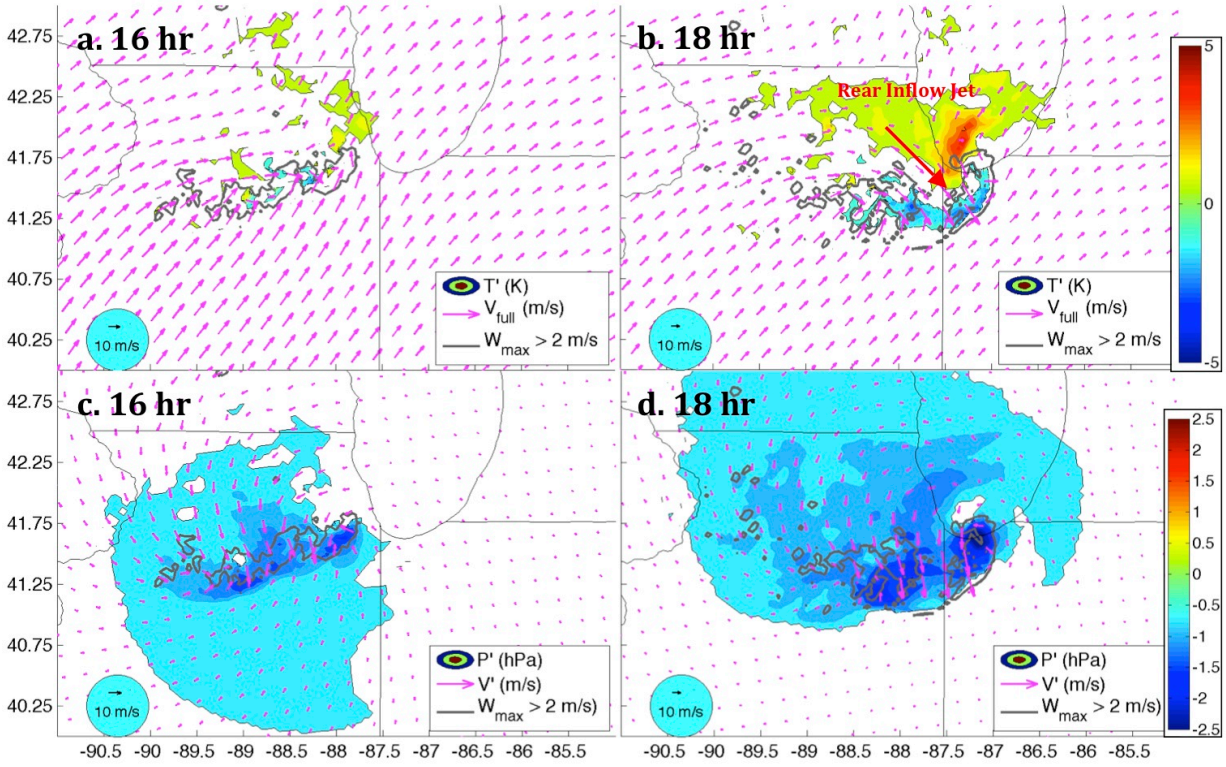

Fig. 4.16. Same as Fig. 4.14, but for 1.5 km AGL.

Again, despite the pre-existing (prior to the cold pool generation) stable boundary layer, the perturbation pressure structure at the surface consisted of locally higher pressure within the cold pool relative to surroundings, and subsequent perturbation flow diverging in all directions from the center of the cold pool (Fig. 4.15c,d). The magnitude of cold-pool meso-high pressure perturbations shown here are small relative to some MCSs that have been documented in previous literature (e.g. Bryan and Parker 2010; Marsham et al. 2011). This is likely a result of the system here producing a comparatively shallow cold pool (see section 4.3.d, where the depth is shown to be generally 750-1000 m).

A rear-inflow-jet structure is developed within the perturbation wind field between t_{sim} = 16-18 hr (Fig. 4.16a,b), with strong northerly-to-northwesterly perturbation flow having developed into the rear of the convective front by t_{sim} = 18 hr. Such rear-to-front accelerations

here were potentially a result of parcel accelerations toward low-pressure anomalies residing along the convective front (evident in Fig. 4.16c,d). It is noteworthy that the ESE movement of the convective system here, combined with the ambient vertical wind profile, resulted in a significant storm-relative southwesterly inflow to the rear of the progressive convective front (Fig. 4.16a,b). This low-level storm-relative flow was essential for the supply of potentially buoyant air into the region upstream of the initial convective system (Fig. 4.11) and facilitated persistent convective re-development here there (this has been documented by previous authors in the context of heavy rain producing MCSs, e.g. Maddox et al. 1979; Chappell 1986; Moore et al. 2003; SJ2005; SJ2008; PS2014).

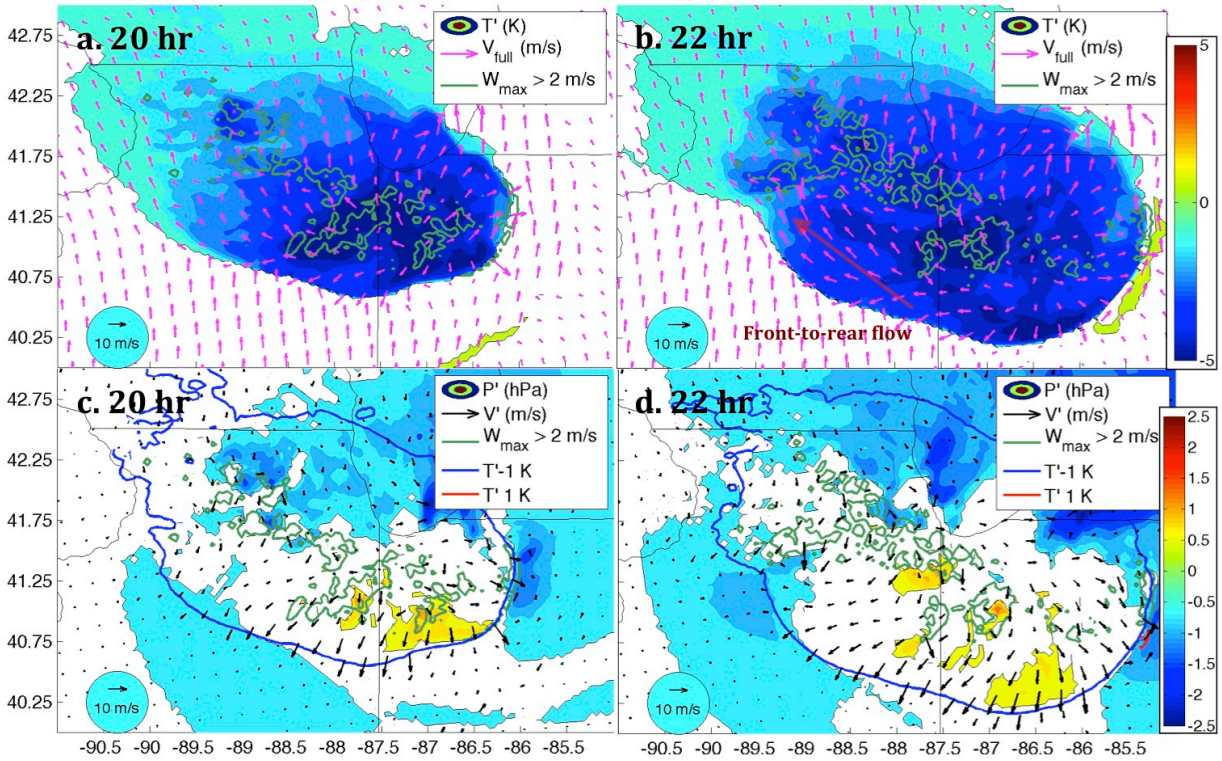

Fig. 4.17. Same as Fig. 4.14, but for simulation hours 20 and 22.

4.3.b. Rearward Off-Boundary Development and Backbuilding

Between t_{sim} = 18 and 20 hr, new convective cells developed to the rear of the progressive MCS and north of the OFB left by this system (ROD). These cells organized into WNW to ESE oriented convective line (evident in Figs. 4.12d,e,f), which became the axis of training convective echoes and the corresponding location of heaviest precipitation production (see Fig. 4.13).

By t_{sim} = 20—22 hr, the southeastern flank of the surface cold pool continued to progress southeastward, whereas the southwestern flank moved very little (Fig. 4.17a,b). This behavior is likely a result of the predominant OFB-parallel flow along the southwestern cold pool flank and predominant OFB-perpendicular flow along the southeastern flank discussed in the previous sub-section, which persisted through the timeframe discussed here.

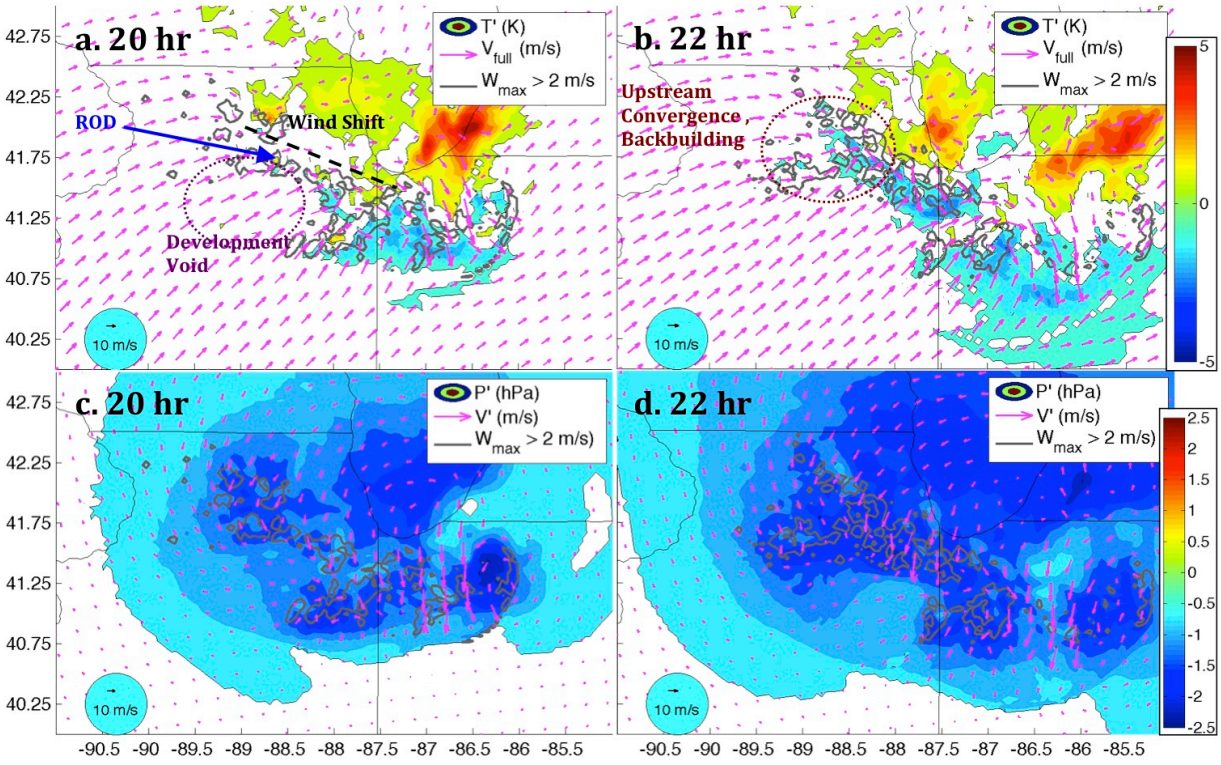

Fig. 4.18. Same as Fig. 4.15, but for simulation hours 20 and 22.

ROD remained significantly north of the southwestern cold pool flank during this timeframe, with a curious "development void" (shown in Fig. 4.18a) where convection was completely absent between the cold pool periphery and the newly training convective echoes (Fig. 4.17a,b). Note also the absence of a significant high-pressure anomaly within the ROD region of the cold pool, where perturbation flow was weak relative to the progressive southeastern flank of the MCS (Fig. 4.16c,d).

At 1.5 km AGL, cold anomalies were restricted to the southeastern progressive convective gust front at t_{sim} = 20 hr (Fig. 4.18a), but a second cold anomaly within the upstream training convective line became apparent by t_{sim} = 22 hr (Fig. 4.18b). The bulk of the cold pool (Fig. 4.17a,b), however, remained below this level during this time frame. A marked horizontal wind shift is apparent at the 1.5 km AGL level along the training convective line, with southwesterly flow to the south of the line, and weaker northwesterly flow to the north of the line (Fig. 4.18, all panels). This flow pattern resulted in convergence into the upstream end of the training convective line, which is especially apparent at t_{sim} = 22 hr (Fig. 4.18b,d). The convective system continued to generate a gradually intensifying regional low-pressure anomaly during this timeframe (Fig. 4.18c,d; presumably a result of latent heating aloft). Locally enhanced low pressure resided within convectively active regions.

4.3.c. Cold Pool Surge and Demise

Geographically fixed upstream backbuilding occurred at the western end of the training convective line between t_{sim} = 20 and 24 hr (see the region denoted in Fig. 4.18b). By t_{sim} = 26 hr convection within the region of echo training surged southeastward and weakened in conjunction with the southwestern periphery of the cold pool having begun to move southward.

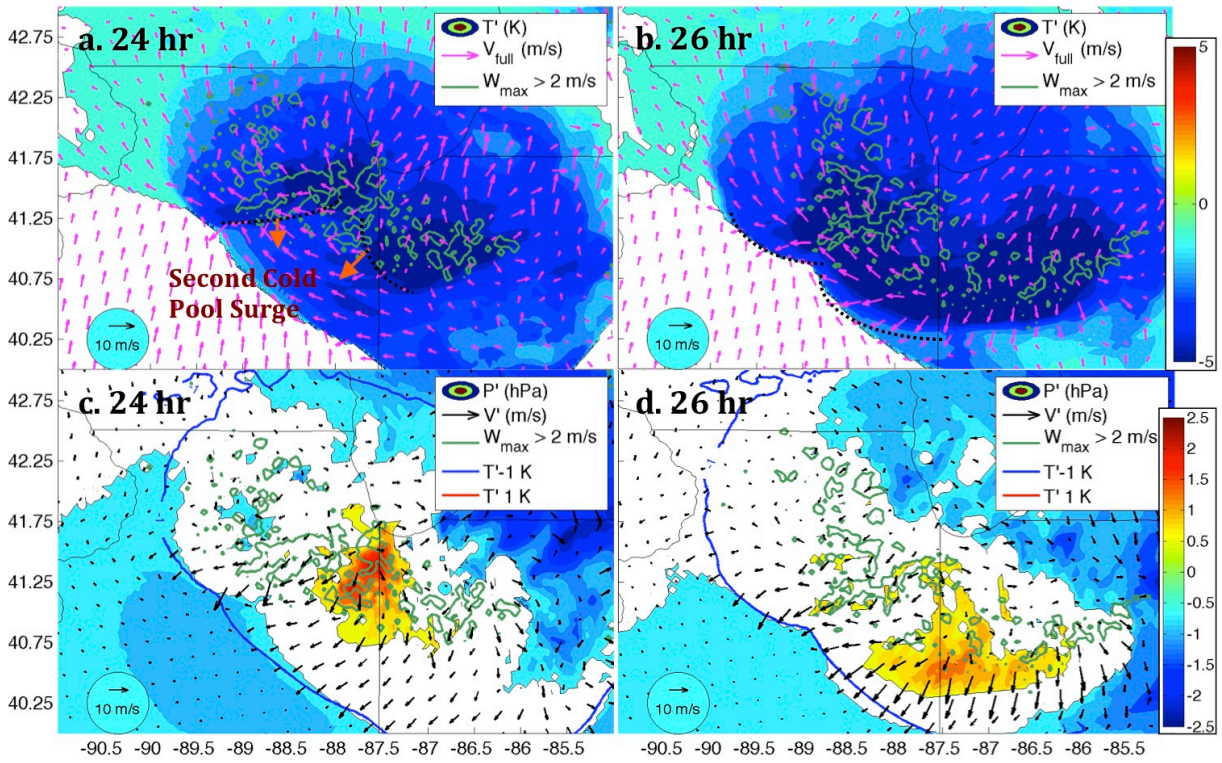

Fig. 4.19. Same as Fig. 4.14, but for simulation hours 24 and 26.

A noticeable OFB perpendicular surface flow component had re-developed along the southwestern cold pool flank by t_{sim} =26 hr (Fig, 4.19b, flow here had been largely OFB parallel here between t_{sim} = 20 and 24 hr, Fig. 4.17a,b, Fig 4.19a). This likely explains why the cold pool surged southward beyond t_{sim} = 26 hr – an event that potentially precipitated the southward movement of the convection out of the region where training and upstream backbuilding were occurring at prior simulation hours (as denoted in the figure). A strong (relative to previous simulation hours) high-pressure anomaly was also evident near the center of the cold pool at t_{sim} = 24 hr (Fig. 4.19c), and had propagated southward by t_{sim} = 26 hr (Fig. 4.19d). There is some indication within the perturbation wind field that increasing pressure within the cold pool relative to surroundings had produced stronger (when compared to previous simulation hours) flow in the direction of the OFB within cold air.

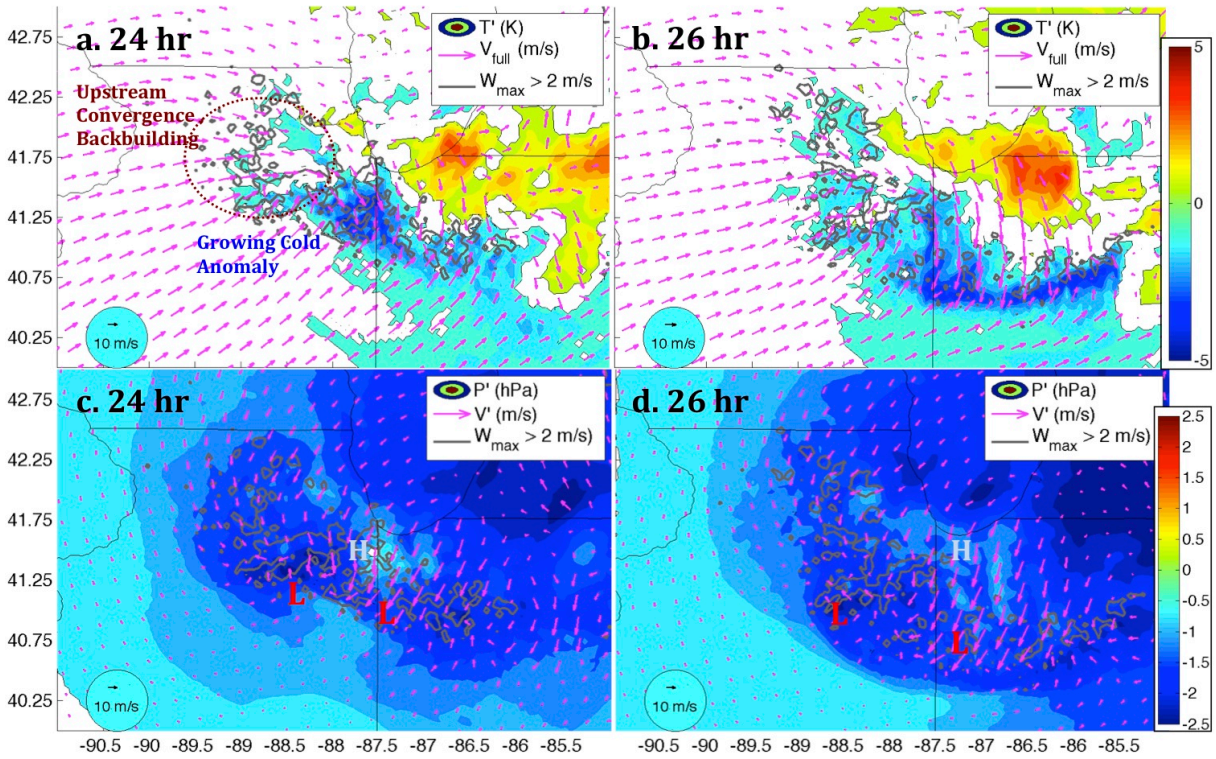

Fig. 4.20. Same as Fig. 4.15, but for simulation hours 24 and 26.

At 1.5 km AGL, pronounced flow convergence remained evident on the upstream flank of the convective system through this time period (Fig. 4.20a), in conjunction with locally minimized pressure within that region (Fig. 4.20c). A more expansive and intense cold anomaly (relative to prior simulation hours) was evident at 1.5 km AGL by 24 hr (Fig. 4.20a) – this anomaly had expanded considerably southward by t_{sim} = 26 hr (Fig. 4.20b). A comparison between regions of cold anomalies at 1.5 km AGL (Fig. 4.20a,b) and surface high pressure anomalies (Fig. 4.19c,d) shows clear correspondence between these features, and suggests that the increasing depth of this anomaly likely played a role in the eventual southward surge of the southwestern cold pool flank (owing to increasing net column integrated negative buoyancy). Strong northerly flow was evident to the north of the eastern part of the convective line (Fig. 4.20a-d), suggestive of a re-developing rear-inflow jet – perhaps as a response to locally higher pressure north of the convective line relative to pressure anomalies along the convective line (as

notated in the figure). This strengthening rear-inflow jet may have also influenced the southward movement of convection during this timeframe.

4.3.d. Cross-Sectional Profiles of Temperature, Winds, and Stability

Convection resided close to the cold pool boundary at t_{sim} = 16 hr (Fig. 4.21a); however, ROD convection at t_{sim} = 24 hr was significantly removed northward from the surface cold pool periphery (Fig. 4.21b). At t_{sim} = 16 hr, the cold-pool-perpendicular vertical shear (Fig. 4.21c, Fig. 22a) was predominantly oriented outward from the cold pool (aside from a shear reversal in the lowest 250 m AGL and relatively weak shear between 500 and 1500 m). In contrast, the cold-pool-perpendicular shear at t_{sim} = 24 hr (Fig. 4.21d, Fig. 4.22b) was significantly weaker (aside from strong shear oriented toward the cold pool in the 0-250 m AGL layer), and exhibited much weaker orientation toward warm air between 250 and 750 m, and slight orientation toward the cold pool between 750 m and 2000 m AGL – in fact, along the side of the averaging box in Fig. 4.18 closest to the cold pool at t_{sim} = 24 hr (Fig. 4.22b), the shear orientation is exclusively toward the cold pool.

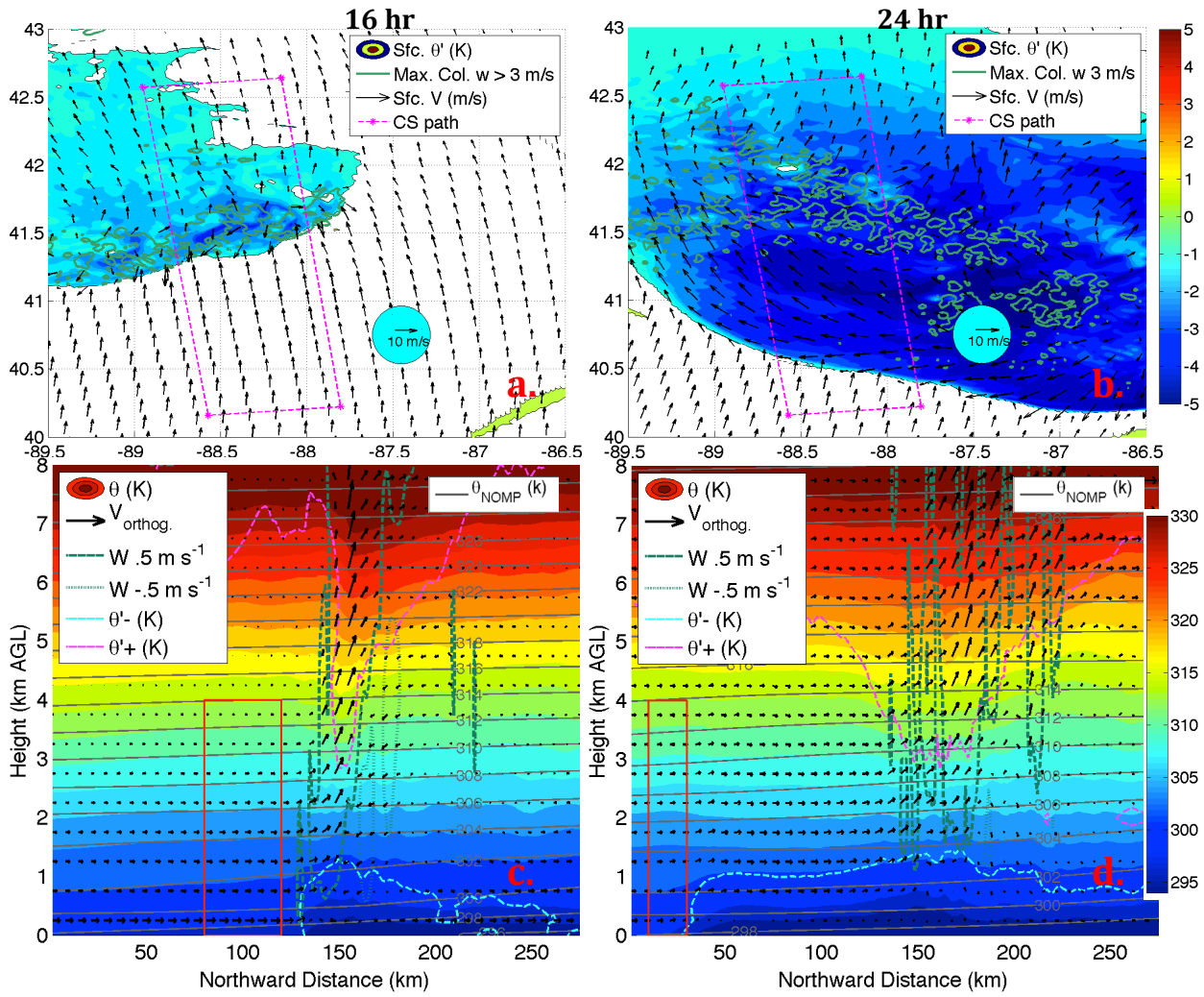

Fig. 4.21. Top panels: Surface θ' (shading, K [with areas of $|\theta'| < 1$ K masked in white]), maximum surface to 300 hPa vertical velocities (green contours at 1, 2, and 3 m/s), and surface wind vectors from the CNTL run (black arrows) for simulation hours 16 (left) and 24 (right). Bottom panels: vertical cross sections (along the dotted magenta boxes in the top panels, with all quantities averaged along the zonal width of the boxes) of θ from the CNTL simulation (shading, K), θ from the NOMP simulation (gray contours, K), θ' from the CNTL simulation (magenta dashed contour at 1 K, with values > 1 K above, and cyan dashed contour at -1 K, with values < -1 K below), OFB-orthogonal wind vectors (defined as $\mathbf{V}_{orthog} = \mathbf{V}_h \cdot \hat{\mathbf{n}} + w\hat{\mathbf{k}}$, where $\mathbf{V}_h$ is the horizontal wind vector, $\hat{\mathbf{n}}$ is a horizontal unit vector orthogonal to the mean orientation of the OFB within the magenta box, w is the full vertical wind, and $\hat{\mathbf{k}}$ is the unit vector in the *z* direction), and vertical velocities (dotted green contours, starting at 1 m/s and at intervals of 1 m/s). Valid times for the bottom panel cross sections are shown at the top of the figure. Red boxes along the bottom of each cross section correspond to the location of vertical profiles shown in Fig. 4.22. Wind speeds may be associated with vector lengths by comparing the lengths of vectors in green boxes to the wind speed profiles shown in Fig. 4.22.

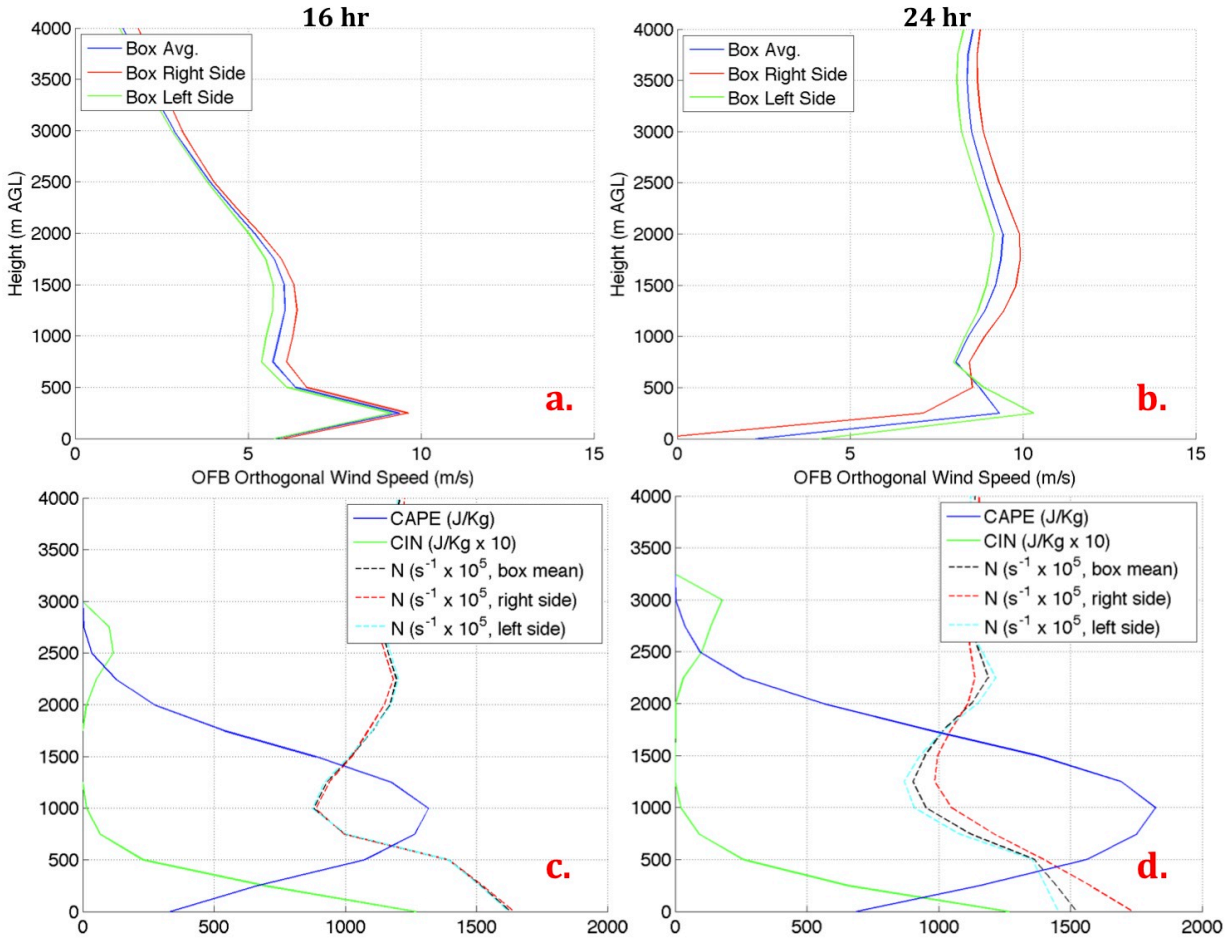

Fig. 4.22. Top panels: vertical profiles of the magnitude of the horizontal component of OFB-orthogonal wind (m/s, as defined in the Fig. 4.21 caption; positive values are toward the cold pool) averaged over the width of the green boxes in the cross sections in Fig. 21 (blue lines), and valid at the left (green) and right (red) sides of the box (with valid times listed on top of the panels). Bottom panels: vertical profiles of box width mean CAPE (blue lines, J/Kg), box width mean CIN (green, J/Kg lines multiplied by 10), box width mean Brunt–Väisälä frequency (black dashed lines, $N = \sqrt{\frac{g}{\theta}\frac{\partial\theta}{\partial z}}$, s^{-1} multipied by 10^5), and Brunt–Väisälä frequency profiles valid along the box left (cyan dotted lines) and box right (red dotted lines) flanks.

Rotunno et al. (1988, hereafter "RKW theory") and Weisman and Rotunno (2004) showed that a low-level wind shear vector over the depth of the cold pool oriented from cold pool air toward warm air is favorable for kinematic lifting along the cold pool boundary (Fig. 4.23a). Specifically when the vorticity tendency owing to the horizontal gradient in buoyancy across this boundary is approximately balanced by the magnitude of the vertical wind shear (i.e., the ratio of the theoretical cold pool speed, *C*, to the vertical wind shear over the depth of the

cold pool, ΔU, is equal to 1). French and Parker (2010) further proposed that for elevated systems with cold pools (such as the case here) the principles of RKW theory extend to the "effective inflow layer," where CAPE is maximized and CIN is minimized (i.e. the shear in a stable boundary layer is less important for kinematic lifting along a cold pool boundary than the shear in an elevated layer with maximum CAPE – see Fig. 4.22b,c.).

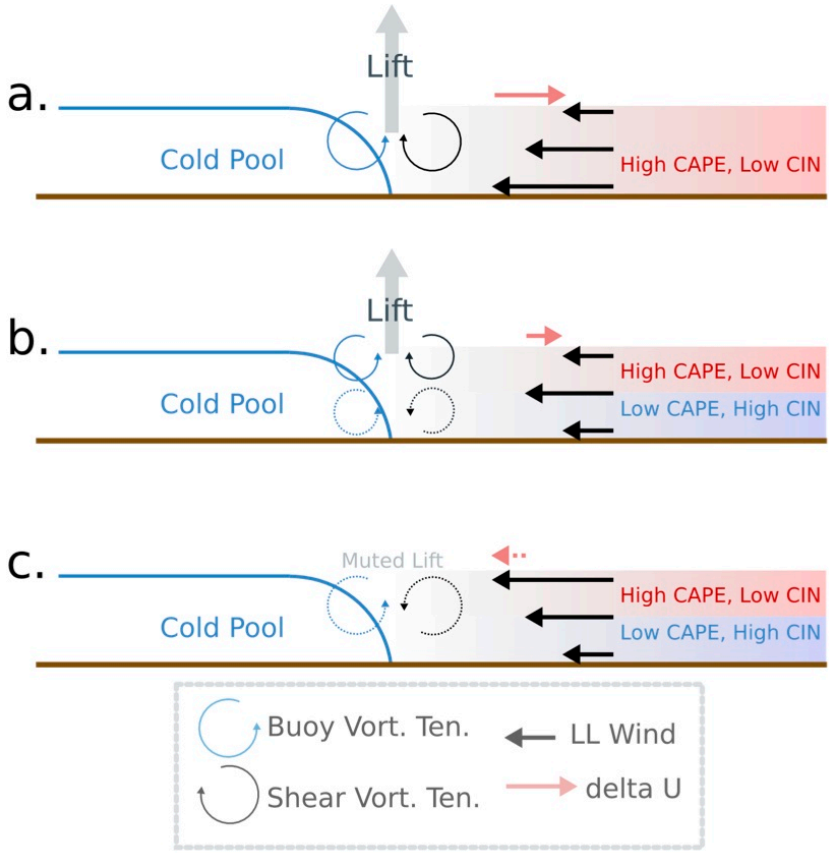

Fig. 4.23. Schematic illustrating the relevance of the concepts of Rotunno et al. (1988) and French and Parker (2010) to the MCS simulated in this study. Red shading indicates the "effective inflow layer," characterized by high CAPE and low CIN, and blue shading indicates a stable boundary layer characterized by low CAPE and high CIN. Red arrows show the orientation and relative magnitude of the vertical wind shear component perpendicular to the cold pool boundary in the effective inflow layer. Black arrows represent the relative magnitudes of low-level wind vectors perpendicular to the cold pool boudary, and circular arrows indicate the sense of vorticity tendency from vertical wind shear (black) and horizontal buoyancy gradients (blue). Panel (a) shows the traditional RKW theory model, where a convective system is surface based, and vertical wind shear through the effective inflow layer is favorably orientated toward warm air from cold air (red arrow). Panel (b) shows the elevated cold-pool-driven situation simulated by French and Parker (2010), in which shear orientation in the elevated effective inflow layer remains favorable for lifting along the cold pool boundary (akin to Fig. 4.21 at 16 hr). Panel (c) is the same as (b), but the wind shear in the effective inflow layer is now unfavorably oriented from warm air to cold air (akin to Fig. 4.21 at 24 hr).

The theories presented by these authors suggest that the shear profile at t_{sim} = 16 hr (Fig. 4.22a,c, compare to Fig. 4.23b) is more favorable for upright kinematic lifting (and thus triggering of convection) along the cold pool boundary than that at t_{sim} = 24 hr (Fig. 4.22b,d, compare to Fig. 4.23c). This is supported by the presence of a shallow .5 m/s vertical jet along the cold pool edge at t_{sim} = 16 hr in Fig. 19 (and generally more vertical motion immediately above this boundary relative to the boundary at 24 hr, Fig. 4.21c), along with the absence of significant lifting along the cold pool boundary at t_{sim} = 24 hr (Fig. 4.21d) (a similar wind shear contrast was identified by Trier et al. 2010 for a simulated upwind propagating MCS). Additionally, the CAPE (static stability) profiles exhibited the greatest (smallest) magnitudes and least convective inhibition above ~ 750 m throughout the simulation (Fig. 4.22c,d) – further implicating this elevated CAPE layer as the primary source of unstable air to the MCS.

It is noteworthy that the low-level temperature perturbations associated with the cold pool are super-imposed upon a gradual isentropic up-slope with northward extent imposed by the large-scale (evident in Figs. 4.22c,d in both the CNTL and NOMP temperature profiles). Any potential enhancement of lifting along the southeastern cold pool flank by large-scale isentropic up-glide has a negligible affect on the interpretation of the role of the boundary in driving the motion of the MCS here, since it is apparent that lifting and isentropic slope are both abruptly enhanced along the boundary (suggesting that upward forcing by the boundary is significantly larger than large-scale upward forcing). Along the southwestern boundary (Fig. 4.22d), isentropic up-glide is minimal near the outflow boundary, and exhibits considerably greater upward slant north of the boundary. Isentropic in the CNTL simulation remained close to their analogies in the NOMP simulation (both slant upward noticeably near the region of deep

convection, and to a lesser extent further south), which suggests that the large-scale may have ultimately regulated where the preferential region of training convection in this region occurred.

4.4. Summary and Discussion

In this research, a 36-hour composite progression of atmospheric fields was used as initial and lateral boundary conditions to a high-resolution quasi-idealized numerical simulation of a quasi-stationary heavy-rain-producing MCS. Composite atmospheric fields were computed from 26 observed heavy-rain-producing MCSs. This strategy added a necessary layer of complexity over fully idealized modeling frameworks, which use horizontally homogeneous initial and lateral boundary conditions and rarely represent the effect of large-scale atmospheric processes (hence the term "quasi-idealized" having been used here), yet the results of our simulation retained generalizability (which is often cited as the advantage to fully idealized modeling frameworks) due to the inclusion of information from multiple observed events in the simulated atmospheric state.

Despite noticeable differences in the evolution of mesoscale and synoptic scale atmospheric fields in the simulated solution relative to the composites used to drive the simulation, a realistic TL/AS MCS initiated and evolved within a simulated environment that was very similar to the environment near the observed MCS locations in the composites.

The evolution of the simulated MCS, and the associated low-level thermodynamic, pressure, and velocity full and perturbation fields are then detailed in terms of three main stages of evolution – (1) *initial progressive MCS*, (2) *rearward off-boundary development and backbuilding*, and (3) *cold pool surge and demise*. During stage (1) an eastward-moving trailing stratiform type MCS developed, generated a robust cold pool, and produced convergent low-

level perturbation flow structures in its wake. Low-level convergence combined with southwesterly potentially buoyant return flow into the wake of the initial system facilitated upstream convective re-development north of the surface cold pool boundary left by the initial system, which characterized the onset of stage 2. Upstream convection then organized into a quasi-linear training line with geographically fixed upstream backbuilding on the western end. Low-level convergence persisted in the region of upstream backbuilding, and we hypothesized that such convergence resulted from low-level perturbation pressure gradients associated with existing convection. Eventually the cold pool deepened and surged southward, resulting in the weakening and slow southward movement of the training-line, which marked evolutionary stage (3) and the demise of the convective system.

Separate analyses of the low-level wind shear orientation relative to the southeastern and southwestern cold pool flanks revealed a predominant vertical wind shear orientation toward the cold pool along the southwestern flank (unfavorable for kinematic lift along the boundary), contrasted with a predominant vertical wind shear orientation away from the cold pool along the southeastern flank (favorable for kinematic lift along the boundary). We hypothesize that these differing wind shear conditions resulted in persistent convection along the southeastern cold pool flank, whereas they allowed low-level flow to override the southwestern cold pool flank. This points to a different mechanism for upstream backbuilding from OFB-lifting (e.g. Parker 2007a in the context of similar parallel stratiform type systems). Fig. 21 provides some evidence that, despite the presence of a cold pool, large-scale environmental lifting ultimately dictates where convection forms (in particular, these results echo those of Trier et al. 2010 in their Fig. 18).

A noteworthy result here is that the features common among observed TL/AS events – training of convection along a quasi-linear axis, rearward off-boundary development, and fixed

upstream backbuilding – were re-produced from an initially smooth (with respect to variability among 10-100 km spatial scales) composite environment broadly characteristic of TL/AS events. Though the MCS-to-storm scale morphology appears to have "emerged" from the upscale growth and organization of convection comprising the MCS of interest (i.e. processes internal to the MCS), the simulation outcome here suggest that the basic dynamics of the upscale emergence of such features are general among TL/AS events. These results support previous evidence of the synoptic regulation of TL/AS systems (e.g. Lorenz 1969; Roebber et al. 2008; Weisman et al. 2008; Peters and Roebber 2014). The regulatory role of the large scale may simply be to provide a region of low-level lift, saturation, and a vertical wind profile characteristic of TL/AS systems.

CHAPTER 5

THE GOVERNING DYNAMICS OF A QUASI-IDEALIZED TL/AS MCS

5.1. Introduction

Mesoscale Convective Systems (MCSs) – specifically those that propagate upwind and involve repetitive motion of individual convective cells over a fixed geographic region – are responsible for a large percentage of warm season extreme rainfall events (Maddox 1979; Doswell et al. 1996; Moore et al. 2003; Schumacher and Johnson 2005, hereinafter SJ2005; Peters and Roebber 2014; Peters and Schumacher 2014, hereinafter PS2014). The typical MCS archetypes associated with these behaviors are known as backbuilding (BB, SJ2005) and training line adjoining stratiform (TL/AS, SJ2005). These types of convective systems exhibit the propensity to remain quasi-stationary, and thereby deliver large amounts of rain to a localized geographic area.

For the purposes of determining why an MCSs may remain quasi-stationary, it is useful to conceptualize the motion of the system as a vector sum of an advective component (usually taken to be the mean wind through a cloud-bearing layer), and a propagation component (i.e. the propensity for new convective cells that constitute the larger MCS to preferentially regenerate in a particular direction) (Corfidi et al. 1996, Corfidi 2003). Whereas the notion of a convective system "blowing with the wind" (advection) is an intuitive concept, the mechanisms for propagation vary significantly among different circumstances, and are understood to a lesser extent (when compared to advection). Previous authors (e.g. Rotunno et al. 1988; Weisman and Rotunno 2004) have shown that robust dynamically forced lifting along the edge of a cold pool (the cold pool edge is hereafter referred to as an outflow boundary, OFB) often serves as a focal point for continuous regeneration of new convective cells (this mechanism for propagation is

hereby referred to as "cold-pool driven"). Following Corfidi (2003), we hereby differentiate *forward propagation*, where the direction of this component is generally downwind (usually a similar direction to advection), from *upwind propagation* (which may sometimes completely cancel advection). The forward propagation of MCSs is frequently cold-pool driven in both surface-based (characterized by the maximum environmental convective available potential energy, CAPE, and minimum environmental convective inhibition, CIN, at ground level) and elevated (characterized by maximum CAPE and minimum CIN above ground level) convective environments (Parker 2008; French and Parker 2010; Trier et al. 2010; Billings and Parker 2012; Keene and Schumacher 2013, hereafter KS2013; Peters and Schumacher 2015a, hereafter PS2015a). In contrast, the upstream flank of upwind propagating MCSs often decouples from, or propagates in the absence of outflow boundaries.

Various factors imposed by meso-α (of order 100-1000 km) to synoptic (of order 1000-2000 km) scale atmospheric circulations (these are referred to as "external factors") play a role in the upstream backbuilding of MCSs. Indeed, Peters and Roebber (2014) showed that a significant portion of the variability in the simulated placement of TL/AS MCSs is explained by uncertainty in analyses of the meso-α to synoptic-scale atmosphere. Specific influencing processes include frontogenetic lift along quasi-stationary frontal boundaries (Maddox et al. 1979; Augustine and Caracena 1994; Moore et al. 2003; SJ2005) and local enhancement of low-level lifting from warm-air advection as a low-level jet (LLJ) encounters isentropic up-slope associated with a frontal zone (e.g. Trier and Parsons 1993; Fritsch and Forbes 2001; Moore et al. 2003, SJ2005; Trier et al. 2014; PS2014). Slow-moving mesoscale convective vortices (MCVs, e.g. Schumacher and Johnson 2009) are another example of an external factor that may

localize warm air advection (for steady conditions, warm air advection equates to isentropic up-glide), and thus serve as a mechanism for persistent low-level lifting.

Processes internal to convection and upscale convective feedbacks have also been implicated in upstream convective backbuilding. In the case of the parallel stratiform (Parker and Johnson 2000; Parker 2007) MCS archetype, intersection points between convective-scale mini-cold pool surges on the upstream end of the convective system re-triggered new convective cells. Schumacher and Johnson (2008) and Schumacher (2009) showed that latent heating associated with a BB type MCS produced a stationary upstream gravity wave – the upward branch of which lifted parcels to their levels of free convection (LFCs) and continuously triggered new convection; Marsham et al. (2010) presented observations of a similarly structured wave. Enhanced upward isentropic slope resulting from the presence of a convective cold pool may also enhance low-level lifting and bring parcels to their LFCs (Trier et al. 2010; KS2013; PS2015a); however, this process often occurs in conjunction with an ambient environmental meso-α scale isentropic slope (i.e. an external factor), and it is unclear whether the slope enhancement resulting from the presence of a cold pool is *necessary* for backbuilding.

Warm-season type TL/AS MCSs (described by PS2014) constitute perhaps the least understood upstream backbuilding scenarios, where forward propagating shear-parallel (we are referring to deep tropospheric shear in this context) convective lines often occur immediately prior to (and sometimes in conjunction with) shear-perpendicular convective lines that exhibit upstream backbuilding (Trier et al. 2010; KS2013; PS2014, PS2015a; Peters and Schumacher 2015b, hereafter PS2015b). For instance, warm season TL/AS MCSs undergo rearward off-boundary development (ROD, PS2014), which occurred twice the case of the 28 Jul 2011 Dubuque, Iowa MCS (studied by PS2015a), and twice in the case of the 4 July 2003 MCS

(studied by KS2013 and Wheatley et al. 2014). This phenomenon is characterized by the simultaneous (i.e. the line develops all at once) development of a convective line upstream (usually to the west) of an eastward moving MCS, and offset (usually north of) from the outflow boundary (OFB) left by the initial system. KS2013 and PS2015a showed that resurgence of elevated high-CAPE air into the region convectively overturned by a forward propagating MCS, and the enhanced isentropic up-slope and baroclinicity associated with the cold pool facilitated ROD.

The goal of the present study is to develop a general dynamical picture for the poorly understood behaviors associated with warm season TL/AS MCSs. We are specifically interested in understanding phenomena such as ROD, fixed upstream backbuilding, and how multiple convective lines with perpendicular orientations to one another occur concurrently, or in immediate temporal succession. To conduct our analysis, we use the numerical modeling framework of PS2015b, where a progression of composite atmospheric was used as the initial and lateral boundary conditions (ICs and LBCs respectively) to a high-resolution convection permitting numerical simulation of a TL/AS system. The organization of this paper is as follows: section 5.2 details the experiment design. Section 5.3 reviews the simulated radar reflectivity characteristics of the simulated MCS. Section 5.4 analyzes external factors, and section 5.5 elucidates upscale convective feedbacks that influenced the convective evolution of the simulated MCS. Section 5.6 summarizes the article findings and discusses the impact of our results on our understanding of TL/AS MCS behavior.

5.2. Experiment Design

PS2015b provides a thorough documentation of the development of a modeling framework for two simulations – abbreviated CNTL, for "*Control,"* and NOMP, for "*No Microphysics"* – both of which will be used in this study. These model configurations used version 3.4.1 of the Advanced Research Weather Research and Forecasting Model (WRF-ARW; Klemp et al. 2007; Skamarock et al. 2008), with composite atmospheric conditions (generated from 26 observed warm season TL/AS cases – see PS2014) used as initial and lateral boundary conditions. Other attributes of the CNTL simulation, including grid dimensions, grid spacing, and physics parameterizations are included in Table 1. The purpose of using composite ICs and LBCs was to retain the horizontally heterogeneous structures on meso-α to synoptic scales that are suspected to influence the evolution of TL/AS MCSs (discussed in section 1); while excluding (by means of the smoothing that results from composite analysis) the meso-β (of O 10-100 km) to meso-γ (of O 1-10 km) noise that is common in case study simulations (such as the effects of convective episodes concurrent with, or prior to the MCS of interest) as well as other complexities such as heterogeneities in the underlying land surface.. The CNTL simulation reproduced many of the salient characteristics of warm-season TL/AS MCSs. PS2015a analyzed the structure of the kinematic and thermodynamic fields of the simulated MCS in detail. In section 3a, we briefly reiterate these characteristics.

The NOMP simulation was run with the microphysics parameterization turned off, and an otherwise identical model configuration to the CNTL. The results of this second simulation allowed the authors to isolate the processes within the CNTL simulation that specifically resulted from latent heating (since no such heating was permitted the NOMP run). As in PS2015b, perturbation fields, denoted by primes, are defined as $F'(x,y,z,t) \equiv F_{CNTL}(x,y,z,t) - F_{NOMP}(x,y,z,t)$,

where F is any arbitrary scalar or vector quantity. F_{NOMP} is assumed to represent "external" atmospheric processes, and F'_{CNTL} upscale convective feedbacks (see PS2015b for an in-depth justification of this definition). The outer domain of the simulation was run for 30 hours, and simulation times are hereby referred to in terms of the time elapsed since the outer domain simulation began.

Table 1. Summary of the WRF-ARW configuration used for the CNTL simulation.

Domain	**Outer Domain**	**Inner Domain**	*Notes*
Grid Spacing	4 km	4/3 km	Inner domain start: i=300,j=300 on outer domain
Domain Dimensions	2712 x 2712 km	1000 x 800 km	
Vertical Sigma Levels	36	""	
Model Top Pressure	100 hPa	""	
ICs and LBCs	NARR composites	""	
Microphysics	Thompson	""	Thompson et al. (2008)
Longwave Radiation	RRTM	""	Miawer et al. (1997)
Shortwave Radiation	Dudhia	""	Dudhia (1989)
Surface Layer	Eta Similarity	""	
Land Surface Model	*none*	*none*	
Boundary Layer Physics	MYJ	""	Janjic (1994)
Cumulus Parameterization	*none*	*none*	

5.3. Precipitation characteristics of the simulated MCSs

An overview of the simulated radar reflectivity evolution of the CNTL simulation is provided (see PS2015b for a more in-depth analysis). Convection began as a grouping of individual convective cells that grew upscale into a southeastward moving trailing stratiform (TS: Houze et al. 1989, Parker and Johnson 2000) type MCS between t_{sim} = 14 and 18 hours (Fig. 5.1a,b) and produced a surface cold pool (this cold pool persisted at the location of the MCS through its lifetime). This initial stage will hereafter be referred to as the "initial forward-propagating convection." The second evolutionary stage (between t_{sim} = 18 and 22 hours was) characterized by ROD (rearward off-boundary development, defined in section 5.1), where a discrete grouping of new convective cells developed in the wake of this initial progressive MCS, and north of the OFB left by the initial system (Fig. 5.1c). Steady backbuilding ensued at the upstream end of this new grouping of convection, with individual cells training from the region

of backbuilding (notated in Fig. 5.1d-e) eastward between t_{sim} = 21 and 25 hours (evident in Fig. 5.1d-f). Convection began propagating southward at t_{sim} = 22 hours, and the MCS gradually moved southward away from the region where training of convection occurred beyond simulation hour 25 (Fig. 5.1f).

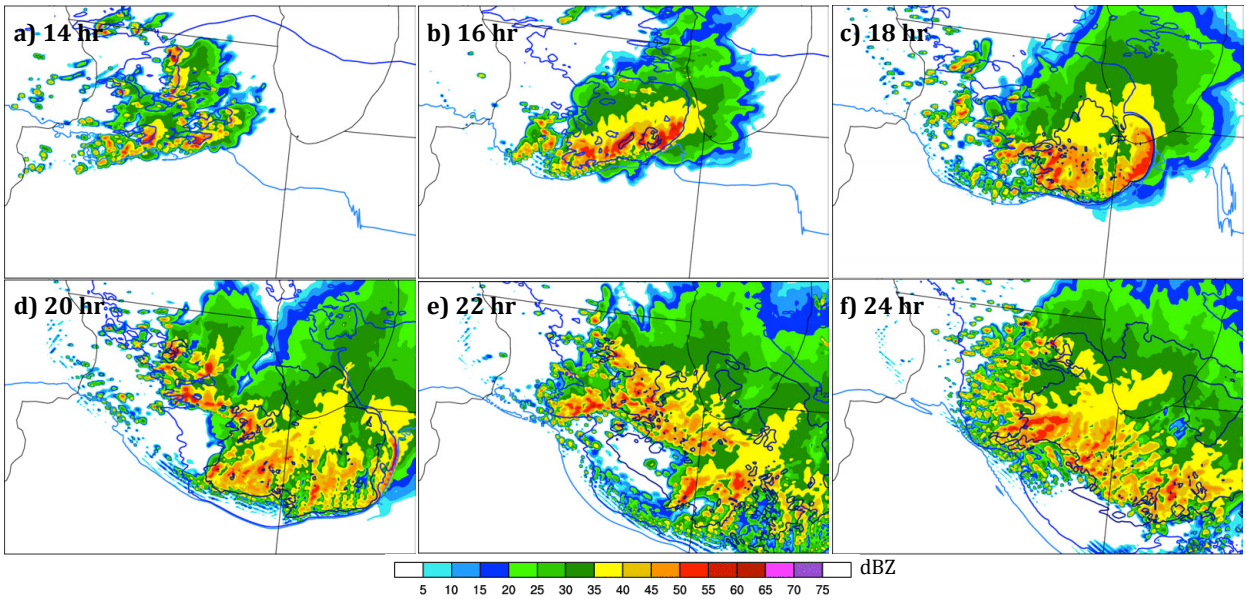

Fig. 5.1. Simulated composite radar reflectivity images from the CNTL run (shading, dBz), and surface temperature contours (dark blue: 21 C; blue: 22 C; light blue: 23 C) at t_{sim} = (a) 14, (b) 16, (c) 18, (d) 20, (e) 22, and (f) 24 hr . In this and subsequent figures, the geographic boundaries are shown only to give a sense of scale; the simulation has a homogeneous land surface (PS2015b).

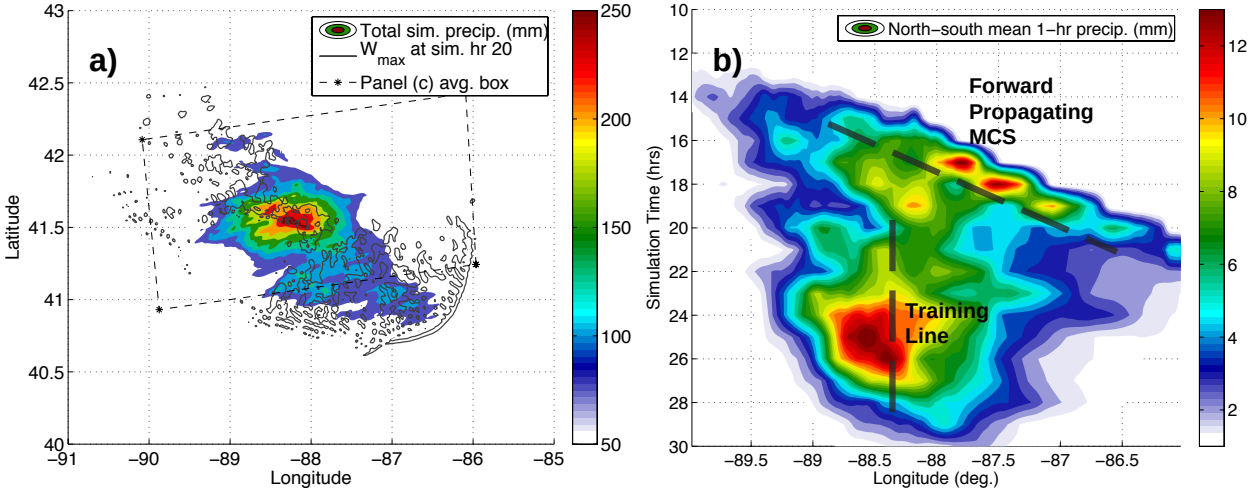

Fig. 5.2. Panel a: total simulation accumulated precipitation from the CNTL simulation (shading, mm), and maximum column vertical velocities (2 m s^{-1}, dark gray contour; included to illustrate the positioning of the training convective line). Panel b: Hovmöller diagram of 1-hour North-to-South grid-point-averaged precipitation accumulation (shading, mm) computed over the box denoted by a dotted black line in panel a. Adapted from PS2015b.

The MCS produced a swath precipitation totals greater than 200 mm that was collocated with the approximate axis of the training line, with maximum point totals near 250 mm (Fig. 5.2a). The quasi-stationary nature of the training line is evident in a Hovmoller diagram (Fig. 5.2b) as a longitudinally stationary precipitation maxima between t_{sim}=20-28 hrs.

5.4. External Factors Influencing Convective Evolution

Low-level warm air advection was locally maximized near the western flank of the MCS between t_{sim} = 12 and 21 hr in the NOMP simulation (Fig. 5.3a-d). A nearly identical pattern of WAA was present in the CNTL simulation to the southwest of the MCS region (not shown; the pattern was disrupted where convective overturning occurred). A broad plume of maximized most unstable CAPE (MUCAPE) was also persistently supplied to the MCS location, and the flow approaching the MCS within the LLJ was saturated with respect to water vapor throughout the lifetime of the MCS (Fig. 5.4a-d). The prolonged presence of all three ingredients for convection – moisture, CAPE, and lift – at a fixed geographic location satisfied the minimum requirements for sustained convection.

We introduce here an ingredients-based propagation index (*IPI*) parameter:

$$IPI_{SYNOP} \equiv \frac{1}{N_{IPI}} \underbrace{\mathbf{V}_H(x,y,z)\cdot\nabla\theta(x,y,z)}_{\text{from NOMP}} \underbrace{CAPE(x,y,z)}_{\text{from CNTL}}, \text{ and} \tag{5.1}$$

$$N_{IPI} \equiv \underbrace{\max_H\left(\mathbf{V}_H\cdot\nabla\theta\right)}_{\text{from NOMP}} \underbrace{\max(CAPE)}_{\text{from CNTL}}, \tag{5.2}$$

where N_{IPI} is a normalization factor, $\mathbf{V}_H(x,y,z)\cdot\nabla\theta(x,y,z)$ is horizontal temperature advection from the *NOMP* simulation, CAPE is assessed for parcels lifted at every grid point within the *CNTL* simulation, '$\max_H$' denotes the maximum horizontal value of a quantity as a function of

height at a given time, and 'max' denotes the maximum domain value of a quantity at a given time. IPI_{SYNOP} is set to zero for points with $|CIN| > 10\ J\ Kg^{-1}$ and relative humidity (RH) < 100 %, and set to zero where equation (1) yields a negative value.

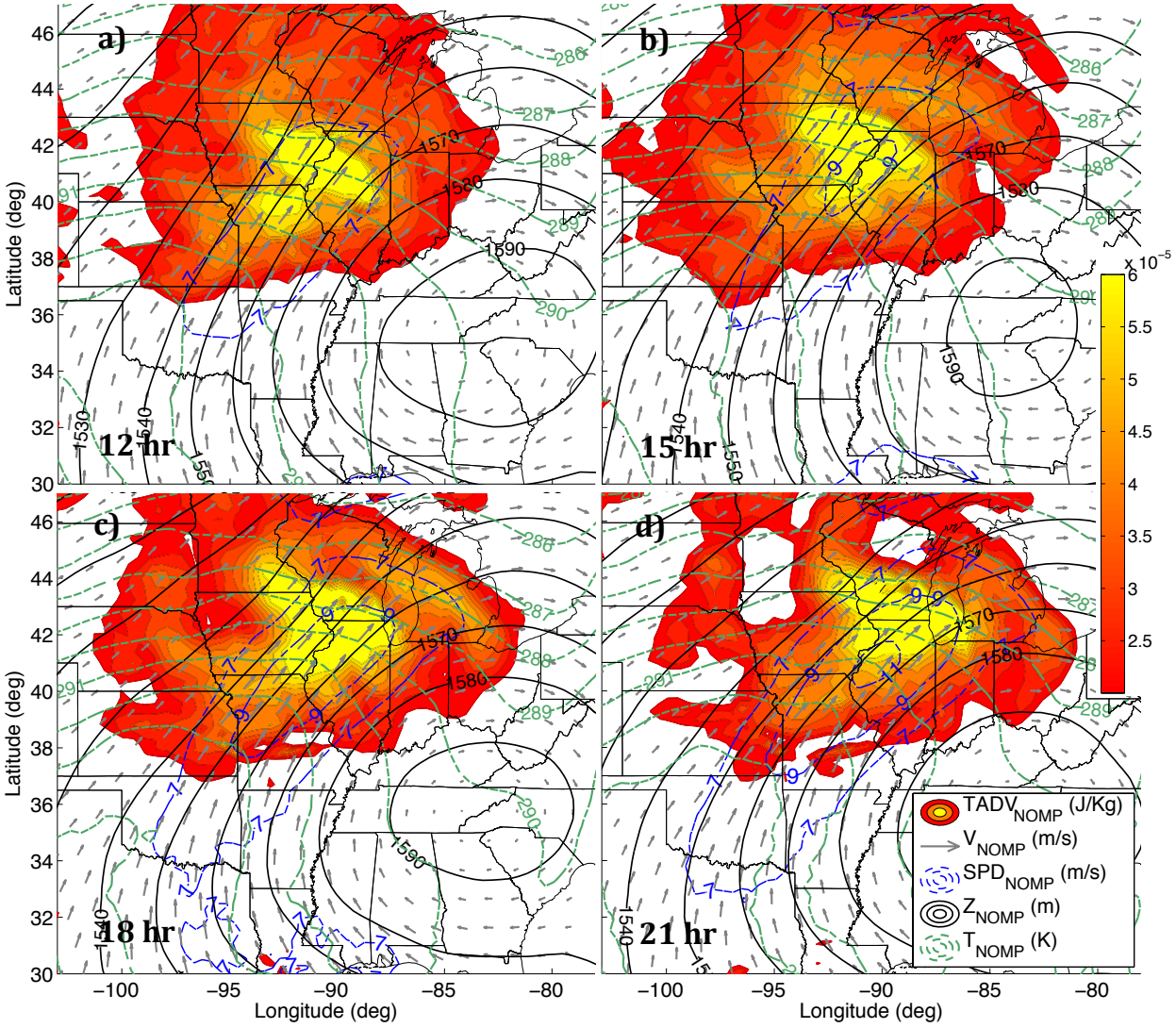

Fig. 5.3. 850 hPa warm air advection (WAA, shading, K s^{-1}), wind vectors (gray arrows, m/s), wind speed (blue dashed contours, m/s), geopotential height (black contours, m), and temperature (green dashed contours, K) from the NOMP outer domain solution. Simulation times are listed in the lower-left corners.

We normalize horizontal temperature advection on every vertical level by the maximum domain value on that level, since the value of this quantity ranges considerably in the vertical direction, and CAPE by the maximum domain value at any level. This normalization results in a parameter range between 0 and 1. The purpose of this quantity is to identify regions where parcels are

near/at their levels of free convection (as determined by the *CIN* and *RH* restrictions), and are likely undergoing ascent (as determined by the inclusion of temperature advection) driven by large-scale atmospheric processes (this is the reason for including temperature advection from the NOMP simulation only). In these regions, the overlap between the three necessary ingredients of convection, and the subsequent probability of new convective initiation, is maximized. Examples of where this parameter is locally maximized are regions of where flow with nonzero CAPE crosses strong horizontal temperature gradients, such as the intersection region between a moist low-level jet and a synoptic front.

A maximum in IPI_{SYNOP} fixed on western side of the MCS between t_{sim} = 16 hr and 22 hr (Fig. 5.5a-d), which corroborates that processes external to the MCS drove the westward propagation of the system. Mean 1-10 km winds (a reasonable estimate for advection of convective cells) were oriented toward the east-northeast, and a general cancellation between this advection direction and westward propagation was likely responsible for the quasi-stationary nature of the convective system during the t_{sim} = 16 hr and 22 hr timeframe. IPI_{SYNOP} values decreased considerably between t_{sim} = 24 hr and 26 as a response to a separation of the strongest CAPE (Fig. 5.6a-b; which remained on the western side of the system) from the strongest low-level WAA (Fig. .56c-d; which moved to the northeast of the convective system). This suggests that externally driven propagation weakened beyond t_{sim}=24 hr, and that another process was responsible for propagation late in the system's lifetime.

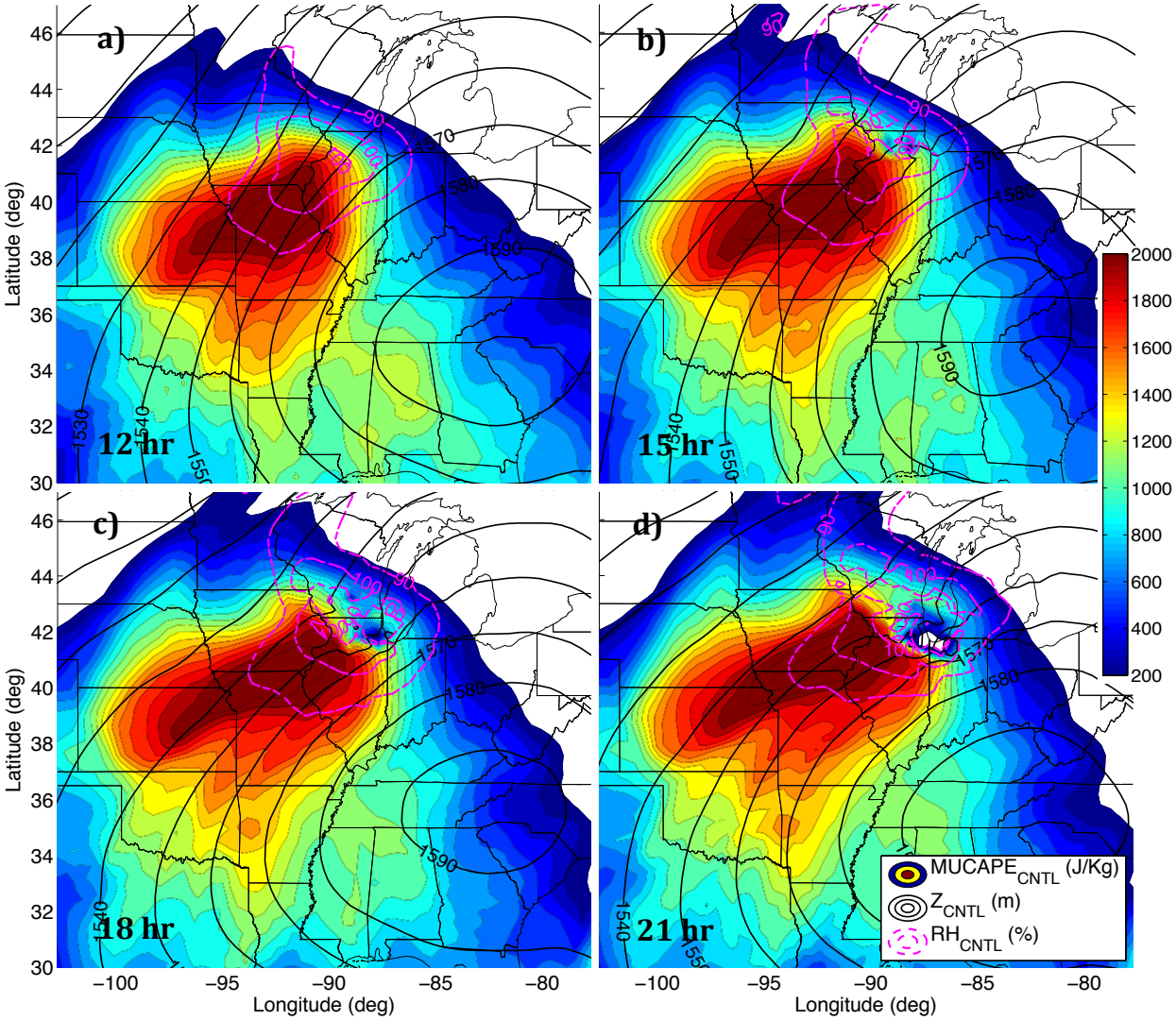

Fig. 5.4. Most unstable CAPE (shading, J/Kg), 850 hPa geopotential height (black contours, m), and 850 hPa relative humidity (magenta dashed contours, %) from the CNTL outer domain solution. Simulation times are listed in the lower-right corners.

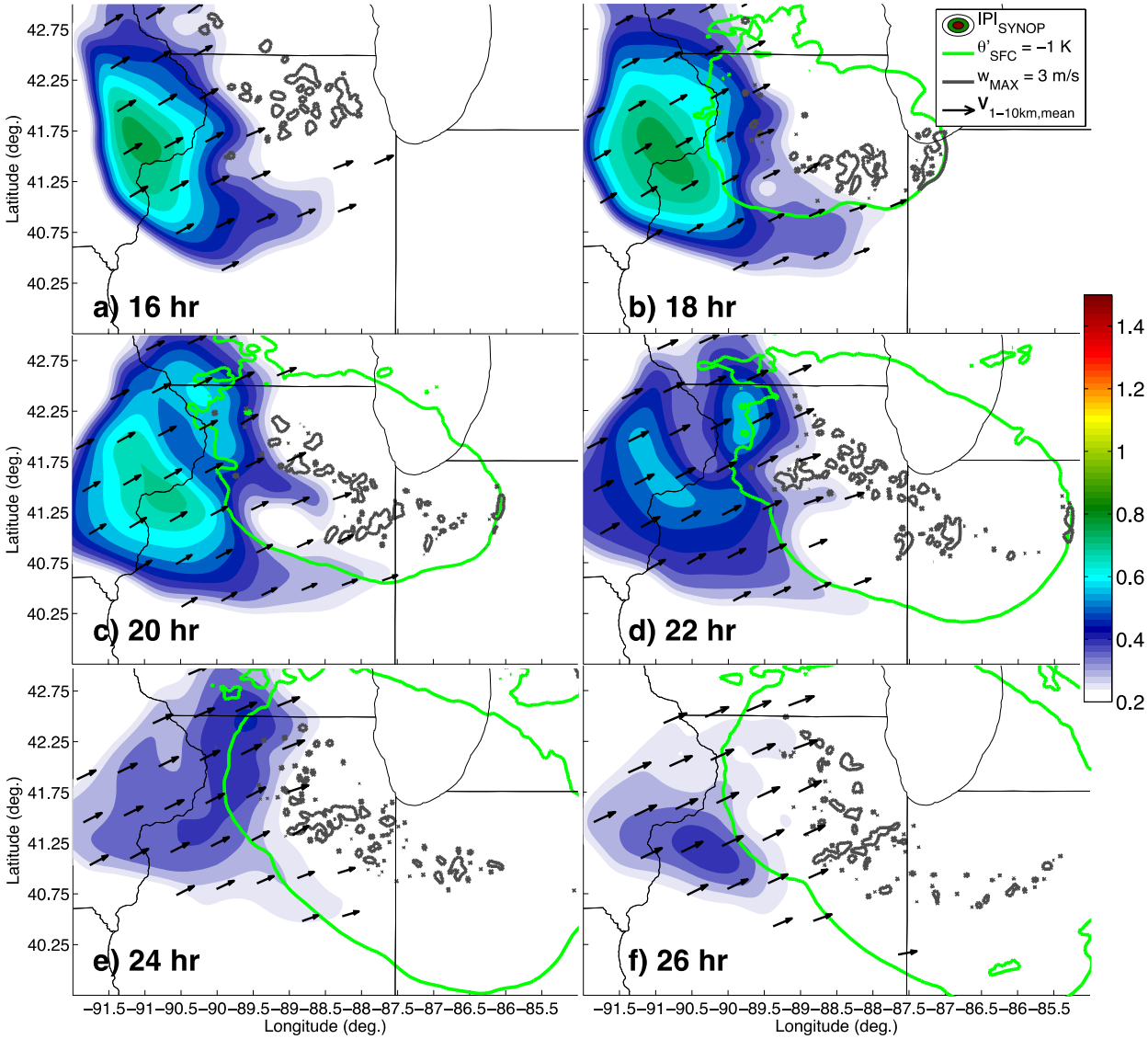

Fig. 5.5. All panels: Maximum column IPI_{SYNOP} (shading), maximum column vertical velocity > 3 m s^{-1} (gray contours), the -1 K surface θ' contour (green line), and the direction of the 1-10 km mean wind (black arrows) at t_{sim} = (a) 16 h, (b) 18 h, (c) 20 h, (d) 22, (e) 24, and (d) 26 h.

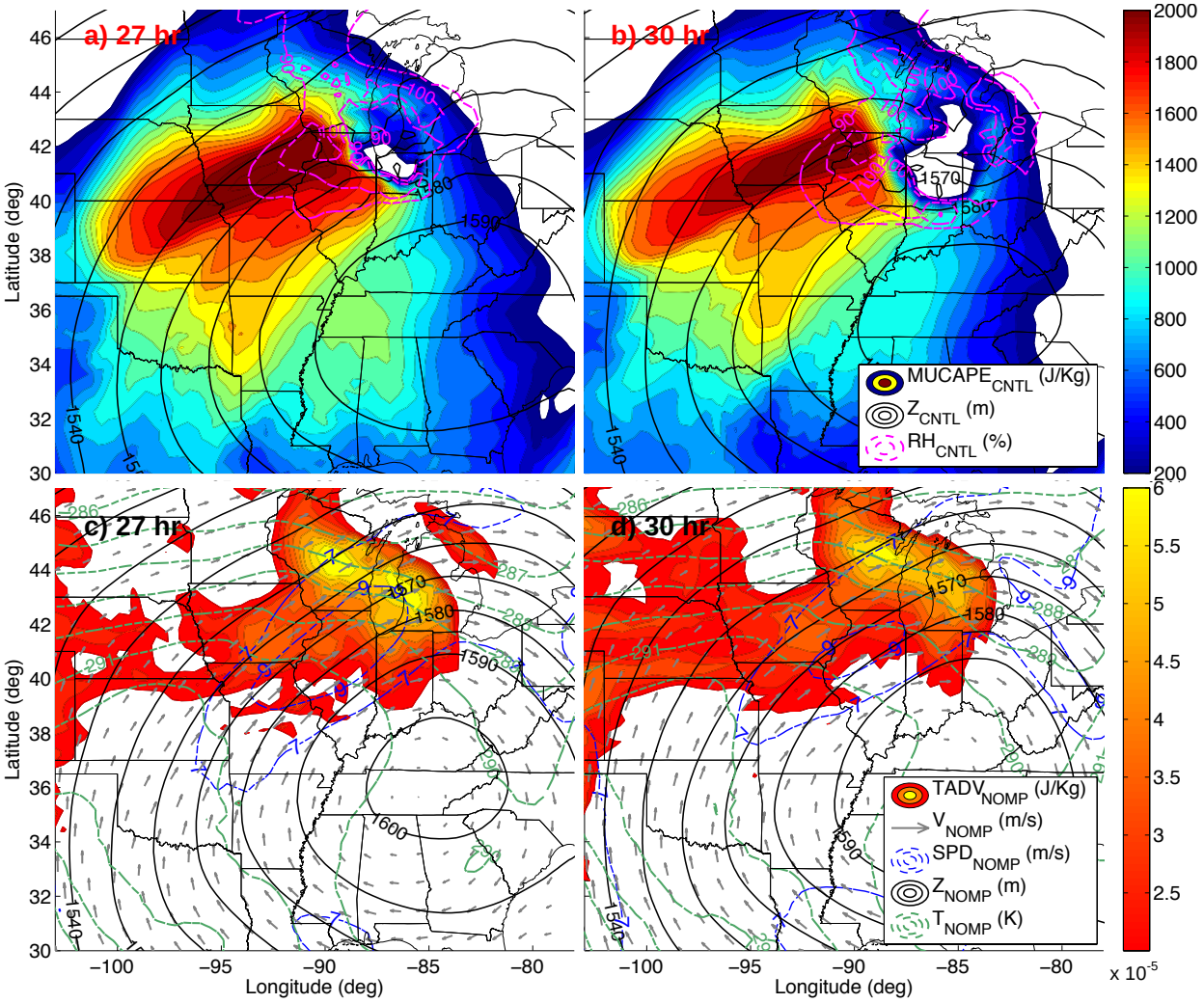

Fig. 5.6. Top panels: same as Fig. 5.4, but for t_{sim} = 27 hr (panel a) and t_{sim} = 29 hr (panel b). Bottom panels: same as Fig. 5.3, but for t_{sim} = 27 hr (panel c) and t_{sim} = 29 hr (panel d).

5.5. Upscale Convective Feedbacks Influencing Convective Evolution

5.5.a. Initial forward-propagating convection

The initial forward-propagating convection closely followed the movement of the southeastern flank of the OFB produced by initial convection (Fig. 5.7a; this cross section path is hereby referred to as path *a*). The cold pool edge was vertically oriented here at a depth of 1 km, and produced robust vertical lifting greater than 1 m/s between .5 and 1.5 km AGL (Fig. 5.7b). Despite the maximum in CAPE outside the OFB residing at 1 km AGL (e.g. the system was elevated), a 1 m/s vertical jet along the OFB served as a triggering mechanism for deep

convective updrafts (which encompass a region between 5 and 40 km behind the OFB, above ~ 2 km AGL, Fig. 5.7b; compare to Trier et. al 2010, Fig. 18, French and Parker 2010 Fig 6, and Billings and Parker 2012 Fig. 14b, where similar outflow-driven motion of elevated forward-propagating MCSs was demonstrated).

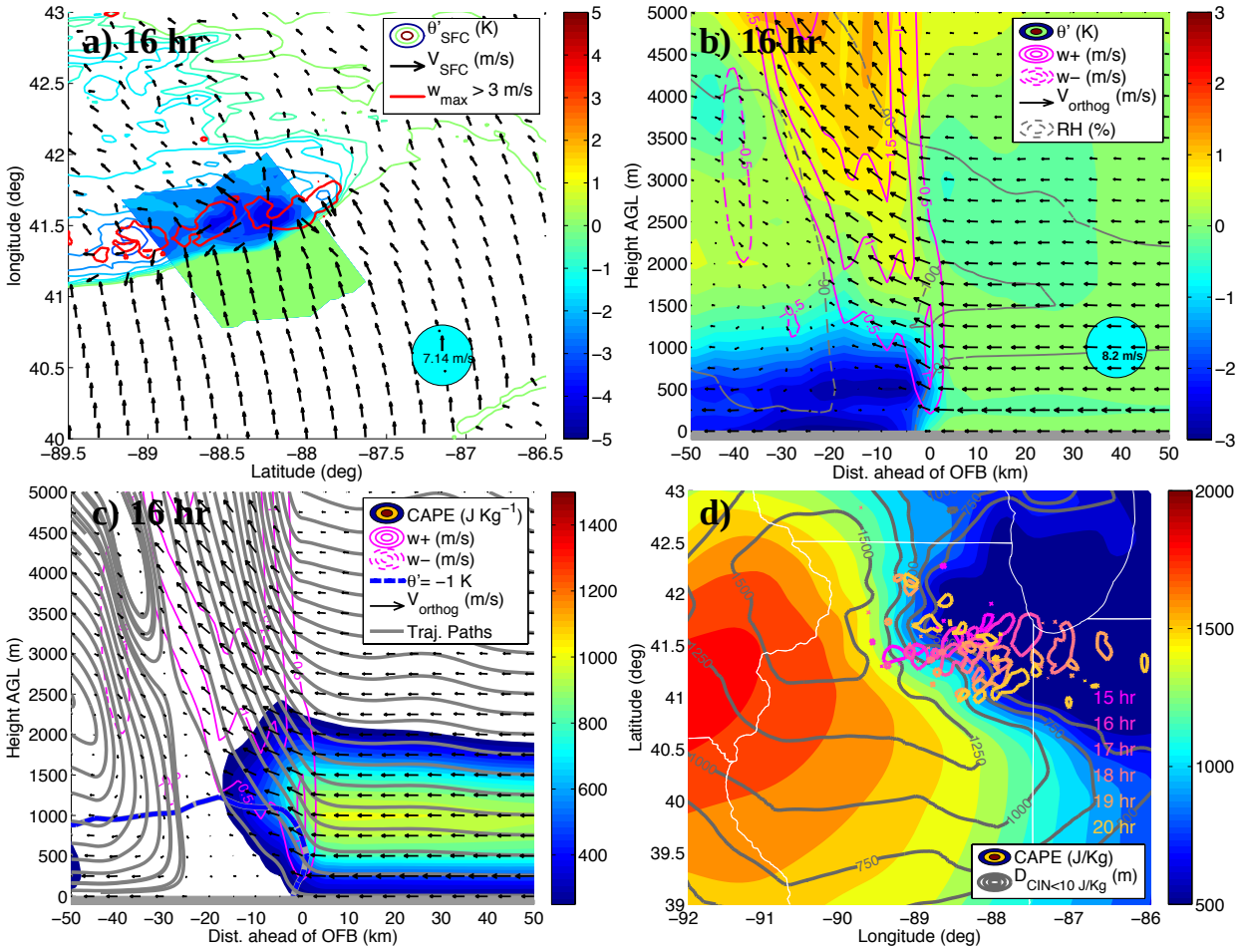

Fig. 5.7. Panel a: Surface θ' (K, color contours; cross section path for panels b-c color shaded), surface wind vectors (black arrows, m/s), and maximum column vertical velocity > 3 m/s (red contours). Panel b: cross section of θ' (shading, K), outflow-boundary orthogonal wind vectors (black arrows, m/s), vertical velocity (positive: magenta solid contours; negative: magenta dashed contours), and relative humidity (gray dashed contours, %). Panel c: CAPE (shading, J/Kg), vertical velocity (as in panel b), cross section perpendicular winds (as in panel b), the -1 K θ' contour (blue dashed line), and streamlines (gray lines). Panel c: most unstable CAPE (shading, J/Kg), the depth of CIN < 10 J/Kg (gray contours, m), and maximum column vertical velocity > 3 m/s contours for simulation times 15-20 hr (magenta through tan contours).

It is also noteworthy that the orientation of outflow-boundary perpendicular flow between .25 km and 1.75 km (this was the layer of non-negligible CAPE) featured a generally decreasing OFB-

perpendicular wind speed with height (Fig. 5.8) through the effective inflow layer (EIL, e.g. French and Parker 2010), which we loosely define it as the layer of > 1000 J/Kg of CAPE. This condition is favorable for initiating convection along the boundary (Rotunno et al. 1988; Weisman and Rotunno 2003; French and Parker 2010), and usually results in cold-pool driven MCS propagation. Southeastward moving convection along the southeast cold pool flank weakened considerably between t_{sim}=17 hr and 21 hr (evident in Fig. 5.1b-d), and gradually receded behind the OFB. This weakening likely resulted from the southeastern OFB driving the eastern flank of the MCS away from the region of maximum most unstable CAPE (MUCAPE) and minimum CIN (Fig. 5.7d).

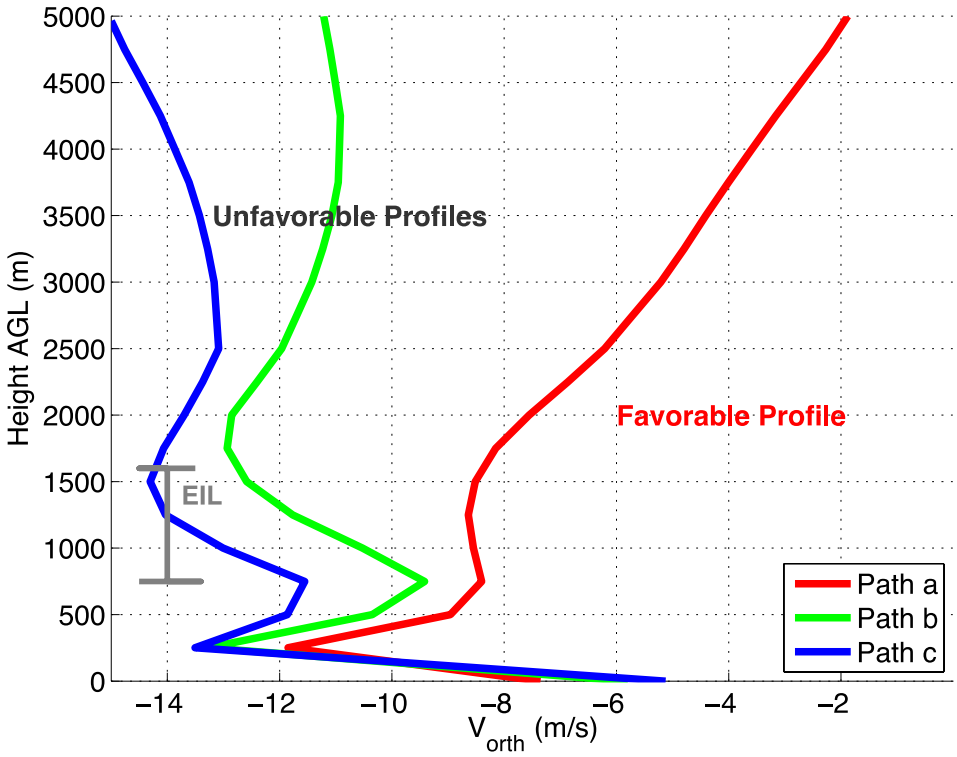

Fig. 5.8. Comparison of the OFB orthogonal wind profiles 20 km ahead of the OFB (outside the cold pool) for cross section path *a* (red line, Fig. 5.5a), path *b* (green line, Fig. 10a), and path *c* (blue line, Fig. 5.10b). OFBs in favorable (unfavorable) profiles are likely (less likely) to initiate convection.

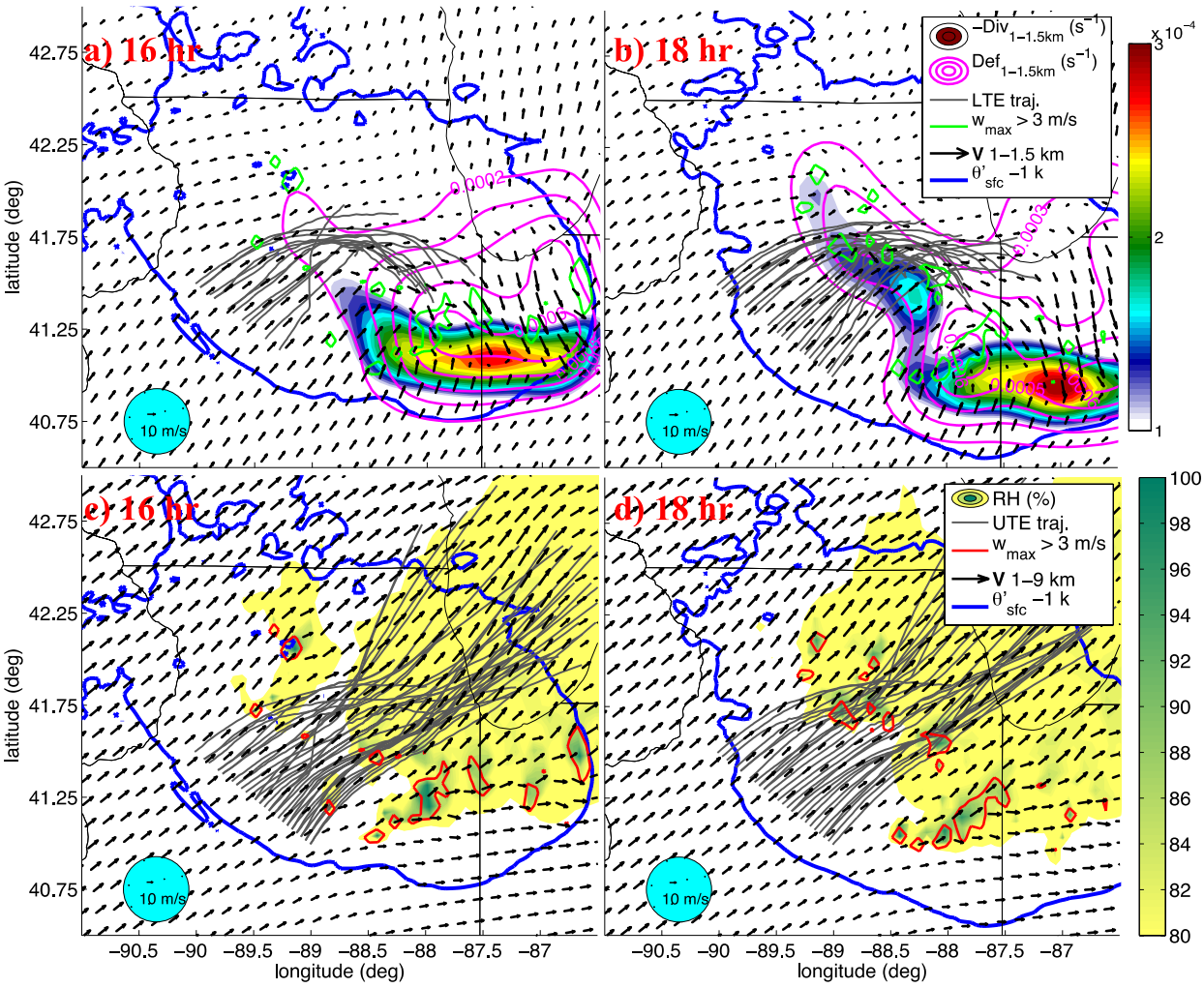

Fig. 5.9. Top panels: 1-1.5 mean convergence (shading, s^{-1}), deformation (magenta contours, s^{-1}), the horizontal path of LTE trajectories released at the time in the upper left corner (gray lines), maximum column vertical velocities > 3 m/s (green contours; panel a: 17 hr; panel b: 19 hr), 1.5 km AGL wind vectors (black arrows, m/s), and the -1 K surface θ' contour (blue line, K). Bottom panels: 9 km AGL relative humidity (shading, %), maximum column vertical velocities > 3 m/s (as in top panels, but green contours), the -1 K surface θ' contour (as in top panels), 1-9 km mean wind vectors (black arrows, m/s) UTE trajectories (gray lines) released at t_{sim}= (a, c) 16 and (b, d) 18 hr.

5.5.b. The influence of the initial forward-propagating convection on subsequent rounds of convective activity

As discussed by PS2015b, the passage of the initial forward-propagating convective system was accompanied by a shift in the low-level wind field from southwesterly (prior to the MCS passage) to northwesterly within the region immediately affected by the MCS (Fig. 5.9a,b). This resulted in a northwest-to-southeast aligned convergence and deformation zone that

coincided with the axis of training of convection (Fig. 5.9a,b). Forward trajectories were initialized at t_{sim}=17 and 18 hr to the southwest of this low-level deformation and convergence zone (within the LLJ inflow region to the training line) at heights of 1 and 1.5 km AGL (within, and just above the layer of maximum CAPE), and were tracked for 3 hours. We then separated them (trajectories) into two populations in order to distinguish paths that ascended through deep tropospheric updrafts from paths that remained in the lower troposphere: upper-tropospheric-ending (UTE) trajectories exceeded 5 km in height at least one point along their path (all of these trajectories also ended above 5 km), and lower-tropospheric-ending (LTE) trajectories did not exceed 5 km in height at any point along their path. LTE trajectories initially traveled toward the northeast along the LLJ and entered the region of convergence and deformation. They then turned sharply toward the southeast and traveled southeastward along the convergence and deformation zone for the remainder of their paths. UTE trajectories began with northeastward movement identical to LTE trajectories; however, upon entering the region of convergence and deformation, UTE trajectories quickly ascended into the upper troposphere through convective updrafts and exited the MCS to the northeast. This air parcel behavior potentially explains the quasi-linear organization of convective cells within the training convective line, where parcels with high CAPE were either quickly transported away from low-levels by convective updrafts, or traveled southeastward, parallel to the training convective line and region of convergence and deformation. The low-level flow pattern did not allow trajectories to travel northeastward of the convective line at low-levels and invigorate additional convection to the northeast of where training was occurring (if this occurred, it would have disrupted the along-convective-line symmetry). The behavior of upper-level trajectories also explains the adjoining stratiform morphology of the convective line, in that upper level trajectories exiting the MCS to the

northeast transported high relative humidity (RH) air (and presumably hydrometeors) aloft in this direction (Fig. 5.9c,d).

In order to connect distinct physical processes to the changes to the low-level wind field shown in Fig. 9a-b, we temporally integrated the right-hand side (RHS) of prognostic equations (see PS2015a). For instance, the inviscid anelastic horizontal momentum equation is

$$\frac{\partial \mathbf{V}_h}{\partial t} = \underbrace{-\left(\mathbf{V}_h \cdot \nabla\right)\mathbf{V}_h}_{\substack{\text{horizontal momentum} \\ \text{advection (HM)}}} \underbrace{-w\frac{\partial \mathbf{V}_h}{\partial z}}_{\substack{\text{vertical momentum} \\ \text{advection (VM)}}} \underbrace{-\frac{1}{\rho_0}\nabla p - f\hat{\mathbf{k}} \times \mathbf{V}}_{\substack{\text{pressure gradient} \\ \text{adjustment (PG)}}}, \tag{5.3}$$

where $\mathbf{V}_h$ is the horizontal wind velocity vector, $\hat{\mathbf{k}}$ is the unit vector in the vertical direction, and all other terms retain their traditional meanings. We then separated the contributions to the local time tendency into those due to the separate terms on the RHS of equation (5.3) and integrate these terms over a specified period of time to obtain the changes in wind resulting from specific processes. For instance:

$$\Delta\mathbf{V}_{PG} = \left\langle \Delta u_{PG}, \Delta v_{PG} \right\rangle = \int_{t_1}^{t_2} \left(-\frac{1}{\rho_0}\nabla p - f\hat{\mathbf{k}} \times \mathbf{V} \right) dt, \tag{5.4}$$

where the Δ symbol denotes the local difference in a particular quantity between t_2 and t_1, and u and v are the i and j components of the horizontal wind respectively. Analogous temporal integrations to equation (5.4) were conducted for HM and VM, resulting in $\mathbf{\Delta V}_{HM}$ and $\mathbf{\Delta V}_{VM}$ respectively (these quantities and notations were introduced in PS2015a).

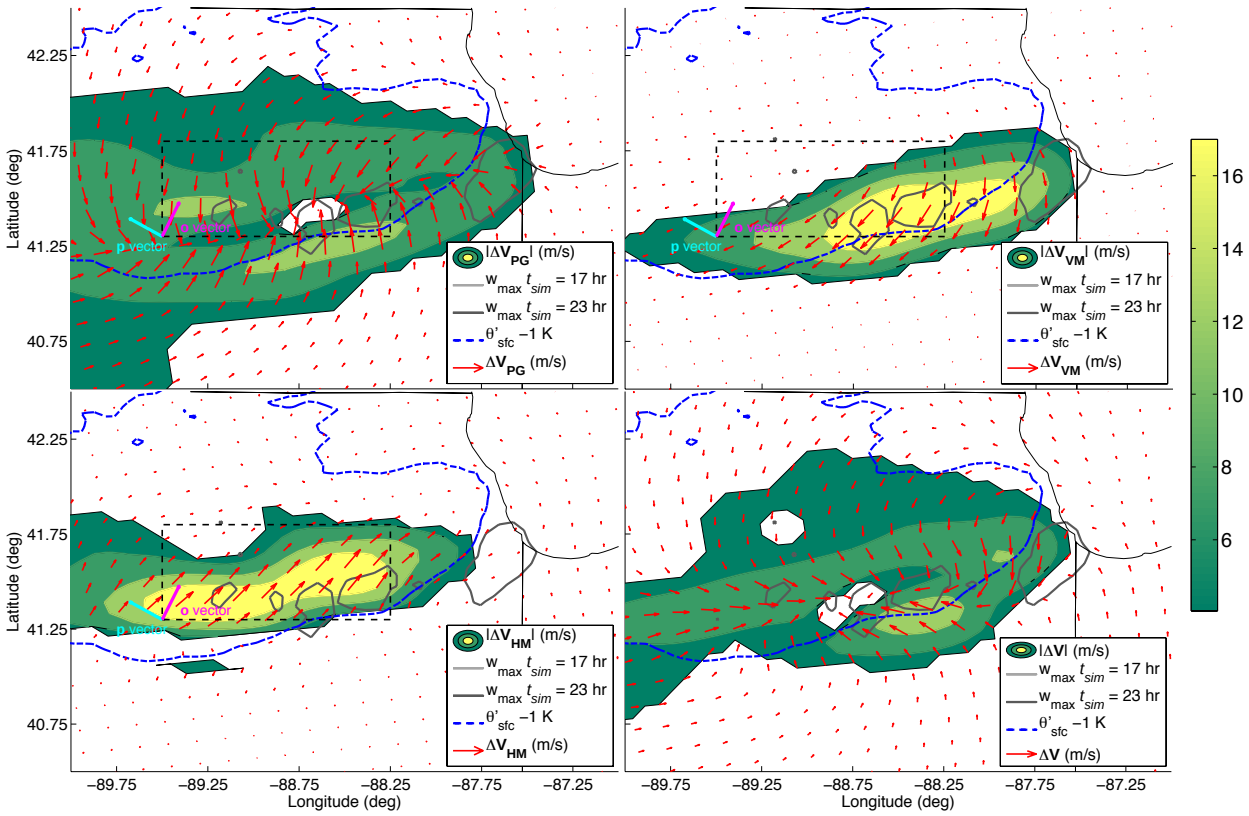

Fig. 5.10. ΔV magnitudes (shading, m/s), and vectors (red arrows, m/s) due to PG (panel a), VM (panel b), HM (panel c), and the sum of PG, VM, and HM (panel d); maximum column vertical velocities > 3 m/s (light gray contours at t_{sim}=10 hr, and dark gray contours at t_{sim}=17 hr), and surface θ' = -1 K at the surface a t_{sim}=17 hr (blue dashed line).

In order to understand the role of the passage of the initial progressive convective system on the generation of low-level convergence and deformation in its wake, we examined the spatial patterns of $\mathbf{\Delta V}_{PG}$, $\mathbf{\Delta V}_{HM}$, and $\mathbf{\Delta V}_{VM}$ respectively between t_{sim}=10 and 17 hr (Fig. 5.10; the timeframe of the passage of the initial progressive MCS). As in the case of the MCS studied by PS2015a, $\mathbf{\Delta V}_{PG}$ induced a flow change that generally converged into the region affected by convection (Fig. 5.10a), which presumably resulted from flow accelerations toward low-level low pressure anomalies along the convective line that resulted from mid tropospheric latent heating. $\mathbf{\Delta V}_{HM}$ contributed southwesterly flow changes within the region affected by convection (Fig. 5.10c). This may be conceptualized as parcels with high momentum within the southwesterly LLJ "replacing" parcels with lower momentum in the region that was convectively

overturned, thereby inducing a southwesterly flow tendency (see PS2015a). $\mathbf{\Delta V}_{VM}$ contributed an opposing northeasterly flow change (Fig. 5.10b). This may be conceptualized as updrafts removing high southwesterly momentum from the LLJ and depositing this momentum at upper levels, and thereby "decelerating" the low-level flow (see, PS2015a). The sum of these three contributions (Fig. 5.10d) exhibits a pattern nearly identical to that contributed by $\mathbf{\Delta V}_{PG}$ alone, suggesting that (a) the contributions by $\mathbf{\Delta V}_{HM}$ and $\mathbf{\Delta V}_{VM}$ predominantly canceled each other (aside from contributing minor directional changes in Fig. 5.10d), and (b) $\mathbf{\Delta V}_{PG}$ was the predominant contributor to the generation of convergence and deformation as convection moved through the region. In other words, the flow response to pressure perturbations in convective updrafts (rather than momentum transport) was the primary generator of deformation and convergence to the rear of the initial forward propagating MCS. PS2015b demonstrated similar findings for an observed TL/AS MCS, and these authors noted that the patterns of low-level flow change are consistent with the dynamics of rear-inflow jets (e.g. Weisman 2003). KS2013 also showed that such low-level flow changes played a key role in the morphological evolution of the bow-and-arrow phenomena (which is a specific instance of ROD where the upstream convective line occurs to the rear of a bowing TS type convective line).

5.5.c) The temporal offset of ROD from the initial forward-propagating convection

In this sub-section we consider the components of the HM, VM, and PG (from equation 3horizontal wind tendencies normal to the OFB to better understand how these processes influenced convective evolution. Note that in contrast with the previous section, were we focused on time-integrated changes to the wind, we are now analyzing the temporal evolution of instantaneous wind tendencies (e.g. VM corresponds to $-w\frac{\partial \mathbf{V}_h}{\partial z}$). We defined the "normal"

vector, $\mathbf{n}_{OFB}$, as the average orientation of the temperature gradient along the southwestern OFB flank at t_{sim} = 21 hr. For instance,

$$\frac{\partial V_{orth}}{\partial t} \equiv \frac{\partial \mathbf{V}}{\partial t} \cdot \mathbf{o}_{OFB}, \quad (5.5)$$

These quantities yield insight into how horizontal flow accelerations affected fluxes of momentum and equivalent potential temperature (θ_e) across the southwestern surface OFB, and toward the convective line, where "positive fluxes" are defined as fluxes toward the cold pool and "negative fluxes" are defined as fluxes away from the cold pool. The analogous acceleration to equation (5), but parallel to the boundary is:

$$\frac{\partial V_{parr}}{\partial t} \equiv \frac{\partial \mathbf{V}}{\partial t} \cdot \mathbf{p}_{OFB}, \quad (5.6)$$

where $\mathbf{p}_{OFB} \equiv \hat{\mathbf{k}} \times \mathbf{o}_{OFB}$. We focus our analysis on the 1-2 km AGL layer, where CAPE and θ_e were maximized. Relative minima in the cross-boundary component of flow and θ_e are evident between t_{sim}=17 and 21 hr (Fig. 5.11a; convection associated with the leading convective line exited the region between t_{sim}=19 and 20 hr). Between t_{sim}=17 and 20 hr (the convectively active timeframe), VM contributed a strong negative tendency between .5 and 3 km AGL, along with a positive tendency above 3.5 km AGL (Fig. 5.11c). This signature shows that southwesterly flow within the low-level jet was being transported aloft, or "overturned" by convective updrafts, and that this overturning was responsible for the mentioned minima in southwesterly flow to the MCS between t_{sim}=17 and 21 hr (Fig. 5.11a, all other forces contributed near-neutral to positive tendency during this timeframe, Fig. 5.11b-d). The coincidence of the minimum in southwesterly flow with a minimum in 1-1.5 km θ_e show that as southwesterly flow overturned in convective updrafts, the supply of high θ_e to the region where ROD would eventually occur was temporarily disrupted. Between t_{sim}=19 and 21 hr, HM contributed strong positive tendency

between 1 and 2.5 km AGL (Fig. 5.11c). This HM tendency represents the re-introduction of convectively unaltered southwesterly flow by the low-level jet, and resulted in an increase in southwesterly flow and θ_e between t_{sim}=19 and 22 hr.

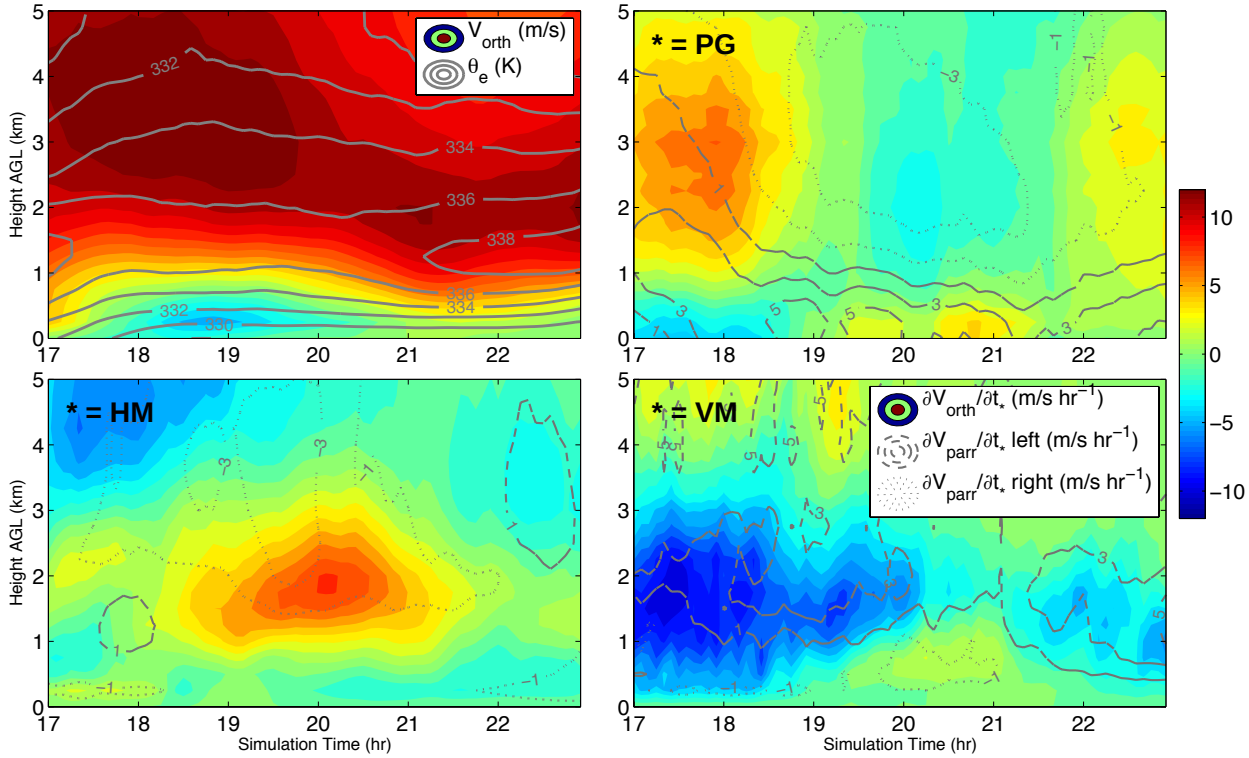

Fig. 5.11. Quantities averaged over the black dashed box in Fig. 10, where the magenta **o** vector in Fig. 10 is the orthogonal vector, and the cyan **p** vector is the parallel vector. Panel a: V_{orth} (shading, m/s), and box-average θ_e (gray contours, K). Panels b-d: $\frac{\partial V_{orth}}{\partial t}$ (shading, m/s hr^{-1}), and $\frac{\partial V_{par}}{\partial t}$ (m/s hr^{-1}; gray dashed contours, leftward, and gray dotted contours, rightward, where leftward is in the direction of the **p** vector) due to PG (panel b), HM (panel c), and VM (panel d).

A defining characteristic of ROD is that the upstream development of a convective line is temporally offset from the passage of the initial progressive convective system (rather than the upstream convective line having resulted from continuous upstream backbuilding from the initial progressive MCS), and the line develops all-at-once. For instance, there is no evidence of the development of an upstream convective line at t_{sim}=16 hr (Fig. 5.1b); by t_{sim}=18 hr (Fig. 5.1c), the initial convective cells associated with ROD had suddenly initiated, and quickly organized into a training line thereafter (the mature training line is evident at t_{sim}=21 hr, Fig. 5.1d). We

explain this behavior by the disruption of southwesterly inflow (and alleviation of convective instability) to the upstream region of the MCS (in this case, the western flank) by upward momentum transport, and the finite time period required for the gradual re-introduction of southwesterly inflow and convective instability via horizontal momentum transport into the convectively overturned region.

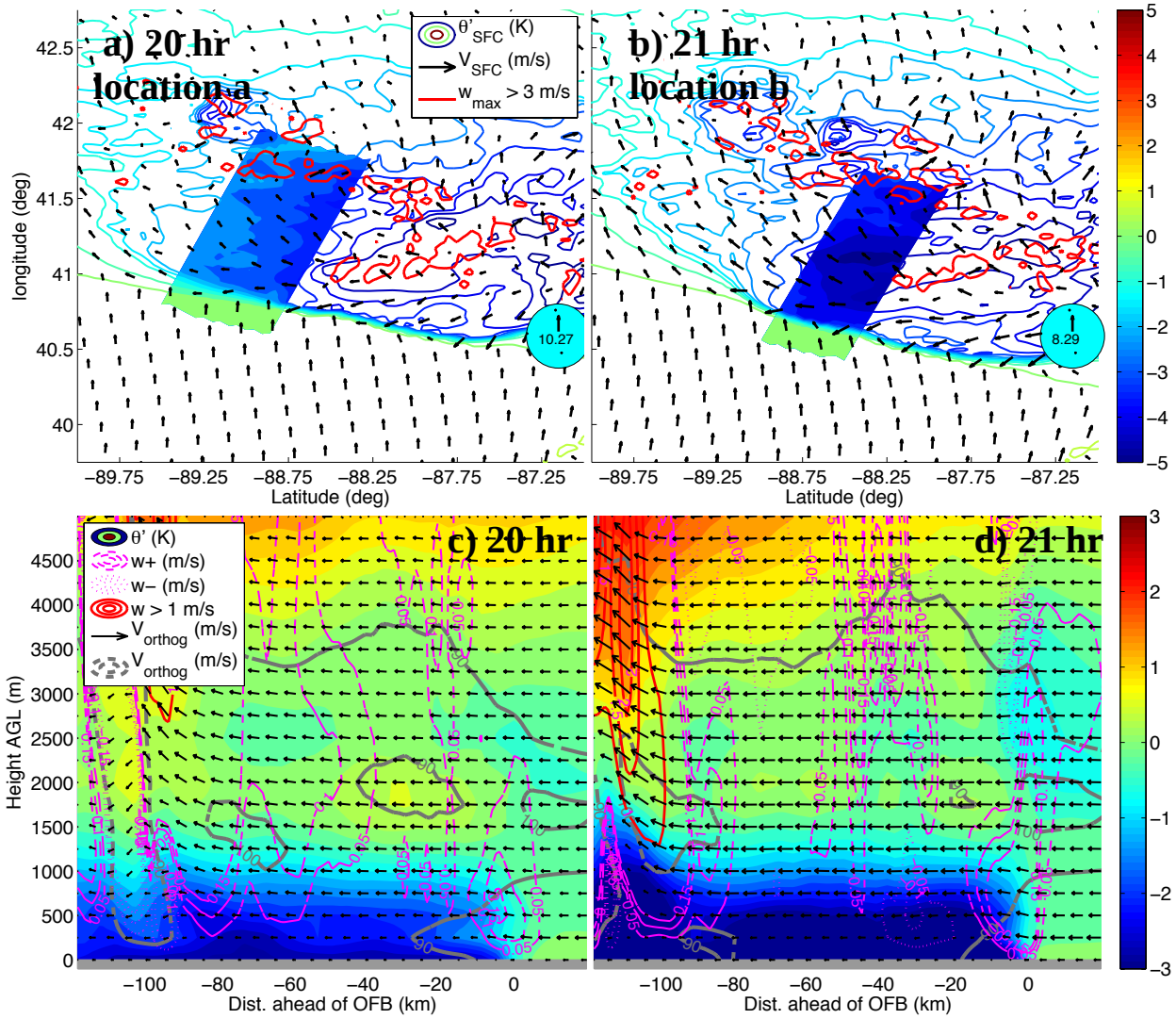

Fig. 5.12. Top panels: as in Fig. 5.7a, but for t_{sim} = 20 hr (panel a; referred to as path a) and t_{sim} = 21 hr (panel b; referred to as path b). Bottom panels: cross section of θ' (shading, K), outflow-boundary orthogonal wind vectors (black arrows, m/s), vertical velocity (magenta dashed contours: .05 m/s, .1 m/s, and .15 m/s; magenta dotted contours: -.05 m/s, -.1 m/s, and -.15 m/s; red contours > 1 m/s) from t_{sim} = 20 hr (panel c) and t_{sim} = 21 hr (panel d).

5.5.d. The geographic offset of ROD convection from the southwestern outflow boundary

As discussed in section 3, the training convective line that developed upstream of the initial forward-propagating MCS was offset to the north of the OFB between t_{sim}=19 and 24 hrs. In this sub-section, we investigate the dynamics that (a) prohibited persistent convection near the OFB, and (b) were responsible for the locations where convection did persist.

Cross sections oriented perpendicular to the southwestern OFB at t_{sim}=20 and 21 hrs (Fig. 5.11 referred to as paths *b* and *c* respectively) reveal markedly reduced lifting when compared to the southeastern OFB at t_{sim}=16 hrs (Fig. 5.7b), with maximum vertical velocities within 5 km of the boundary being on the order of 15 cm/s at 20 hr (Fig. 5.12c), and 25 cm/s at 21 hr (Fig 5.12d; compared to > 1 m/s along path a). As discussed by PS2015b, the vertical wind profile orthogonal to the OFB here was less favorable for robust lifting along the boundary, when compared to path a. This explains the disparity in the magnitude of lifting between the southeastern and southwestern outflow boundaries.

The vertical profile of θ in the NOMP simulation along path (b) featured a gradual upward slope θ with northward extent (Fig. 13a). The presence of the surface cold pool in the CNTL simulation effectively displaced the 300 and 302-K isentropes upward from their location in the NOMP simulation; however, aside from an abrupt rise in these isentropes along the cold pool edge in the CNTL simulation, there is little difference in upward isentrope slope with northward extent in the CNTL simulation, when compared to the NOMP simulation (Fig. 13a). Large-scale forcing, therefore, appears to have been the predominant forcing mechanism to lift parcels to their point of saturation (rather than enhanced isentropic up-glide that resulted from the presence of the cold pool).

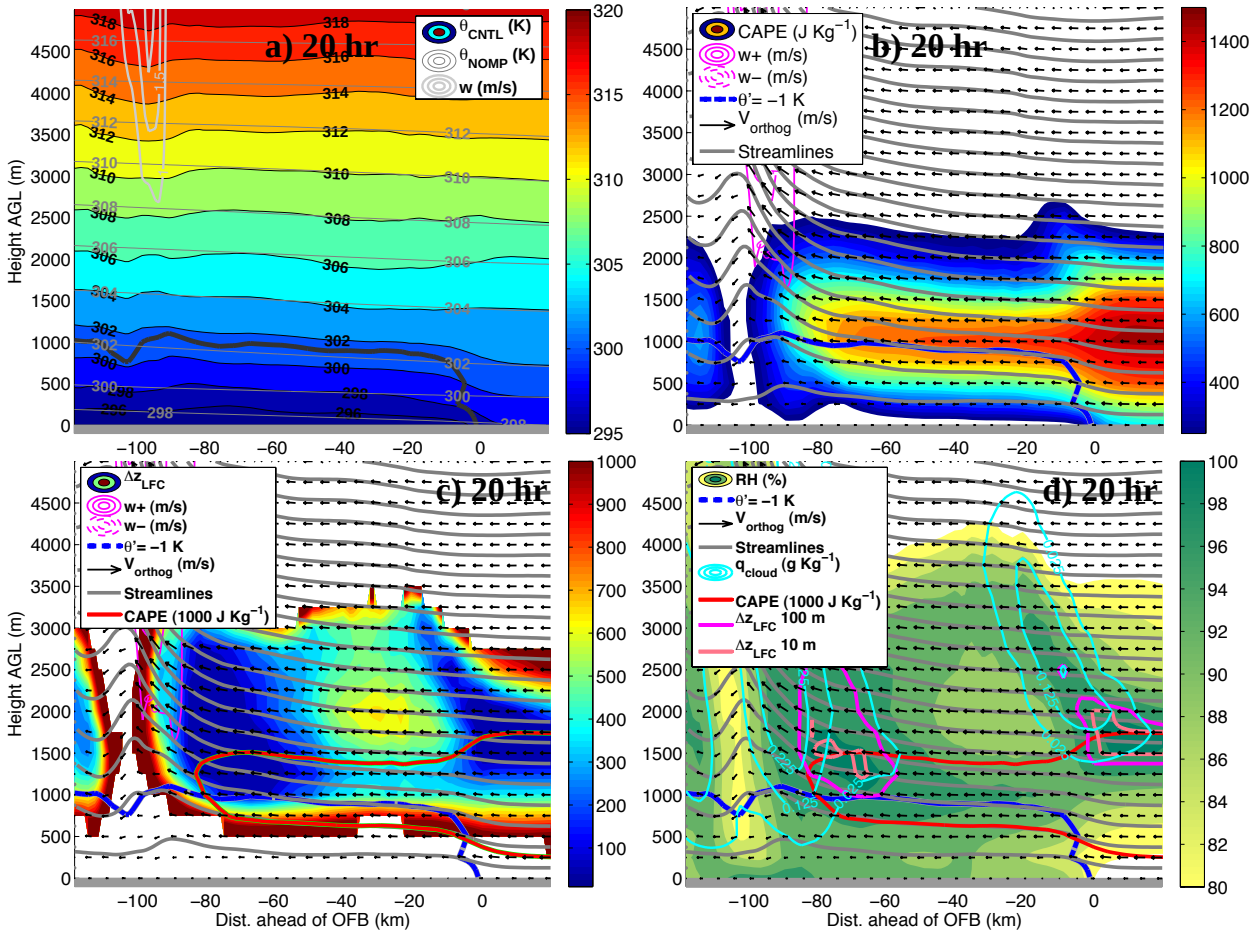

Fig. 5.13. Cross section along path b. Panel a: θ_{CNTL} (shading, K), θ_{NOMP} (dark gray contours), and vertical velocity (light gray contours, m/s). Panel b: as in Fig. 4c, but for path a. Panel c: Δz_{LFC} (shading, m), vertical velocity (positive: magenta solid contours; negative: magenta dashed contours), the -1 K θ' contour (as in panel b), cross-section parallel wind vectors (as in panel 4c), streamlines (as in panel 4c), and the 1000 J/Kg CAPE contour (red). Panel d: Relative humidity (shading, %), the -1 K θ' contour (as in panel b), cross-section parallel wind vectors (as in panel 4c), streamlines (as in panel b), and the 1000 J/Kg CAPE contour (as in panel c), the 100 m (magenta) and 10 m (tan) Δz_{LFC} contours.

South of the OFB, CAPE was maximized ("maximized" will hereafter refer to CAPE > 1000 J Kg^{-1}) for parcels between .25 km and 1.75 km, with the highest values reaching 1500 J Kg^{-1}. North of the boundary the maximized CAPE layer contracted to the .5-1.5 km layer north of the OFB, and maximum values dropped into the 1000-1200 J/Kg range. We hereafter refer to the quantity Δz_{LFC}, which we define as $\Delta z_{LFC} \equiv z_{LFC} - z_0$, where z_{LFC} is the level of free convection (LFC) for a parcel lifted from an initial height of z_0. This quantity is highly

correlated with CIN and B_{min} (defined in Trier et al. 2014), where high (low) values of Δz_{LFC} represent high (low) values of convective inhibition. The definition and units (meters), however, are more easily interpretable in terms of physical processes; e.g. the upward distance a physical process must lift a parcel to achieve buoyant convection. Δz_{LFC} values were high below 1 km AGL within the maximized CAPE layer south of the OFB, and approached zero above 1 km AGL (suggesting that the upper portion of this layer was "primed" for convection, Fig. 5.13c). Indeed clouds are apparent in the 1.5-5 km layer, directly above the OFB, and scattered weak convective cells are apparent in Fig. 5.1d-e along the outflow boundary.

Upon flow interacting with the OFB, Δz_{LFC} values in the maximized CAPE layer nearly instantaneously jumped from near zero to 250-750 m with an even greater increase above this layer. This suggests that the interaction of the flow with the OFB temporarily stabilized the high CAPE layer. Δz_{LFC} values again approached zero between 50 and 80 km north of the OFB (prior to their entry into convective updrafts). Relative humidity values within the maximized CAPE layer gradually increased between the OFB and the cloudy region near convective updrafts (Fig. 13d), which suggests that the re-erosion of Δz_{LFC} resulted from parcels having been gradually lifted the required distance to reach their LFCs. A simple calculation assuming an average Δz_{LFC} of 300 m through the maximized CAPE layer (based on Fig. 13c), an average lifting value of 5 cm/s (based on Fig. 12c), and an average horizontal flow speed of 10 m/s (based on Fig. 12) between the OFB and ~ 60 km behind the OFB (where parcels in the maximized CAPE layer had reached saturation and begun to form clouds) yields a requirement of 60 km of northward travel from the OFB for parcels to reach their LFCs (which is reasonably close to the observed separation between the OFB and the region of cloud formation associated with deep convection in fig. 12c). Similar patterns are apparent along path *c*, suggesting that the aforementioned flow

behavior was coherent in time (Fig. 14). The drop in CAPE as flow passed the OFB is more pronounced than along path b (the maximized CAPE layer shrank from .25-1.75 km to 1-1.5 km and maximum values drop by nearly 500 J/Kg), and cloud formation was deeper and more pronounced above the OFB (though deep convection has not yet developed here).

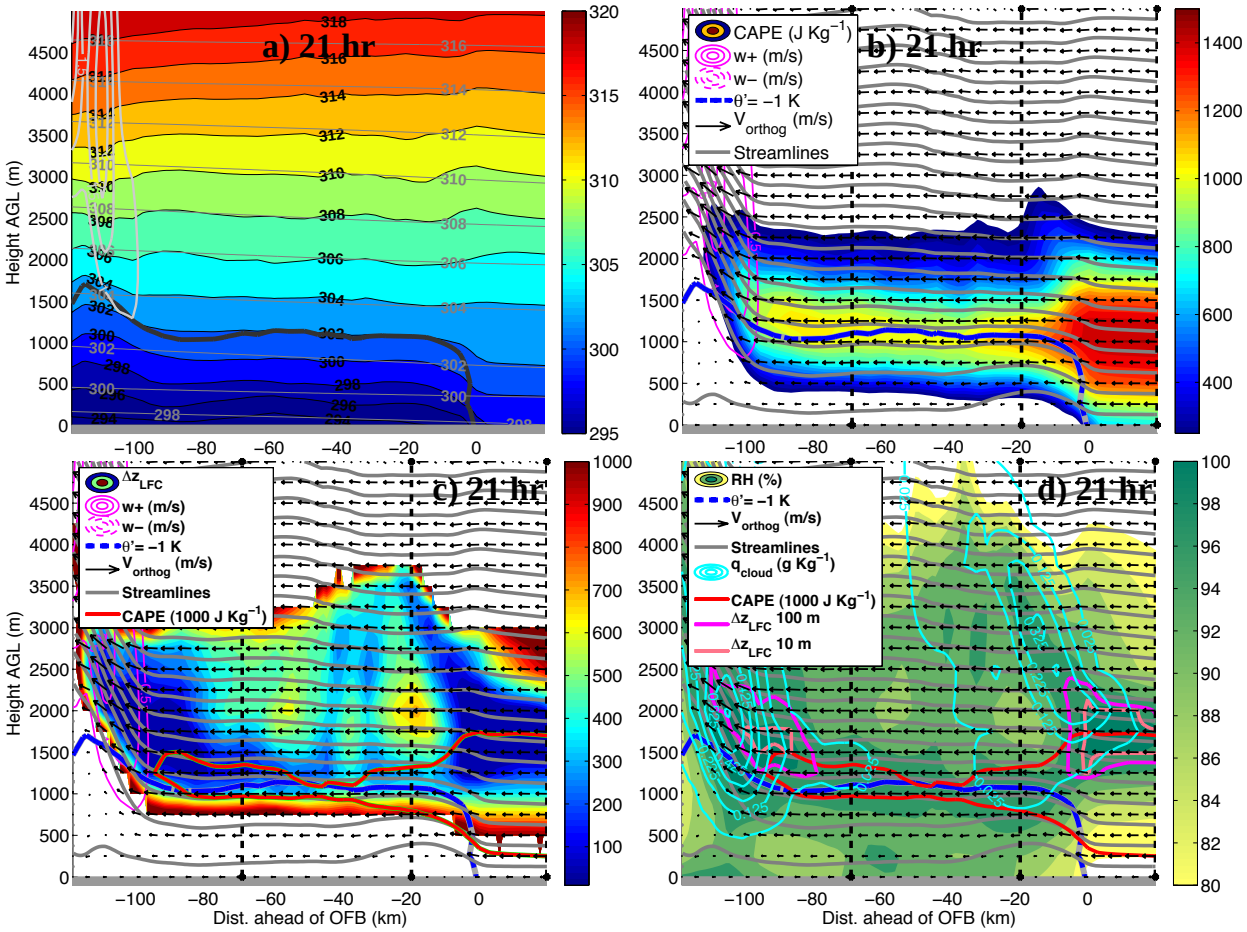

Fig. 14. As in Fig. 5.12, but for path c.

Additional aspects of the flow interaction with the OFB are revealed by three-dimensional forward trajectories initialized southwest of the surface OFB (this interaction occurred between 50 and 75 minutes after initialization for all trajectories; Fig. 5.15a). We disseminated trajectories into three populations (1000 m, 1750 m, and 2500 m), based on their origin heights. We then computed the average, and standard deviation time series' of various

quantities for each of these three populations (Fig. 5.14). Parcels originating from 1000 m and 2500 m AGL were sub-saturated prior to OFB interaction, whereas parcels originating from 1750 m were saturated (Fig. 5.15b). The variance in RH increased dramatically for the 1750 m and 2500 m parcels, and to a lesser extent for the 1000 m parcels (Fig. 5.15b). The average RH among all parcels was below 100% beyond 50 minutes; however, maximum values in the 1750 m and 2500 m parcels exceeded 100% (Fig. 5.15b). This suggests a pattern of scattered to isolated cloud formation interspersed with clear air (supersaturated regions are assumed to contain cloud water). The variance in vertical trajectory displacements also increased dramatically among the 1750 m and 2500 m populations (and to a lesser extent among the 1000 m population) after the flow interaction with the boundary (Fig. 5.16c). This suggests that the cloud formation incited by the OFB interaction consisted of scattered shallow convective overturning, with interspersed weak updrafts and downdrafts. Water vapor mixing ratio was generally reduced, θ was generally increased, and θ_e was generally decreased with increasing vertical displacement over the first 100 min of trajectory paths. Furthermore, parcels 1750 m lost water vapor, increased in θ, and decreased in θ_e, whereas 2500 m parcels gained water vapor, decreased in θ, and increased in θ_e. These patterns likely illustrate latent heating and cloud formation within 1750 m parcels (hence the increasing θ and decreasing water vapor), the detrainment and evaporation of cloud water into 2500 m parcels (hence the decreasing θ and increasing water vapor), and ultimately "mixing" of high θ_e from 1750 m parcels into 2500 parcels, reducing values in the former and increasing values in the later.

To better understand the mechanisms for the thermodynamic stabilization of flow as it was lifted over the southwestern OFB, we compare the vertical profiles of θ (Fig. 5.17a) and $\frac{\partial \theta}{\partial z}$ (Fig. 5.17b) 20 km south of the boundary to the analogous profiles 20 km north of the outflow

boundary. The terms “warming” and “cooling” (in the context of this discussion) refer to changes in potential temperature at a given height between profile south of the boundary and the profile north of the boundary. The lifting of the flow over the OFB cooled the θ profile between the surface and 1.25 km, and warmed the profile above 1.25 km.

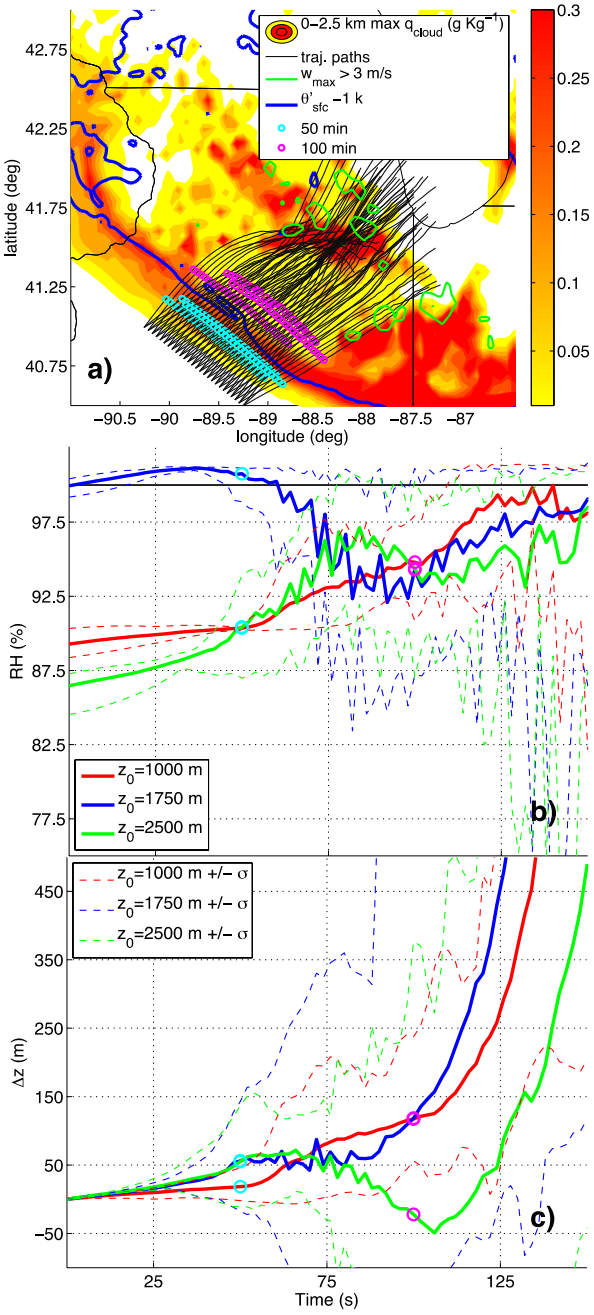

Fig. 5.15. Top panel: 0-2.5 km max cloud water mixing ratio (q_{cloud}, shading), the horizontal paths of trajectories initialized at t_{sim}=19 hr (black lines), maximum column vertical velocity > 3 m s^{-1} (green contour), surface θ’= -1 K (blue contour), and the locations of trajectories 50 minutes after their

initialization (cyan circles), and 100 minutes after their initialization (magenta circles). Panel b: time series of the average relative humidity (%) of trajectories initialized from 1000 m AGL (red line), 1750 m (blue line), 2500 m (green line), and the maximum and minimum values from these populations (dashed). Panel c: same as panel b, but time series of parcel displacement from their initial positions.

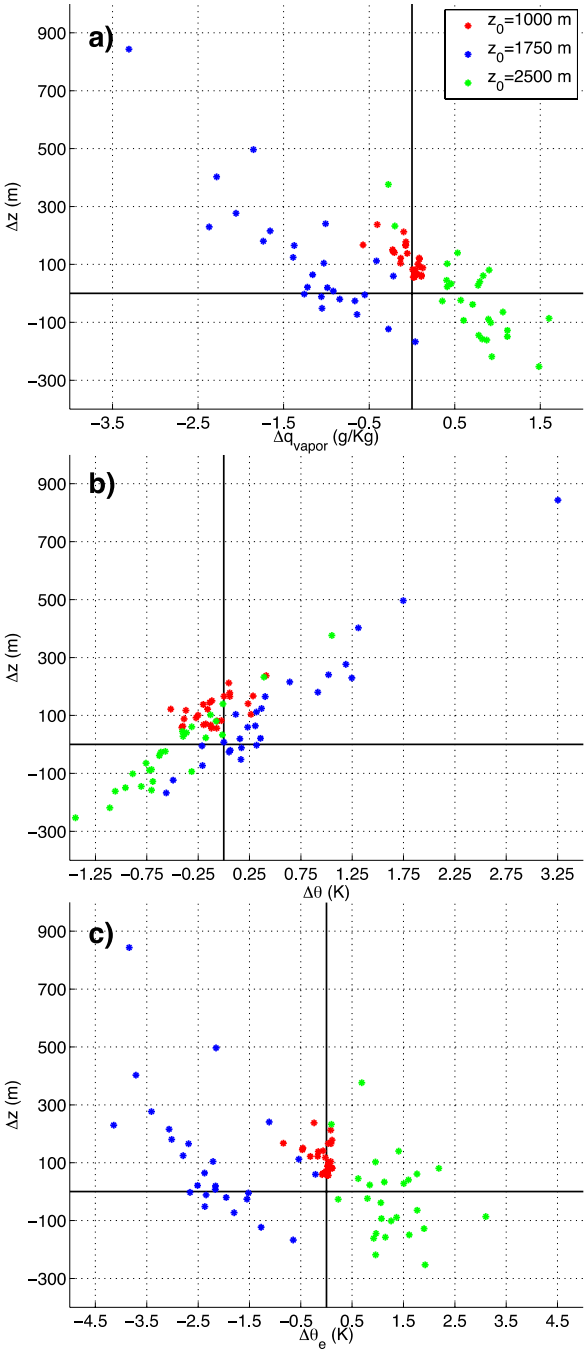

Fig. 5.16. Scatter plots of the change in water vapor mixing ratio (Δq_{vapor}, g Kg^{-1}, panel a), θ (K, panel b), and θ_e (K, panel c) between values at parcel initialization and 100 minutes after initialization. Trajectories initialized at 1000 m are red dots, 1750 m are blue dots, and 2500 m are green dots.

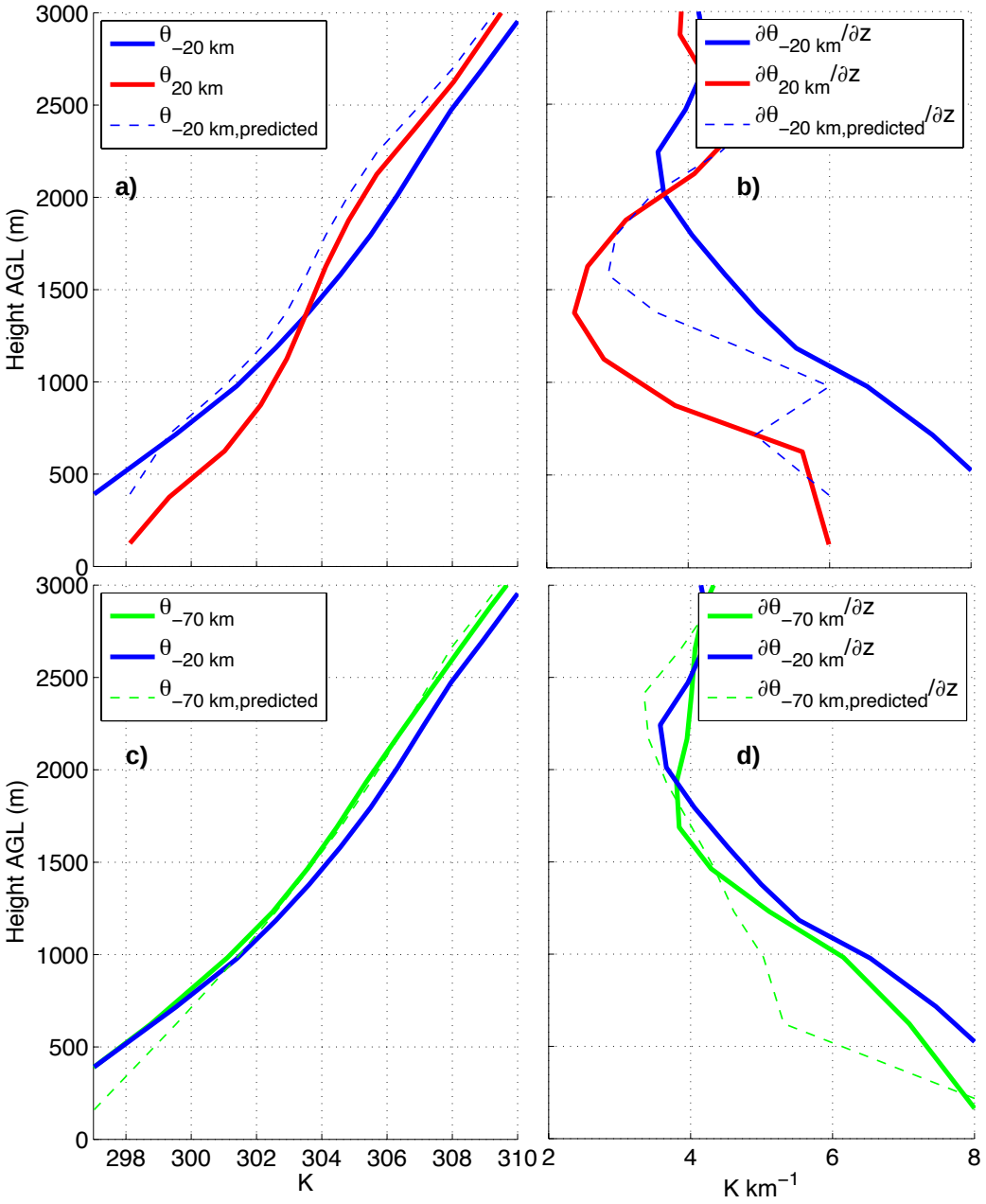

Fig. 5.17. Top panels: vertical profile of θ (panel a) and $\frac{\partial\theta}{\partial z}$ (panel b) 20 km south of (red line) and 20 km north of (blue line) the OFB in path c, and the predicted profile of θ (panel a) and $\frac{\partial\theta}{\partial z}$ 20 km north of the OFB if parcels from 20 km south of the OFB conserved θ along streamlines. Bottom panels: same as top panels, but for profiles 20 km north of the OFB (blue line) and 70 km north of the OFB (green line)

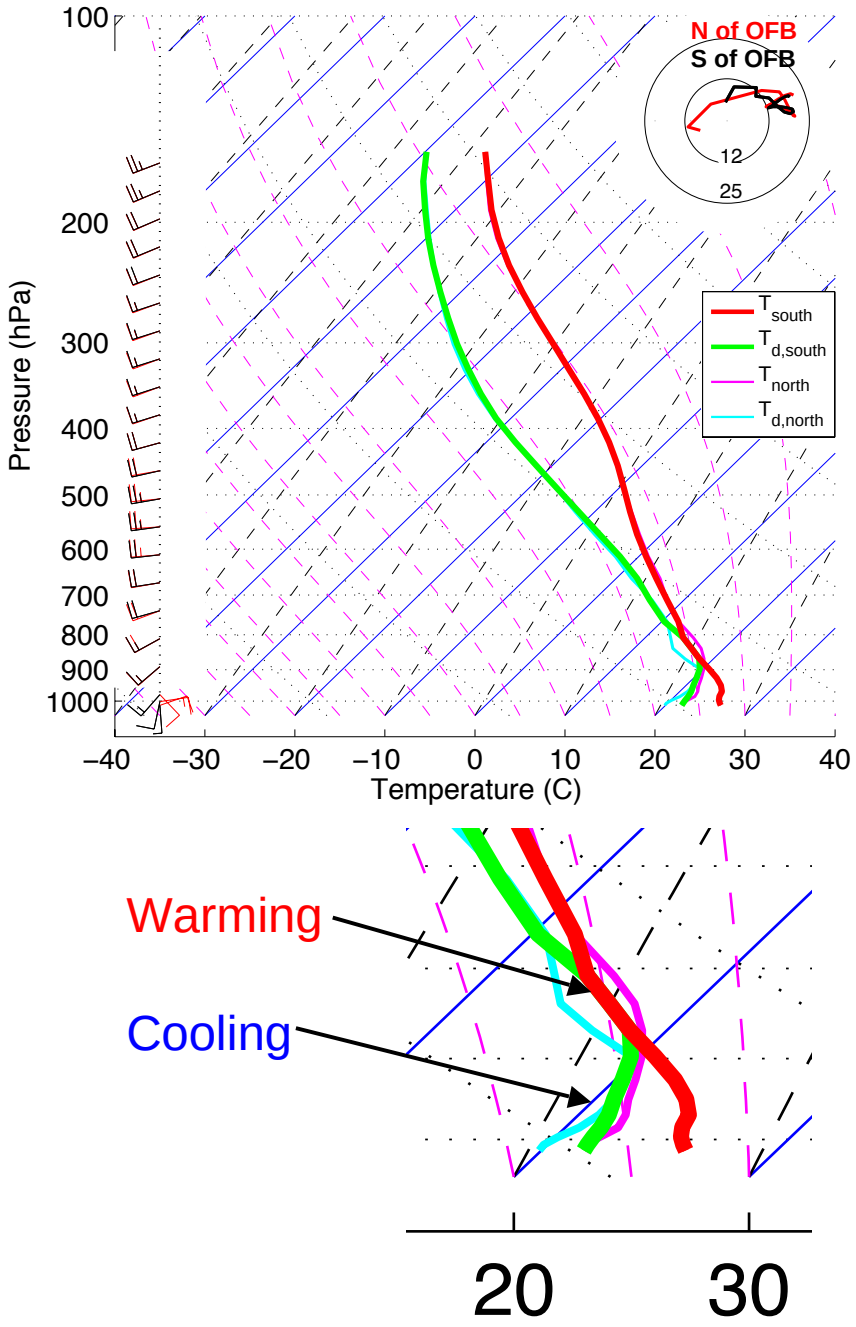

Fig. 5.18. Top: Skew-T log-P diagram of temperature (red line) and dew point (T_d, green line) immediately south of the OFB, and temperature (magenta line) and dew point (cyan line) immediately north of the OFB. Bottom: zoomed in view of the lowest portion of the top plot.

The low-level cooling closely resembles the magnitude of cooling expected from adiabatic lift, suggesting that adiabatic cooling associated with lift was the primary thermodynamic forcing there. The profile above 1.25 km, however, was 1-2 K warmer than

what would have resulted from adiabatic processes, suggesting that latent heating played a significant role in the temperature changes there. This "warming over cooling" pattern resulted in a marked increase in static stability below 2 km (Fig. 17b), and likely explains both the reduction in CAPE and increase in Δz_{LFC} across the boundary evident in Figs 5.13c and 5.14c. An analogous comparison of the profiles at -20 km and -70 km shows only small changes to both the θ (Fig. 5.17c) and $\frac{\partial \theta}{\partial z}$ (Fig. 5.17d) profiles, with these changes being close to what would have resulted from adiabatic processes. This suggests that (a) the latent heating induced changes to the static stability profile that occurred as the flow moved across the OFB persisted between 20 and 70 km behind the OFB (since there is no apparent "reversal" of the latent heating observed in Fig. 5.17a in Fig. 5.17), and (b) the primary driving force in the reduction of Δz_{LFC} between -20 and -70 km involved parcels simply being lifted to their LFC (rather than comparatively complex processes having been at work, such as the "warming over cooling" observed as flow lifted over the OFB). The effect of this warming-over-cooling pattern on the skew-T profile of temperature and dew point is shown in Fig. 18, where the cooling below 900 hPa upon the passage of flow over the boundary had moved lifted parcel paths to the left on the diagram (and therefore reduced CAPE in that layer), and the profiles are nearly unchanged by the OFB interaction above 800 hPa (suggesting that processes aloft were not responsible for the CAPE and Δz_{LFC} changes.

In order to determine the processes responsible for the flow stabilization (evident in Fig. 16a,b) as parcels were lifted over the OFB, we examined the Lagrangian budget for the vertical θ lapse rate. Here we assume that gradients in θ parallel to the OFB are small in profiles b and c, conditions are changing slowly through time, and that the average trajectory paths in the OFB parallel direction through this region are well represented by the streamlines shown in Fig.

5.14b-d. The inviscid prognostic equation for the vertical potential temperature gradient following an air parcel is given by

$$(5.7) \quad \frac{d\Gamma}{dt} = \underbrace{-\frac{\partial\theta}{\partial x}\frac{\partial u}{\partial z}}_{\substack{\text{tilting}\\(\text{TIL})}} \underbrace{-\Gamma\frac{\partial w}{\partial z}}_{\substack{\text{divergence}\\(\text{DIV})}} + \underbrace{\frac{\partial\dot{\Theta}}{\partial z}}_{\substack{\text{latent heating}\\(\text{LAT})}}, \text{ where}$$

$\Gamma \equiv \frac{\partial\theta}{\partial z}$, $\dot{\Theta}$ is a latent heating term, and positive (negative) contributions to $\frac{d\Gamma}{dt}$ are referred to as "stabilizing" and "destabilizing" tendencies respectively. TIL represents the tilting of isentropes between a horizontal and vertical orientation, and may be alternatively interpreted as a vertical differential in the horizontal advection of θ. DIV represents the vertical "compression" or "extension" of isentropes in the presence of a vertically varying vertical velocity profile, and may be alternatively interpreted as a vertical differential in the vertical advection of θ.

In temporally integrating (5.7) in an analogous manner to (5.4), we obtain the individual contributions to the temporal differences in Γ along a trajectory from HT and VS respectively. For instance,

$$(5.8) \quad \delta\Gamma_{DIV} = -\int_{t_1}^{t_2}\left(\Gamma\frac{\partial w}{\partial z}\right)dt,$$

where the δ quantity denotes the difference in a particular quantity along a trajectory between t_2 and t_1 (we hereby refer to these quantities by their subscripts; e.g, DIV, TIL) Since the direct computation of latent heating from standard model outputted variables is difficult, we directly compute TIL and DIV only, and infer processes related to latent heating by observing the

difference in adiabatic predicted, and actual temperature profiles in Fig. 5.17b.

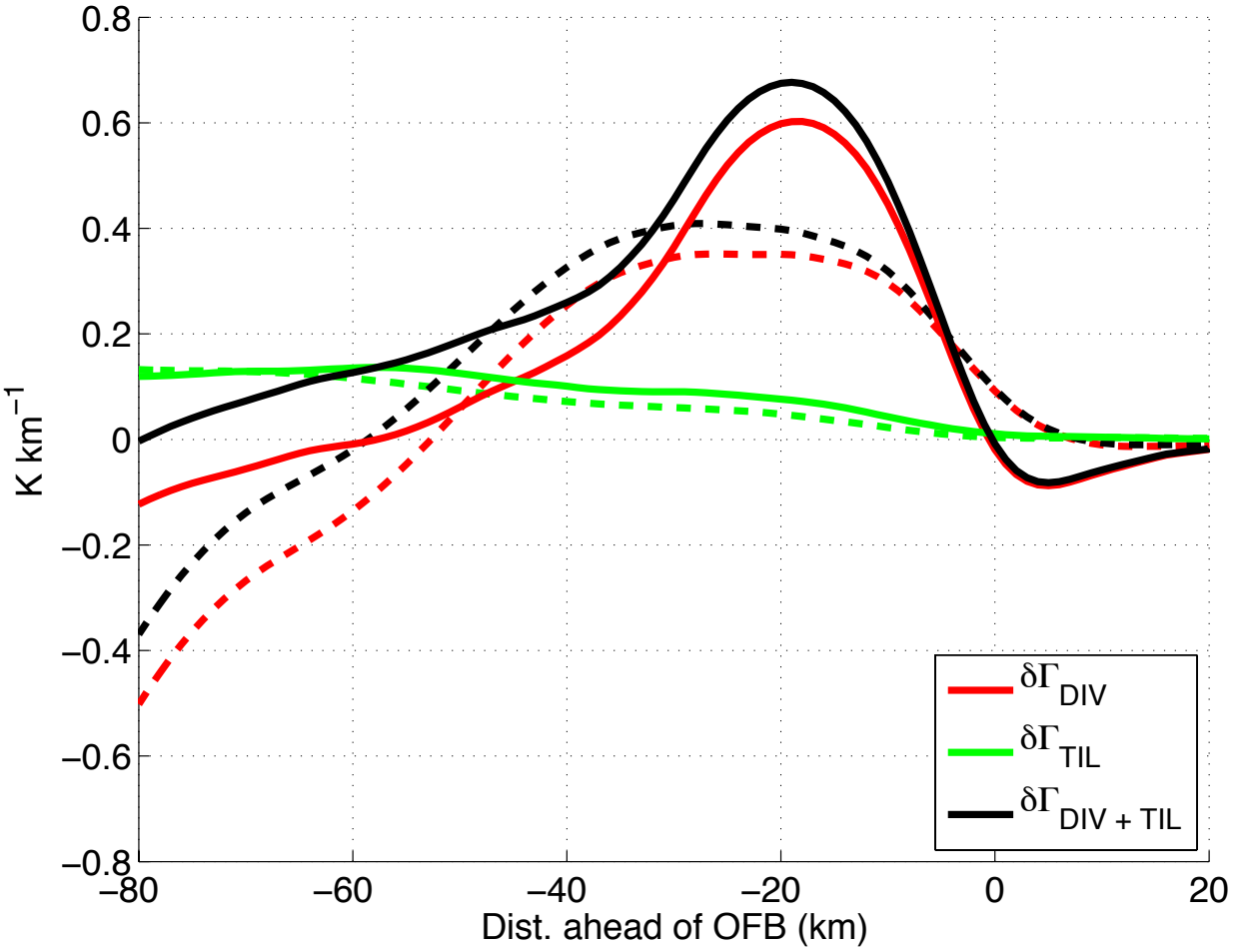

Fig. 5.19. δT_{DIV} (red dashed line: path a; red solid line: path b), δT_{TIL} (green dashed line: path a; green solid line: path b), and $\delta T_{DIV}+\delta T_{TIL}$ (black dashed line: path a; black solid line: path b). Equation 5.8 is evaluated along streamlines where t_1 is the time when parcels were 20 km south of the OFB, and t_2 is the time when parcels were at the locations listed on the *x* axis.

DIV contributed a strong stabilizing change to the thermodynamic profile for parcels originating south of the OFB with over 1000 J/Kg of CAPE, and between 0 and 40 km behind the OFB along both cross section paths (Fig. 5.19). DIV was also the predominant contributor to the net adiabatic contribution to the change in lapse rate (e.g. the sum of DIV and TIL). Since the environment in both soundings was vertically stratified, the primary factor dictating sign of the contribution by DIV was the sign of the vertical gradient in *w* (vertical velocity), where a

decrease (increase) in *w* with height yielded a stabilizing (destabilizing) contribution by DIV. As evident, the vertical profile of *w* directly over the outflow boundary in paths *b* and *c*, *w* was maximized at .5 km, decreased with height from .5 km through ~ 3 km, and most importantly decreased through the layer of maximum CAPE (Fig. 5.20; this explains why DIV stabilized the maximized CAPE layer).

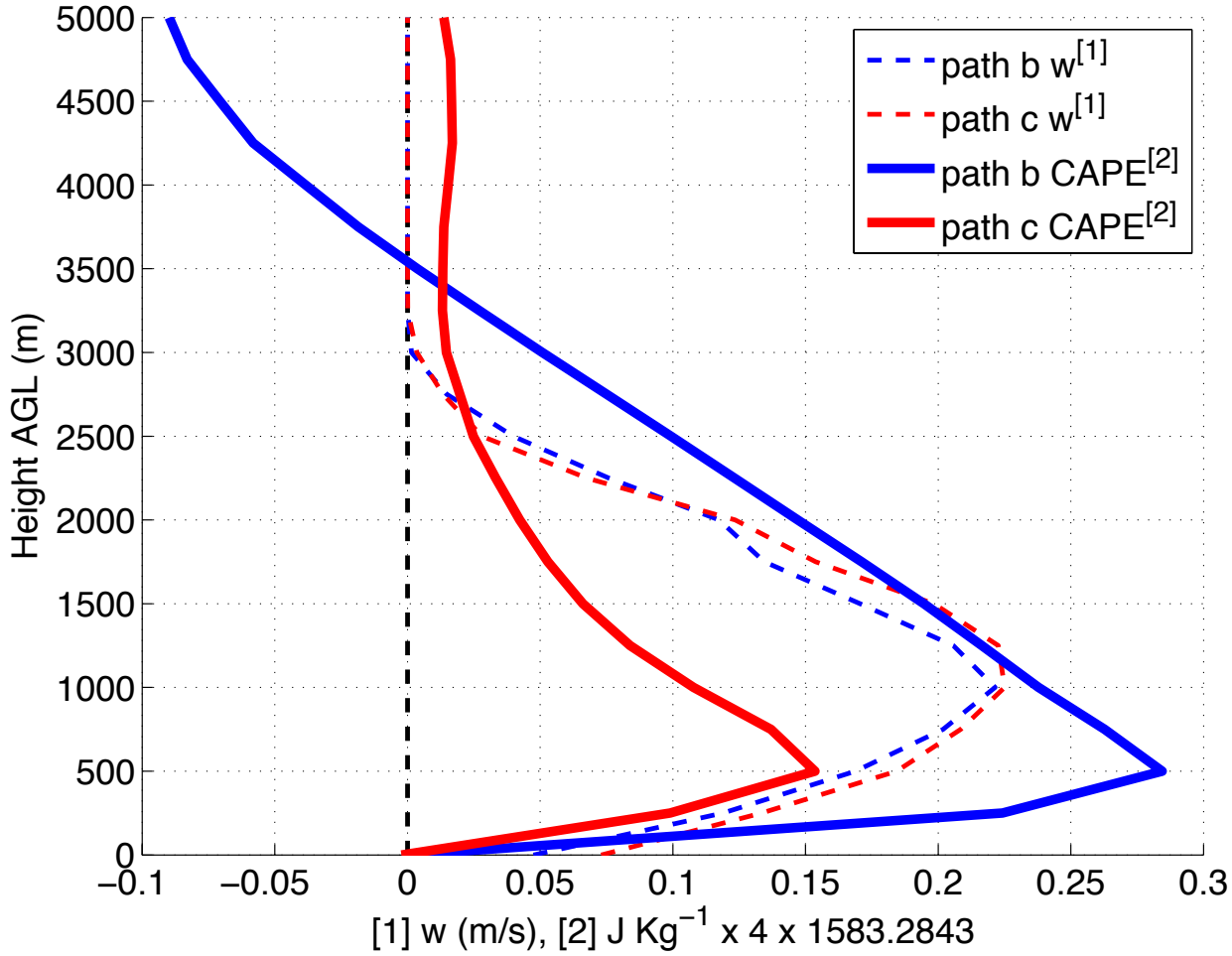

Fig. 5.20. Vertical profiles of *w* above the surface OFB along path b (blue solid line) and c (red solid line), and vertical profiles of CAPE above the surface OFB in paths b (blue dashed line) and c (red dashed line)

5.5.e. Southward cold pool surge

To further examine the spatial and temporal evolution of the influence of upscale convective feedbacks on the eventual southward propagation of the MCS, we define a mesoscale ingredients-based propagation index parameter, where

$$IPI_{MESO}(x,y,z) \equiv \frac{1}{N_{IPI}}\left(V_{H,CNTL}\cdot\nabla\theta_{CNTL} - V_{H,NOMP}\cdot\nabla\theta_{NOMP}\right)CAPE_{CNTL}, \quad (5.9)$$

The only difference between equation (5.1) and equation (5.9) is that here we subtract the temperature advection field from the NOMP simulation from that of the CNTL simulation so that regions of probable isentropic lift resulting from influences of convection on its nearby environment are emphasized. The parameter is still normalized by the same value (N_{IPI}) as IPI_{SYNOP} so that values are comparable between the two parameters. IPI_{MESO} is maximized in regions where isentropic lift from upscale convective feedbacks is occurring in the presence of moisture, high CAPE, and low CIN, and thus new convective initiation is probable.

IPI_{MESO} values at t_{sim}=20 hr were nontrivial 40-90 km north of the surface OFB, and in the 1-2 km AGL layer (Fig. 5.13a). A "slanted" gravity wave (streamlines rose near the OFB, subsided between 20-40 km north of the OFB, and then rose again beyond 40 km north of the OFB) response to latent heating or flow interaction with the cold pool was likely responsible for the enhanced isentrope slant between CNTL 40-70 km north of the OFB in the CNTL over the NOMP simulation. By t_{sim}=21 hr the deepening cold pool beneath convection had tilted isentropes further into the vertical (Fig. 5.14a) 100-120 km north of the OFB in the 1-2 km AGL layer (when compared to t_{sim}=21 hr), contributing to an increase in IPI_{MESO} values from t_{sim}=20 hr. The horizontal distribution of IPI_{MESO} was locally maximized on the SW flank of the training line at all hours, though its values increased between t_{sim}=22-26 hr (Fig.5.21) as a response to the

intensification and southward expansion of the deeper cold pool region (compare Fig. 5.5c to Fig. 5.22b, where the deeper cold pool region expanded to the edge of the surface OFB).

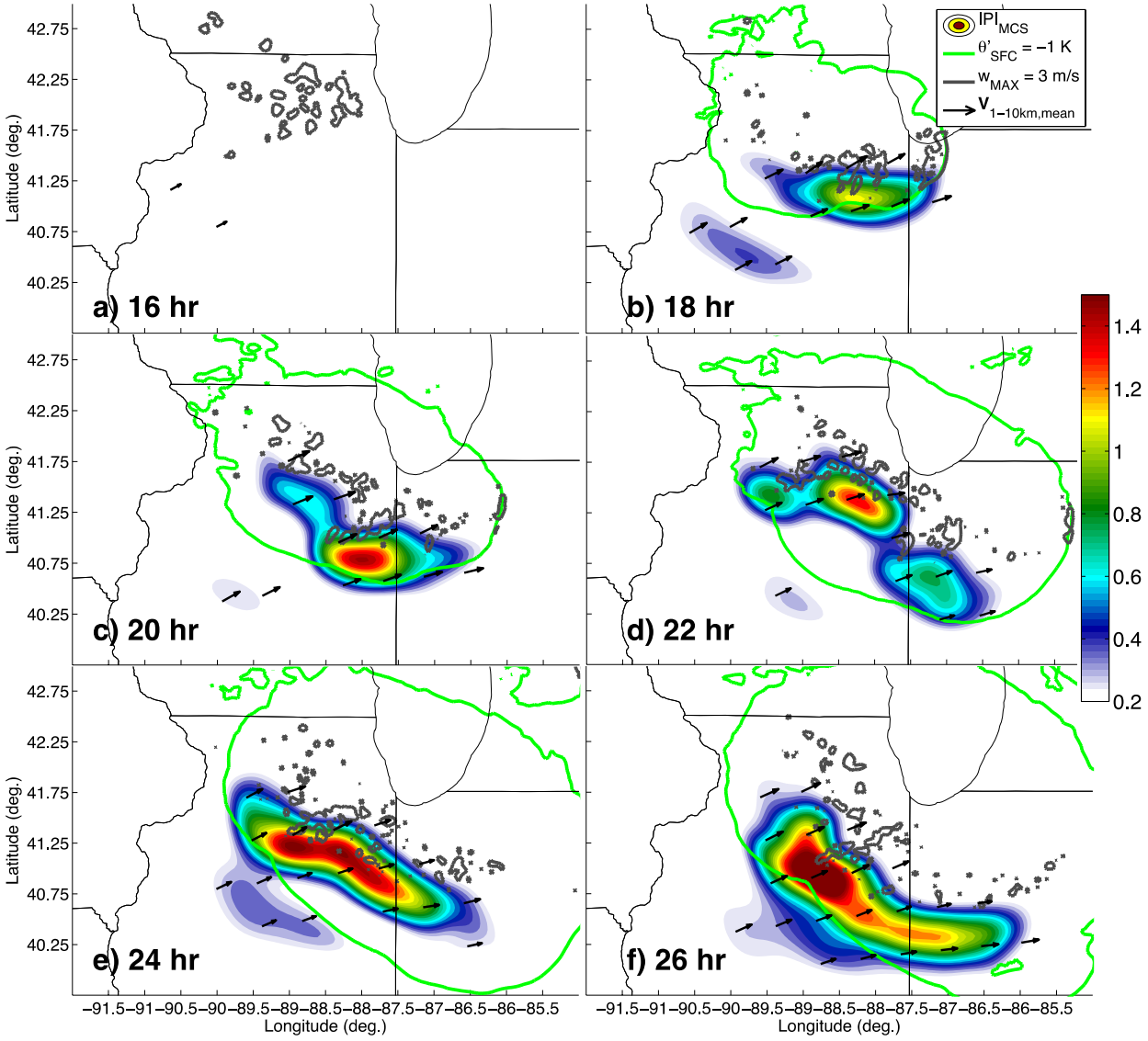

Fig. 5.21. As in Fig. 5.4, but with maximum column IPI_{MESO} shaded.

Weak southwestward convectively induced propagation (from the gravity wave mentioned above) prior to t_{sim}=21 hr appears to have combined with westward propagation by the large-scale environment and east-northeastward advection to result in a nearly stationary net system motion (compare Fig. 5 with Fig. 5.22; also note only trivial changes in the position of convection on the western flank of the system between t_{sim} =18 and 22 hr). However, as the cold

pool produced by the training line deepened from < 1 km to ~ 1.5 km, parcels were apparently lifted a sufficient distance over the boundary to overcome the stabilization affects discussed in section 5d, and the southwestern flank of the deeper cold pool region became a direct source for convective initiation (this is inferred from Fig. 5.21). The spatial coverage and maximum values of IPI_{MESO} gradually increased along the SW flank of the convection beyond t_{sim} =22, suggesting that the cold pool continued to deepen, and that this lift over the cold pool was sufficient to trigger convection (Fig. 5.22c-f). Convection therefore followed this deeper cold pool region moved southwestward (Fig. 5.22) beyond t_{sim} =22 hr, and the MCS ultimately moved southward away from the region where heavy rainfall was produced (this increase southward "pull" by processes related to IPI_{MESO} occurred in conjunction with a weakening of the westward "pull" by synoptic scale processes).

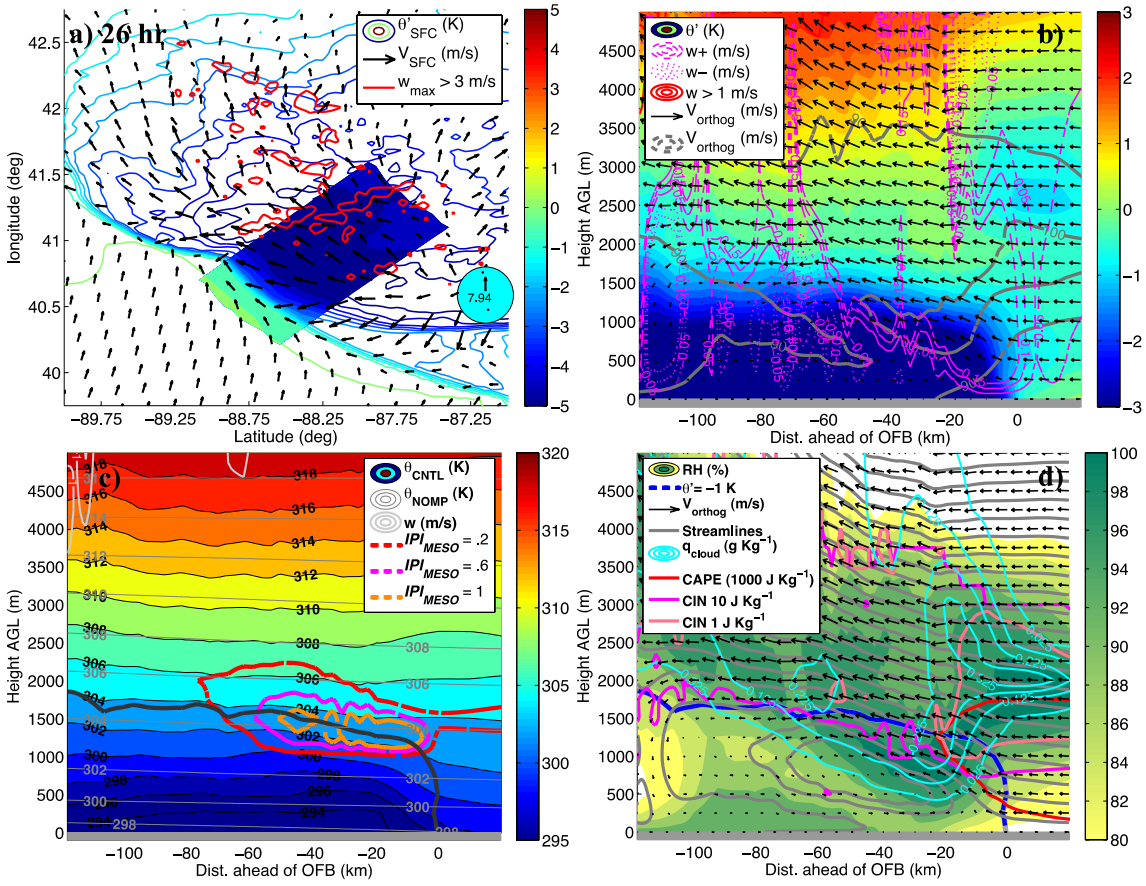

Fig. 5.22. Panel a: as in Fig. 5.11a, but at t_{sim}=26 hr. Panel b: as in Fig. 5.11c, but at t_{sim}=26 hr. Panel c: as in Fig. 5.12a, but for t_{sim}=26 hr. Panel d: as in Fig. 5.12d, but for t_{sim}=26 hr.

5.6. Summary and Discussion

In this research, a simulation of a training line – adjoining stratiform (TL/AS) MCS (conducted by PS2015b) was analyzed in order to elucidate the systems governing dynamics. Composite atmospheric fields were used as initial and lateral boundary conditions (ICs and LBCs) for this simulation. These ICS and LBCs included the meso-γ to synoptic scale features that are typically present in heavy-rain-producing quasi-stationary MCS events, such as a low-level jet terminus, quasi-stationary low-level frontal zone, upper level jet entrance region, and a region of locally maximized low-level ascent. The simulation produced an MCS that well emulated the typical observed characteristics of TL/AS events, and produced rainfall totals in excess of 200 mm.

An initial forward propagating MCS developed along the nose of the low-level jet, and was driven southeastward by kinematic lifting along its OFB. The large-scale environment persistently lifted parcels with high CAPE and RH to their levels of free convection upstream of the initial MCS, which explains upstream propagation of the system. Low-level low-pressure perturbations along the initial MCS generated deformation and convergence in the systems wake, which facilitated the organization of the backbuilding convection on the western side of the system into a training line. Horizontal advection of momentum and high θ_e air by the low-level jet took 1-2 hours to replenish high θ_e to the western flank of the MCS (where it had been overturned by the initial non-stationary convection). This resulted in the development of an upstream training line 1-2 hours after, rather than in immediate succession with passage of the initial MCS.

Unlike the southeast flank of the OFB, the wind shear profile over the depth of the southwest flank of the OFB was unfavorable for robust kinematic lifting and triggering of convection. Additionally, a heating-over-cooling pattern stabilized flow as it passed over the southwestern OFB. This stabilization process resulted from latent release in the upper portion of the high CAPE layer, and adiabatic cooling from ascent in the lower portion of the high CAPE layer. The flow then traveled 80-100 km north of the OFB, was gradually lifted to the point of saturation, and entered convective updrafts within the training line. This additional northward travel and lift required to destabilizes parcels explains the geographic separation between the southwestern OFB and the training line.

We have discussed three general scenarios of flow interaction with the OFB in our simulation. In the favorable wind shear scenario for kinematic lifting along the OFB (Fig. 6.23a), the strong kinematic lifting apparently dominates over any thermodynamic stabilizing affects similar to those discussed in section 5d. In the unfavorable wind shear scenario (where lifting along the OFB is gradual), whether or not convection triggers near the boundary (e.g. within O 10 km of the boundary) depends on – at the least – the depth of the cold pool, where a deeper cold pool (in this case, ~ 1.25-1.5 km) results in convection near the boundary (Fig. 5.23c), and a shallower cold pool (in this case. < 1 km) results in thermodynamic stabilization of the flow that encounters it (Fig. 6.23b). The unfavorable wind shear scenario is likely additionally sensitive to a variety of factors: e.g. near-surface moisture, CAPE and CIN (as demonstrated by Schumacher 2015), the height of maximum CAPE, and the strength of low-level wind shear. We seek to test these sensitivities with an array of simulations – the results of which will be summarized in future articles.

The initiation and positioning of the initial forward-propagating MCS, and upstream back-building during the period of training of convection were accomplished by gradual lifting associated with large-scale warm air advection. As the cold pool depended, and large scale lifting decreased in intensity later in the systems lifetime, propagation of the MCS was "handed off" from large-scale lift produced by the LLJ encountering the mesoscale cold pool,

Our results provide valuable reconciliation between previous studies of TL/AS-like MCSs, where enhanced lifting of parcels over a cold pool was heavily implicated in upstream propagation in some cases (e.g. Keene and Schumacher 2013; PS2015a), whereas other systems are thought to be predominately "externally driven", such as "frontal overrunning" (e.g. Maddox et al. 1979; Moore et al. 2003; Schumacher et al. 2011) events. Specifically, this study suggests that there is likely a continuum between "frontally driven" and "cold-pool-driven" propagation of TL/AS MCS events (where many events feature both modes of propagation, and some feature one or the other). What is, in fact, important to system propagation is that isentropic up-glide occurs in the presence of moisture and instability, regardless of this up-glide is accomplished by flow encountering an outflow boundary or a synoptic front. From a forecasting standpoint, externally driven events are likely more predictable (due to their dependence on synoptic flow patterns) than cold-pool driven events, and it may be useful for forecasters to discriminate between the two types of forcing mechanisms. Future work will address whether the *IPI* parameters introduced in this study may yield utility in predicting the motion of nocturnal MCSs, and discriminating synoptically driven from cold pool driven events.

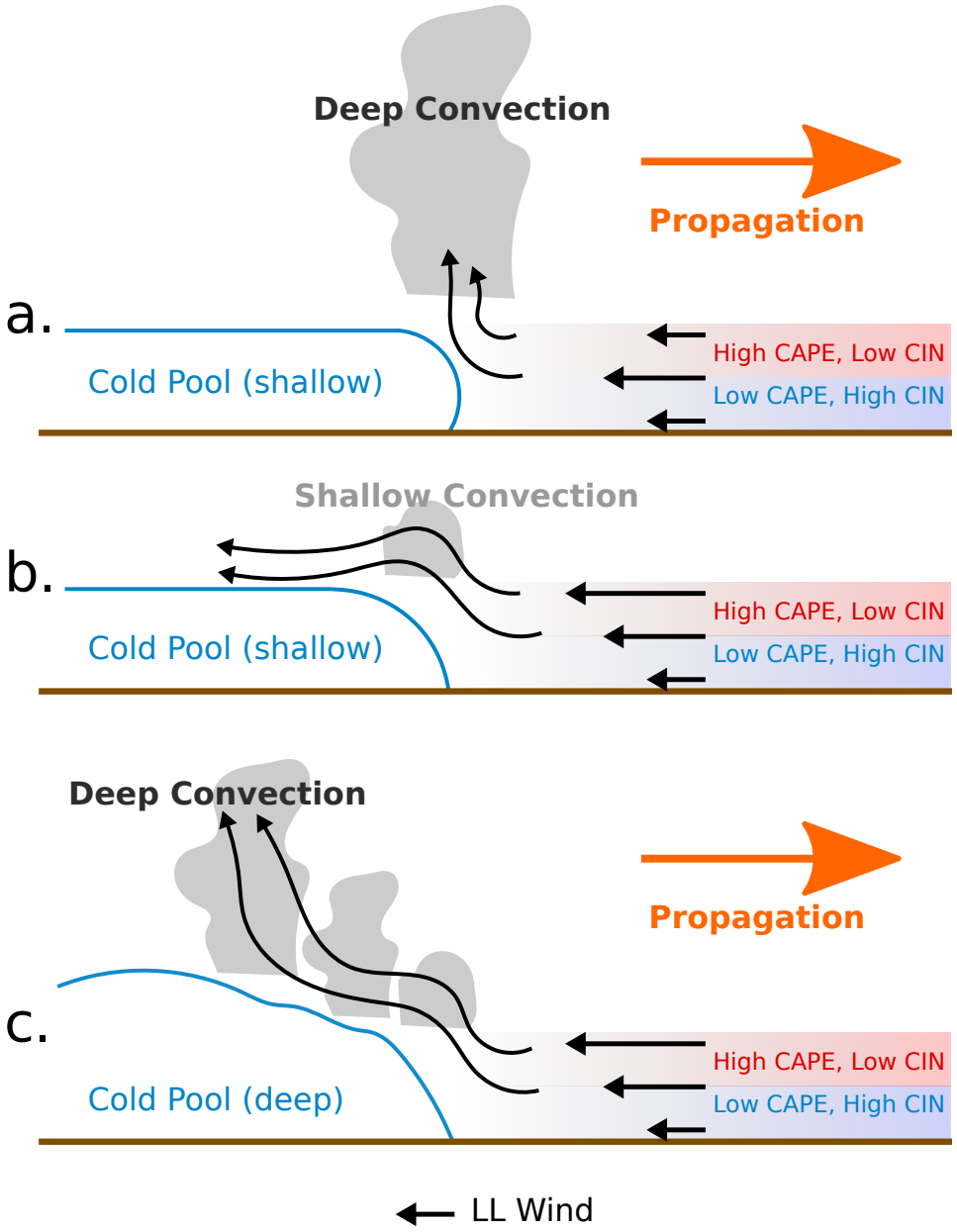

Fig. 5.23. Schematic of the three types of flow interactions with outflow boundaries identified in the MCS simulated in this study. Panel a: wind shear in the high CAPE layer is favorable for strong kinematic lifting along the boundary, which triggers new convective cells along the OFB and leads to propagation in the direction of the OFB movement. Panel b: wind shear in the high CAPE layer is unfavorable for strong kinematic lifting along the boundary (in this scenario, convection initiates from large-scale lifting ~ 60-80 km after flow encounters the boundary). Despite the cold pool depth being similar to the situation in panel a, the magnitude of lifting over the boundary is considerably smaller. The weak lifting that is present stabilizes the flow, and no deep convection forms along the boundary. Panel c: wind shear in the high CAPE layer is unfavorable for strong kinematic lifting along the boundary; however, flow is forced to gradually ascend a sufficient distance over the deeper cold pool for most parcels to reach their LFCs. Deep convection is initiated near the OFB, and the system propagates in the direction of the OFB motion.

CHAPTER 6

ONGOING AND FUTURE WORK

6.1. Justification of the usage of the NOMP simulation in chapters 4 and 5

Several persons (including a peer reviewer) mentioned the potential for unrealistic atmospheric processes in the NOMP simulation, where no microphysical processes – including latent heating – were allowed to occur. The reviewer was specifically concerned with unrealistically high surface pressure forming in the NOMP simulation beneath the region of locally maximized warm air advection due to a lack of compensation for ascent-driven adabatic cooling with latent heating.

We investigated the potential for unrealistically high surface pressure (per suggestion from reviewer 2) in the NOMP simulation. If there were substantial unrealistic low-level cooling in the region of low-level saturation (where microphysics are not acting to offset adiabatic cooling from ascent), this would result in a region of locally high column integrated buoyancy and likely manifest in the surface pressure field as region where pressure increases with time to a greater extent than surrounding regions (where saturation is not achieved aloft, and vertical motion is presumably slower).

There is no evidence of locally high pressure in the region of saturation in the NOMP simulation (Figs. 6.1, 6.2) – in fact, there is a weakly evident low-pressure trough extending from southern IA through the region of saturation. While pressure increased everywhere between 16 hr and 24 hr, the increase was minimized within the region of saturation (Fig. 6.3 this minimized pressure increase likely reflects large-scale dynamic forcing). The peer reviewer found similar results when examining their simulation of a similar upstream propagating MCS.

While it appears unlikely that realistic cooling is occurring based on the analysis shown here, readers must approach the interpretation of the perturbations with caution, given that there are really two latent-heat related processes in the CNTL simulation that are not represented in the NOMP simulation. The dominant process appears to be latent heating associated with deep convection (this assertion is corroborated by temperature anomalies at 1.5 km AGL having been restricted to the immediate region of convection). The secondary process is the upscale influence of broad low-level saturation and latent heating from synoptic scale ascent. We now emphasize this point in the text.

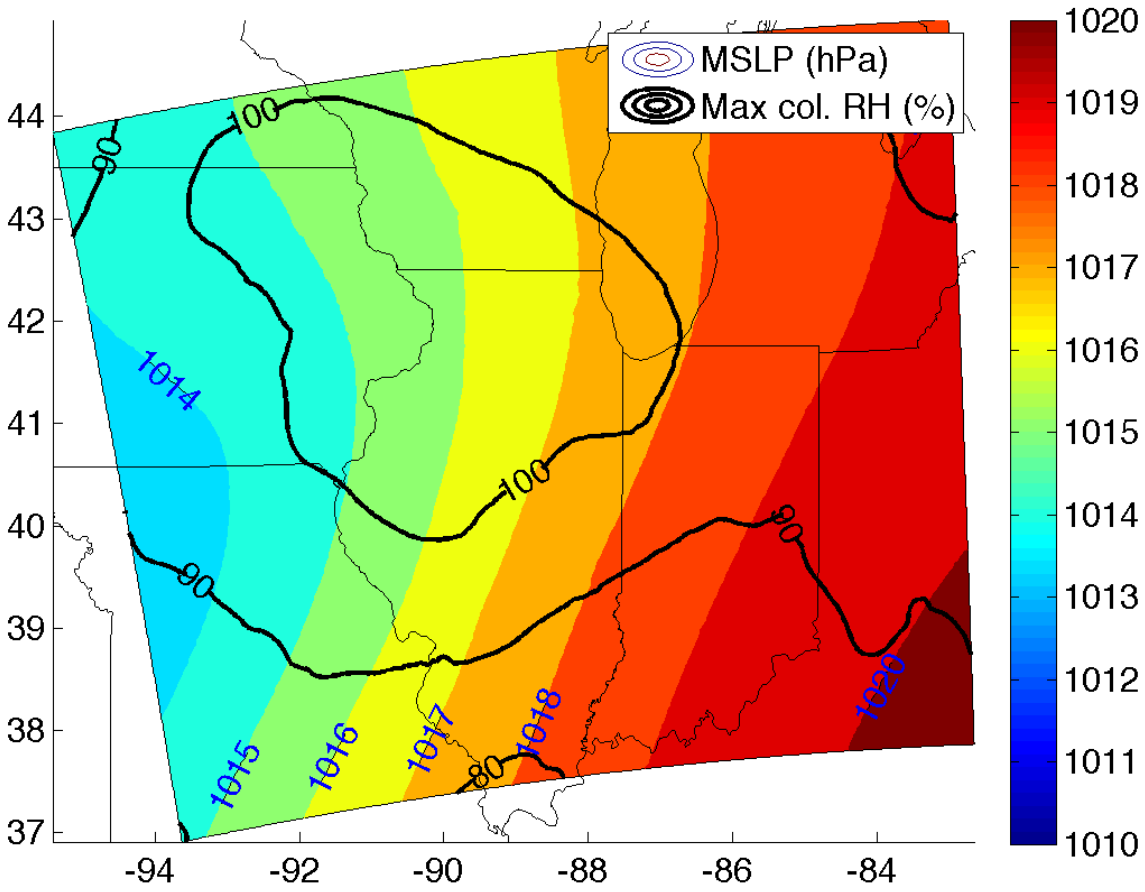

Fig. 6.1. Surface pressure (shading, hPa), and maximum column relative humidity (black contours, %) from the inner domain of the NOMP simulation at t_{sim}=16 hr.

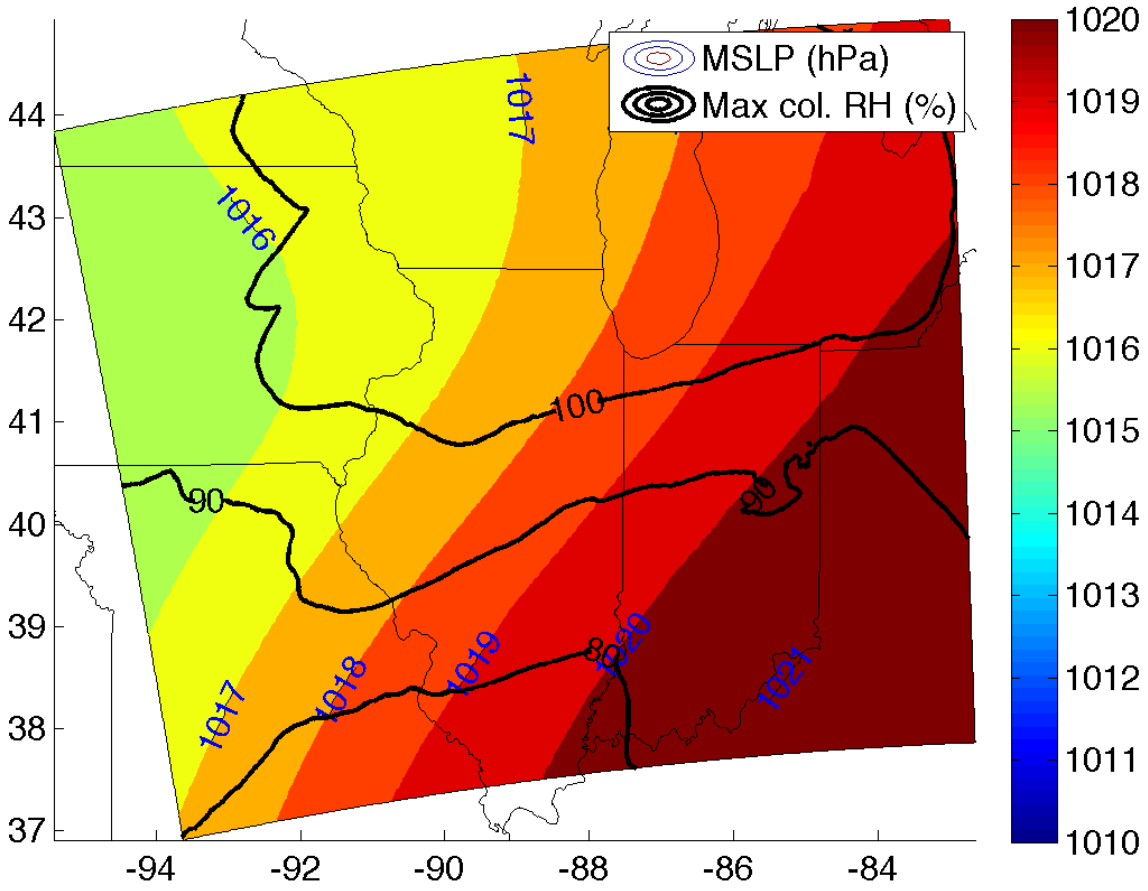

Fig. 6.2. Same as Fig. 1, but at t_{sim}=24 hr.

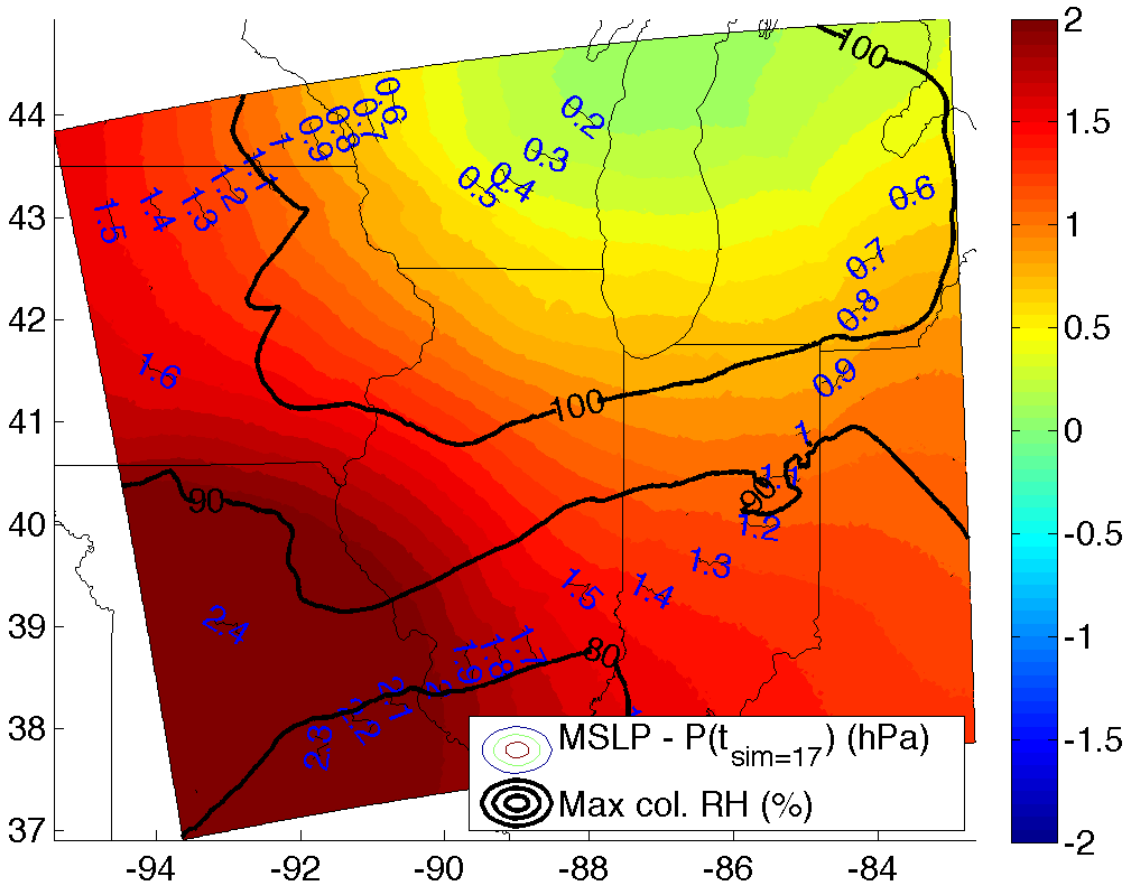

Fig. 6.3. Surface pressure difference between t_{sim}=16 hr and t_{sim}=24 hr (shading, hPa), and maximum column relative humidity at t_{sim}=24 hr (black contours, %).

6.2. Sensitivity analysis of the quasi-idealized simulation

In addition to the CNTL simulation of Chapters 4 and 5, we conducted the Added-Moisture (ADMS) simulation, where equation (4.2) was modified:

$$RH_m(p) = \begin{cases} RH_i(p) + A\exp\left[-\dfrac{(p_{ref}-p)^2}{\sigma^2}\right] & \text{if } (p_{ref}-p) \le p_{cutoff}, (p_{ref}-p) > 0 \\ RH_i(p) & \text{if } (p_{ref}-p) > p_{cutoff}, (p_{ref}-p) > 0. \\ RH_i(p) + A & \text{if } (p_{ref}-p) \le 0 \end{cases} \quad (6.1)$$

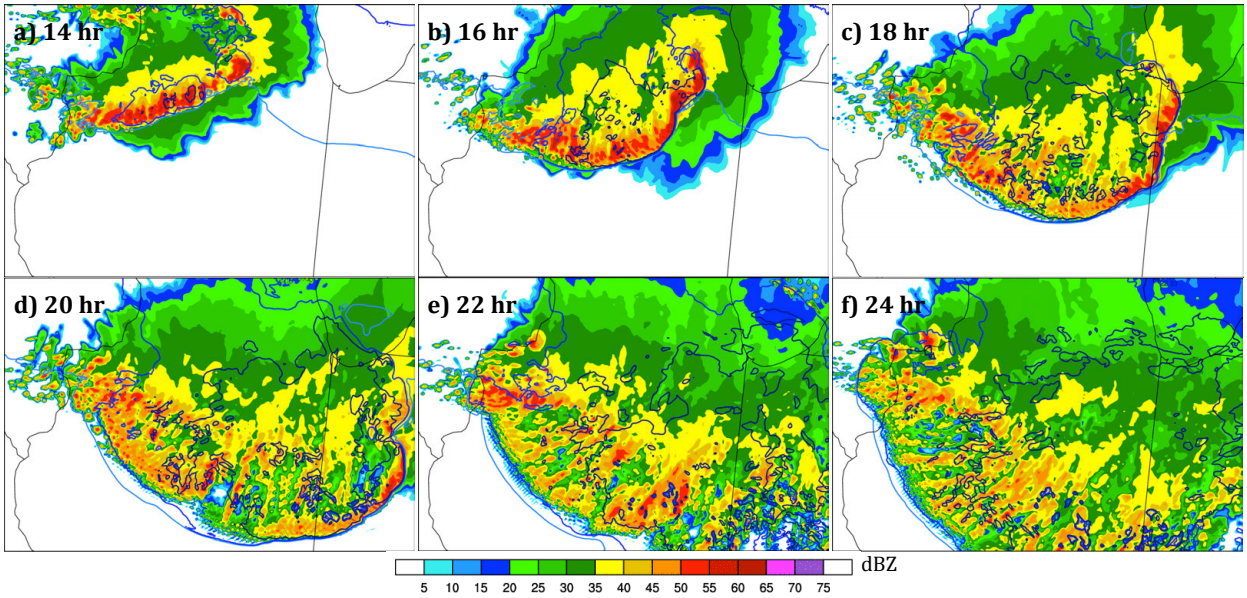

Fig. 6.4. Simulated composite radar reflectivity images from ADMS run (shading, dBZ, with an otherwise identical model configuration to the CNTL run). Simulation times for the 4-km domain are shown in the lower right panel of each figure. The peak 1-hour rainfall in the composites occurred at simulation hour 12. Same as Fig. 4.14.

Here, the added RH was uniformly 10% below p_{ref} (rather than having decreased exponentially from 10% below p_{ref} as in equation 4.1). This modification resulted in a small dew point increase, large CAPE increase, and CIN decrease in the PBL. The initial hypothesis was that the increased CAPE and decreased CIN in the PBL would mitigate the stabilization affect as flow encountered the southwestern OFB (discussed in chapter 5), and that convection would occur closer to the southwestern OFB in the ADMS run, when compared to the CNTL simulation. Indeed, Fig. 6.4 confirms that, while training of convection still occurs in the ADMS run, ROD no longer occurs, and the training convective line remains very close to the southwestern outflow boundary.

We also conducted a run analogous to the CNTL simulation, but with 41 vertical levels (Rather than 31 in the case of the CNTL simulation) in order to test the sensitivity of the simulated evolution to vertical model resolution. While we do not explicitly report on the results

here, they were *very* similar to that of the CNTL run, with similar rainfall totals and a simulated radar reflectivity evolution.

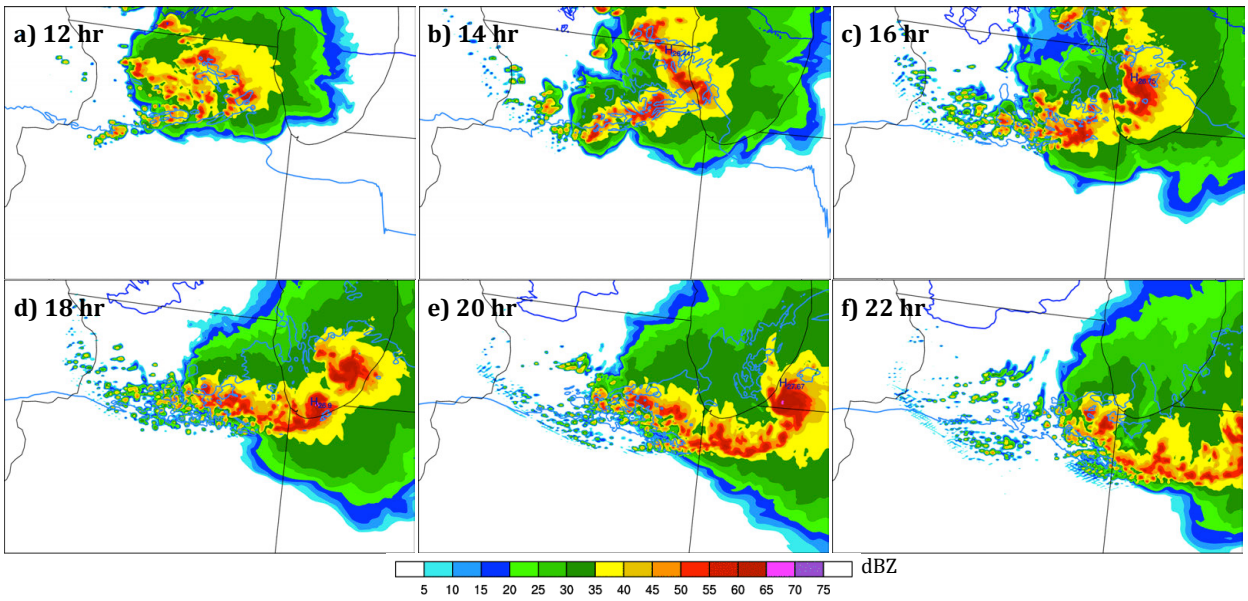

Fig. 6.5. Same as Fig. 6.1, but for the NOEV run.

We presented evidence in chapter 5 that large-scale (i.e. *external*) atmospheric lift was predominately responsible for where upstream backbuilding and training occurred (rather than enhanced isentropic upglide over the systems cold pool). To further test this theory, we conducted the No Evaporation (NOEV) run, where the temperature tendency due to evaporation was turned off (this modification precluded the formation of a surface cold pool). Fig. 6.5 confirms that convection trained over a nearly identical geographic region with a surface cold pool absent.

In a future article, we seek to analyze the results of sensitivity simulations such as these in order to refine the theories developed in Chapters 4 and 5, and to test new hypotheses. Additional proposed simulations include those with identical configurations to the CNTL, but different microphysical parameterization schemes, and idealized 2-dimensional simulations of flow interactions with outflow boundaries to more comprehensively test the sensitivity of the

thermodynamic stabilization affect discussed in chapter 5 to the low-level temperature and moisture profile.

6.3. Analysis of the quasi-idealized simulation of a synoptic-type TL/AS MCS

As discussed in Chapter 4.3, a synoptic-type TL/AS MCS (Fig. 6.6) was simulated for composite ICs and LBCs using the model configuration described in Chapter 4, but with composites generated from synoptic type events (rather than warm season events).

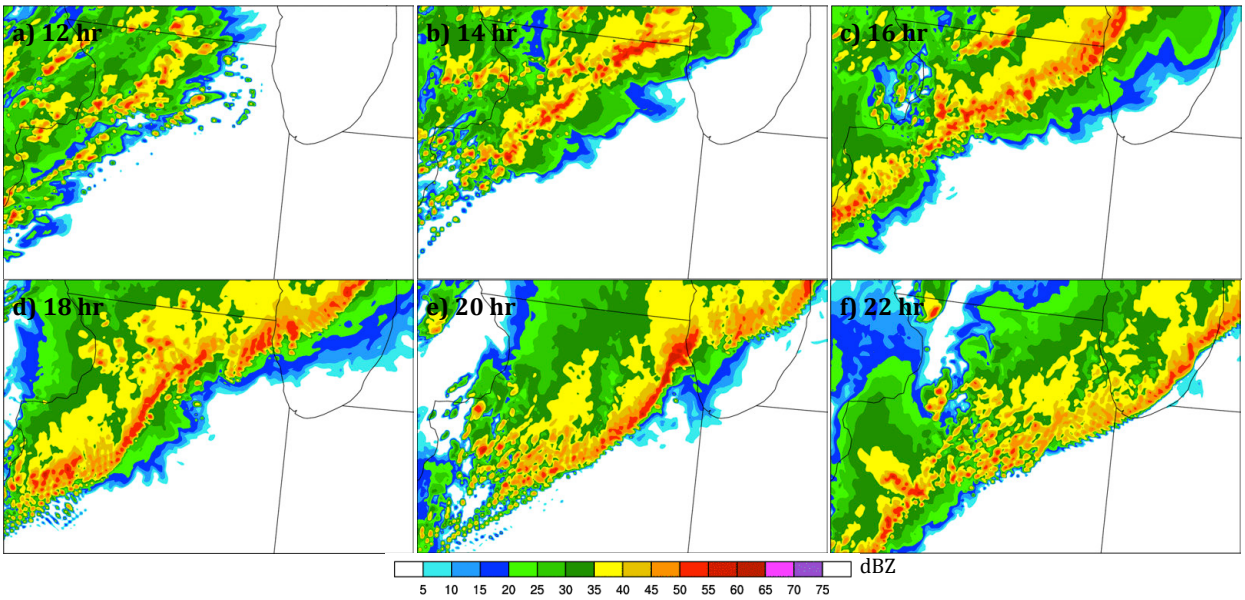

Fig. 6.6. Simulated composite radar reflectivity images from the simulation driven by synoptic-type composite initial and lateral boundary conditions (shading, dBZ, with an otherwise identical model configuration to the CNTL run). Simulation times for the 4-km domain are shown in the lower right panel of each figure. The peak 1-hour rainfall in the composites occurred at simulation hour 12. Same as Fig. 4.14.

This simulation reproduced many of the radar-reflectivity characteristics that occur in observed synoptic type TL/AS systems. The structure, evolution, and dynamics of this simulated system will be analyzed in a future article.

6.4. Other Related Proposed Projects

- A comparison of the synoptic environments from non-stationary, non-training nocturnal MCSs to quasi-stationary, training nocturnal MCSs.
- Simulations from composite atmospheric fields of different MCS archetypes.
- An analysis of observations of elevated systems obtained from the Plains Elevated Convection at Night (PECAN) field campaign.
- Idealized simulations to test the sensitivity of upscale growth from supercells to MCSs to a stabilizing PBL, increasing low-level jet strength, and increasing low-level convergence as convection transitions from a daytime to nocturnal regime.

CHAPTER 7

SUMMARY OF OVERALL CONCLUSIONS

- **Heavy rain producing Training Line – Adjoining Stratiform (TL/AS) MCSs** primary fall within **two distinct large-scale atmospheric environmental setups**. Both types of events typically occur within the right entrance region to an upper-level jet streak, along the nose of a low-level jet, along a quasi-stationary east-to-west oriented synoptic fontal zone, and within a region of **locally maximized low-level warm air advection**.

  Synoptic Events occur during the spring and fall, to the east of a large-amplitude upper level trough, and in conjunction with strong large-scale forcing for ascent (when compared to warm season events). Their aspect ratios (*aspect ratio* refers to the along-convective-line to across convective line ratio) are larger than unity, and they are frequently followed by the passage of a forward moving squall line and cold front.

  Warm Season Events occur during the summer months, along the northwestern periphery of a large-scale high-pressure ridge, and where large-scale forcing for ascent is weaker than synoptic events. Their aspect ratios are closer to unity than synoptic events, and they are frequently **proceeded by the passage of a forward moving trailing stratiform (TS) type MCS**. Their radar reflectivity evolutions are complex, featuring **multiple convective lines with different ground-relative orientations**. This research primarily addresses the dynamics of warm season Events.

- **External factors** (e.g. processes occurring on larger scales than the MCS, and unrelated to upscale convective feedbacks) that contribute to the **quasi-stationary nature of warm-season events** (e.g. their propensity to propagate upstream) include the **persistent supply of the ingredients for convection to a fixed location** – e.g. moisture and

instability transport along a southeasterly low-level jet, and low-level lifting associated with persistent and locally maximized warm air advection.

- **Internal factors** (e.g. processes resulting from upscale convective feedbacks) that influence convective evolution of warm season TL/AS MCSs include:
  - **Surface cold pool** production by rain cooled outflow. Convection tends to propagate with (**does not propagate with**) the southeastern (**southwestern**) flank of the **outflow** boundary due to favorable (**unfavorable) vertical wind shear** conditions over the depth of the cold pool. This explains why progressive (eastward moving) convective systems often preceded training convective lines (e.g. convection likes to 'follow' the southeastern outflow boundary, but 'ignores' the southwestern outflow boundary).
  - **Southwesterly flow along the low-level jet** requires 1-2 hours to **re-enter the region** that was **convectively overturned** by the progressive convective system, resulting in a **temporal offset** between the passage of **the initial convective system**, and the development of a **new training line**. A combination **of large-scale warm air advection**, and sometimes-**enhanced isentropic up-glide** as parcels ascend over the cold pool usually serves as a **triggering mechanism** for the upstream convective line. These processes **gradually lift** the flow as it moves past the surface outflow boundary (**contrasted with the strong, abrupt lifting along the southeastern outflow boundary**), and additional northward travel of flow is required beyond the surface outflow boundary before convection can trigger.
  - Flow is **thermodynamically stabilized** as it **ascends over the southwestern outflow boundary**, due to a pattern of adiabatic cooling under latent heating within the layer

of maximum CAPE. This prohibits convective development near the outflow boundary. Gradual lift must then re-erode the newly enhanced connective inhibition as flow continues to move north of the outflow boundary. This explains the **geographic offset between the southwestern outflow boundary and training convection**.

- In many cases, the **training line** (which may persist for several hours at a fixed location) will **eventually move southeastward**. This results when the **cold pool becomes sufficiently strong** to **drive a newly enhanced surface outflow boundary southeastward**. As this newly enhanced boundary moves southeastward, it once again encounters favorable wind shear conditions for triggering of new convective cells, and convection therefore propagates along it.

REFERENCES

Augustine, J. A., and F. Caracena, 1994: Lower-Tropospheric Precursors to Nocturnal MCS Development over the Central United States. *Wea. Forecasting,* **9**, 116–135.

Barnes, S., 1964: A technique for maximizing details in numerical weather map analysis. *J. Appl. Meteor.*, **9(3)**, 396‑409.

Benjamin, S. G., Grell, G. A., Brown, J. M., and Smirnova, T. G., 2003: Mesoscale weather prediction with the RUC hybrid isentropic / terrain-following coordinate model. *Mon. Wea. Rev.* **132.** 473-494.

Bosart, L. F., and F. Sanders, 1981: The Johnstown Flood of July, 1977: a long-lived convective system. *J. Atmos. Sci.*, **38**, 1616–1642.

Bryan, G. H., J. C. Wyngaard, and M. Fritsch, 2003: Resolution requirements for the simulation of deep moist convection. Mon. Wea. Rev., 131, 2394–2416,

Bryan, G. H. and M. D. Parker, 2010: Observations of a Squall Line and Its Near Environment Using High-Frequency Rawinsonde Launches during VORTEX2. *Mon. Wea. Rev.* **138**. 4076-4097.

Chappell, C. F., 1986: Quasi-stationary convective events. *Mesoscale Meteorology and Forecasting*, P.S. Ray, Ed., Amer. Meteor. Soc., 289-310.

Coniglio, M. C., and D. J. Stensrud, 2001: Simulation of a progressive derecho using composite initial conditions. Mon. Wea. Rev., **129**, 1593-1616.

Corfidi, S. F., J. H. Merritt, and J. M. Fritsch. 1996: Predicting the Movement of Mesoscale Convective Complexes. *Wea. Forecasting*, **11**, 41-46.

Corfidi, S. F., 2003: Cold Pools and MCS Propagation: Forecasting the Motion of Downwind-Developing MCSs. *Wea. Forecasting*. **18**, 997-1017.

Corfidi, S. F., S. J. Corfidi, and D. M. Schultz, 2008: Elevated convection and castellanus: Ambiguities, significance, and questions. *Wea. Forecasting*, **23**, 1280–1303.

Crook, N. A., and M. W. Moncrieff, 1988: The effect of large-scale convergence on the generation and maintenance of deep moist convection. *J. Atmos. Sci.*, **45**, 3606–3624.

Dee, D.P., with 35 co-authors, 2011: The ERA-Interim reanalysis: configuration and performance of the data assimilation system. *Quart. J. R. Meteorol. Soc.*, **137**, 553-597

Doswell, C. A., Brooks, H. E., and Maddox, R. A. 1996: Flash Flood Forecasting: An Ingredients-Based Methodology. *Wea. Forecasting*. **11.** 560-581.

Du, Y., and R. Rotunno, 2014: A Simple Analytical Model of the Nocturnal Low-Level Jet over the Great Plains of the United States. *J. Atmos. Sci.*, **71**, 3674–3683.

Dudhia, J., 1989: Numerical study of convection observed during the Winter Monsoon Experiment using a mesoscale two-dimensional model. *J. Atmos. Sci*., **46**, 3077-3107.

Fovell, R. G., and P. S. Dailey, 1995: The temporal behavior of numerically simulated multicell-type storms. Part I. Modes of behavior. *J. Atmos. Sci.*, **52**, 2073–2095.

Fovell, R. G., and Tan, P. H., 1995: The temporal behavior of numerically simulated multicell-type storms. Part II. The convective cell life cycle and cell regeneration. *Mon. Wea. Rev.*, **126**, 551-577.

French, A. J., and M. D. Parker, 2010: The response of simulated nocturnal convective systems to a developing low-level jet. *J. Atmos. Sci.*, **67**, 3384-3408.

Fritsch, J.M., J. D. Murphy, and J. S. Kain, 1994: Warm-core vortex amplification over land. *J. Atmos. Sci.*, **51**, 1780–1807.

Galarneau Jr., T. J., Bosart, L., Schumacher, R. S., 2010: Predecessor Events ahead of Tropical Cyclones. *Mon. Wea. Rev.* **138.** 3272-3297.

Grell, G. A. and D. Devenyi, 2002: A generalized approach to parameterizing convection combining ensemble and data assimilation techniques. *Geoph. Res. Let*., **29**, 10.1029/2002GL015311, 2002.

Houze, Robert A., M. I. Biggerstaff, S. A. Rutledge, B. F. Smull, 1989: Interpretation of Doppler Weather Radar Displays of Midlatitude Mesoscale Convective Systems. *Bull. Amer. Meteor. Soc.*, **70**, 608–619.

Houze, R.A., Jr., B.F. Smull, and P. Dodge, 1990: Mesoscale organization of springtime rainstorms in Oklahoma. *Mon. Wea. Rev*., **118**, 613–654.

Janjić, Z. I., 1994: The step-mountain eta coordinate model: further developments of the convection, viscous sublayer and turbulence closure schemes. *Mon. Wea. Rev*., **122**, 927-945.

Johns, R. H., and C. A. Doswell III, 1992: Severe local storms forecasting. *Wea. Forecasting*, **7**, 588–612.

Jones, T. A., K. M. McGrath, and J. T. Snow, 2004: Association between NSSL mesocyclone detection algorithm-detected vortices and tornadoes. *Wea. Forecasting*, **19**, 872–890.

Junker, N. W., R. S. Schneider, and S. L. Fauver, 1999: A Study of Heavy Rainfall Events during the Great Midwest Flood of 1993. *Wea. Forecasting*, **14**, 701–712.

Keene, K.M., and R.S. Schumacher, 2013: The bow and arrow mesoscale convective structure. *Mon. Wea. Rev*., **141**, 1648-1672.

Kessler, E. (1969), On the Distribution and Continuity of Water Substance in Atmospheric Circulation, *Meteor. Monogr.*, No. 32, 84 pp., Am. Meteorol. Soc., Boston, Massachussetts.

Klemp, J. B., W. C. Skamarock, and J. Dudhia, 2007: Conservative split-explicit time integration methods for the compressible nonhydrostatic equations. *Mon. Wea. Rev.*, **135**, 2897–2913.

Laing, A. G., and J. M. Fritsch, 2000: The large-scale environments of the global populations of mesoscale convective complexes. *Mon. Wea. Rev*., **128**, 2756–2776.

Lin, Y. and K. E. Mitchell, 2005: The NCEP Stage II/IV hourly precipitation analyses: development and applications. Preprints, *19th Conf. on Hydrology, American Meteorological Society*, San Diego, CA, 9-13 January 2005, Paper 1.2.

Lorenz, E. N., 1969: The predictability of a flow which possesses many scales of motion. *Tellus*, **21**, 289–307.

Maddox, R. A., C. F. Chappell, and L. R. Hoxit, 1979: Synoptic and meso-α-scale aspects of flash flood events. *Bull. Amer. Meteor. Soc.*, **60**, 115–123.

Maddox, R. A., 1980: Meoscale Convective Complexes. *Bull. Amer. Meteor. Soc.*, **61**, 1374–1387.

Maddox, R. A., 1983: Large-Scale Meteorological Conditions Associated with Midlatitude, Mesoscale Convective Complexes. *Mon. Wea. Rev.*, **111**, 1475–1493.

Mahoney, K. M., G. M. Lackmann, and M.D. Parker, 2009: The role of momentum transport in the motion of a quasi-idealized mesoscale convective system. *Mon. Wea. Rev.*, **137**, 3316–3338.

Marsham, J. H., S. B. Trier, T. M. Weckwerth, and J. W. Wilson, 2011: Observations of Elevated Convection Initiation Leading to a Surface-Based Squall Line during 13 June IHOP_2002. *Mon. Wea. Rev.*, **139**, 247–271.

Mercer, A. E., C. M. Shafer, C. A. Doswell, L. M. Leslie, and M. B. Richman, 2012: Synoptic composites of tornadic and nontornadic outbreaks. *Mon. Wea. Rev*., **140**, 2590-2608.

Mesinger, F., and Coauthors, 2006: North American Regional Reanalysis. *Bull. Amer. Meteor. Soc.*, **87**, 343–360.

Mitchell, K. E., D. Lohmann, P. R. Houser, E. F. Wood, J. C. Schaake, A. Robock, B. A. Cosgrove, J. Sheffield, Q. Duan, L. Luo, R. W. Higgins, R. T. Pinker, J. D. Tarpley, D. P. Lettenmaier, C. H. Marshall, J. K. Entin, M. Pan, W. Shi, V. Koren, J. Meng, B. H. Ramsay, and A. A. Bailey, 2004: The multi-institution North American Land Data Assimilation System (NLDAS): Utilizing multiple GCIP products and partners in a continental distributed hydrological modeling system, *J. Geophys. Res*., **109**, doi:10.1029/2003JD003823.

Mlawer, E. J., S. J. Taubman, P. D. Brown, M. J. Iacono, and S. A Clough, 1997: Radiative transfer for inhomogeneous atmosphere: RRTM, a validated correlated-k model for the longwave. *J. Geophys. Res.* , **102**, 16663-16682.

Monaghan, A. J., D. L. Rife, J. O. Pinto, C. A. Davis, and J. R. Hannan, 2010: Global Precipitation Extremes Associated with Diurnally Varying Low-Level Jets. *J. Climate*, **23**, 5065–5084.

Moore, J. T., Glass, F. H., Graves, C. E., Rochette, S. M., and Singer, M. J., 2003: The Environment of Warm-Season Elevated Thunderstorms Associated with Heavy Rainfall over the Central United States. *Wea. Forecasting*, **18**, 861-878.

Morrison, H., and W. W. Grabowski, 2008: A novel approach for representing ice microphysics in models: Description and tests using a kinematic framework. *J. Atmos. Sci.*, **65**, 1528–1548.

National Weather Service Quad Cities Office, cited 2014: Historic Heavy Rain and Flash Flooding in Dubuque and Jo Daviess Counties 07/27-07/28/2011. [Available online at http://www.crh.noaa.gov/dvn/?n=event_072711_dubuqueflashflood.]

Naylor, J., and M. S. Gilmore, 2012: Convective initiation in an idealized cloud model using an updraft nudging technique. *Mon. Wea. Rev.*, **140**, 3699–3705.

Parker, M.D. and R.H. Johnson, 2000: Organizational modes of midlatitude mesoscale convective systems. *Mon. Wea. Rev*., **128**, 3413-3436.

Parker, M. D., and R. H. Johnson, 2004a: Simulated convective lines with leading precipitation. Part I: Governing dynamics. *J. Atmos. Sci.*, **61**, 1637-1655.

Parker, M. D., and R. H. Johnson, 2004c: Structures and dynamics of quasi-2D mesoscale convective systems. *J. Atmos. Sci.*, **61**, 545–567.

Parker, M. D., and R. H. Johnson, 2004b: Simulated convective lines with leading precipitation. Part II: Evolution and maintenance. *J. Atmos. Sci.*, **61**, 1656-1673.

Parker, M. D., 2007: Simulated Convective Lines with Parallel Stratiform Precipitation. Part I: An Archetype for Convection in Along-Line Shear. *J. Atmos. Sci.*, **64**, 267–288.

Parker, M. D., 2008: Response of simulated squall lines to low-level cooling. *J. Atmos. Sci.*, **65**, 1323–1341.

Peters, J. M. and P. J. Roebber, 2014: Synoptic Control of Heavy-Rain-Producing Convective Training Episodes. *Mon. Wea. Rev.*, **142**, 2464–2482.

Peters, J. M. and R. S. Schumacher, 2014: Objective Categorization of Heavy-Rain-Producing MCS Synoptic Types by Rotated Principal Component Analysis. *Mon. Wea. Rev.*, **142**, 1716–1737.

Peters, J. M. and Russ S. Schumacher, 2015a: Mechanisms for Organization and Echo Training in a Flash-Flood-Producing Mesoscale Convective System. *Mon. Wea. Rev.*, **143**, 1058–1085.

Peters, J. M. and Russ S. Schumacher, 2015b: The Simulated Structure and Evolution of a Quasi-Idealized Warm Season Convective System with a Training Convective Line. *J. Atmos. Sci.*, In Press.

Pitchford, K. L., and J. London, 1962: The Low-Level Jet as Related to Nocturnal Thunderstorms over Midwest United States. *J. Appl. Meteor.*, **1**, 43–47.

Richman, M. B., 1986: Rotation of principal components. *J. Climatol*., **6**, 293–335.

Raymond. D. J. and H. Jiang. A Theory for Long-Lived Mesoscale Convective Systems. *J. Atmos. Sci.* **47**. 3067-3077.

Roebber, P. J., K. L. Swanson, and J. K. Ghorai, 2008: Synoptic control of mesoscale precipitating systems in the Pacific Northwest. *Mon. Wea. Rev.,* **136,** 3465-3476.

Rotunno, Richard, Joseph B. Klemp, 1982: The Influence of the Shear-Induced Pressure Gradient on Thunderstorm Motion. *Mon. Wea. Rev.*, **110**, 136–151.

Rotunno, R., J. B. Klemp and M. L. Weisman, 1988: A theory for strong long-lived squall lines. *J. Atmos. Sci.*, **45**, 463–485.

Schmidt, J. M., and W. R. Cotton, 1990: Interactions between up- per and lower tropospheric gravity waves on squall line structure and maintenance. *J. Atmos. Sci.*, **47**, 1205–1222.

Schumacher, R. S., and R. H. Johnson, 2005: Organization and environmental properties of extreme-rain-producing mesoscale convective systems. *Mon. Wea. Rev*., **133**, 961-976.

Schumacher, R.S., and R.H. Johnson, 2006: Characteristics of United States Extreme Rain Events During 1999-2003. *Wea. Forecasting*, **21**, 69-85.

Schumacher, R. S., and R. H. Johnson, 2008: Mesoscale Processes Contributing to Extreme Rainfall in a Midlatitude Warm-Season Flash Flood. *Mon. Wea. Rev*., **136**, 3964-3986.

Schumacher, R. S., and R. H. Johnson, 2009: Quasi-Stationary, Extreme-Rain-Producing Convective Systems associated with Midlevel Cyclonic Circulations. *Wea. Forecasting*, **24**, 555-575.

Schumacher, R.S., 2009: Mechanisms for Quasi-Stationary Behavior in Simulated Heavy-Rain-Producing Convective Systems. *J. Atmos. Sci.*, **66**, 1543-1568.

Schaefer, J., and C. A. Doswell III, 1984: Empirical orthogonal function expansion applied to progressive tornado outbreaks. *J. Meteor. Soc. Japan*, **62**, 929–936.

Schwartz C. S., J. S. Kain, S. J. Weiss, M. Xue, D. R. Bright, F. Kong, K. W. Thomas, J. J. Levit, and M. C. Coniglio, 2009: Next-Day Convection-Allowing WRF Model Guidance: A Second Look at 2-km versus 4-km Grid Spacing. Mon. Wea. Rev., **137**, 3351–3372.

Skamarock, W. C, J. B. Klemp, J. Dudhia, D. O. Gill, D. M. Barker, Duda, M. G, Huang, X., W. Wang, and J. G. Powers, 2008: A description of the Advanced Research WRF version 3. NCAR Tech. Note NCAR/TN- 475 STR, 105 pp.

Smull, B. F., and R. A. Houze, Jr., 1987: Rear inflow in squall lines with trailing stratiform precipitation. *Mon. Wea. Rev.*, **115**, 2869-2889.

Stensrud, D. J., and J. M. Fritsch, 1993: Mesoscale convective systems in weakly forced large-scale environments. Part I: Observations. *Mon. Wea. Rev.*, **121,** 3326–3344.

Thompson, G., R. P. Field, R. M. Rasmussen, and W. D. Hall, 2008: Explicit Forecasts of Winter Precipitation Using an Improved Bulk Microphysics Scheme. Part II: Implementation of a New Snow Parameterization. *Mon. Wea. Rev*., **136**, 5095-5115.

Thompson, D.W.J., and J.M. Wallace, 1998: The Arctic Oscillation signature in the wintertime geopotential height and temperature fields. *Geophys. Res. Lett*., **25**, 1297-1300.

Trier, S. B., and C. A. Davis, 2002: Influence of balanced motions on heavy precipitation within a long-lived convectively generated vortex. *Mon. Wea. Rev.*, **130**, 877–899.

Trier, S. B., C. A. Davis, and D. A. Ahijevych, 2010: Environmental controls on the simulated diurnal cycle of warm-season precipitation in the continental United States. *J. Atmos. Sci.*, **67**, 1066–1090.

Trier, S.B., J.H. Marsham, C.A. Davis, and D. Ahijevych, 2011: Numerical simulations of the post-sunrise reorganization of a nocturnal mesoscale convective system during 13 June IHOP_2002. *J. Atmos. Sci.*, **68**, 2988-3011.

Trier, S. B., C. A. Davis, D. A. Ahijevych, and K. W. Manning, 2014: Use of the parcel buoyancy minimum (Bmin) to diagnose simulated thermodynamic destabilization. Part II: Composite analysis of mature MCS environments. *Mon. Wea. Rev.*, **142**, 967–990.

Tuttle, J.D., and C.A. Davis, 2006: Corridors of warm season precipitation in the central United States. *Mon. Wea. Rev.*, **134,** 2297–2317.

Weisman, M. L. and Klemp. J. B. 1984: The Structure and Classification of Numerically Simulated Convective Storms in Directionally Varying Wind Shears. *Mon. Wea. Rev.,* **112.** 2479-2498.

Weisman, M. L., 1992: The Role of Convectively Generated Rear-Inflow Jets in the Evolution of Long-Lived Mesoconvective Systems. *J. Atmos. Sci.*, **49**, 1826-1847.

Weisman, M. L., W. Skamarock, and J. B. Klemp, 1997: The resolution dependence of explicitly modeled convective systems. *Mon. Wea. Rev.* **125**. 527-548.

Weisman, M. L. and R. Rotunno, 2004: “A theory of strong, long-lived squall lines” revisited. *J. Atmos. Sci.*, **61**, 361-382.

Weisman, M. L., C. Davis, W. Wang, K. W. Manning, and J. B. Klemp, 2008: Experiences with 0–36-h explicit convective forecasts with the WRF-ARW Model. *Wea. Forecasting,* **23,** 407-437.

Wilks, D. S., 2006: *Statistical Methods in the Atmospheric Sciences*. Academic Press, 627 pp.

Wilson, J.W., and R. D. Roberts, 2006: Summary of convective storm initiation and evolution during IHOP: Observational and modeling perspective. *Mon. Wea. Rev.*, **134**, 23–47.